FERMILAB-PROPOSAL-0922

922

A Proposal for a Precision Measurement of the Decay $K_L \to \pi^0 \nu\overline{\nu}$ and Other Rare Processes at Fermilab Using The Main Injector - KAMI

April 2, 2001

T. Alexopoulos
National Technical University of Athens, Greece

C.O. Escobar
Universidade de Campinas, UNICAMP, Campinas, Brasil

J. Nix, G. Perdue, E. Pod, H. Sanders, Y. Wah*
The Enrico Fermi Institute, The University of Chicago, Chicago Illinois 60637

A. R. Barker
University of Colorado, Boulder, Colorado 80309

R. Ford, Y. B. Hsiung, D. A. Jensen, X. R. Qi, R. E. Ray*
Fermi National Accelerator Laboratory, Batavia Illinois 60510

W. Slater
University of California at Los Angeles, Los Angeles, California 90095

K. Kotera, M. Matsumoto, K. Sakashita, T. Ishikawa, T. Yamanaka
Department of Physics, Osaka University, Toyonaka, Osaka, Japan

A.V.Artamonov, I.G.Britvich, V.S.Burtovoy, A.P.Kozhevnikov, V.F.Kurshetsov, L.G.Landsberg, A.A.Lednev, V.V.Molchanov, V.A.Mukhin, V.F.Obraztsov, D.I.Patalakha, V.K.Semenov, V.I. Shelikhov, E.V. Vlasov
Institute for High Energy Physics, Protvino, Russia

M. D. Corcoran
Rice University, Houston, Texas 77005

R. Barbosa, P. Gouffon
University of Sao Paulo, Sau Paulo, Brazil

M. Arenton, B. Cox, E. Frelez, A. Ledovskoy, K.S. Nelson, D. Pocanic
University of Virginia, Charlottesville, VA 22901

* Spokespersons: R. Ray (rray@fnal.gov) and Y. Wah (wah@hep.uchicago.edu)

Acknowledgments

We would like to thank the following individuals for many useful contributions, suggestions and discussions:

K. Arisaka, E. Blucher, E. Cheu, R. Kessler, J. Kilmer, T. Kobilarcik, Ang Lee, V. Prasad, M. G. Schepkin, S. Taeger, A. Toukhtarov, A. Tripathi, M. Votava, B. Wands, B. Winstein

In particular, we acknowledge the generous contribution of A. R. Barker and S. Kettell to the first chapter of this proposal.

Contents

Executive Summary **14**

1 Theoretical Background and Motivation **19**
1.1 Introduction . . . 19
1.2 Standard Model Kaon Triangle . . . 19
1.3 $K_L \to \pi^0 \nu\bar{\nu}$ . . . 21
1.4 Other Standard Model Physics . . . 22
1.4.1 $K_L \to \pi^+\pi^- e^+ e^-$ . . . 22
1.4.2 $K_L \to \mu^+\mu^-$ . . . 24
1.4.3 $K_L \to \gamma\gamma$ and Related Decays . . . 25
1.4.4 $K_L \to \pi^0\gamma\gamma$ . . . 27
1.5 Beyond the Standard Model . . . 28

2 $K_L \to \pi^0 \nu\bar{\nu}$ at KAMI **29**
2.1 Introduction . . . 29
2.2 Experimental Status . . . 30
2.3 The KAMI Experiment . . . 30
2.4 Detector concepts . . . 31
2.5 Kaon Flux . . . 34
2.6 Physics sensitivity . . . 34
2.6.1 Signal and Background Signatures . . . 35
2.6.2 $K_L \to \pi^0 \nu\bar{\nu}$ Acceptance . . . 36
2.6.3 Accidental Losses . . . 37
2.6.4 Summary . . . 39

3 Backgrounds to $K_L \to \pi^0 \nu\bar{\nu}$ **41**
3.1 The KAMI Monte Carlo . . . 41
3.2 $K_L \to 2\pi^0$ . . . 41
3.3 $K_L \to 3\pi^0$ . . . 47
3.4 $K_L \to \pi^+\pi^-\pi^0$ . . . 48
3.5 $K_L \to \pi^\pm e^\mp \nu$ . . . 48
3.6 $K_L \to \gamma\gamma$ . . . 49
3.7 $\Lambda \to \pi^0 n$ . . . 49
3.8 Ξ Decays . . . 50
3.9 Neutron Interactions . . . 51
3.10 K_L Interactions . . . 53
3.11 Discriminating a $K_L \to \pi^0 \nu\bar{\nu}$ Signal From Backgrounds . . . 53
3.11.1 Variation of Background due to Inefficiency Uncertainties . . . 55
3.11.2 Variation of Background Level due to Veto Threshold . . . 55
3.12 Summary . . . 55

4 Other Rare and Very Rare Decay Modes **58**
4.1 Introduction . . . 58
4.2 $K_L \to \pi^+\pi^-e^+e^-$ . . . 58
4.3 $K_L \to \pi^0\pi^0e^+e^-$ . . . 61
4.4 Decays of the type $K_L \to \gamma^*\gamma$ and $K_L \to \gamma^*\gamma^*$ . . . 62
4.4.1 $K_L \to \mu^+\mu^-\gamma$ . . . 62
4.4.2 $K_L \to e^+e^-e^+e^-$ . . . 65
4.4.3 $K_L \to \mu^+\mu^-e^+e^-$ . . . 66
4.4.4 $K_L \to e^+e^-\gamma\gamma$ and $K_L \to \mu^+\mu^-\gamma\gamma$ . . . 67
4.5 $K_L \to \mu^+\mu^-$ . . . 68
4.6 $K_L \to \pi^0\mu^+\mu^-$ . . . 68
4.7 Lepton Flavor Violating Modes . . . 70
4.7.1 $K_L \to \pi^0\mu e$ . . . 71
4.7.2 $\pi^0 \to \mu^\pm e^\mp$ tagged from $K_L \to \pi^0\pi^0\pi^0$ . . . 72
4.7.3 $K_L \to \mu^\pm\mu^\pm e^\mp e^\mp$ . . . 73
4.7.4 Other Lepton Flavor Violating Modes . . . 73
4.8 Summary . . . 73

5 Beams **75**
5.1 Primary Beam . . . 75
5.2 Target . . . 76
5.3 Neutral Beam . . . 77
5.4 Alignment . . . 78
5.5 KAMI Test Run Beam Studies . . . 78

6 The KAMI Detector **82**
6.1 Overall Geometry . . . 82
6.2 Pure CsI Calorimeter . . . 82
6.2.1 The KTeV Calorimeter . . . 82
6.2.2 The KAMI Calorimeter . . . 84
6.3 Photon Veto detectors . . . 87
6.3.1 General Design Considerations . . . 87
6.3.2 Mask Anti detector . . . 91
6.3.3 Vacuum Veto Detector . . . 91
6.3.4 CsI Anti detector . . . 92
6.3.5 Expected Performance . . . 92
6.4 Beam Anti System . . . 105
6.5 Charged Particle Spectrometer . . . 109
6.5.1 Scintillating fiber tracker . . . 111
6.5.2 Spectrometer Magnet . . . 112
6.6 Vacuum System and Vacuum Window . . . 114
6.7 Muon Range Stack . . . 115
6.8 Electronics . . . 116
6.9 Trigger and Data Acquisition System . . . 119
6.9.1 L1 Trigger . . . 120

6.9.2 L2 Trigger 120
6.9.3 L3 Trigger and DAQ 121

7 Alternative Methods for Separating Signal and Background 123
7.1 Maximum Likelihood Analysis of Background in Beam Anti 123
7.2 Neural Networks and Selection of $K_L \to \pi^0 \nu\bar{\nu}$ Decays 125
7.2.1 Introduction 125
7.2.2 Training of Networks 125
7.2.3 The Input Values for Training 125
7.2.4 Training and Result 126

A Comparison with the BNL KOPIO Experiment 134
A.1 Signal and Background 134
A.2 Particle Production and Beam Characteristics 136
A.3 Rate and Acceptance 136

B Results From The 2000 KAMI Beam Test 139
B.1 KAMI Measurements of Neutral Hadron Beam Rates 139
B.1.1 Overview of the Measurement 139
B.1.2 Definition of Flux 139
B.1.3 KTeV Beamline and Detector 140
B.1.4 Kaon Rates 141
B.1.5 Neutron Rates 143
B.1.6 Flux and Absorber Studies 144
B.1.7 Summary 147
B.2 Beam Test Results for a Prototype Beam Anti 148

C Photon Veto Inefficiency 153
C.1 Inefficiency Due to Photo-Nuclear Interactions 153
C.2 Total Inefficiency Including Sampling Effects 155

D Overview of FCNC Processes 158
D.1 General Considerations 158
D.2 Physics of $K \to \pi\nu\bar{\nu}$ decays in the Standard Model 159
D.3 Other rare kaon decays arise by FCNC processes 165
D.3.1 $K_L^0 \to \pi^0 l^+ l^-$ decays 165
D.3.2 $K_L^0 \to \pi^0 e^+ e^-$ decay with direct CP violation. 167
D.3.3 $K_L^0 \to \pi^0 e^+ e^-$ decay with indirect CP violation. 168
D.3.4 $K_L^0 \to \pi^0 e^+ e^-$ without CP violation. 169
D.3.5 $K_L^0 \to \pi^0 \mu^+ \mu^-$ decay. 170
D.3.6 Experimental situation for $K_L^0 \to \pi^0 l^+ l^-$ 170
D.3.7 $K_L^0 \to \mu^+ \mu^-$ decay 170
D.3.8 $K_L^0 \to e^+ e^-$ decay 174
D.4 B-meson experiments and unitarity triangle 174
D.5 Over-constraining the Unitary Condition and Detecting Effects Beyond the SM176

D.6 Lepton flavor violating processes in kaon decays 182

List of Figures

1 Schematic of the KAMI detector. 18
2 Unitarity triangle for the K system (not to scale). 20
3 Traditional representation of the unitarity triangle. Measurements of B meson decays introduce constraints, and contributions from the two golden kaon decay modes are marked as shown. 20
4 Feynman diagrams for the decays $K \to \pi\nu\overline{\nu}$ 21
5 Processes contributing to $K_L \to \pi^+\pi^-e^+e^-$. a) CP-violating bremsstrahlung process b) CP-conserving M1 γ emission c) CP-violating E1 γ emission d) Charge radius process e) direct CP violating short distance E1 photon emission 23
6 Feynman diagrams for the short-distance component of the decay $K_L \to \mu^+\mu^-$. 24
7 The P_t distribution from the one day 800 GeV KTeV run after all cuts except the final P_t cut. The arrow designates the signal region. The simulated backgrounds from K_L and Λ decays are overlaid on the data. The two events above 190 MeV/c are consistent with neutron interactions in the vacuum window. 31
8 Schematic of the KAMI detector. 33
9 The reconstructed P_t spectrum for $K_L \to \pi^0\nu\overline{\nu}$ decays. An unbalanced P_t spectrum is a characteristic feature of the decay. 36
10 The kaon momentum spectrum 90 m from the production target for a 15 mrad targeting angle. 40
11 The Z decay vertex generated by the $K_L \to 2\pi^0$ Monte Carlo. Each entry in the plot is weighted by the product of the inefficiencies of the two photons that are not used to form the π^0. When the Z vertex for these events is calculated, assuming they originate from a single π^0, they all reconstruct between 100 m and 165 m. Resolution and the effect of mis-reconstruction of odd background leads to upstream decays being shifted into the fiducial volume. 44
12 The effect of the P_t cut on the signal and background from $K_L \to 2\pi^0$ decays is shown. The top plot shows the variation of the $K_L \to \pi^0\nu\overline{\nu}$ acceptance vs. P_t cut. The acceptance is calculated relative to the number of decays between 90-183 m. The bottom plot shows the ratio of the $K_L \to \pi^0\nu\overline{\nu}$ signal to the background from $K_L \to 2\pi^0$ vs. P_t cut. A P_t cut of 0.130 GeV/c is ultimately selected. 45
13 The effect of the downstream Z vertex cut on the $K_L \to \pi^0\nu\overline{\nu}$ signal and background from $K_L \to 2\pi^0$ decays is shown. The top plot shows the variation of the $K_L \to \pi^0\nu\overline{\nu}$ acceptance vs. Z vertex cut. The acceptance is calculated relative to the number of decays between 90-183 m. The bottom plot shows the ratio of the $K_L \to \pi^0\nu\overline{\nu}$ signal to the background from $K_L \to 2\pi^0$ vs. vertex cut. A Z vertex cut of 165 m is ultimately selected. 46

14 The shower-shape χ^2 distribution in the KTeV CsI calorimeter for photons and charged pions from clean $K_L \to \pi^+\pi^-\pi^0$ decays. A typical cut requires $\chi^2 < 4$. 49
15 The reconstructed center-of-energy (ECEN) distributions for $K_L \to \gamma\gamma$ (left) and $K_L \to \pi^0\nu\overline{\nu}$ (right). Note the dramatically different horizontal scales. . . 50
16 The hadron energy spectrum measured during the 2000 KAMI beam test at 15 mr and no beryllium absorber. 51
17 The total energy deposited in the CsI calorimeter for $nn \to nn\pi^0$ events. The plot on the left is for events generated with the t distribution from Ref [80]. The plot on the right is for events generated uniformly in phase space. 52
18 The $K_L \to \pi^0\nu\overline{\nu}$ and $K_L \to 2\pi^0$ P_t spectra for various detection thresholds in the photon veto detectors. The top left plot is for a 5 MeV threshold; top right is for a 10 MeV threshold; bottom left is for a 15 MeV threshold; and bottom right is for a 20 MeV detection threshold. The nominal conditions for this proposal assume a 10 MeV detection threshold. 54
19 Variation of $K_L \to \pi^0\pi^0$ background P_t spectra, shown in the plot on the left, obtained by varying the vacuum veto, mask anti, and CsI inefficiency maps in photon energy regions where the expected inefficiencies are less than 10^{-5} Errors are the statistics expected from one year of operation. The right plot shows the ratio of background spectra obtained with different inefficiency maps to the background spectrum obtained with the baseline KAMI inefficiencies. 56
20 $M_{\pi^+\pi^-e^+e^-}$ invariant mass 59
21 a) Observed ϕ and b) $\sin\phi\cos\phi$ angular distributions: The data are shown as dots. The histogram is a Monte Carlo simulation based on the model of Sehgal and Wanninger ref. [25]. 59
22 a) E_γ^* spectrum of data (dots), Monte Carlo using a constant $|g_{M1}|$ (dashed histogram), Monte Carlo with E_γ^* dependent form factor (solid histogram); b) Likelihood contours of a_1/a_2 and $|\tilde{g}_{M1}|$; Constant asymmetry contours calculated from the data are superimposed 60
23 Various measurements of the charge radius of the neutral kaon 61
24 Likelihood fit of the relative phase of the M1 and bremsstrahlung amplitudes using presently available measurements of ϕ_{+-} and δ_0, δ_1 62
25 a) The $sin\theta_{e^+}sin\phi$ distribution in which direct CP is supposed to appear as an asymmetry between $sin\theta_{e^+}sin\phi \geq 0.$ and $sin\theta_{e^+}sin\phi \leq 0.$ b) The $sin\theta_{e^+}sin\phi$ asymmetry as a function of M_{ee} mass cut 63
26 The reconstructed $m_{\mu^+\mu^-\gamma}$ distribution after final cuts. The large peak centered at 380 MeV/c^2 is $K_L \to \pi^+\pi^-\pi^0$. $K_{\mu3}$ dominates the background from ~400 MeV/c^2 out to 600 MeV/c^2 with a slight enhancement at 450 MeV/c^2 from $K_{\mu3\gamma}$. 64
27 The dimuon mass distributions for data and for Monte Carlo with no form factor (top). The data/Monte Carlo ratio is a direct measurement of the form factor (bottom). The Monte Carlo is normalized to the total number of data events. 64

28 The 4e invariant mass distribution after all cuts except the invariant mass cut. The dots represent the data and the histogram represents the Monte Carlo simulation. There are 436 events in the signal region between the arrows. The decay $K_L \to \pi^{\pm}e^{\pm}\nu e^{+}e^{-}$ is seen in the lower mass region. 66
29 $M_{ee\mu\mu}$ for data (dots) and the scaled sum of $K_L \to \pi^+\pi^-\pi^0_D$ and $K_L \to \pi^+\pi^-e^+e^-$ background simulations (line), with $P_t^2 \leq 250$ (MeV/c)^2. 67
30 Signal and background rates for $K_L \to \pi^0\mu^+\mu^-$, versus the branching fraction. The diagonal lines show the predicted number of observed signal events in one year for perfect reconstruction efficiency (solid), and 20% reconstruction efficiency (dashed). The horizontal lines show the expected background from $K_L \to \mu^+\mu^-\gamma\gamma$ only (dot-dashed) and also other background sources (dotted). 69
31 Signal divided by square root of background for $\pi^0\mu^+\mu^-$ in one year of running for the 4 combinations of signal and background shown in Figure 30 71
32 $M_{\pi^0\mu e}$ invariant mass 72
33 KAMI Primary Beam Envelope 76
34 KAMI γ/K^0 production ratios for various targets 77
35 KAMI n/K^0 production ratios for various targets 77
36 Comparison of "ring number" (essentially a P_t distribution) from the KAMI beam test (dots) and simulation (solid line) 79
37 Target and collimator geometry in the vertical plane used to simulate the KAMI beam. 80
38 KAMI neutral beam simulation with a precision middle collimator. 81
39 The KAMI CsI calorimeter. 85
40 The E/P ratio for electrons from K_{e3} decays in the KTeV CsI calorimeter is shown on the left. The energy resolution vs. momentum for electrons from K_{e3} decays in the KTeV CsI calorimeter is shown on the right. The estimated contribution from the momentum resolution has been removed. 86
41 Monte Carlo of the efficiency of separating fused photons vs. the distance between the two photons. 87
42 The energy spectra (in GeV) of the two photons in the veto system for $K_L \to 2\pi^0$ decays with two photons in the CsI. The plot on the left is the energy spectrum of the higher energy photon and the plot on the right is the spectrum for the lower energy photon. 89
43 The correlation between the energies (in GeV) of the two photons in the veto system for $K_L \to 2\pi^0$ decays with two photons in the CsI. The events in the bottom plot have been weighted by the product of the inefficiencies of the two photons from Table 9. 95
44 Layout of a scintillator tile with fiber grooves for KAMI. 96
45 3D illustration of a 90-layer lead/scintillator hermetic vacuum photon veto barrel section. 97
46 The front view and cross section of a 90-layer lead/scintillator vacuum photon veto design. 98
47 The current design layout of a trapezoidal vacuum veto module. 99

48 Plan view of 8 trapezoidal modules assembled into a vacuum veto section. The gaps between the modules allow for efficient vacuum pumping, but do not line up with incident photon trajectories. 100
49 3D illustration of an fully assembled trapezoidal vacuum veto section. 101
50 The measured photo-nuclear inefficiencies of several lead/scintillator sampling detectors (left) and pure CsI (right). KAMI will use a lead/scintillator detector with 1 mm thick lead sheets and 5 mm thick scintillator tiles. 102
51 The detection inefficiency due to sampling fluctuations and photo-nuclear interactions as a function of the incident photon energy for fine sampling lead/scintillator calorimeters using detection thresholds of 1, 5 and 10 MeV. The inefficiencies are the sum of simulated sampling losses and measured photo-nuclear inefficiencies. 103
52 Illustration of the $K_L \to 2\pi^0$ background as a function of the K_L momentum for detection thresholds of 1, 5 and 10 MeV in fine sampling lead/scintillator calorimeters. 104
53 The beam anti configuration 105
54 Preliminary configuration of BA3 107
55 Estimated BA inefficiencies as a function of photon energy outside and inside the neutral beam region for various cuts discussed in the text. 110
56 Upper curve: expected photon energy spectrum per year due to $K_L \to \pi^0\pi^0$ background in the BA system after application of all vetoes *except* the BA itself; lower curve the residual energy spectrum per year that survives the BA veto due to BA inefficiencies. 110
57 KAMI Spectrometer Magnet. A 3.75 m diameter vacuum vessel is shown inscribed in the magnet aperture. The upper and lower most coils are set in to nest into the inner coils - minimizing the overall length of of the magnet. 113
58 KAMI Spectrometer Magnet - By(gauss) vs Z(meters). The monotonic line is B_y at x=y=0, where the other line is for the field at x=y=1.8m. The field integral at x=y=0 is 245 MeV/c. 114
59 Elevation view of the muon range stack. 116
60 Distribution in the transverse plane of hits from $K_L \to \mu^+\mu^-$ decays at 1m depth in the muon range stack. 117
61 Basic architecture of the KAMI data acquisition system. 122
62 Longitudinal distribution of the most upstream interaction in the Beam Anti for signal and background. The signal distribution (extended z distribution) is due to events with neutron interactions only and background (early showering peak) are events with photon interaction superimposed on neutron interactions. 124
63 Three-layers neural nets: a) with two input nodes; b) with seven input nodes. 126
64 The neural network output distribution for a net with input values $P_{t\pi^0}$ and δS after ten epochs. 127
65 The neural network output distribution for a net with input values $P_{t\pi^0}$ and δS after one hundred epochs. 127
66 The neural network output distribution for a net with input values $P_{t\pi^0}$ and δS, $E_{\gamma 1,2}$, $P_{t\gamma 1,2}$ and Z_V after ten epochs. 127

67 The neural network output distribution for a net with input values $P_{t\pi^0}$ and δS, $E_{\gamma 1,2}$, $P_{t\gamma 1,2}$ and Z_V after one hundred epochs. 127
68 The results of the signal-to-background (S/B) study demonstrating the relative merits of kinematical constraints at low energy and photon vetoing at high energy. 135
69 E/p measured in the CsI calorimeter at the end of the beam test with 150 GeV protons on target. The mean and sigma are from a Gaussian fit in the region $0.90 < E/p < 1.10$. 142
70 Ratio of UCAL energy to track momentum for protons tagged via $\Lambda \to p\pi^-$ decays. The top plot is for data; the bottom plot is from a **GEANT**-based simulation. 142
71 The corrected kaon energy spectrum based on $K_L \to 3\pi^0$ decays, at 12, 15 and 20 milliradians. The data are shown with solid dots and the Malensek-based prediction is shown by the histogram. The flux units (vertical axis) are $\times 10^{-6}/\text{prot}/\mu\text{str}/GeV$. 143
72 The kaon flux for energies above 6 GeV vs. beam-detector angle. Both data from this experiment (dots) and the predictions (open squares) are shown. . 144
73 Neutron energy spectrum with 150 GeV beam at 20 mrad. The data are shown in **dots** after subtracting the kaon energy spectrum (crosses) at the UCAL Z-location. The thick line histogram is a **GEANT**-based prediction after re-scaling to have the same area as the data. 145
74 The neutron flux ($\mathcal{F}_n$) for energies above 2 GeV vs. beam-detector angle. Both data from this experiment (dots) and the predictions (open squares) are shown. 146
75 The neutron/kaon ratio vs. beam-detector angle. 146
76 The neutron to kaon ratio (n/k) is shown as a function of Be absorber thickness (left). The right plot shows the n/k ratio *relative* to the n/k ratio with no Be absorber. 150
77 Electron energy spectrum in the BAG obtained in the KAMI beam test from K_{e_3} decays in units of MIPs; the x axis is $\ln(E/E_\mu)+1$; the peak at zero is the pedestal, the intermediate peak at 1 MIP is the peak due to charged particles mainly muons and the large peak centered at 4 is the electron peak 151
78 Muon energy spectrum in the BAG obtained in the KAMI beam test 151
79 Plan view of the ES171 experiment. 154
80 The plot on the left shows the inefficiency of lead/scintillator sampling detectors due to photo-nuclear interactions for 3 different sampling ratios. The default design for KAMI consists of 1 mm thick lead sheets and 5 mm thick scintillator tiles. The plot on the right shows the inefficiency of a pure CsI detector due to photo-nuclear interactions. The data in both plots was taken with a 10 MeV detection threshold. 155
81 Total detection inefficiency as a function of the incident photon energy for (a) 0.5 mm Pb/5 mm scintillator and (b) 1 mm Pb / 5 mm scintillator sampling ratios. The detection threshold is 10 MeV. 156
82 Diagrams for FCNC $s \to d\nu\bar{\nu}$ decays ($K \to \pi\nu\bar{\nu}$ decays): a) penguin diagrams, b) box diagram. 158

83 Diagrams containing SUSY contributions to the $Zd\bar{s}$ vertex. 158
84 Graphical representation in the $\bar{\rho}$, $i\bar{\eta}$ plane of the unitarity condition $V_{ud}V_{ub}^* + V_{td}V_{tb}^* = -V_{cd}V_{cb}^*$. 164
85 The ideal unitary triangle. For illustration, the value of $\bar{\eta}$ has been chosen to be higher than the fitted central value (reproduced from [14, 15]). 165
86 The limitations for parameters of the unitary triangle from existing data for ε, Δm_{B_d}, Δm_{B_s}, $|V_{ub}/V_{cb}|$, $\sin 2\beta$ (from $B^0(\bar{B}^0) \to J/\psi K_S^0$) — see [30]. . . . 166
87 Direct and indirect CP violation in the decay $K^0 \to \pi^0 l^+ l^-$ 166
167
171
90 A possible outcome for $\overline{\eta}$, $\overline{\rho}$, and β obtained from future K-meson and B-meson experiments. The light region includes possible theoretical uncertainties in BR($K^+ \to \pi^0 \nu\overline{\nu}$ connected with the influence of c-quarks [58]. 177
91 A model with four generations of fundamental fermions with quark doublets [38]. a) Unitary quadrangle for this model. b) The correlation between $BR(K^+ \to \pi^+ \nu\bar{\nu})$ and $BR(K_L^0 \to \pi^0 \nu\bar{\nu})$ in this model; the dotted line rectangle corresponds to the SM predictions. 178
92 Diagrams for LFV processes and $K^0 \rightleftarrows \bar{K}^0$ mixing in horizontal boson exchange model with ΔG selection rule. 183
93 Branching fractions for $K_L \to e\mu$ (a) and $K \to \pi e\mu$ (b) as function of the scale parameter $M_X = M_H$ in (101) (assuming $g_X = g$ – weak constant). In (a) the solid (dotted) curves correspond to A(P) exchange. In (b) the K_L^0 mode is represented by the solid (S) and dashed (V) curves while the K^+ mode is represented by the dash-dotted (S) and dotted (V) curves (see [60]). Here V, A, S, P correspond to vector, axial-vector,scalar and pseudoscalar interactions, respectively. 184
94 Diagrams for $K \to \mu e$ and $K \to \pi\mu e$ in SUSY model with R-parity non-conservation [89] 186

List of Tables

1 Summary of the current best results and the expected KAMI sensitivity for various decay modes with charged particles. The KAMI yield or sensitivity assumes one year of running with $6 \times 10^{13} K_L$ decays. SES denotes single event sensitivity. Except for $K_L \to \mu^+\mu^-$ and $K_L \to \mu^\pm e^\mp$ the current best results are all from KTeV. 16
2 Summary of results of kaon decays to two photons and related modes 26
3 Summary of $K \to \pi\gamma\gamma$ results 28

4 Kaon flux vs. target angle from 2000 KAMI beam test for $E_K > 6$ GeV. The flux is measured 90 m from the production target in units of $\times 10^{-6}$/proton/μstr. The incident proton beam energy is 150 GeV with no beryllium absorber in the neutral beam. Also shown are the correction factors obtained from the Malensek parameterization [60] to account for the difference in kaon production from 150 GeV and 120 GeV primary protons. The expected flux at 120 GeV is also listed. 34
5 Rate of kaon decays vs targeting angle for 120 GeV proton beam from the Main Injector. Each Main Injector pulse contains 3×10^{13} protons. The beam is 0.41 μstr in size and no beryllium absorber is included in the neutral beam. 35
6 Acceptance for $K_L \to \pi^0\nu\overline{\nu}$ decays between 90 m and 183 m. The applied cuts are described in the text. 37
7 The neutron flux, neutron interaction rate in BA3 and the rate at which these neutron interactions mimic photons vs targeting angle and beryllium absorber thickness. The neutron fluxes and beryllium attenuation factors for each set of beam conditions were measured during the 2000 KAMI beam test. 38
8 The overall fraction of events lost due to accidental activity in the detector, the effective number of kaon decays per year after correcting for accidental losses, and the resulting number of $K_L \to \pi^0\nu\overline{\nu}$ events per year for various targeting angles and beryllium absorber configurations. The number of $K_L \to \pi^0\nu\overline{\nu}$ events per year were calculated using a branching ratio of 3×10^{-11} and the acceptances listed in Table 6. The number of events per year for our nominal running conditions of 15 mrad and no beryllium absorber is highlighted. 39
9 Photon inefficiencies as a function of energy for the various KAMI detectors. MA, VV, BA1, BA2 and BA3 refer to the Mask Anti, Vacuum Veto, Beam Anti1 Beam Anti2 and Beam Anti3 detectors, respectively (see Figure 8). The inefficiencies in this table are used in the background simulations. 42
10 The fusion separation inefficiencies in the CsI used in the Monte Carlo, binned according to the distance which separates the two photons. 43
11 The sequential acceptance factors for the analysis and trigger cuts applied to the background from $K_L \to 2\pi^0$ decays. 47
12 The background to $K_L \to \pi^0\nu\overline{\nu}$ obtained after variation of the vacuum veto and CsI inefficiency maps over the range of $\pm2 \times 10^{-6}$ in the photon energy region above 1 GeV. 56
13 Estimated background levels per year of running. 57
14 Summary of the current best results and KAMI sensitivity for various decay modes with charged particles. The KAMI yield or sensitivity assumes one year of running with $6 \times 10^{13} K_L$ decays. SES denotes single event sensitivity. 74
15 GEANT simulations of 3 center collimator configurations: 1) KAMI Beam test; 2) 2 cm square: 3) optimized for KAMI beam. 80
16 Locations and inner/outer dimensions of all the KAMI detector elements. . . 83

17 Preliminary results on the comparison of different scintillating tile/WLS fiber combinations. A THORN EMI 9903KB PMT with a rubidium bialkali photocathode was used. N is the average photo-electron yield per MIP passing through a 2 mm scintillator tile (the KAMI tiles are 5 mm thick); fwhm is the full width half maximum of the output pulse; τ is the decay time constant of the output signal. a) designates injection molded tiles; b) designates tiles fabricated by extrusion; and c) designates tiles manufactured by a bulk-polymerization technique. 90
18 KAMI Beam Region Veto Configuration 105
19 $NaBi(WO_4)_2$ Properties 106
20 Photon inefficiencies from a GEANT simulation of the BA3 detector. The inefficiencies are for the portion of the BA3 detector that is shadowed by the neutron beam. 109
21 The Basic performance specifications for the KAMI Visible Light Photon Counter (VLPC) readout for the scintillating fiber tracker detector. 111
22 Breakdown of the number of channels required for the KAMI fiber tracking system. 112
23 Summary of the trigger rates discussed in the text. 121
24 Statistical uncertainty on signal rate measurement as a function of background level. The background level is for a sample of events before the likelihood analysis is applied. The last column is a ratio of the statistical error and $\sqrt{N_{signal}}$. 125
25 Kaon flux ($\mathcal{F}_k$) vs. target angle compared with Malensek predictions; $E_K >$ 6 GeV and $Z_K = 90$ m. The incident proton beam energy is 150 GeV with no Be absorber in the neutral beam. The flux units are $\times 10^{-6}$/prot/μstr and the errors are systematic only. $< E_K >$ refers to the average kaon energy in GeV. 147
26 Summary of absolute neutron flux with $E_n > 2$ GeV, and comparison with predictions. The incident beam energy is 150 GeV with 0" Be absorber in the neutral beam. All flux ($\mathcal{F}$) units are $\times 10^{-6}$/prot/μstr. 148
27 Main parameters of CKM matrix and Standard Model which are important for evaluation of $K \to \pi\nu\nu$ branching ratios and other values [32, 34] – see also [29-31],[33]. 187
28 Determination of $\sin 2\beta$ and $|V_{td}|$ from branching ratios $BR(K^+ \to \pi^+\nu\bar{\nu})$ and $BR(K_L^0 \to \pi^0\nu\bar{\nu})$ (see [15-18]). 188
29 Branching ratios $BR(\pi^+\nu\bar{\nu})$, $BR(\pi^0\nu\bar{\nu})$ and $BR(\pi^0 e^+e^-)_{CP-dir}$ for various new physics scenarios. 189
29 (continuation) 190
30 The dependence of branching ratios for decays $K \to \pi\nu\bar{\nu}$ and $K_L^0 \to \pi^0 e^+e^- |_{CP-dir}$ in the SUSY model [66] on the parameters λ_t and Λ_t. 191
31 Lepton flavor violation in kaon decays 191
32 Classification of some rare generation changing processes. 191

Executive Summary

Introduction

We propose to measure the CKM parameter η to an accuracy of better than 10% by collecting at least 100 $K_L \to \pi^0\nu\overline{\nu}$ "golden mode" events with a signal-to-background between 4 to 5. We choose to perform this measurement at the Fermilab Main Injector fixed target facility where the advantages of a high energy kaon beam can be fully exploited. The detector will consist of a state-of-the-art pure CsI calorimeter, high-performance totally hermetic photon veto detectors and a high-rate scintillating fiber tracking system. The logistics of using a high energy neutral kaon beam and the required performance of the beam and detectors to achieve a good signal-to-background ratio have been described in detail. KAMI represents a major advance in physics sensitivities on a broad front, extending approximately two orders of magnitude beyond the formidable reach of KTeV.

The flux available from the Main Injector, combined with the superb resolution and rate capabilities of the detector, allows KAMI to mount a rich and diverse physics program that confronts the Standard Model and probes CP violation to significant levels. It is interesting to note that in the 1994 compilation of the Particle Data Group (PDG), the world sample of $K_L \to \mu^+\mu^-\gamma$ was a single event. In 1998, the world sample reported by the PDG was almost 200 events. In KAMI we will record more than 700k $K_L \to \mu^+\mu^-\gamma$ events in a year. KAMI will more than double the sensitivity of KTeV-E799 every week. KAMI also has the sensitivity to search for physics beyond the Standard Model at the 100 TeV mass scale with lepton flavor violating decays. KAMI's unprecedented flux and precision will allow precise measurement of many rare and very rare decays, potentially opening many new windows of opportunity.

Physics Goals

KAMI's primary physics goal is to detect the very rare $K_L \to \pi^0\nu\overline{\nu}$ decay, measure its branching ratio, and extract a value for the CKM parameter η to an accuracy of better than 10%. Within the context of the Standard Model, η is the parameter responsible for all CP violating effects. While the value of η is interesting in its own right, the primary motivation is to combine this with other measurements of fundamental CKM parameters from kaon and B meson decays to over-constrain the CKM matrix and challenge the Standard Model. For example, it is possible to measure the angle β of the unitarity triangle from the ratio B($K_L \to \pi^0\nu\overline{\nu}$)/B($K^+ \to \pi^+\nu\overline{\nu}$) and from the CP-violating asymmetry in the decay $B_d^\circ \to \psi K_S$. $K \to \pi\nu\overline{\nu}$ and $B_d^\circ \to \psi K_S$ are distinctly different processes that new physics might impact differently. Measuring this parameter in both systems is a sensitive test of the Standard Model.

KAMI's physics agenda comprises a rich and diverse program that extends well beyond the $K_L \to \pi^0\nu\overline{\nu}$ measurement. The flux and energy of the Main Injector combined with a superb high-rate, high resolution hermetic detector allows KAMI to directly confront issues of direct CP violation, lepton flavor violation and new physics phenomena. None of the other

proposed $K_L \to \pi^0 \nu\overline{\nu}$ experiments has this capability.

$K_L \to \pi^0 \nu\overline{\nu}$ at KAMI

To meet the stated goal of collecting at least 100 $K_L \to \pi^0 \nu\overline{\nu}$ events, it is necessary to have a sufficient flux of kaons and a large acceptance. The loss of events due to accidental activity in the detector can severely reduce the number of collected events and must be clearly understood. It is demonstrated that KAMI can collect ~90 events per year, assuming B($K_L \to \pi^0 \nu\overline{\nu}$) = 3×10^{-11}. This event yield depends on *measured* kaon fluxes and a realistic and conservative estimate of losses due to accidental activity in the detector. Additionally, there is sufficient headroom to still meet our goals in a reasonable period of time if the B($K_L \to \pi^0 \nu\overline{\nu}$) is smaller than expected by a factor of 2 or 3.

Backgrounds to $K_L \to \pi^0 \nu\overline{\nu}$

The dominant source of background to the $K_L \to \pi^0 \nu\overline{\nu}$ signal is $K_L \to 2\pi^0$ decays where two of the photons are not detected. Controlling this background requires a hermetic, state-of-the-art photon veto system. The CsI calorimeter, used to detect the two photons from the signal mode, must do a good job of identifying individual photon clusters that are close to one another since photons can escape detection if they merge with other clusters. An exhaustive study of the $K_L \to 2\pi^0$ background has been performed with the conclusion that a signal-to-background of 4.6 can be attained. To obtain this level of background suppression we rely, in large part, on the performance of the photon veto system. Our expectations for the detection efficiency of the photon veto system over a broad photon energy range are based on a combination of beam tests and simulations.

There are many other potential sources of background from decays of kaons and hyperons and from interactions of the neutral beam in residual gas inside the vacuum decay volume and the vacuum window. These have been carefully studied and found to be negligible compared to the background from $K_L \to 2\pi^0$ decays.

Other Rare and Very Rare Decay Modes

There are many rare and very rare kaon decays other than $K_L \to \pi^0 \nu\overline{\nu}$ which are of considerable interest for a variety of reasons. There are very rare kaon decays which are sensitive to direct CP violation including $K_L \to \pi^0 \mu^+ \mu^-$. The branching ratio predicted by the Standard Model for this decay is within reach of KAMI. KAMI will also have the capacity to perform sensitive searches for other rare and forbidden decays. These include processes forbidden by the Standard Model, such as the lepton flavor violating decays $K_L \to \pi^0 \mu^\pm e^\mp$ and $K_L \to \mu^\pm e^\mp$. K_L decays to 4 leptons will be abundant in KAMI. Decays such as $K_L \to \mu^+ \mu^- e^+ e^-$ and $K_L \to e^+ e^- e^+ e^-$ provide critical insight into the $K_L \gamma^* \gamma^*$ form factor. Additionally, the angular distribution between the decay planes of the lepton pairs is sensitive to direct CP violation. A large sample of $K_L \to \pi^+ \pi^- e^+ e^-$ events will also be collected by KAMI. This decay, first observed by KTeV, has opened a new

Decay Mode	Physics Probed	BR (meas. or pred.)	Current Best (events or 90% C.L.)	Events per Year or Sensitivity for KAMI
$K_L \to \pi^0\mu^+\mu^-$	CPV	$0.3 - 1.0 \times 10^{-11}$	$< 3.8 \times 10^{-10}$	$< 2 \times 10^{-11}$
$K_L \to \pi^+\pi^-e^+e^-$	CPV, K Radius	3.2×10^{-7}	6000	678,000
$K_L \to \mu^+\mu^-$	V_{td}	7.2×10^{-9}	6200	45,000
$K_L \to \mu^+\mu^-\gamma$	$K_L\gamma^*\gamma$	3.7×10^{-7}	9327	711,000
$K_L \to e^+e^-e^+e^-$	CPV, $K_L\gamma^*\gamma^*$	3.7×10^{-8}	441	34,000
$K_L \to \mu^+\mu^-e^+e^-$	CPV,$K_L\gamma^*\gamma^*$	2.5×10^{-9}	38	1600
$K_L \to \pi^0\mu^\pm e^\mp$	LFV	-	$< 4.4 \times 10^{-10}$	4×10^{-13} (SES)
$K_L \to \mu^\pm e^\mp$	LFV	-	$< 4.7 \times 10^{-12}$	2×10^{-13} (SES)
$\pi^0 \to \mu^\pm e^\mp$	LFV	-	$< 7.9 \times 10^{-10}$	8×10^{-12} (SES)
$K_L \to \mu^\pm\mu^\pm e^\mp e^\mp$	LFV	-	$< 1.4 \times 10^{-10}$	3×10^{-13} (SES)

Table 1: Summary of the current best results and the expected KAMI sensitivity for various decay modes with charged particles. The KAMI yield or sensitivity assumes one year of running with $6\times10^{13}K_L$ decays. SES denotes single event sensitivity. Except for $K_L \to \mu^+\mu^-$ and $K_L \to \mu^\pm e^\mp$ the current best results are all from KTeV.

window on CP violation through the study of final-state angular distributions. This rich and diverse program of charged-mode physics is completely compatible with the program to measure the rate of $K_L \to \pi^0\nu\bar{\nu}$ and is not possible to execute at any of the other proposed $K_L \to \pi^0\nu\bar{\nu}$ experiments.

Table 1 summarizes KAMI's sensitivity for the various charged modes discussed in the proposal as well as their current status. Except for $K_L \to \mu^+\mu^-$ the current best results are all from KTeV. The physics issues addressed by each decay mode is also listed.

Beams

KAMI uses 120 GeV protons from the Main Injector to strike a target and produce a well collimated, high-intensity neutral beam that contains primarily K_L and neutrons by the time it reaches the detector. The Main Injector delivers beam in a 1 second spill that repeats every 3 seconds. KAMI is requesting a proton intensity of 3×10^{13} per spill. The angle at which the beam strikes the target relative to the horizontal is variable between 10 to 20 mrad to allow the relative kaon/neutron ratio to be optimized to the final detector capabilities. Additional absorber can be inserted into the beam to enhance the kaon/neutron ratio at the expense of lost kaon flux.

The neutral beam must be well collimated to minimize beam halo which can interact with detector materials and produce backgrounds. Excessive halo can also cause radiation damage to the CsI calorimeter in the area around the calorimeter beam hole. The current

design reduces the halo by a factor of 10^5 relative to the central core of the beam.

The KAMI Detector

A sketch of the KAMI detector appears in Figure 1. The key design features include:

1. A high-resolution pure CsI calorimeter with a demonstrated record of exceptional performance in KTeV;
2. A hermetic photon veto system based on a fine sampling calorimeter consisting of alternating layers of 1 mm thick lead sheets and 5 mm thick plastic scintillator;
3. A highly segmented beam anti system based on fast, radiation-hard $NaBi(W0_4)_2$ crystals;
4. High rate precision tracking using scintillating fibers with Visible Light Photon Counter (VLPC) readout;
5. A wide-gap spectrometer magnet;
6. A well segmented muon range stack;
7. A high speed, high throughput, fully buffered, dead-timeless trigger and data acquisition system.

Each of these detector elements are discussed in detail in Section 6 of the proposal.

Conclusion

KAMI is a powerful and precise scientific instrument with the sensitivity and reach to challenge the Standard Model. In addition to measuring the fundamental CKM parameter η to better than 10%, KAMI has the potential to discover new physics in rare and very rare kaon decays.

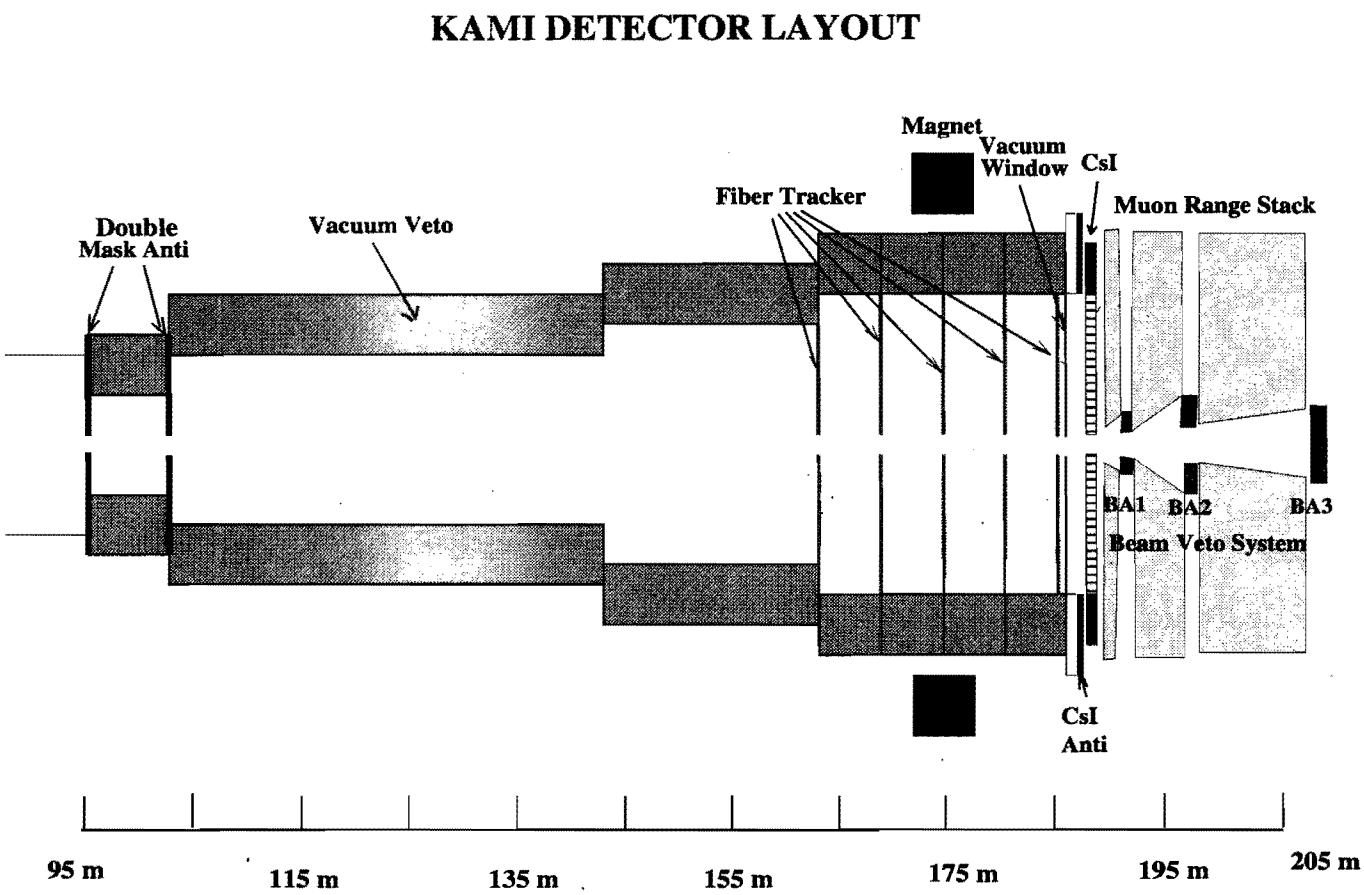

Figure 1: Schematic of the KAMI detector.

1 Theoretical Background and Motivation

1.1 Introduction

The field of rare kaon decays has a long and rich history: the discovery of the kaon in 1949 [1], the postulation of "strangeness" [2], the τ–θ puzzle [3] and the understanding of parity violation [4], the understanding of quark mixing [5,6], the discovery of *CP* violation [7], the small rate for $K_L \to \mu^+\mu^-$ and flavor-changing neutral currents (FCNCs) in general, and the development of the Glashow, Iliopoulos, Maiani (GIM) mechanism [8] and the prediction of the charm quark mass [9]. As the field has evolved, so has the definition of "rare" decays, from branching ratios of $\sim 10^{-3}$ to the current levels of $\sim 10^{-12}$. There are several detailed reviews of this subject [10–17].

1.2 Standard Model Kaon Triangle

The weak decay of quarks is described through the unitary CKM matrix [5,6]. This matrix and the Wolfenstein parameterization [18,19] are shown below:

$$\begin{aligned} V_{\rm CKM} &= \begin{pmatrix} V_{ud} & V_{us} & V_{ub} \\ V_{cd} & V_{cs} & V_{cb} \\ V_{td} & V_{ts} & V_{tb} \end{pmatrix} \\ &\simeq \begin{pmatrix} 1-\lambda^2/2 & \lambda & A\lambda^3(\rho - i\eta) \\ -\lambda & 1-\lambda^2/2 & A\lambda^2 \\ A\lambda^3(1-\rho-i\eta) & -A\lambda^2 1 & \end{pmatrix} + \mathcal{O}(\lambda^4) \end{aligned} \tag{1}$$

where λ is the sine of the Cabibbo angle, $\lambda \equiv \sin\theta_C \simeq 0.22$.

The unitarity of this matrix can be expressed in terms of six unitarity conditions which can be represented graphically in the form of triangles, all of which have the same area. The area of these triangles is equal to one half of the Jarlskog invariant, J_{CP} [20]. This is the fundamental measure of *CP* violation in the standard model.

The unitarity triangle is most readily expressed for the kaon system as follows:

$$\begin{aligned} V_{us}^* V_{ud} + V_{cs}^* V_{cd} + V_{ts}^* V_{td} &= 0 \\ \text{or} \\ \lambda_u + \lambda_c + \lambda_t &= 0, \end{aligned} \tag{2}$$

with the three vectors $\lambda_i \equiv V_{is}^* V_{id}$ converging to form a very elongated triangle in the complex plane. This is illustrated graphically in Figure 2. The first vector, $\lambda_u = V_{us}^* V_{ud}$, is well known. The height will be measured by $K_L \to \pi^\circ \nu\overline{\nu}$ and the third vector, $\lambda_t = V_{ts}^* V_{td}$, will be measured by the decay $K^+ \to \pi^+ \nu\overline{\nu}$. The theoretical ambiguities in interpreting all of these measurements are very small. It may be possible to extract additional constraints on the height of the triangle from $K_L \to \pi^\circ \ell^+ \ell^-$ decays and on $Re(\lambda_t)$ from $K_L \to \mu^+\mu^-$ decays.

The base of this triangle has the length $b \equiv \lambda_u = V_{us}^* V_{ud}$, determined from the decay rate of $K \to \pi e \nu_e$ and nuclear beta decay. If we assume unitarity then b is determined completely from $K \to \pi e \nu_e$ and $b = |V_{us}|$ to very good approximation. The value of λ, the

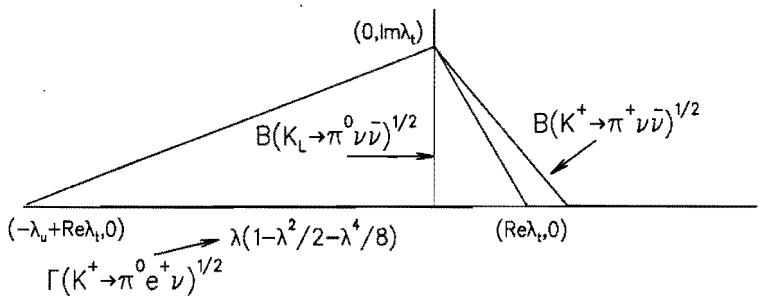

Figure 2: Unitarity triangle for the K system (not to scale).

best-known of the Wolfenstein parameters, is extracted [21] from the measurement of the $K \to \pi e \nu_e$ rate [22]. The height of the triangle, $h \equiv Im(\lambda_t)$ can be derived from a measurement of the $K_L \to \pi^\circ \nu\overline{\nu}$ branching ratio. The area of the triangle, a, is then given by two kaon decay measurements as

$$J_{CP} = 2a = b \times h = \lambda_u \times Im(\lambda_t) = 0.976 \times \lambda \times Im(\lambda_t); \tag{3}$$

the ultimate uncertainty on $Im(\lambda_t)$ and a will be limited, not by theoretical ambiguities, but by experimental uncertainties on B($K_L \to \pi^\circ \nu\overline{\nu}$), to $\mathcal{O}(5-10\%)$ which is the purpose of this proposal. This compares favorably to the B system, where three (four without the unitarity assumption) measurements are needed.

One of the possible unitarity relations that is frequently cited in the literature is

$$V_{ub}^* V_{ud} + V_{cb}^* V_{cd} + V_{tb}^* V_{td} = 0. \tag{4}$$

This equation can be represented graphically, as in Figure 3, where we have divided all sides by $V_{cb}^* V_{cd}$, which is a real quantity to $\mathcal{O}(\lambda^6)$. This particular representation provides

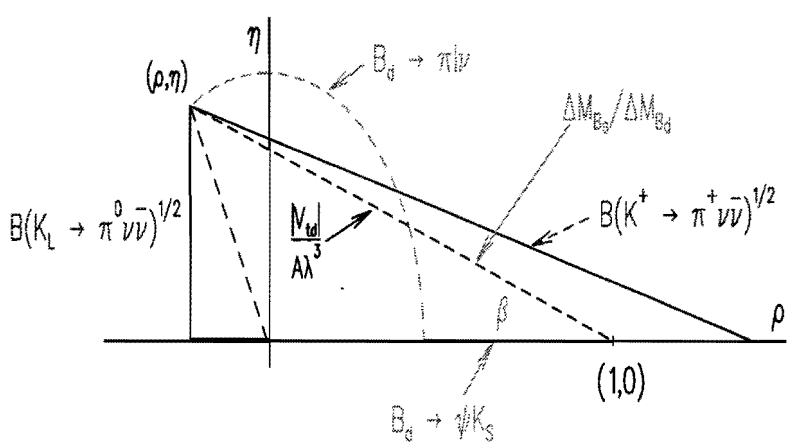

Figure 3: Traditional representation of the unitarity triangle. Measurements of B meson decays introduce constraints, and contributions from the two golden kaon decay modes are marked as shown.

a convenient display, with the apex of the triangle given by the two least well-known of the

Wolfenstein parameters, $\overline{\rho}$ and $\overline{\eta}$ where $\overline{\rho}$ and $\overline{\eta}$ are related to the Wolfenstein parameters ρ and η by $\overline{\rho} \equiv \rho(1-\lambda^2/2)$ and $\overline{\eta} \equiv \eta(1-\lambda^2/2)$.

The best information currently comes from several measurements of B meson decays, as well as the measured value of ϵ from kaon decays. All of the unitarity triangles should be tested; it is desirable to over-constrain each of the unitarity relations and to measure J_{CP} in each of the triangles.

The most powerful tests of our understanding of *CP*-violation and quark mixing will come from comparison of the results from B meson and kaon decays with little theoretical ambiguity.

The current value of the fundamental level of *CP* violation in the Standard Model, $J_{CP} = (2.7 \pm 1.1) \times 10^{-5}$, is known, primarily from measurements of B meson decays, with about 40% uncertainty [23]. Measurement of J_{CP} in the kaon system is very clean theoretically (uncertainty of ~2%) and should be measured to ~5% within a decade by this proposed experiment and others. While measurement of J_{CP} in the B system is difficult and is plagued by theoretical uncertainties, it is possible that a 15% measurement is possible. If this could be pushed to the same level expected from the kaon system, the comparison of these values will also be an important test of the SM.

1.3 $K_L \to \pi^\circ \nu\overline{\nu}$

$K_L \to \pi^\circ \nu\overline{\nu}$ proceeds through loops dominated by the top quark, as shown in Figure 4. The hadronic matrix element for these decays can be extracted from the well-measured

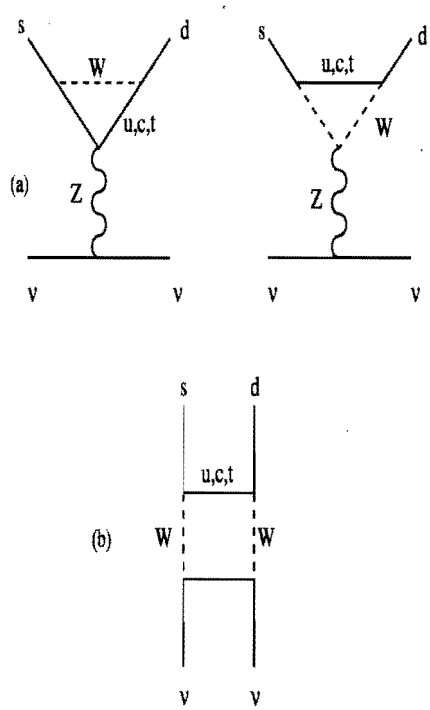

Figure 4: Feynman diagrams for the decays $K \to \pi\nu\overline{\nu}$.

$K^+ \to \pi^\circ e^+ \nu_e$ (K_{e3}) decay. The branching ratio can be expressed as [29]:

$$B(K_L \to \pi^\circ \nu\overline{\nu}\ ) \;=\; \frac{\tau_L}{\tau_{K^+}} \frac{\kappa_L \alpha^2 B(K_{e3})}{2\pi^2 \sin^4\theta_W |V_{us}|^2} \sum_l |Im(\lambda_t) X_t|^2. \tag{5}$$

The factors κ_L and κ_+ refer to the isospin corrections relating $K \to \pi\nu\overline{\nu}$ to $K^+ \to \pi^\circ e^+ \nu_e$. The Inami-Lim functions [15,39], X_q, are also functions of x_q; these contain QCD corrections. The sum is over the three neutrino generations. This equation can be rewritten in terms of the Wolfenstein parameters, and based on our current understanding of standard-model parameters, the branching ratios are predicted to be

$$\begin{aligned} B(K_L \to \pi^\circ \nu\overline{\nu}\ ) &= 4.08 \times 10^{-10} A^4 \eta^2 \\ &= (3.1 \pm 1.3) \times 10^{-11}. \end{aligned} \tag{6}$$

The decay amplitude $K_L \to \pi^\circ \nu\overline{\nu}$ is direct-*CP*-violating, and offers the best opportunity for measuring the Jarlskog invariant J_{CP}.

Reference 30 points out that in a generic supersymmetric extension to the standard model, an enhanced Zds or sdg vertex that contributes to ϵ'/ϵ will also enhance either $K_L \to \pi^\circ \nu\overline{\nu}$ or $K_L \to \pi^\circ e^+ e^-$. An enhancement in these rare modes would be much easier to interpret than in ϵ'/ϵ.

1.4 Other Standard Model Physics

In addition to the rare kaon decays that directly probe Standard-Model parameters (as discussed in the preceding section), and those that are sensitive to beyond Standard Model physics (as discussed in the following section), there is an impressively broad array of other decay modes on which substantial experimental progress has been made in recent years. Although these results receive less attention, they provide critical information in a variety of areas.

Sometimes the study of these less well-known modes can turn up new phenomena of considerable interest. For example, an interesting observation of a *CP*-violating and *T*-odd angular asymmetry in the $K_L \to \pi^+\pi^- e^+ e^-$ decay was observed for the first time by the KTeV experiment. This is the largest *CP*-violating effect yet seen, and the first *CP*-violating effect ever observed in an angular distribution.

1.4.1 $K_L \to \pi^+\pi^- e^+ e^-$

The $K_L \to \pi^+\pi^- e^+ e^-$ decay mode, first observed [24] in the KTeV E799 experiment at Fermilab, has proved to be both complex and rich in opportunities for new physics. The various tree level processes that can contribute to the $K_L \to \pi^+\pi^- e^+ e^-$ decay, based on the model of Sehgal and co-workers [25], include (i) Indirect CP violating bremsstrahlung process; (ii) CP conserving M1 photon emission; (iii) CP conserving charge radius process; (iv) Indirect CP violating E1 photon emission process; and (v) Direct CP violating short distance (SD) E1 photon emission.

The five diagrams associated with these $K_L \to \pi^+\pi^- e^+ e^-$ decay amplitudes are shown in Fig. 5. The dominant processes are the CP violating bremsstrahlung amplitude and the

M1 photon emission both of which have been observed by the KTeV experiment. In the bremsstrahlung process, the $\pi\pi ee$ final state occurs through the CP violating $K_L \to \pi^+\pi^-$ decay followed by the radiation and internal conversion of a photon from one of the charged pions. In both the CP violating bremsstrahlung and the CP conserving M1 photon process, the M1 photon internally converts to give the e^+e^- pair.

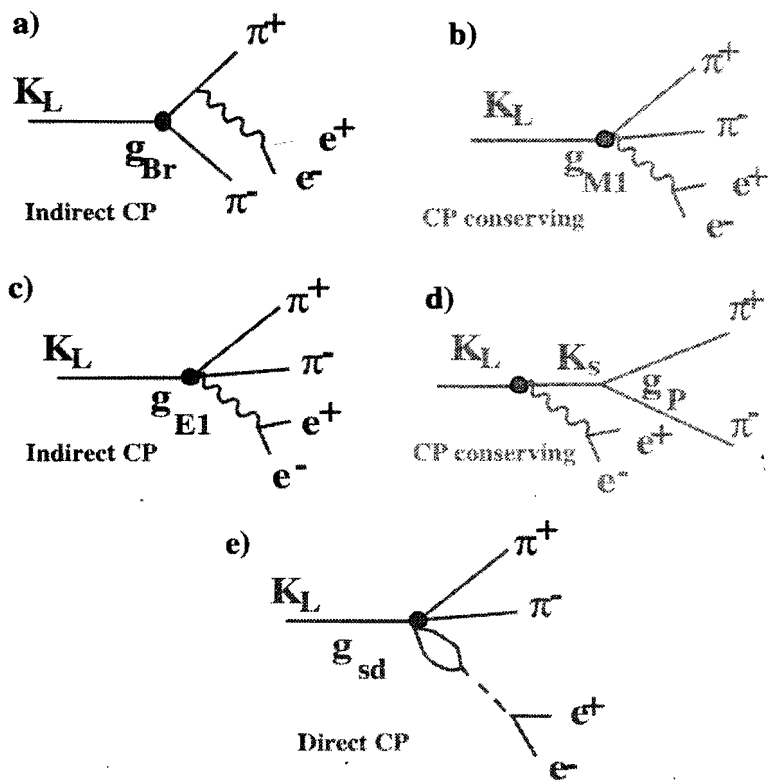

Figure 5: Processes contributing to $K_L \to \pi^+\pi^-e^+e^-$. a) CP-violating bremsstrahlung process b) CP-conserving M1 γ emission c) CP-violating E1 γ emission d) Charge radius process e) direct CP violating short distance E1 photon emission

Asymmetry in the T-odd angle between the planes of the pions and the electrons in the kaon center-of-mass was first observed by KTeV [26]. This predicted asymmetry [25] arises from the interference between the M1 and bremsstrahlung amplitudes. Other physics issues include the following topics:.

The Neutral Kaon Charge Radius: The "charge radius" process which has a great similarity to coherent regeneration $K_L \to K_S$ from atomic electrons has been observed by KTeV and provides an alternative way to determine the charge radius of the neutral K since the amplitude for the charge radius diagram at tree level is

$$|g_P| = -1/3 < R^2(K^0) > M_K^2. \tag{7}$$

In addition, via simple models [33], the mass difference of the constituent s and d quarks in the K^0 can be determined from the charge radius.

The Indirect CP Violating E1 Photon Emission: A detection of E1 direct photon emission will provide the observation of another indirect CP violating process heretofore not observed.

Measurement of the "CPT" phase: The phases of the M1 and bremsstrahlung amplitudes are respectively

$$\Phi_{br} = e^{i\delta_0(M_K^2)+\phi_{+-}}, \ \Phi_{M1} = ie^{i\delta_1(M_{\pi\pi}^2)}. \tag{8}$$

The extra factor of i in the M1 amplitude is required by CPT conservation. So if δ_0, δ_1 and ϕ_{+-} are known, a measurement of the relative phase of M1 and bremsstrahlung amplitudes can be considered to be a check of CPT conservation via the detection of the extra $\pi/2$ phase. Alternatively, assuming CPT conservation, a measurement of the relative phase can be used to determine the $\pi\pi$ strong interaction phase shifts.

Direct CP violation of an E1 photon emission is expected to cause asymmetries in various angular distributions as discussed in Section 4.2.

1.4.2 $K_L \to \mu^+\mu^-$

There has historically been strong interest in the $K_L \to \mu^+\mu^-$ decay as a probe of weak interaction dynamics, specifically $Re(V_{td})$, through its short-distance amplitude. But the short-distance amplitude is known to be quite small compared with the long-distance part, involving the $\gamma\gamma$ and $\gamma^*\gamma^*$ intermediate states. An accurate determination of the $K_L\gamma^*\gamma^*$ form factor is needed in order to evaluate the long-distance contribution, which is needed in turn to extract $Re(V_{td})$ from B($K_L \to \mu^+\mu^-$).

The decay $K_L \to \mu^+\mu^-$ is dominated by the process of $K_L \to \gamma\gamma$ with the two real photons converting to a $\mu^+\mu^-$ pair. This contribution can be precisely calculated in QED [32] based on a measurement of the $K_L \to \gamma\gamma$ branching ratio. However, there is also a long-distance dispersive contribution, through off-shell photons. This contribution needs additional input from ChPT [34, 35], which may be aided by new, improved measurements of the decays $K_L \to e^+e^-\gamma$, $K_L \to \mu^+\mu^-\gamma$, $K_L \to e^+e^-e^+e^-$ and $K_L \to \mu^+\mu^-e^+e^-$ (see Section 1.4.3), although there is some dispute as to the reliability of such calculations [36, 37]. Most interesting is the short-distance contribution which proceeds through internal quark loops, dominated by the top quark (see Figure 6). This contribution is sensitive to the real part

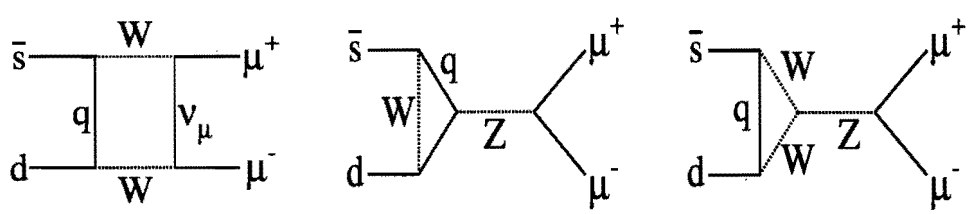

Figure 6: Feynman diagrams for the short-distance component of the decay $K_L \to \mu^+\mu^-$.

of the poorly known CKM matrix element V_{td} or equivalently to ρ [15, 38]. If this were the only contribution to the decay, the branching ratio $B_{SD}(K_L \to \mu^+\mu^-$) could be written as

$$\begin{aligned} B_{SD}(K_L \to \mu^+\mu^-) &= \frac{\tau_L}{\tau_{K^+}} \frac{\alpha^2 B(K_{\mu 2})}{\pi^2 \sin^4\theta_W |V_{us}|^2} [Y_c Re(\lambda_c) + Y_t Re(\lambda_t)]^2 \\ &= 1.51 \times 10^{-9} A^4 (\rho_0 - \overline{\rho})^2, \end{aligned} \tag{9}$$

with $\rho_0 = 1.2$ and the Inami-Lim functions [15,39], Y_q, are functions of $x_q \equiv M_q^2/M_W^2$ where M_W is the mass of the W boson and M_q is the mass of the quark q. This mode has now been measured with impressively high statistics [40] (6200 events) by the BNL E871 collaboration. The branching ratio, $\mathrm{B}(K_L \to \mu^+\mu^-) = (7.18 \pm 0.17) \times 10^{-9}$, is a factor of three more precise than previous measurements, and the error on the rate relative to $K_L \to \pi^+\pi^-$,

$$\frac{\Gamma(K_L \to \mu^+\mu^-)}{\Gamma(K_L \to \pi^+\pi^-)} = (3.474 \pm 0.054) \times 10^{-6}, \tag{10}$$

no longer dominates the error on the ratio

$$\frac{\Gamma(K_L \to \mu^+\mu^-)}{\Gamma(K_L \to \gamma\gamma)} = (1.213 \pm 0.030) \times 10^{-5}, \tag{11}$$

contributing only ~1.5% of the 2.5% error. The remaining significant sources of uncertainty,

$$\frac{\Gamma(K_L \to \gamma\gamma)}{\Gamma(K_L \to \pi^\circ\pi^\circ)} = 0.632 \pm 0.009\,, \qquad \frac{\Gamma(K_S^\circ \to \pi^+\pi^-)}{\Gamma(K_S \to \pi^\circ\pi^\circ)} = 2.186 \pm 0.028, \tag{12}$$

will need to be improved in the near future.

This measured ratio is only slightly above the unitarity bound from the on-shell two-photon contribution

$$\frac{\Gamma(K_L \to \mu^+\mu^-)}{\Gamma(K_L \to \gamma\gamma)} = 1.195 \times 10^{-5} \tag{13}$$

and limits possible short-distance contributions. With a recent estimate of the long-distance dispersive contribution [34], a limit on ρ was extracted: $\rho > -0.33$ at 90% confidence level (CL) [40].

1.4.3 $K_L \to \gamma\gamma$ and Related Decays

Like the π°, the neutral kaons couple to two photons. The effective interaction term for the CP-conserving interaction between a pseudoscalar meson field P of mass M_P and the electromagnetic field $F_{\mu\nu}$ is given by

$$\mathcal{L} = \frac{i f_{P\gamma\gamma}}{4M_P} \epsilon_{\mu\nu\lambda\sigma} F^{\mu\nu} F^{\lambda\sigma} P \tag{14}$$

which leads to a $\gamma\gamma$ partial width of

$$\Gamma_{\gamma\gamma}(P) = \frac{f_{P\gamma\gamma}^2 M_P}{16\pi}. \tag{15}$$

The coupling $f_{K_S\gamma\gamma}$ is determined in $\mathcal{O}(p^4)$ ChPT, without any free parameters, leading to the prediction [43] $\mathrm{B}(K_S \to \gamma\gamma) = 2.0 \times 10^{-6}$. This is in good agreement with the experimental value [42] (see Table 2), although the experimental errors are still rather large.

The interaction term for two real photons can be extended to off-shell photons with nonzero k^2. In this case, the coupling $f_{P\gamma^*\gamma^*}$ can depend on the two k^2 values. Typically, a form factor $F_{P\gamma\gamma}$ is introduced, so that

$$f_{P\gamma^*\gamma^*}(k_1^2, k_2^2) = f_{P\gamma\gamma} F_{P\gamma\gamma}(k_1^2, k_2^2), \tag{16}$$

Decay Mode	Branching Ratio	events	Experiment
$K_S \to \gamma\gamma$	$(2.6 \pm 0.4 \pm 0.2) \times 10^{-6}$	148	NA48-00 [42]
$K_L \to \gamma\gamma$	$(5.92 \pm 0.15) \times 10^{-4}$	110000	NA31-87 [48]
$K_L \to \mu^+\mu^-$	$(7.24 \pm 0.17) \times 10^{-9}$	6200	E871-00 [40]
$K_L \to e^+e^-$	$(8.7^{+5.7}_{-4.1}) \times 10^{-12}$	4	E871-98 [41]
$K_L \to e^+e^-\gamma$	$(1.06 \pm 0.02 \pm 0.02 \pm 0.04) \times 10^{-5}$	6854	NA48-99 [46]
$K_L \to \mu^+\mu^-\gamma$	$(3.66 \pm 0.04 \pm 0.07) \times 10^{-7}$	9105	KTeV-00 [47]
$K_L \to e^+e^-e^+e^-$	$(3.77 \pm 0.18 \pm 0.13 \pm 0.21) \times 10^{-8}$	436	KTeV-00 [47]
$K_L \to \mu^+\mu^-e^+e^-$	$(2.50 \pm 0.41 \pm 0.15) \times 10^{-9}$	38	KTeV-00 [47]
$K_L \to \mu^+\mu^-\mu^+\mu^-$	no limit		
$K_S \to \mu^+\mu^-$	$< 3.2 \times 10^{-7}$	0	CERN-73 [49]
$K_S \to e^+e^-$	$< 1.4 \times 10^{-7}$	0	CPLEAR [50]
$K_L \to e^+e^-\gamma\gamma$	$(5.84 \pm 0.15 \pm 0.32) \times 10^{-7}$	1543	KTeV-00 [51]
$K_L \to \mu^+\mu^-\gamma\gamma$	$(1.42^{+1.0}_{-0.8} \pm 0.10) \times 10^{-9}$	4	KTeV-00 [52]

Table 2: Summary of results of kaon decays to two photons and related modes

and the form factor is consequently normalized to the point $F_{P\gamma\gamma}(0,0) = 1$. The form factor $F_{K_L\gamma\gamma}$ is needed to accurately calculate the long-distance contribution to $K_L \to \mu^+\mu^-$ and $K_L \to e^+e^-$, which both have important contributions from the $\gamma^*\gamma^*$ intermediate state. As is discussed in Section 1.4.2, this long-distance contribution must be subtracted from the precise experimental measurement of $K_L \to \mu^+\mu^-$ in order to determine the interesting short-distance part of the amplitude for that decay, which can be related to the real part of the CKM matrix element V_{td} or, equivalently, to the standard-model parameter ρ.

A number of models are available for the form factor. The simplest approach is to determine the coefficient of the first few terms in a Taylor series expansion in the parameters $x_i = k_i^2/M_K^2$. An alternative parameterization [34] assumes that the form factor can be written in terms of vector-meson poles:

$$F(k_1^2, k_2^2) = 1 + \alpha \left(\frac{k_1^2}{k_1^2 - M_V^2} + \frac{k_2^2}{k_2^2 - M_V^2} \right) + \beta \frac{k_1^2 k_2^2}{(k_1^2 - M_V^2)(k_2^2 - M_V^2)}. \tag{17}$$

Rare kaon decays can be used to study the $K\gamma\gamma$ form factors in several regions. For example, the electron and muon Dalitz decays $K_L \to e^+e^-\gamma$ and $K_L \to \mu^+\mu^-\gamma$ are sensitive to the form factor with $k_2^2 = 0$ and $4m^2 < k_1^2 < M_K^2$, where m^2 is the lepton mass. From lepton universality [44] the form factors obtained in the electron and muon modes should be the same. As Table 2 shows, accurate measurements are now available in both of these $\ell\ell\gamma$ modes. Experiments analyzing $l^+l^-\gamma$ data have usually fit for the α_{K^*} parameter in the Bergström, Massó & Singer form factor model [45],

$$F(k^2, 0) = \frac{k^2}{k^2 - M_\rho^2} + \frac{2.5\alpha_{K^*} k^2}{k^2 - M_{K^*}^2} \left(\frac{4}{3} - \frac{k^2}{k^2 - M_\rho^2} - \frac{k^2/9}{k^2 - M_\omega^2} - \frac{2k^2/9}{k^2 - M_\phi^2} \right). \tag{18}$$

This model is based on a vector-dominance picture of pseudoscalar - pseudoscalar transitions (the first term) and vector-vector transitions involving K^*V vertices (the second term). This

form provides an acceptable fit to the data. Two recent fits based on high-statistics analyses yield rather different values, though. A recent fit [46] to the NA48 $K_L \to e^+e^-\gamma$ data yields $\alpha_{K^*} = -0.36 \pm 0.06$, somewhat more negative than the best fit values from earlier experiments studying the same mode. A new KTeV result [47] based on the $K_L \to \mu^+\mu^-\gamma$ mode finds $\alpha_{K^*} = -0.157 \pm 0.027$, a value about three sigma different from the new NA48 result. The k^2 region sampled by the $K_L \to \mu^+\mu^-\gamma$ data is much more heavily weighted to large k^2 values, such that a different form factor model might reduce the discrepancy.

The rarer double-internal-conversion modes, where the final state consists of two lepton pairs, are sensitive to the form factor in the region constrained by $4m_1^2 < k_1^2 < (M_K - 2m_2)^2$ and $4m_2^2 < k_2^2 < (M_K - 2m_1)^2$, where m_1 and m_2 are the two lepton masses. Three such modes are expected: $K_L \to e^+e^-e^+e^-$, $K_L \to \mu^+\mu^-e^+e^-$ and $K_L \to \mu^+\mu^-\mu^+\mu^-$. The production of muon pairs requires virtual photons at much higher k^2 and is strongly suppressed. The largest sample of $e^+e^-e^+e^-$ decays reported to date is from KTeV, with 436 events in the 1997 data sample. KTeV has also reported seeing 38 $e^+e^-\mu^+\mu^-$ events. The predicted branching ratio for the $K_L \to \mu^+\mu^-\mu^+\mu^-$ mode is below 10^{-12}.

1.4.4 $K_L \to \pi^\circ\gamma\gamma$

The measurement of such modes as $K_L \to \pi^\circ\gamma\gamma$ and $K_L \to e^+e^-\gamma\gamma$ is important for a different reason. $K_L \to \ell^+\ell^-\gamma\gamma$ is an important background in the search for $K_L \to \pi^\circ\ell^+\ell^-$. In particular, large samples of these events must be studied to determine the effectiveness of kinematic cuts necessary to observe this extremely rare decay. The decay $K_L \to \pi^\circ\gamma\gamma$ can be used to determine the *CP*-conserving part of the amplitude of $K_L \to \pi^\circ e^+e^-$ and $K_L \to \pi^\circ\mu^+\mu^-$.

Additional contributions from the $\pi^\circ\gamma^*\gamma^*$ intermediate state with off-shell photons are also important. These can be determined from ChPT models, but there are undetermined parameters that must be extracted by studying kinematic distributions in $K_L \to \pi^\circ\gamma\gamma$ and the related mode $K_L \to \pi^\circ e^+e^-\gamma$.

The decay rate and spectral shape of $K_L \to \pi^\circ\gamma\gamma$ are calculated at $\mathcal{O}(p^4)$ of ChPT, without any free parameters [43]. The prediction of the spectral shape is a striking success of ChPT. However, the decay rate is a factor of three too small. To match the experimental value, a model-dependent contribution from $\mathcal{O}(p^6)$ is needed, which is usually parameterized with a constant a_V [53] that measures the vector meson exchange contribution to the amplitude. This parameter is of particular importance because the *CP*-conserving contribution to $K_L \to \pi^\circ e^+e^-$ depends on the value of a_V. Based on half of the total data sample, KTeV has recently measured $a_V = -0.72 \pm 0.05 \pm 0.06$ [54], implying a contribution of $1\text{–}2 \times 10^{-12}$ to $K_L \to \pi^\circ e^+e^-$. NA48 has also reported a preliminary result [56], based on almost 1400 events from part of the 1998 and 1999 runs, of $\mathrm{B}(K_L \to \pi^\circ\gamma\gamma\ ) = (1.51 \pm 0.05 \pm 0.20) \times 10^{-6}$, with $a_V = -0.45$.

Table 3 summarizes the experimental measurements of $K \to \pi\gamma\gamma$. The KTeV measurement of $K_L \to \pi^\circ e^+e^-\gamma$ should improve by a factor of three and the measurement of $K_L \to \pi^\circ\gamma\gamma$ should improve by a factor of two.

Because of their low energy release and wide variety of final states, kaon decays provide an excellent testing ground for the predictions of ChPT. For example, the $K \to \pi\gamma\gamma$ modes and the direct-emission component of radiative semileptonic decay modes have proven to be good testing grounds for comparing $\mathcal{O}(p^4)$ to $\mathcal{O}(p^6)$ calculations. ChPT calculations of $\pi\pi$

Decay Mode	Branching Ratio	events	Experiment
$K_L \to \pi^\circ\gamma\gamma$	$(1.68 \pm 0.07 \pm 0.08) \times 10^{-6}$	884	KTeV (1999) [54]
$K_L \to \pi^\circ e^+e^-\gamma$	$(2.20 \pm 0.48 \pm 0.11) \times 10^{-8}$	18	KTeV (1999) [55]

Table 3: Summary of $K \to \pi\gamma\gamma$ results

scattering can likewise be tested by measuring the form factors of $K \to \pi\pi\ell\nu_\ell$ ($K_{\ell 4}$) decays.

1.5 Beyond the Standard Model

All experimental evidence to date supports the exact conservation of an additive quantum number for each family of charged leptons. Thus $K_L \to \mu^+\mu^-$ and $K_L \to e^+e^-$ are allowed, although suppressed by the GIM mechanism and by helicity suppression, whereas $K_L \to \mu e$ appears to be absolutely forbidden. If neutrino masses are nonzero, some very tiny mixing effects could permit such a decay in the standard model, but it would occur at at very small levels, many orders of magnitude beyond the present experimental sensitivity. Any observation of a signal for the decays $K_L \to \mu e$ or $K_L \to \pi^\circ\mu e$ would thus be conclusive evidence for new physics beyond the standard model [27].

Although this lepton-flavor-number conservation law appears to be respected in the standard model, there is no fundamental reason or underlying symmetry to explain why this should be so. Indeed, many possible extensions to the standard model predict new interactions involving heavy intermediate gauge bosons that could mediate the otherwise forbidden LFV decays. Some of the specific models that lead to LFV decays include [28] compositeness of quarks and leptons, left-right symmetric models, technicolor, some supersymmetric models, unified theories with horizontal gauge bosons, leptoquarks, and string theories.

It is important to look for both $K_L \to \mu e$ and the modes with an extra pion, $K_L \to \pi^\circ\mu e$, because the $K_L \to \mu e$ decay is sensitive to pseudoscalar and axial vector coupling, whereas the other modes are sensitive to scalar or vector couplings. In both cases, the excellent sensitivity of these experiments probes mass scales that are very large. Of course, the sensitivity of the experiments to new interactions depends on the coupling constants involved. If the new coupling for an intermediate vector boson of mass M_X is g_X, then the lower bound on M_X implied by an upper limit on $B(K_L \to \mu e\ )$ is given in terms of the electroweak coupling g by the approximate expression

$$M_X \simeq 200\text{TeV}/c^2 \times \frac{g_X}{g} \times \left[\frac{10^{-12}}{B(K_L \to \mu e\ )}\right]^{1/4} . \tag{19}$$

Thus, upper limits in the range of 10^{-12} will yield impressive lower bounds on M_X, at least if g_X is comparable to g.

2 $K_L \to \pi^0 \nu\overline{\nu}$ at KAMI

2.1 Introduction

We summarize here the concepts that drive the design of the KAMI detector and the $K_L \to \pi^0 \nu\overline{\nu}$ physics measurement. These concepts are discussed in detail in the sections that follow.

In order to attain a clear observation of $K_L \to \pi^0 \nu\overline{\nu}$, three basic criteria must be met. The first of these involves the flux of kaons and neutrons. Appendix B describes the actual measurements of the kaon and neutron fluxes made using 150 GeV protons on target with the KTeV detector in January, 2000. The flux expected for KAMI is described in Section 2.5. At the highest energy (800 GeV from the Tevatron) there is not a sufficient flux of protons to produce the kaon flux needed for very rare decay searches. At very low energy (e.g. 12 GeV at KEK and 28 GeV at BNL), the neutron/kaon ratio is very large, between a few hundred to a few thousand. The optimal energy is somewhere in between. The Main Injector, at 120 GeV provides the most favorable flux ratio of any existing machine.

The second criterion is the signal-to-background (S/B) ratio, where the background comes almost entirely from $K_L \to 2\pi^0$ decays. In KAMI, we achieve a S/B of 4 to 5 using hermetic calorimetry. The performance that will be required of the key detector components are described in detail in Sections 3 and 6. Most important is the photo-nuclear inefficiency for photons in the CsI and the photon veto detectors. Appendix C describes beam test measurements of photo-nuclear inefficiency in CsI and lead/scintillator photon veto modules using a tagged photon beam at KEK. It is important not only to achieve high efficiency photon detection, but to monitor the efficiency throughout the life of the experiment. Various methods and techniques are being developed for this purpose. The ratio of $K_L \to 3\pi^0$ $/K_L \to 2\pi^0$ and the ratio of 5 to 6 cluster events from $K_L \to 3\pi^0$ decays can both be used as a cross-check of the $K_L \to 2\pi^0$ $/K_L \to \pi^0 \nu\overline{\nu}$ S/B while $e^{\pm}$ from $K_L \to \pi^{\pm} e^{\mp} \nu$ decays, muons and photons from $K_L \to 3\pi^0$ and $K_L \to \pi^+\pi^-\pi^0$ decays can be used to monitor the day-to-day performance of the detector. The KAMI charged spectrometer plays an indispensable role in monitoring and calibrating the detector. Work is underway to develop a spectrum of additional tools to understand the S/B ranging from traditional methods of tagging photons from 3π decays, to maximum likelihood fits (see Section 7.1) to neural network algorithms (see section 7.2).

The third criterion is acceptance, which includes geometry, analysis cuts and deadtime from accidentals. The product of the geometrical acceptance and the analysis cuts is 8.4% in KAMI (see section 2.6.2). Accidental losses result from kaon decays and target muons but are dominated by neutron interactions in the Beam Anti detector. Based on beam test results and detailed simulations (see Section 6.4) of a fully active, finely segmented device ($NaBi(W0_4)_2$ crystals) the overall rate of accidental losses from all sources are no worse than 45%. This will improve when better algorithms can be developed for separating neutron interactions from photons.

There are other important issues including CsI radiation damage (see section 6.2.1), collimator scattering (beam halo) and achieving the lowest possible photon veto threshold. These are all discussed in subsequent sections.

In the studies described in this proposal we have tried to make conservative assumptions,

with the exception of the photon veto inefficiency which will clearly represent a technological step forward. In our simulations we use 10 MeV photon veto thresholds, though we expect to do better in practice. We use a 20 ns veto time window for the photon veto system, though we believe in practice we can do better. We assume that 20% of the interacting neutrons in the Beam Anti will have a component that is indistinguishable from photons, though again we believe we can do better. We believe that we are on solid ground with respect to all truly fundamental issues.

2.2 Experimental Status

Explicit attempts to detect the decay $K_L \to \pi^0 \nu\overline{\nu}$ thus far have all been made at Fermilab. With one exception, these attempts have relied on observation of the Dalitz decay mode of the π^0 to $e^+e^-\gamma$. The charged vertex from the e^+e^- provides kinematical constraints which allow for simple reconstruction of the π^0 and effective rejection of backgrounds to the sensitivity levels reached thus far. The best published limit to date for the decay is 5.9×10^{-7} (90% CL) from KTeV-E799 [57]. Previously, a limit of 5.8×10^{-5} (90% CL) was obtained from from Fermilab experiment E799-I [58] using the Dalitz mode.

The 2γ decay mode of the π^0 provides two orders of magnitude higher sensitivity per unit time than the Dalitz mode, but at the cost of increased background due to fewer kinematical constraints. Attempts to measure this decay in the future must rely on the 2γ mode to take advantage of this increased sensitivity.

The only attempt to date to measure $K_L \to \pi^0 \nu\overline{\nu}$ using the 2γ decay mode has been made by KTeV in a dedicated one day run in December, 1996. During this special run, one of KTeV's two parallel neutral beams was collimated down to 4 cm x 4 cm (at the CsI) in order to obtain better P_t resolution on the decay. The second beam was completely closed off. Figure 7 shows the P_t distribution of π^0 events passing all other cuts. This special run was performed at 800 GeV where background from hyperons are a concern. This will not be the case for KAMI with a 120 GeV primary protons.
An upper limit on the branching ratio of 1.6×10^{-6} (90% CL) was obtained [59]. At the time, this represented a factor of 30 improvement over the best existing limit from E799-I using the Dalitz decay mode of the π^0. The sensitivity of the measurement was limited by beam neutrons interacting in the vacuum window approximately 30 m upstream of the CsI calorimeter. This points out the danger posed to high-sensitivity rare decay searches when any material is present in the beam region. The evacuated region in KAMI will extend to the front face of the CsI calorimeter with no material in the beam region until reaching the vacuum window, just upstream of the CsI. This will reduce the neutron induced background to a negligible level.

2.3 The KAMI Experiment

The next step in the continuing neutral kaon program at Fermilab will be KAMI (Kaons At the Main Injector). KAMI benefits greatly from our experience with its many predecessors; most recently KTeV. The experience gained over time in working in intense neutral beams will be of great benefit to KAMI, particularly with respect to issues like beam halo, collimation, sweeping, absorber configurations, collimator scattering and secondary production, etc.

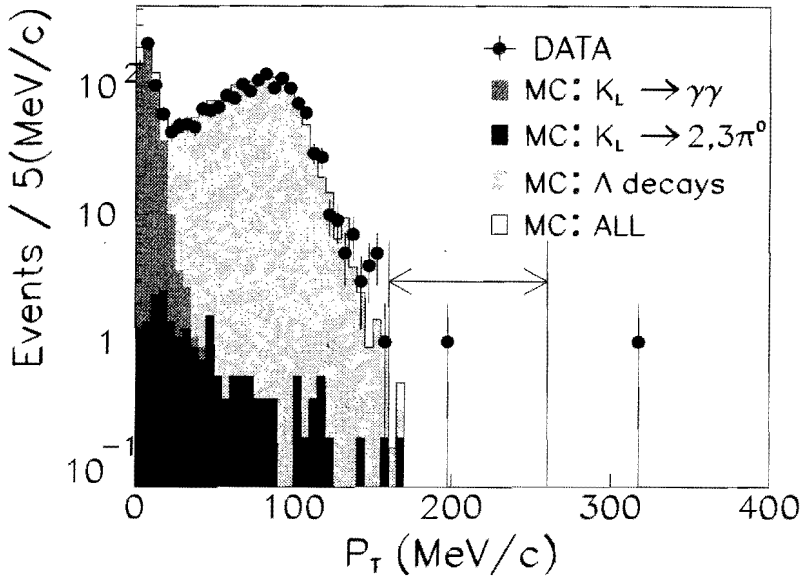

Figure 7: The P_t distribution from the one day 800 GeV KTeV run after all cuts except the final P_t cut. The arrow designates the signal region. The simulated backgrounds from K_L and Λ decays are overlaid on the data. The two events above 190 MeV/c are consistent with neutron interactions in the vacuum window.

Many of these effects are difficult to simulate to sufficient accuracy, so extensive experience and direct measurements are a definite advantage.

KAMI's primary physics goal is to detect the very rare $K_L \rightarrow \pi^0\nu\overline{\nu}$ decay, measure its branching ratio, and extract a value for the CKM parameter η to an accuracy of better than 10%. Within the context of the Standard Model, η is the parameter responsible for all CP violating effects. While the importance of this measurement cannot be overstated, KAMI will mount a rich and diverse physics program that extends well beyond the $K_L \rightarrow \pi^0\nu\overline{\nu}$ measurement. The flux and energy of the Main Injector combined with a superb high-rate, high resolution hermetic detector allows KAMI to directly confront issues of direct CP violation, lepton flavor violation and new physics phenomena on a broad front. None of the other proposed $K_L \rightarrow \pi^0\nu\overline{\nu}$ experiments has this capability.

2.4 Detector concepts

A clear observation of the decay $K_L \rightarrow \pi^0\nu\overline{\nu}$ will be the highest priority for KAMI. The KAMI detector must be optimized with this principle in mind. At the same time, we would like to explore other important rare decay modes such as $K_L \rightarrow \mu^+\mu^-$, $\pi^+\pi^-e^+e^-$, $\pi^0\mu^\pm e^\mp$ and $\mu^\pm e^\mp$. In order to achieve these physics goals with minimum investment, the KAMI detector has been designed according to the following principles:

1. Utilize the existing KTeV infrastructure to the greatest extent possible. This includes the experimental hall, the CsI calorimeter, and significant parts of the vacuum system;

2. For $K_L \to \pi^0 \nu \overline{\nu}$, install newly constructed hermetic photon veto detectors;

3. For charged decay modes, to monitor the detector, and to maintain our ability to calibrate the CsI calorimeter to the required accuracy, insert scintillating fiber tracking planes inside of the vacuum tank. The vacuum tank will pass through the gap of the analysis magnet.

Figure 8 shows the layout of a detector design based on the above concepts.

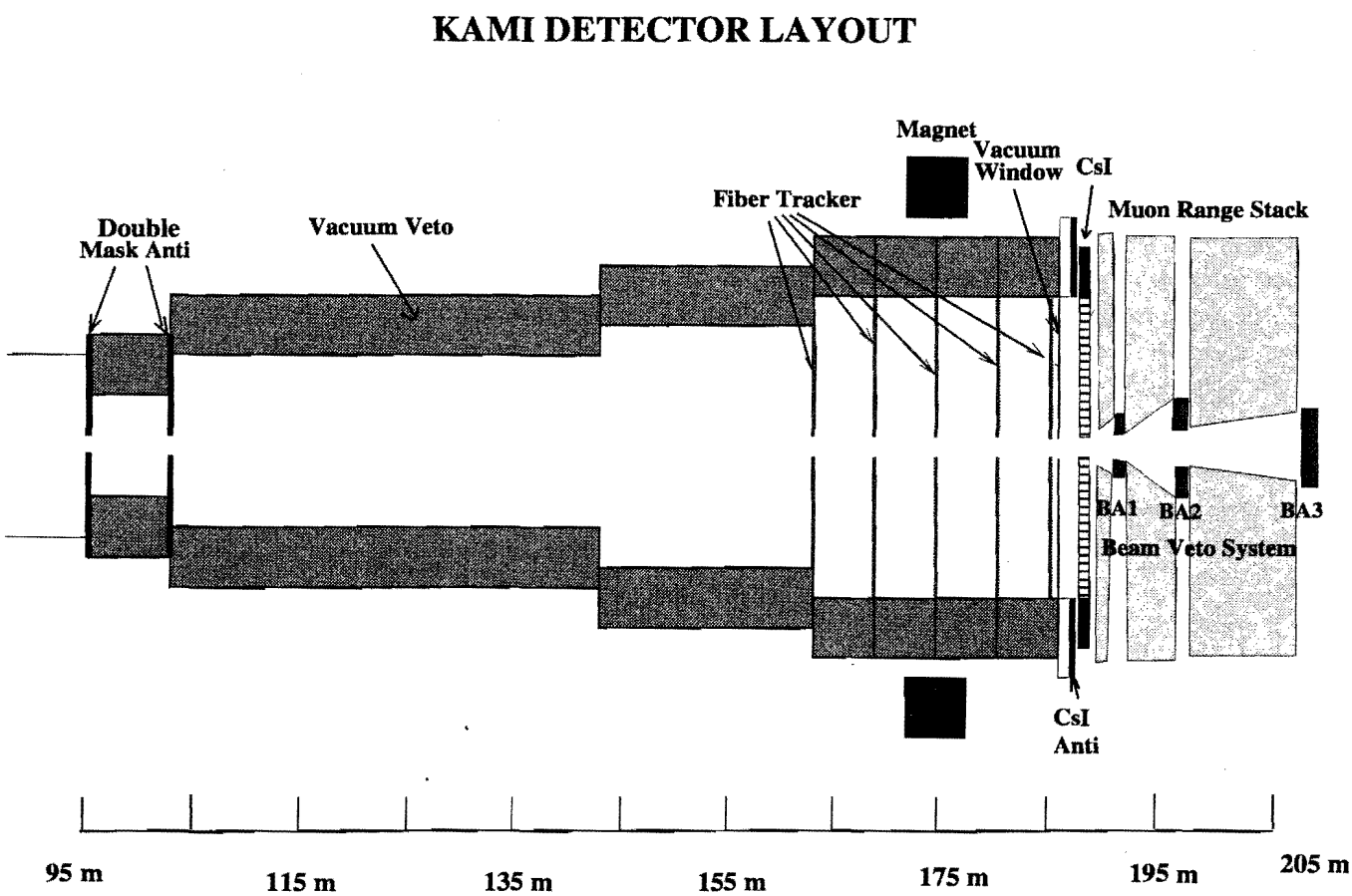

Figure 8: Schematic of the KAMI detector.

2.5 Kaon Flux

The expected flux of kaons in KAMI resulting from 120 GeV protons on target can be accurately estimated from data obtained during the 2000 KAMI 150 GeV beam test. Results from the beam test are discussed in detail in Appendix B. The flux numbers must be multiplied by a correction factor to account for the difference in kaon production from 150 GeV and 120 GeV primary protons. The scale factors are obtained using the Malensek parameterization [60]. The measured kaon flux from the beam test for 3 different targeting angles is shown in Table 4. The correction factors and the flux expected from 120 GeV protons are also listed. The flux is measured at 90 m from the target. A 3 inch thick lead absorber was present in the neutral beam to absorb photons produced at the target during the KAMI beam test. The approximately 50% attenuation of the kaon flux which results from the lead filter is included in all KAMI flux estimates since this filter will continue to be necessary in the future.

target angle (mrad)	Measured K_L Flux (150 GeV)	150→120 GeV Correction Factor	Expected K_L Flux (120 GeV)
12 ± 1	8.92 ± 1.87	0.72	6.42
15 ± 1	6.86 ± 1.44	0.73	5.01
20 ± 1	4.16 ± 0.87	0.74	3.08

Table 4: Kaon flux vs. target angle from 2000 KAMI beam test for $E_K > 6$ GeV. The flux is measured 90 m from the production target in units of $\times 10^{-6}$/proton/μstr. The incident proton beam energy is 150 GeV with no beryllium absorber in the neutral beam. Also shown are the correction factors obtained from the Malensek parameterization [60] to account for the difference in kaon production from 150 GeV and 120 GeV primary protons. The expected flux at 120 GeV is also listed.

From the expected K_L flux and momentum spectrum at 120 GeV, the number of decaying kaons can be calculated in the fiducial volume from 90 m to 183 m (the CsI calorimeter is located at 186 m). We assume 3×10^{13} protons per pulse delivered from the Main Injector. The protons are unbunched with a spill duration of 1 second and a cycle time of 3 seconds. The beam is 0.41 μstr in size, which corresponds to a 12 cm$\times$12 cm beam spot at the CsI calorimeter. We further assume that the Main Injector delivers fixed target beam 2×10^7 seconds per year [61] with a duty factor of 1/3. This corresponds to 2.0×10^{20} protons per year delivered to KAMI. The number of kaon decays under these conditions are listed in Table 5 for the three targeting angles for which we have test beam data.

2.6 Physics sensitivity

The primary goal of KAMI is to detect the very rare decay $K_L \to \pi^0\nu\overline{\nu}$, measure its branching ratio, and extract a value for the fundamental CKM parameter η. In order for the value of η to be meaningful, at least 100 signal events must be collected. This will result in the precision needed to make comparisons with measurements in the B physics sector. A precise

	12 mrad	15 mrad	20 mrad
K_L Flux at 90 m	7.9×10^7	6.2×10^7	3.8×10^7
Decay probability (90-183 m)	0.143	0.152	0.172
Kaon decays/sec. (90-183 m)	1.1×10^7	9.4×10^6	6.5×10^6
Kaon decays/year (90-183 m)	7.3×10^{13}	6.3×10^{13}	4.3×10^{13}

Table 5: Rate of kaon decays vs targeting angle for 120 GeV proton beam from the Main Injector. Each Main Injector pulse contains 3×10^{13} protons. The beam is 0.41 μstr in size and no beryllium absorber is included in the neutral beam.

measurement of η will also provide a useful constraint on the CKM triangle where our goal is to over-constrain the triangle to search for deviations from the Standard Model. Using even the most conservative of estimates, will collect at least 100 events over a period of 3 years.

The sensitivity for $K_L \to \pi^0\nu\overline{\nu}$ is determined by the kaon flux, acceptance and running time. Accidental activity in the detector from kaon decays, target interactions and beam neutrons can result in random vetoes that reduce the signal sensitivity and must be included in any realistic estimate.

2.6.1 Signal and Background Signatures

The signature for a $K_L \to \pi^0\nu\overline{\nu}$ decay is a single unbalanced π^0. Exactly two neutral clusters are required in the CsI calorimeter with no accompanying activity in any of the veto counters. Reconstructing the two clusters to the mass of a π^0 allows a determination of the decay vertex along the beam direction. Using the small angle approximation, the Z vertex is expressed as:

$$Z = Z_{CsI} - (r_{12}/m_{\pi^0})\sqrt{E_1 \cdot E_2} \tag{20}$$

where Z_{CsI} is the position of the CsI calorimeter, r_{12} is the distance between the two photons in the calorimeter, m_{π^0} is the π^0 mass and E_i is the energy of the i-th photon. No information is available to determine the transverse decay vertex, so it is assumed to be at the center of the beam. From the measured energies and positions in the CsI calorimeter and the calculated decay vertex, the transverse momentum (P_t) of the reconstructed π^0 can be determined. An unbalanced P_t spectrum is a characteristic feature of the $K_L \to \pi^0\nu\overline{\nu}$ decay, as shown in Figure 9. The P_t resolution is smeared by the finite transverse beam size.

The primary background to $K_L \to \pi^0\nu\overline{\nu}$ is $K_L \to 2\pi^0$ where two of the photons escape detection. Photons can be missed because of various inefficiency mechanisms in the photon veto system. Photons can also escape detection by fusing with a nearby cluster in the CsI calorimeter. There are three primary handles on reducing the $K_L \to 2\pi^0$ background; photon vetoing, P_t cuts and vertex cuts. The $K_L \to 2\pi^0$ background will be discussed in detail in Section 3.2.

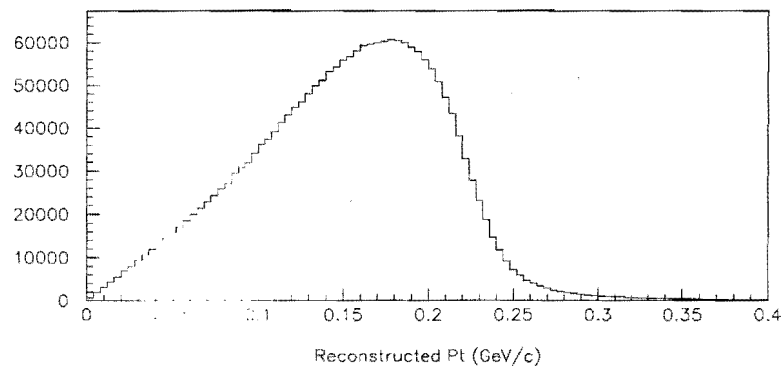

Figure 9: The reconstructed P_t spectrum for $K_L \to \pi^0\nu\overline{\nu}$ decays. An unbalanced P_t spectrum is a characteristic feature of the decay.

2.6.2 $K_L \to \pi^0\nu\overline{\nu}$ Acceptance

The acceptance for $K_L \to \pi^0\nu\overline{\nu}$ events is the product of the geometrical acceptance and the efficiency of the cuts used to reduce background contamination. A fast Monte Carlo with realistic resolution smearing, measured K_L momentum distributions and beam halos obtained from GEANT simulations of the beamline is used to calculate the acceptance. $K_L \to \pi^0\nu\overline{\nu}$ decays are generated using the matrix element for $K^+ \to \pi^+\nu\overline{\nu}$ which depends on the measured form factors from $K_L \to \pi^\pm e^\mp \nu$ and $K_L \to \pi^\pm \mu^\mp \nu$ [62]. $K_L \to \pi^0\nu\overline{\nu}$ and $K^+ \to \pi^+\nu\overline{\nu}$ are related by isospin and the amplitudes for decays of the CP eigenstates K_1 and K_2 into $K_L \to \pi^0\nu\overline{\nu}$ are equal to the real and imaginary parts, respectively, of the amplitude for $K^+ \to \pi^+\nu\overline{\nu}$ [63] [64].

A set of cuts have been developed to reject the anticipated backgrounds while maintaining good acceptance for $K_L \to \pi^0\nu\overline{\nu}$ decays. The cuts used for this analysis are:

1. Reconstructed P_t between 0.130 GeV/c and 0.250 GeV/c;
2. Reconstructed Z vertex between 100 m and 165 m;
3. Energy of each CsI cluster greater than 1.25 GeV;
4. Sum of the two CsI cluster energies greater than 5.0 GeV;
5. Center-of-energy of the two CsI clusters greater than 0.1 m;
6. Distance between two CsI clusters greater than 30 cm;
7. Photons in the CsI calorimeter must be outside a 30 cm × 30 cm area centered on the neutral beam axis (the CsI beam hole is 15 cm × 15 cm);
8. Photons in the CsI calorimeter must be more than 5 cm inside the outer edge of the array;

The first 4 cuts are primarily intended to reduce the background from $K_L \to 2\pi^0$. Cut 3, the cluster energy cut, also reduces the impact of accidental photons, which are strongly peaked at low energy. The center-of-energy cut, along with the P_t cut, is intended to eliminate the background from $K_L \to \gamma\gamma$. Cut 6, the cluster separation cut, is intended to reduce backgrounds from hadron interactions in the vacuum window. The fiducial cut around the beam hole and around the outer edge of the CsI calorimeter are intended to eliminate clusters that are poorly measured because of energy leakage. The fiducial cut around the beam hole also helps to eliminate background from upstream $K_L \to 3\pi^0$ decays. These cuts will all be described in greater detail in Section 3 when we explicitly discuss the various background sources.

The acceptance for $K_L \to \pi^0\nu\overline{\nu}$ decays relative to the number of decays between 90 m and 183 m is shown in Table 6 for three different targeting angles. These targeting angles are chosen because they correspond to the targeting angles used during the 2000 KAMI beam test. The acceptance increases for smaller targeting angles as the kaons become more energetic.

Target Angle (mrad)	Acceptance
12	0.091
15	0.084
20	0.067

Table 6: Acceptance for $K_L \to \pi^0\nu\overline{\nu}$ decays between 90 m and 183 m. The applied cuts are described in the text.

2.6.3 Accidental Losses

In order to effectively reject background to the $K_L \to \pi^0\nu\overline{\nu}$ signal, it is necessary to veto on extra particles in the detector down to very low energies (~10 MeV). Every kaon decay in the fiducial volume will result in a signal in at least one veto detector and a significant fraction of the decays upstream of the fiducial volume will also result in signals in veto counters. Decays downstream of the CsI will contribute to the rate of the Beam Anti. Pions and muons from the target which are not successfully swept away or shielded can also generate vetoes. Finally, the interaction of beam hadrons in the Beam Anti will also have to be vetoed when they contain a component that cannot be distinguished from photons.

To minimize accidental losses, KAMI is requesting unbunched beam spread out uniformly over the 1 second spill duration. Based on the size of the KAMI detector and the expected time slewing in detector elements, a veto time window can be determined. Any signal events which are recorded during a veto window will be rejected as background. The veto time window for kaon decays and muons from the target is dominated by the vacuum photon veto system. Based on estimates of the time slewing across the photon veto detectors and the time associated with maximum flight path differences, a very conservative veto window of 20 ns has been chosen. In practice we expect to do better than this by taking advantage

of the TDC information. The veto time window for the Beam Anti, a smaller and faster detector, is chosen to be 10 ns.

To estimate the accidental losses due to kaon decays, the measured flux of kaons at 90 m must be extrapolated back to the target. A fast Monte Carlo is then used to determine the rate of decays between the target and BA3 for which a particle deposits energy in an active detector. This is done for each of the four major decay modes ($K_L \to 3\pi^0$, $K_L \to \pi^+\pi^-\pi^0$, $K_L \to \pi^\pm e^\mp \nu$, $K_L \to \pi^\pm \mu^\mp \nu$), appropriately weighted. Collimators and shielding upstream of the fiducial volume help to reduce the flux of particles into the active part of the detector from upstream decays while every decay downstream of 90 m generates hits in active detectors.

The rate of neutrons that interact in BA3 and cannot be distinguished from photons also contribute to the accidental losses. Detailed GEANT studies of the Beam Anti indicate that 30% of the beam neutrons interact in BA3 and that ~20% of these interactions contain components that mimic photons and require a veto. The neutron rates for various targeting angles and beryllium absorber configurations are listed in Table 7. The neutron fluxes and attenuation factors for each set of beam conditions were measured during the 2000 KAMI beam test (see Appendix B). The performance of the Beam Anti is described in greater detail in Section 6.4.

	Be. Absorber	Neutron Flux	Interaction Rate in BA3	Fake γ Rate
12 mrad				
	0"	760 MHz	228 MHz	46 MHz
	10"	346 MHz	104 MHz	21 MHz
	20"	155 MHz	47 MHz	9 MHz
	38"	42 MHz	13 MHz	3 MHz
15 mrad				
	0"	467 MHz	140 MHz	28 MHz
	10"	198 MHz	59 MHz	12 MHz
	20"	95 MHz	29 MHz	6 MHz
	38"	27 MHz	8 MHz	2 MHz
20 mrad				
	0"	213 MHz	64 MHz	13 MHz
	10"	93 MHz	28 MHz	6 MHz
	20"	42 MHz	13 MHz	3 MHz
	38"	14 MHz	4 MHz	1 MHz

Table 7: The neutron flux, neutron interaction rate in BA3 and the rate at which these neutron interactions mimic photons vs targeting angle and beryllium absorber thickness. The neutron fluxes and beryllium attenuation factors for each set of beam conditions were measured during the 2000 KAMI beam test.

Muons from the target and dump which are not swept away or shielded must also be accounted for. A detailed model that estimates muons from the target and the dump is

not currently in place, but measured muon rates from the KAMI beam test at 150 GeV are available. We scale these measured rates to a proton intensity of 3×10^{13}/second.

The accidental losses from kaon decays, muons and neutron interactions in the Beam Anti are listed in Table 8 for various targeting angles and beryllium absorber configurations. Using the estimated losses from accidentals, the measured kaon fluxes and beryllium attenuation factors from the KAMI beam test, and assuming 2×10^{20} delivered protons per year, the number of effective or live K_L decays can be calculated. The number of $K_L \to \pi^0 \nu\overline{\nu}$ events per year, corrected for accidental losses, are also calculated using a branching ratio of 3×10^{-11} [65] and the acceptances in Table 6.

For the balance of this proposal we will assume running conditions of 15 mrad and no beryllium absorber in the neutral beam. The kaon momentum spectrum at 15 mrad is shown in Figure 10.

	Be. Absorber	Accidental Loss Fraction	Effective K_L Decays per Year	$K_L \to \pi^0 \nu\overline{\nu}$ Events per Year
12 mrad				
	0"	55%	3.3×10^{13}	91
	10"	36%	2.8×10^{13}	77
	20"	24%	2.2×10^{13}	61
	38"	13%	1.1×10^{13}	30
15 mrad				
	0"	45%	3.5×10^{13}	**88**
	10"	28%	2.5×10^{13}	63
	20"	20%	2.0×10^{13}	50
	38"	11%	9.1×10^{12}	23
20 mrad				
	0"	31%	3.0×10^{13}	60
	10"	20%	2.4×10^{13}	48
	20"	14%	1.5×10^{13}	30
	38"	9%	7.4×10^{12}	15

Table 8: The overall fraction of events lost due to accidental activity in the detector, the effective number of kaon decays per year after correcting for accidental losses, and the resulting number of $K_L \to \pi^0 \nu\overline{\nu}$ events per year for various targeting angles and beryllium absorber configurations. The number of $K_L \to \pi^0 \nu\overline{\nu}$ events per year were calculated using a branching ratio of 3×10^{-11} and the acceptances listed in Table 6. The number of events per year for our nominal running conditions of 15 mrad and no beryllium absorber is highlighted.

2.6.4 Summary

A careful and conservative estimate of KAMI's sensitivity to the decay mode $K_L \to \pi^0 \nu\overline{\nu}$ has been made. The sensitivity depends on *measured* kaon fluxes and a realistic and conservative estimate of losses due to accidental activity in the detector.

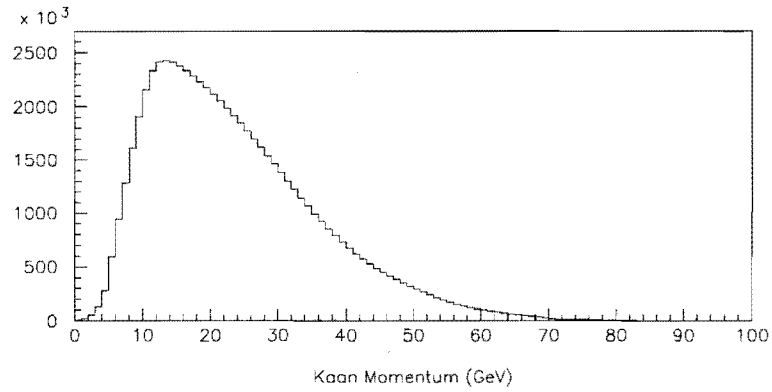

Figure 10: The kaon momentum spectrum 90 m from the production target for a 15 mrad targeting angle.

Table 8 demonstrates that in one year of running significant progress can be made toward the stated goal of at least 100 events. With a 15 mrad targeting angle and no beryllium absorber ~90 events can be collected per year.

Because the benchmark of 100 $K_L \rightarrow \pi^0\nu\overline{\nu}$ events is so important, it is useful to examine the strength of the underlying assumptions and the accuracy of the parameters used to make the estimate. The branching ratio for $K_L \rightarrow \pi^0\nu\overline{\nu}$ within the context of the Standard Model is $(3.1 \pm 1.3) \times 10^{-11}$ where the error depends almost entirely on the input CKM parameters [65]. All of the calculations in this document assume a value of 3.0×10^{-11}. If BR($K_L \rightarrow \pi^0\nu\overline{\nu}$) is as small as 1.0×10^{-11} KAMI would only collect ~30 events per year (other experimenters attempting this measurement would be similarly affected). The $K_L \rightarrow 3\pi^0$ flux measured during the KAMI beam test is accurate to ~20% which could, in concert with a smaller branching ratio, further reduce the $K_L \rightarrow \pi^0\nu\overline{\nu}$. Similarly, a branching ratio as large as 4.0×10^{-11} would result in 120 events per year using our nominal flux number. The acceptance for $K_L \rightarrow \pi^0\nu\overline{\nu}$ with a 2 m × 2 m CsI calorimeter (the KTeV calorimeter) is 5.76% which results in ~60 events per year using the nominal branching ratio and beam flux, but drops to 16 events per year in the pessimistic scenario described above. This is the primary motivation for expanding the size of the CsI calorimeter. The expanded calorimeter being proposed makes it possible for KAMI to still collect nearly 100 events in three years of running in the event of the pessimistic scenario described above.

The yield of $K_L \rightarrow \pi^0\nu\overline{\nu}$ events could also fall short if the required number of protons are not available. We assume 2.0×10^{20} protons per year based on a running time of 2×10^7 seconds per year, a duty factor of 1/3 and 3×10^{13} protons per pulse. The management of the Fermilab Beams Division believes it will be possible to run the Main Injector, a conventional accelerator without superconducting magnets, for 2×10^7 seconds a year [61] (K0PI0 at Brookhaven is also assuming $\sim 2 \times 10^7$ seconds of running per year). Less running time will have a straightforward impact on the event yield. There are also issues of proton economics related to sharing the beam with other potential users. It is difficult to project 4 or 5 years into the future with much accuracy, but ultimately proton resources are a laboratory management issue.

3 Backgrounds to $K_L \to \pi^0\nu\overline{\nu}$

3.1 The KAMI Monte Carlo

The $K_L \to 2\pi^0$ background is estimated using a fast Monte Carlo with realistic resolution smearing, measured K_L momentum distributions and beam halos obtained from GEANT simulations of the beamline. The performance of the CsI calorimeter has been parameterized based on extensive experience with the KTeV CsI calorimeter. The performance of the photon veto detectors is based on a combination of beam tests (see Appendix B) and Monte Carlo simulations (see Section 6.3). The inefficiencies of the various detectors to photons, as a function of energy, are listed in Table 9. The considerably higher inefficiencies in the BA3 are due to to the fact that this detector sits directly in the hadron beam. No efficiency is assumed below 1 GeV in BA3 for the purpose of estimating backgrounds, though Monte Carlo studies indicate that some sensitivity at low energy will be possible. A photon veto threshold of 10 MeV is used in all of the simulations.

The background rejection is estimated from a sample of $K_L \to 2\pi^0$ decays which pass all the analysis cuts. For each event a weight is constructed from the product of the detection inefficiencies of the two extra photons. The weight is the probability that the event will not be vetoed. Fused photons in the CsI calorimeter are handled in a similar way. Nearby clusters are fused into one based on the distance which separates them and the probabilities listed in Table 10. Interactions of kaons and neutrons in residual gas in the vacuum decay volume and in the vacuum window are also simulated as are the interactions of K_L decay products in the fiber tracking planes and the vacuum window. These interactions will be discussed in more detail in the relevant sections which follow.

3.2 $K_L \to 2\pi^0$

The dominant background to the $K_L \to \pi^0\nu\overline{\nu}$ signal is $K_L \to 2\pi^0$ decays where two photons are detected by the CsI calorimeter and the other two photons go undetected. There are several ways for two photons to escape detection. The photons can go undetected in the photon veto detectors, the Beam Anti or the CsI. Additionally, two photons can fuse together in the CsI and be detected as a single cluster.

There are three primary handles on reducing the $K_L \to 2\pi^0$ background; photon vetoing, P_t cuts and vertex cuts. The $K_L \to 2\pi^0$ background can be separated into two distinct categories. "Even" background events are those where the two detected photons originate from the same π^0. Even background events reconstruct with an accurate decay vertex and transverse momentum, subject to resolution effects. "Odd" background events are those where the two detected photons originate from different π^0s. In this case the reconstructed vertex, and hence the reconstructed P_t, can differ substantially from the actual values because of the incorrect assumption that the two detected photons originate from the same π^0. This can result in odd background from outside of the fiducial volume being shifted into the fiducial volume. This effect is demonstrated in Figure 11 where the generated Monte Carlo Z decay vertex for $K_L \to 2\pi^0$ events is plotted. Each entry in the plot is weighted by the product of the inefficiencies of the two photons (from Table 9) that are not used to form the π^0. Each of the events in the plot has a *reconstructed* Z vertex between 100 m and 165 m.

Energy Low-High	MA/VV/BA1/BA2 Inefficiency	CsI Inefficiency	BA3 Inefficiency
0.000 - 0.010	1.00	1.00	1.00
0.010 - 0.020	3.0×10^{-2}	1.5×10^{-3}	1.00
0.020 - 0.030	2.0×10^{-3}	1.0×10^{-3}	1.00
0.030 - 0.040	1.0×10^{-3}	9.0×10^{-4}	1.00
0.040 - 0.060	8.0×10^{-4}	8.0×10^{-4}	1.00
0.060 - 0.080	7.0×10^{-4}	6.5×10^{-4}	1.00
0.080 - 0.100	5.0×10^{-4}	5.0×10^{-4}	1.00
0.100 - 0.150	4.0×10^{-4}	3.0×10^{-4}	1.00
0.150 - 0.200	3.0×10^{-4}	1.8×10^{-4}	1.00
0.200 - 0.250	2.5×10^{-4}	1.5×10^{-4}	1.00
0.250 - 0.300	1.0×10^{-4}	5.5×10^{-5}	1.00
0.300 - 0.350	7.0×10^{-5}	3.5×10^{-5}	1.00
0.350 - 0.400	4.0×10^{-5}	2.0×10^{-5}	1.00
0.400 - 0.450	3.0×10^{-5}	1.5×10^{-5}	1.00
0.450 - 0.500	2.0×10^{-5}	5.5×10^{-6}	1.00
0.500 - 0.550	1.5×10^{-5}	3.0×10^{-6}	1.00
0.550 - 0.600	1.0×10^{-5}	1.5×10^{-6}	1.00
0.600 - 0.650	9.0×10^{-6}	1.0×10^{-6}	1.00
0.650 - 0.700	7.0×10^{-6}	1.0×10^{-6}	1.00
0.700 - 0.750	5.0×10^{-6}	1.0×10^{-6}	1.00
0.750 - 0.800	4.0×10^{-6}	1.0×10^{-6}	1.00
0.800 - 0.850	3.0×10^{-6}	1.0×10^{-6}	1.00
0.850 - 0.900	2.0×10^{-6}	1.0×10^{-6}	1.00
0.900 - 0.950	1.5×10^{-6}	1.0×10^{-6}	1.00
0.950 - 1.000	1.0×10^{-6}	1.0×10^{-6}	1.00
1.000 - 3.000	1.0×10^{-6}	1.0×10^{-6}	1.0×10^{-1}
3.000 - 10.00	1.0×10^{-6}	1.0×10^{-6}	1.0×10^{-2}
10.00 - infinite	1.0×10^{-6}	1.0×10^{-6}	1.0×10^{-3}

Table 9: Photon inefficiencies as a function of energy for the various KAMI detectors. MA, VV, BA1, BA2 and BA3 refer to the Mask Anti, Vacuum Veto, Beam Anti1 Beam Anti2 and Beam Anti3 detectors, respectively (see Figure 8). The inefficiencies in this table are used in the background simulations.

Distance Low-High (cm)	Inefficiency 2.5×2.5 cm^2 crystals	Inefficiency 5.0×5.0 cm^2 crystals
0.0 - 1.0	1.000	1.000
0.0 - 1.2	0.800	1.000
0.0 - 1.4	0.725	1.000
0.0 - 1.6	0.625	0.850
0.0 - 1.8	0.550	0.750
0.0 - 2.0	0.450	0.650
0.0 - 2.2	0.375	0.500
0.0 - 2.4	0.300	0.450
0.0 - 2.6	0.250	0.400
0.0 - 2.8	0.160	0.350
0.0 - 3.0	0.125	0.300
0.0 - 3.2	0.080	0.250
0.0 - 3.4	0.070	0.200
0.0 - 3.6	0.040	0.150
0.0 - 3.8	0.025	0.100
0.0 - 4.0	0.020	0.080
0.0 - 5.0	0.000	0.050
0.0 - 7.5	0.000	0.020

Table 10: The fusion separation inefficiencies in the CsI used in the Monte Carlo, binned according to the distance which separates the two photons.

Resolution and the effect of mis-reconstruction of odd background leads to upstream decays being shifted into the fiducial volume.

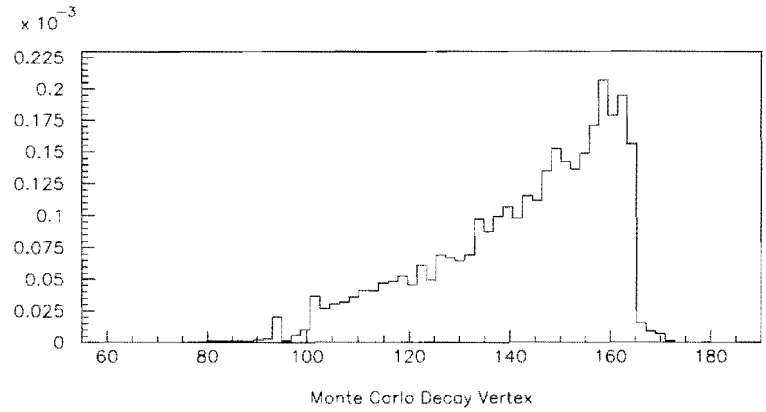

Figure 11: The Z decay vertex generated by the $K_L \to 2\pi^0$ Monte Carlo. Each entry in the plot is weighted by the product of the inefficiencies of the two photons that are not used to form the π^0. When the Z vertex for these events is calculated, assuming they originate from a single π^0, they all reconstruct between 100 m and 165 m. Resolution and the effect of mis-reconstruction of odd background leads to upstream decays being shifted into the fiducial volume.

In spite of the fact that the P_t resolution is smeared due to the transverse size of the beam (12 cm $\times$ 12 cm at the CsI) it still provides good background rejection. In Figure 12, the P_t cut is varied to determine its effect on the signal and background. The signal-to-background curve begins to plateau at a P_t cut of about 0.125 GeV/c. All of the cuts listed in Section 2.6.2 have been applied except for the nominal P_t cuts at 0.130 GeV/c and 0.250 GeV/c.

The reconstructed Z vertex of the π^0 decay is also a powerful tool for reducing background from $K_L \to 2\pi^0$ decays. In Figure 13 the $K_L \to \pi^0\nu\overline{\nu}$ acceptance is plotted vs. the downstream vertex cut. Also shown is the ratio of the $K_L \to \pi^0\nu\overline{\nu}$ signal to the background from $K_L \to 2\pi^0$ vs. vertex cut. The selected cut at 165 m is clearly a compromise between maximizing the signal yield and rejecting background. Variation of this cut along with the P_t cut in the offline analysis can help to understand the relative level of signal-to-background.

The implications for the $K_L \to 2\pi^0$ background of photon conversions in the scintillating fiber tracking planes has been studied using a GEANT simulation of the KAMI detector. The entire tracking system, including the carbon fiber support structures, comprises a maximum of 2.3% of a radiation length. In order for conversions to be a background concern, the resulting e^+e^- pair must fail to register hits in downstream detectors or be bent through large trajectories by the magnetic field such that their arrival time at an active detector (fiber tracker, photon veto or CsI) is outside the veto time window. Studies indicate that this only occurs for low energy photons below our veto threshold of 10 MeV. Since no efficiency is assumed for photons below 10 MeV in the simulations, conversions have no impact on our background.

Fused photon clusters in the CsI calorimeter do not contribute significantly to the

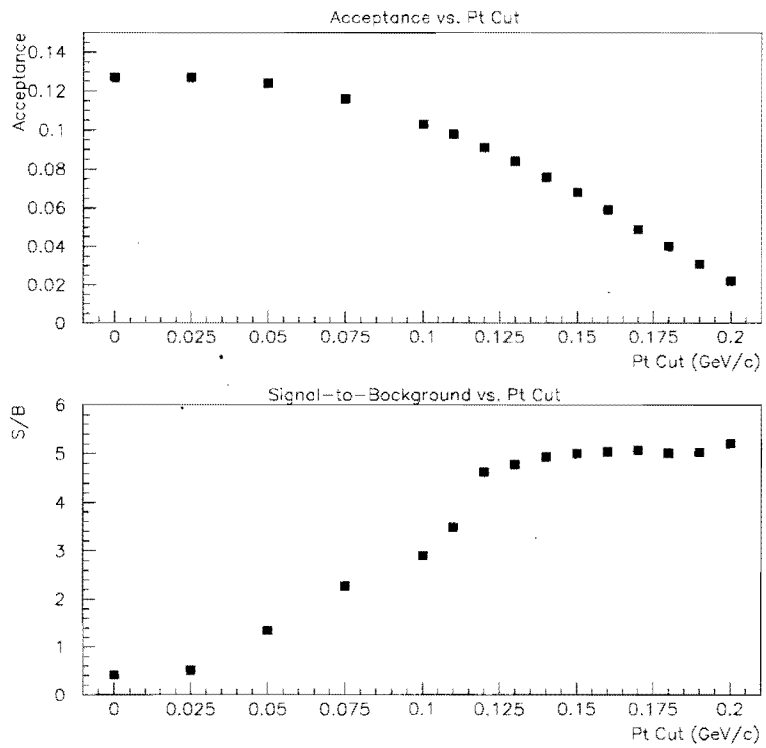

Figure 12: The effect of the P_t cut on the signal and background from $K_L \to 2\pi^0$ decays is shown. The top plot shows the variation of the $K_L \to \pi^0\nu\overline{\nu}$ acceptance vs. P_t cut. The acceptance is calculated relative to the number of decays between 90-183 m. The bottom plot shows the ratio of the $K_L \to \pi^0\nu\overline{\nu}$ signal to the background from $K_L \to 2\pi^0$ vs. P_t cut. A P_t cut of 0.130 GeV/c is ultimately selected.

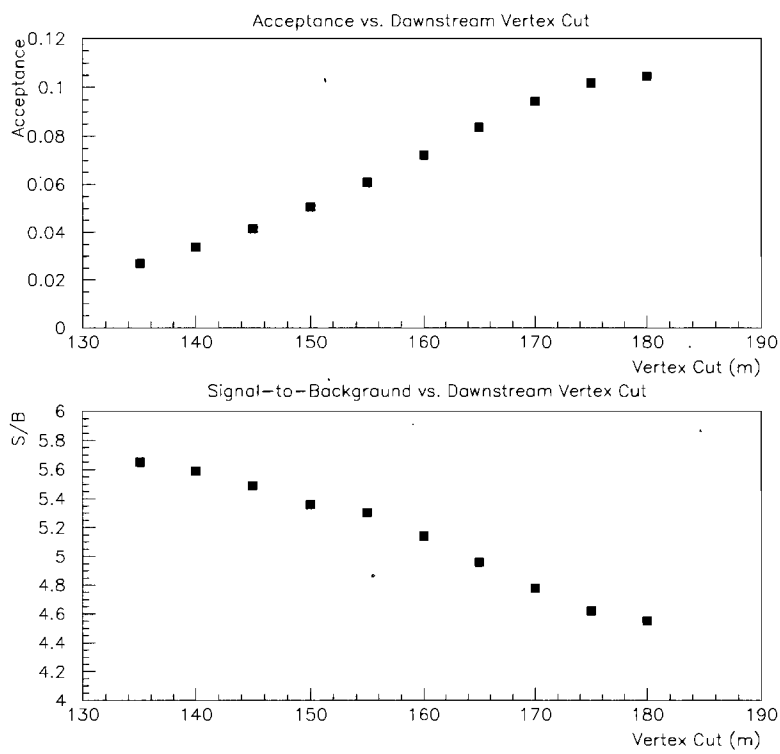

Figure 13: The effect of the downstream Z vertex cut on the $K_L \to \pi^0 \nu\overline{\nu}$ signal and background from $K_L \to 2\pi^0$ decays is shown. The top plot shows the variation of the $K_L \to \pi^0 \nu\overline{\nu}$ acceptance vs. Z vertex cut. The acceptance is calculated relative to the number of decays between 90-183 m. The bottom plot shows the ratio of the $K_L \to \pi^0 \nu\overline{\nu}$ signal to the background from $K_L \to 2\pi^0$ vs. vertex cut. A Z vertex cut of 165 m is ultimately selected.

$K_L \to 2\pi^0$ background. Only 0.1% of $K_L \to 2\pi^0$ events have two photons which hit the calorimeter within 5 cm of one another and the fraction of events with two sets of clusters within 5 cm is 6×10^{-6}. In the latter case, there is some probability that only two clusters will be reconstructed in the CsI. However, because the full kaon energy is deposited in the CsI for these double fusion events, the center of energy of the event is small and fails the ECEN cut at 0.1 m.

The sequential acceptance factors for the $K_L \to 2\pi^0$ background are listed in Table 11. The acceptance is calculated relative to the decay rate between the the target (0 m) and 183 m because odd background from upstream can reconstruct inside the fiducial volume (see Figure 11). Multiplying the acceptance for $K_L \to 2\pi^0$ decays by the branching ratio and the number of kaon decays between the target and 183 m and correcting for losses due to accidental activity in the detector (see Section 2.6.3), we arrive at a background level of 19 events per year. This compares to 88 signal events per year for a signal-to-background of 4.6.

Cut	Acceptance
$\geq$ 2 CsI clusters with energy > 1.25 GeV	0.43
Total CsI Energy > 5.0 GeV	0.41
Center-of-Energy > 0.1 m	0.33
Cluster Separation > 0.3 m	0.31
P_t between 0.130 GeV/c and 0.250 GeV/c	0.14
Z vertex between 100 m and 165 m	0.10
CsI fiducial cuts	0.09
Photon vetoes	2.6×10^{-10}

Table 11: The sequential acceptance factors for the analysis and trigger cuts applied to the background from $K_L \to 2\pi^0$ decays.

3.3 $K_L \to 3\pi^0$

$K_L \to 3\pi^0$ decays occur at a high rate, but the abundance of additional photons allow for efficient vetoing. Photons which fuse to form a single cluster in the CsI calorimeter could be more problematic for this background, but the segmentation of the CsI is sufficient to minimize this complication. 1.6% of all $K_L \to 3\pi^0$ events have 1 pair of photons within 5 cm of one another in the CsI calorimeter and the fraction of events with 2 pair of photons within 5 cm is 5×10^{-4}. Fused photons in the CsI calorimeter only increase the $K_L \to 3\pi^0$ background by 0.03%, compared to the case where every photon in the calorimeter is perfectly resolved.

The most serious background from $K_L \to 3\pi^0$ arises from decays upstream of the Mask Anti (MA) (see Section 6.3.2). If four photons go undetected (as is often the case for decays upstream of the active fiducial volume) and two photons from different π^0s pass through the Mask Anti and reach the CsI calorimeter, the vertex position reconstructed from the mis-paired photons can be shifted downstream into the fiducial decay region. To reject these events, the upstream section of the beam pipe is completely surrounded by the double stage Mask Anti and the vacuum veto system. This increases the probability that at least one

of the extra photons will be detected. Additionally, a ± 15 cm fiducial cut around the CsI beam hole is used to help reject photons from upstream which pass through the beam holes of the Mask Anti. The background contribution from $K_L \to 3\pi^0$ is determined to be 0.5 events per year.

3.4 $K_L \to \pi^+\pi^-\pi^0$

The background from $K_L \to \pi^+\pi^-\pi^0$ is easily reduced to negligible levels using a combination of signals in the photon veto detectors, the scintillating fiber tracker and a P_t cut. The standard geometrical, fiducial and energy cuts reduce the acceptance to about 10%. The P_t cut further reduces the acceptance to 7×10^{-4}. The efficiency of detecting charged particles at each of the scintillating fiber stations is assumed to be 98%. This is a conservative estimate since four of the five stations consist of xx′ and yy′ layers, each of which should be at least this efficient. Following the prescription of Inagaki *et al.* [66] for vetoing charged particles in scintillation counters, we assume an inefficiency of 1×10^{-4} for π^- and 1×10^{-5} for π^+ in the photon veto counters. Inagaki's measurements were made using a single piece of 10 mm thick scintillator. The KAMI photon veto detectors consist of 5 mm thick scintillator sheets separated by 1 mm thick lead sheets. In the absence of any interactions, charged particles will traverse many scintillator sheets, resulting in efficient detection. Charge exchange reactions of the type $\pi^-p \to \pi^0 n$ can reduce the detection efficiency if the π^0 deposits most of its energy in the lead. Additionally, processes such as $\pi^- + C \to n + n$ can limit the charged detection efficiency. K0PI0 has studied these reactions in the energy range relevant to their experiment [67] where the cross sections are larger than at KAMI energies. They also conclude that charged particle inefficiencies of 1×10^{-4} for π^- and 1×10^{-5} for π^+ are reasonable. The background contribution from $K_L \to \pi^+\pi^-\pi^0$ is determined to be less than 0.003 events per year.

3.5 $K_L \to \pi^\pm e^\mp \nu$

The $K_L \to \pi^\pm e^\mp \nu$ decay is similar to $K_L \to \pi^+\pi^-\pi^0$ in that it relies on the charged vetoing capabilities of the 5 fiber tracking planes and the photon veto detectors. Analysis of cluster shapes in the CsI calorimeter results in an additional factor of 10 rejection for charged pions based on measurements using the KTeV CsI. This can be seen in Figure 14 where the shower-shape χ^2 is plotted for photons and charged pions from clean $K_L \to \pi^+\pi^-\pi^0$ decays. The shower-shape χ^2 is a measure of how closely the cluster conforms to the profile of an electromagnetic shower. A typical cut requires a value of less than 4.

Background from $K_L \to \pi^\pm e^\mp \nu$ decays can result when the π^- and the e^+ react in a fiber tracking station via charge exchange $\pi^-p \to \pi^0 n$ and annihilation $e^+e^- \to \gamma\gamma$. Charge exchange reactions generated with the appropriate t-distribution [73] and positron annihilation have been included in the simulation with the result that the background contribution from $K_L \to \pi^\pm e^\mp \nu$ decay is <2 events per year. Charge exchange reactions and positron annihilation in the fiber tracking planes can result in detectable signals in the fibers, depending on where the reaction takes place. No attempt has been made to exploit this possibility. The addition of a scintillator hodoscope downstream of the final fiber tracker could reduce

this background to negligible levels. The inefficiency of a 1 cm thick scintillator hodoscope is between 1×10^{-4} and 1×10^{-5} for $e^{\pm}$ and $\pi^{\pm}$.

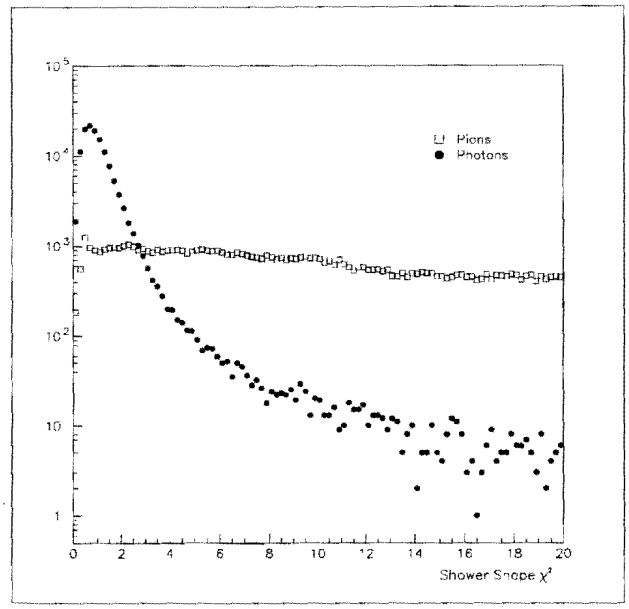

Figure 14: The shower-shape χ^2 distribution in the KTeV CsI calorimeter for photons and charged pions from clean $K_L \to \pi^+\pi^-\pi^0$ decays. A typical cut requires $\chi^2 < 4$.

3.6 $K_L \to \gamma\gamma$

The background from $K_L \to \gamma\gamma$ is distinguished from $K_L \to \pi^0\nu\overline{\nu}$ because the two photons are P_t balanced and deposit the full kaon energy in the CsI calorimeter. However, the reconstructed P_t can be non-zero because of the P_t resolution smearing which results from the finite size of the beam and the incorrect assumption that the two photons result from a π^0 decay. $K_L \to \gamma\gamma$ decays can be effectively eliminated using the reconstructed center-of-energy (ECEN) defined as

$$ECEN = \frac{\sqrt{(X_1 \cdot E_1 + X_2 \cdot E_2)^2 + (Y_1 \cdot E_1 + Y_2 \cdot E_2)^2}}{E_1 + E_2} \tag{21}$$

where X_1 and X_2 are the reconstructed X coordinates of the two photons in the CsI calorimeter, Y_1 and Y_2 are the Y coordinates and E_1 and E_2 are the energies. The ECEN distribution is also smeared by the finite beam size, but it still provides the rejection power necessary to virtually eliminate this source of background. The ECEN distributions from $K_L \to \gamma\gamma$ and $K_L \to \pi^0\nu\overline{\nu}$ are shown in Figure 15. ECEN is required to be greater than 0.1. The background contribution from $K_L \to \gamma\gamma$ is determined to be less than 0.04 events per year.

3.7 $\Lambda \to \pi^0$n

Approximately equal numbers of Λ's and K_L's are produced at the target. The $\Lambda \to \pi^0$n decay has a large branching ratio (36%) but a short lifetime that reduces the flux to negligible lev-

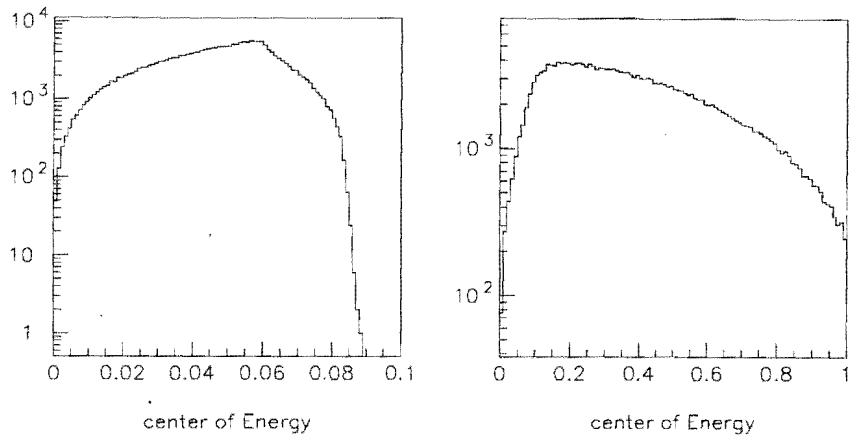

Figure 15: The reconstructed center-of-energy (ECEN) distributions for $K_L \to \gamma\gamma$ (left) and $K_L \to \pi^0\nu\overline{\nu}$ (right). Note the dramatically different horizontal scales.

els 100 m from the target. The few Λ's which do survive to the fiducial volume have a P_t endpoint of 104 MeV/c before smearing due to resolution and transverse beam size. The background has been studied by generating events with a flat vertex distribution from the target to the CsI calorimeter. The events which pass the analysis cuts are weighted by the momentum-dependent probability that the Λ survives to the Z decay vertex position. The lambda flux and spectra are scaled from measurements at 400 GeV [74]. The flux of hyperons measured in KTeV at 800 GeV was consistent with the scaled rates from 400 GeV to within 20%. The background contribution from $\Lambda \to \pi^0$n decays is estimated to be less than 0.2 events per year.

3.8 Ξ Decays

The decay $\Xi \to \Lambda\pi^0 \to n\pi^0\pi^0$ is potentially more troublesome than $\Lambda \to \pi^0$n because the second π^0 can carry a P_t as large as 230 MeV/c. Photons from different π^0's can also reconstruct with large P_t and with a vertex shifted into the fiducial volume. However, this background is easily suppressed by the lifetime of the hyperons and the presence of two additional photons available for vetoing. The Ξ flux and spectra are scaled from measurements at 400 GeV [74]. The flux of hyperons measured in KTeV at 800 GeV was consistent with the scaled rates from 400 GeV to within 20%. The background contribution from $\Xi \to \Lambda\pi^0 \to n\pi^0\pi^0$ decays is determined to be completely negligible.

A related decay is $\Xi \to \Lambda\gamma \to n\pi^0\gamma$ which can also produce a high P_t π^0. This decay mode has a relatively small branching ratio (1.2×10^{-3}) and has one extra photon available for vetoing. The background contribution from this mode is also completely negligible.

3.9 Neutron Interactions

The large flux of beam neutrons in KAMI can interact with the residual gas in the decay volume and in the vacuum window to produce π^0s. Interactions of neutrons in the beam tail with the fiber tracking planes can also produce π^0s. The process $nn \rightarrow nn\pi^0$ is the most dangerous reaction because of the absence of additional photons available for vetoing. The cross section and angular distribution of the similar process $pp \rightarrow pp\pi^0$ can be used to simulate the background [79, 80]. The neutron flux and spectra were measured during the 2000 KAMI beam test (see Appendix B). The hadron energy spectrum measured at 15 mrad and with no beryllium absorber in the beam is shown in Figure 16.

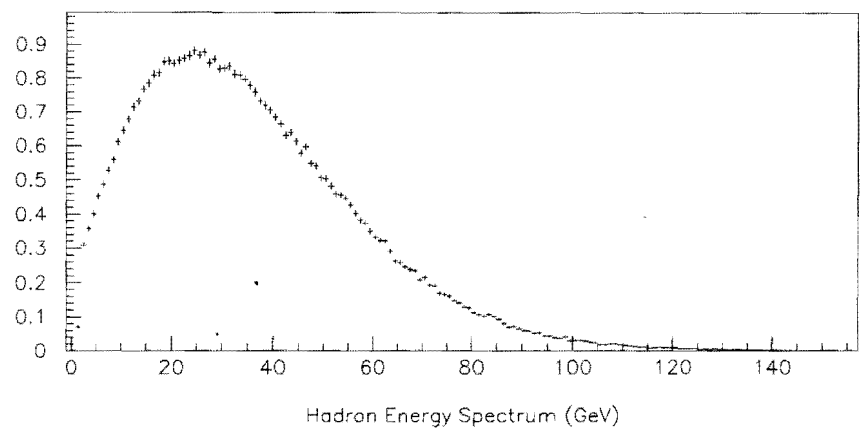

Figure 16: The hadron energy spectrum measured during the 2000 KAMI beam test at 15 mr and no beryllium absorber.

The number of neutron interactions per year in the 186 m long KAMI vacuum decay volume at 10^{-6} torr can be calculated using:

$$A^{1/3} N_n N_T \sigma \tag{22}$$

where A is the average atomic mass of air (14.4), N_n is the number of beam neutrons per year (2.7×10^{15}), N_T is the number of target nuclei along the 186 m of decay volume ($1.2 \times 10^{14}/\text{cm}^2$) and σ is the cross section per nucleon ($\sim$2 mb for the reaction $nn \rightarrow nn\pi^0$ [79]). This results in about 1600 interactions per year. 10^8 $nn \rightarrow nn\pi^0$ reactions were generated with a Monte Carlo between the target and the CsI with the t-dependence from Ref [80]. An acceptance of 2.6×10^{-5} results for a total background contribution of 0.04 events per year. No attempt is made to identify the neutrons, which will often interact in active detectors resulting in additional veto power. If the events are generated according to phase space rather than according to a t distribution, the acceptance rises to 3.0×10^{-4} for a total background contribution of 0.5 events per year. The disparity between these two results is due to the different energy spectrum of the π^0 in the two cases. This is illustrated in Figure 17 where the total energy in the CsI calorimeter is plotted for the events generated using the t

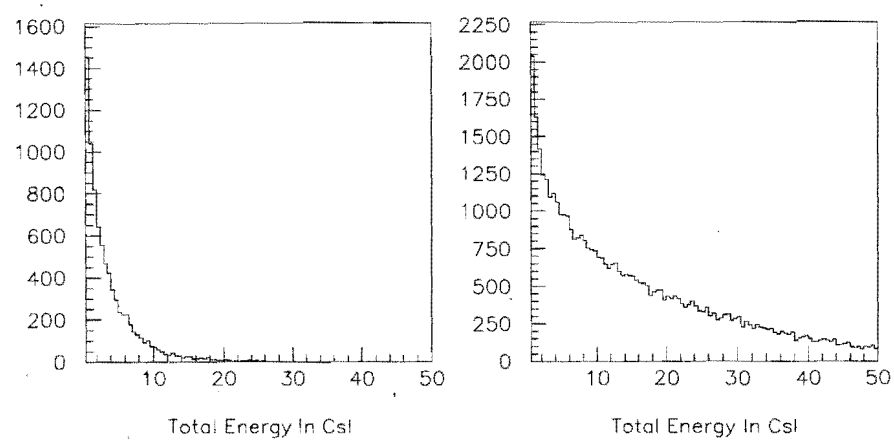

Figure 17: The total energy deposited in the CsI calorimeter for $nn \to nn\pi^0$ events. The plot on the left is for events generated with the t distribution from Ref [80]. The plot on the right is for events generated uniformly in phase space.

distribution and for the events generated using phase space. The t distribution clearly limits the energy of the π^0, reducing the acceptance.

Neutrons can also produce π^0s by interacting in the vacuum window. This was the limiting background source during the one-day dedicated $K_L \to \pi^0\nu\overline{\nu}$ KTeV run in December, 1996 [59]. While the KTeV vacuum window was located well upstream of the CsI calorimeter, the KAMI vacuum window will be located just 0.5 m upstream of the calorimeter. The KAMI vacuum window, similar to the KTeV window but 2.5 times thicker, will be constructed from kevlar cloth and aluminized mylar. The probability of a neutron interacting in the window is $\sim 2.0 \times 10^{-5}$.

10^8 $nn \to nn\pi^0$ reactions have been generated by a Monte Carlo at the vacuum window. No events survive the cuts. The photons often pass through the CsI beam hole or hit the calorimeter very close to the beam hole, failing the ± 15 cm fiducial cut. When the photons do hit the fiducial area of the CsI they typically reconstruct with a P_t that is larger than the 0.250 GeV/c cut and they reconstruct with a Z-vertex well downstream of the 165 m cut.

The reaction $nn \to nn\pi^0\pi^0$ is potentially more problematic because of the potential for mis-paired photons from different π^0s to mis-reconstruct within the fiducial volume. The cross section for the related process $pp \to pp\pi^0\pi^0$ has been measured for 2.8 GeV/c protons to be 0.92 mb [107]. For a 1 mb cross section we expect 775 residual gas interactions per year. 10^8 $nn \to nn\pi^0\pi^0$ reactions were generated with a Monte Carlo between the target and the CsI with a resulting acceptance of 1×10^{-5}. This corresponds to 0.009 background events per year.

High energy neutrons which hit the vacuum window and initiate the reaction $nn \to nn\pi^0\pi^0$ can produce two relatively high energy π^0s which both fuse in the calorimeter, resulting in two CsI clusters which can mis-reconstruct as a π^0 from the fiducial volume with a good P_t. This background is eliminated by the close proximity of the vacuum window to the CsI and by requiring the two CsI clusters to be separated from one another by more than 30 cm.

3.10 K_L Interactions

It is also possible for K_L reactions to occur in the residual beam gas and vacuum window. $K_L n \to \pi^0 \Lambda$ and $K_L N \to K_L N \pi^0$ reactions are both potential background sources. $K_L N \to K_L N \pi^0$ is similar to $nn \to nn\pi^0$, considered above. Because the neutron flux in KAMI is many times larger than the K_L flux, $K_L N \to K_L N \pi^0$ is just a fraction of the $nn \to nn\pi^0$ background of 0.04 events per year.

To estimate the background from $K_L n \to \pi^0 \Lambda$ an analysis similar to that done for neutron interactions is applied. The number of interactions per year is calculated using a K_L flux per year of 4.8×10^{14}. The cross section for the similar reaction $K_L p \to \pi^+ \Lambda$ has been measured to be 0.013 mb at 11 GeV/c. If we assume the $K_L n \to \pi^0 \Lambda$ cross section to be as large as 1 mb over our energy range, a total of 1500 interactions per year results. The acceptance for this reaction is 2.3×10^{-5} because of the additional particles available for vetoing. The total background contribution from $K_L n \to \pi^0 \Lambda$ is estimated to be 0.03 events per year.

3.11 Discriminating a $K_L \to \pi^0 \nu \bar{\nu}$ Signal From Backgrounds

The observation of the $K_L \to \pi^0 \nu \bar{\nu}$ decay with only the two photon energies and positions to distinguish the decay from sizable backgrounds is a challenging task. However, the unique configuration of the KAMI experiment with its small beam size (0.41 μstr resulting in a 12 cm $\times$ 12 cm size at the CsI calorimeter) allows the P_t of the two photon system to be determined. This provides a way to directly observe the presence of a $K_L \to \pi^0 \nu \bar{\nu}$ signal over the major background $K_L \to \pi^0 \pi^0$ (larger by a factor of ten than the next largest contribution).

As shown in Figure 18, the P_t distribution of the $K_L \to \pi^0 \nu \bar{\nu}$ is significantly different than the P_t distribution of background due to $K_L \to \pi^0 \pi^0$ events that have two photons in the CsI which satisfy the trigger criteria and whose remaining two photons are not detected in the veto system. This is shown for four different detection thresholds in the veto counters (5 MeV, 10 MeV, 15 MeV and 20 MeV). The level of the signal and background curves have been normalized to the estimated number of signal and background events expected in one year of running. The plots for the four different detection thresholds make clear the importance of pushing the threshold as low as possible. The $K_L \to \pi^0 \nu \bar{\nu}$ signal is clearly most prominent with a 5 MeV threshold.

The ability to suppress the $K_L \to \pi^0 \pi^0$ background in the signal region depends critically on the inefficiencies for detecting photon showers in the photon veto, the CsI, the Beam Anti system, and the Mask Anti. These detectors and their inefficiencies are discussed elsewhere in this document. However, while the observation of the $K_L \to \pi^0 \nu \bar{\nu}$ signal depends on attaining the KAMI baseline inefficiencies quoted for each detector (which from Figure 18, is apparently more than adequate), precise determination of the background for $K_L \to \pi^0 \pi^0$ depends on *knowing* the magnitude of background in the signal region which in turn depends on knowing with some precision the magnitude and energy dependence of the veto detector inefficiencies. This becomes progressively harder as the level of the inefficiency gets smaller. In particular, above a photon energy of 1 GeV, the inefficiencies of the various veto detectors fall below 10^{-5} where the ability to precisely measure inefficiencies becomes difficult.

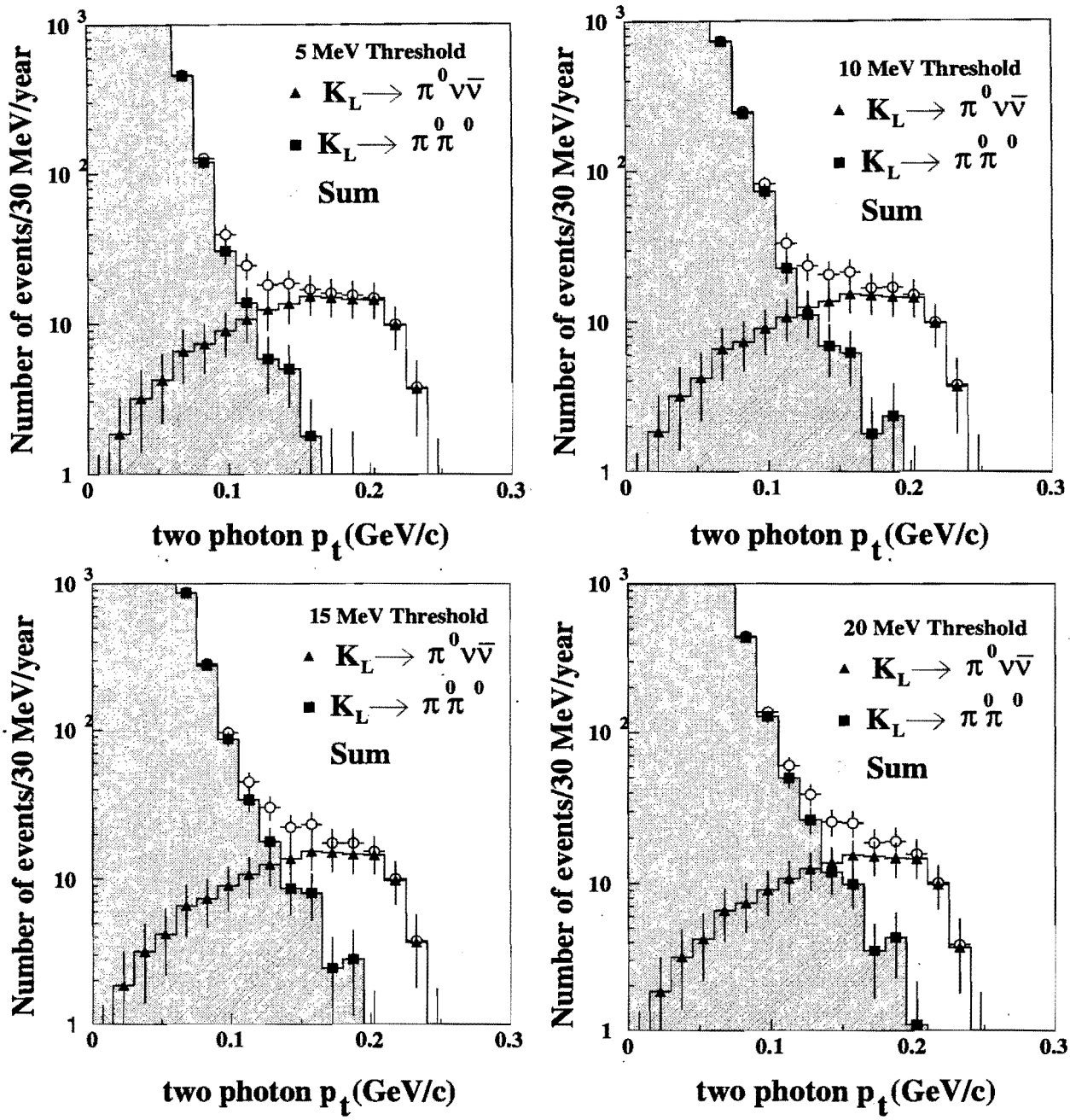

Figure 18: The $K_L \to \pi^0 \nu\bar{\nu}$ and $K_L \to 2\pi^0$ P_t spectra for various detection thresholds in the photon veto detectors. The top left plot is for a 5 MeV threshold; top right is for a 10 MeV threshold; bottom left is for a 15 MeV threshold; and bottom right is for a 20 MeV detection threshold. The nominal conditions for this proposal assume a 10 MeV detection threshold.

3.11.1 Variation of Background due to Inefficiency Uncertainties

To estimate the variation of the level and shape of the $2\pi^0$ background in the signal region due to uncertainties in the inefficiencies of the veto detectors, we have varied our baseline inefficiencies in all detectors in energy regions where the inefficiency falls below 10^{-5}. In Figure 19 we show the magnitude of the various $2\pi^0$ background curves obtained with photon veto and CsI inefficiency maps varied up and down over a reasonable range of $\pm 2 \times 10^{-6}$ in the photon energy region above 1 GeV. The beam anti system inefficiencies are not required to be as small as 10^{-5} and thus have not been varied in this study. Also shown are the ratios of these background curves to the the background obtained using the baseline inefficiencies maps. What can be inferred from these curves is that the $2\pi^0$ background below the signal region is relatively insensitive to variation of the high energy inefficiencies, changing at most by a few percent in magnitude and almost invariant in shape. To the contrary, the background in the signal region is sensitive to the high energy variation of the inefficiencies, especially when the inefficiencies increase. If efficiencies better than the present baseline are achieved, the background level does not decrease significantly since, at that point, the residual background due to photons in other energy regions contribute a base level of background.

In Table 12 the integrated level of background events per year is shown to demonstrate the systematic variation that we can expect in determining the magnitude of the signal (estimated to be approximately 90 events per year), if the veto inefficiencies cannot be measured to better than the quoted variation.

3.11.2 Variation of Background Level due to Veto Threshold

An associated uncertainty in predicting the level of background to the $K_L \to \pi^0 \nu\bar{\nu}$ signal is the attainable threshold levels for observing low energy photons in the CsI, the Mask Anti and the vacuum veto. We have varied the minimum threshold energy to observe its effect on the background. The results of the studies are given in Table 12. Here it seems, the P_t regions that have maximum sensitivity to the threshold are the reverse of those that are sensitive to the high energy photon inefficiencies.

As can be seen from the background yields in the tables, the region below the signal region experiences a greater variation than does the signal region. If KAMI can achieve, as we anticipate, a 5 MeV detection threshold then the background level from $K_L \to \pi^0\pi^0$ could be reduced from 19 events per year to approximately 6 events per year.

3.12 Summary

A thorough survey of the potential background sources to the $K_L \to \pi^0 \nu\bar{\nu}$ signal has been conducted. The only serious background is from $K_L \to 2\pi^0$ decays. The number of background events from $K_L \to 2\pi^0$ decays ultimately depends on the performance of the photon veto system. Based on the inefficiencies in Table 9, we expect 19 such events per year for a signal-to-background of 4.6. The various backgrounds discussed in the text are summarized in Table 13.

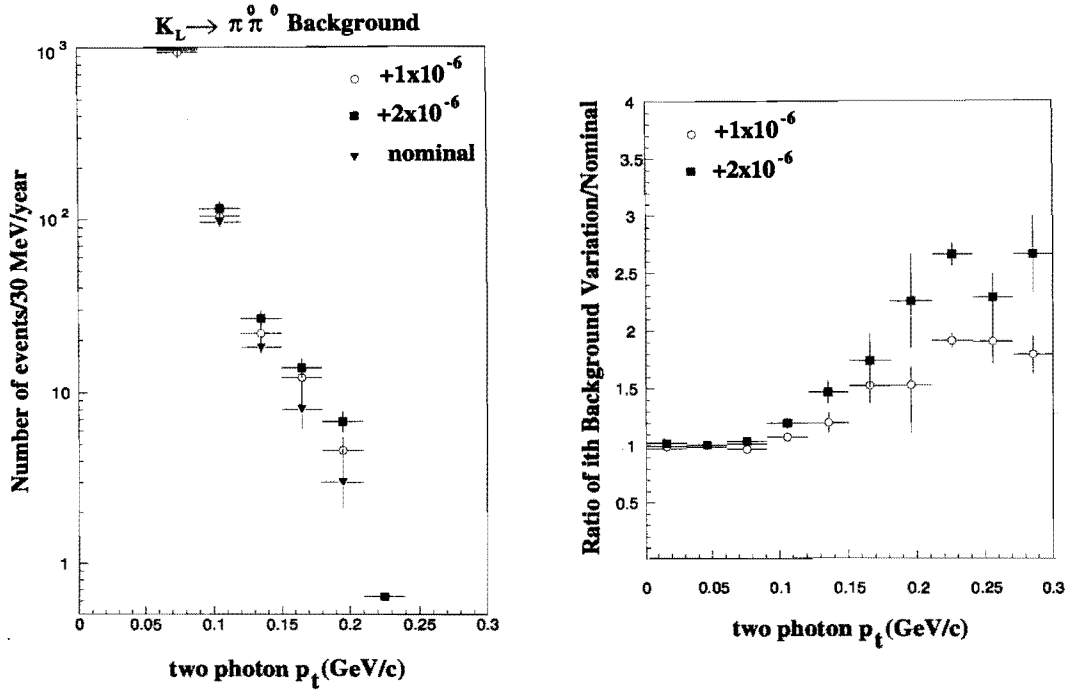

Figure 19: Variation of $K_L \rightarrow \pi^0\pi^0$ background P_t spectra, shown in the plot on the left, obtained by varying the vacuum veto, mask anti, and CsI inefficiency maps in photon energy regions where the expected inefficiencies are less than 10^{-5} Errors are the statistics expected from one year of operation. The right plot shows the ratio of background spectra obtained with different inefficiency maps to the background spectrum obtained with the baseline KAMI inefficiencies.

Inefficiency Map	$K_L \rightarrow \pi^0\nu\bar{\nu}$ Background Events/Year	All P_t
Baseline inefficiencies (10 MeV Threshold)	19 events	99,100 events
$\leq 10^{-5}$ inefficiencies $+1 \times 10^{-6}$	27 events	98,600 events
$\leq 10^{-5}$ inefficiencies $+2 \times 10^{-6}$	33 events	101,100 events
15 Mev threshold - baseline inefficiencies	26 events	165,900 events
20 MeV threshold - baseline inefficiencies	33 events	288,000 events
5 MeV threshold - - baseline inefficiencies	6 events	46,300 events

Table 12: The background to $K_L \rightarrow \pi^0\nu\bar{\nu}$ obtained after variation of the vacuum veto and CsI inefficiency maps over the range of $\pm 2 \times 10^{-6}$ in the photon energy region above 1 GeV.

Mode	Primary Rejection Tool	Events/yr
$K_L \to 2\pi^0$	Photon Vetoes, P_t, Vertex	19
$K_L \to 3\pi^0$	Photon Vetoes, P_t	0.5
$K_L \to \pi^+\pi^-\pi^0$	P_t	0.003
$K_L \to \gamma\gamma$	P_t, center of energy	0.04
$K_L \to \pi^\pm e^\mp \nu$	charged veto	2.0
$\Lambda \to \pi^0$n	P_t, Λ lifetime	0.2
$\Xi \to \Lambda\pi^0 \to n\pi^0\pi^0$	Ξ lifetime, Photon Vetoes	negligible
$\Xi \to \Lambda\gamma \to n\pi^0\gamma$	Ξ lifetime, Photon Vetoes	negligible
$nn \to nn\pi^0$		0.04
$nn \to nn\pi^0\pi^0$		0.09
$K_L n \to \pi^0\Lambda$		0.03
Total Background per year		22

Table 13: Estimated background levels per year of running.

4 Other Rare and Very Rare Decay Modes

4.1 Introduction

There are many rare kaon decays other than $K_L \to \pi^0\nu\overline{\nu}$ which are of considerable interest for a variety of reasons. The large kaon flux provided by the Main Injector combined with a a a large-acceptance detector make KAMI the best place to study these decays. None of the other proposed $K_L \to \pi^0\nu\overline{\nu}$ experiments has this capability.

In addition to $K_L \to \pi^0\nu\overline{\nu}$, there are other rare kaon decays which are sensitive to direct CP violation including $K_L \to \pi^0\mu^+\mu^-$. The branching ratio predicted by the Standard Model for this decay is within reach of KAMI.

KAMI will also have the capacity to perform sensitive searches for other rare and forbidden decays. These include processes forbidden by the Standard Model, such as the lepton flavor violating decays $K_L \to \pi^0\mu^\pm e^\mp$ and $K_L \to \mu^\pm e^\mp$.

K_L decays to 4 leptons will be abundant in KAMI. Decays such as $K_L \to \mu^+\mu^-e^+e^-$ and $K_L \to e^+e^-e^+e^-$ provide critical insight into the $K_L\gamma^*\gamma^*$ form factor. Additionally, the angular distribution between the decay planes of the lepton pairs is sensitive to CP violation in the $K_L \to \gamma^*\gamma^*$ transition. KAMI can collect on the order of 34,000 $K_L \to e^+e^-e^+e^-$ events and 1600 $K_L \to \mu^+\mu^-e^+e^-$ events in one year of running.

A large sample of $K_L \to \pi^+\pi^-e^+e^-$ events will also be collected by KAMI. This decay, first observed by KTeV, has opened a new window on CP violation through the study of final-state angular distributions. A very large asymmetry is measured due to indirect CP violation through mixing. In addition, various direct CP-violating terms can, in principle, be present in the amplitude for this decay. While these terms are not expected to be large in the Standard Model, the study of this mode provides another possible approach to observing direct CP violation that should be pursued. KAMI will observe >600,000 $K_L \to \pi^+\pi^-e^+e^-$ decays per year.

Finally, the decay $K_L \to \pi^0\pi^0e^+e^-$ is the neutral partner of the $K_L \to \pi^+\pi^-e^+e^-$ decay, but does not contain the inner brem term which contributes to the latter decay mode. This mode offers yet another opportunity to observe a non-Standard Model CP violation effect.

As can be seen from the above discussion, the KAMI charged mode program alone represents a rich and diverse physics program which probes the Standard Model and issues of CP violation to significant levels. This program is completely compatible with the KAMI program to measure $K_L \to \pi^0\nu\overline{\nu}$ and is not possible to execute at any of the other proposed $K_L \to \pi^0\nu\overline{\nu}$ experiments. The details of this program are discussed in the sections which follow.

4.2 $K_L \to \pi^+\pi^-e^+e^-$

Discovery of the $K_L \to \pi^+\pi^-e^+e^-$ mode [24] by the KTeV experiment has opened a window which, with adequate statistics, can be used to address several different physics issues. We show in Fig. 20 the $\pi^+\pi^-e^+e^-$ mass spectrum from KTeV which shows approximately 1800 signal events for the $K_L \to \pi^+\pi^-e^+e^-$ decay mode over a negligible background. Based on the measured branching ratio from KTeV of 3.63 ± 0.11 (stat) $\pm$ 0.14 (syst) $\times 10^{-7}$ and an estimated acceptance of 3.5%, a yield of ~678,000 reconstructed $K_L \to \pi^+\pi^-e^+e^-$ events

per year are expected in KAMI.

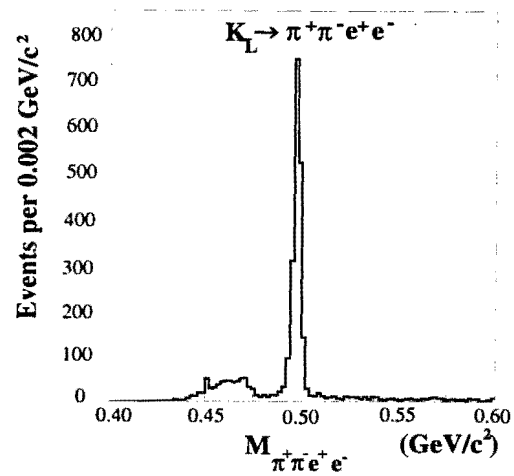

Figure 20: $M_{\pi^+\pi^-e^+e^-}$ invariant mass

The measured branching ratio for this mode will undoubtedly be systematics limited. Determination of the vector form factor $\tilde{g}_{M1}$ (Fig. 5) from the E_γ^* spectrum of the virtual photon energy (Fig. 22) and measurement of the indirect CP violating asymmetry (Fig. 21) in the angle between the e^+e^- and $\pi^+\pi^-$ planes in the K_L center of mass, both of which are currently limited by statistics, will improve.

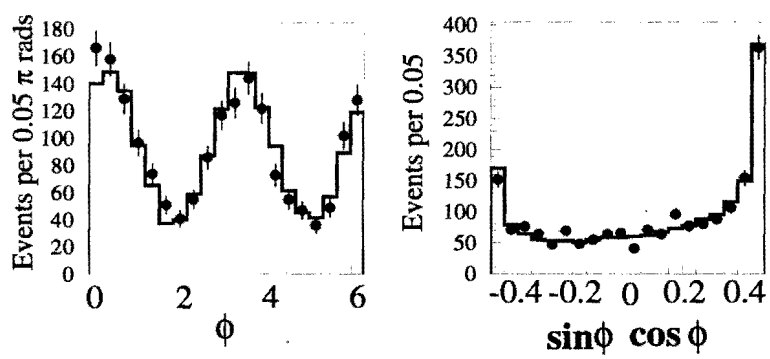

Figure 21: a) Observed ϕ and b) $\sin\phi\cos\phi$ angular distributions: The data are shown as dots. The histogram is a Monte Carlo simulation based on the model of Sehgal and Wanninger ref. [25].

A preliminary measurement of the amplitude $|g_P|$ for the "charge radius" process (Fig. 5) has been made in KTeV. The result

$$|g_P| = 0.100 \pm 0.018(stat) \pm 0.013(syst) \tag{23}$$

has been reported [75]. Using equation 7, a value of $< R^2(K^0) >$ of $-0.047 \pm 0.008(stat) fm^2$ has been obtained. Fig. 23 displays this measurement in comparison with the previous measurements, all achieved using coherent regeneration of K_S from atomic electrons. Using

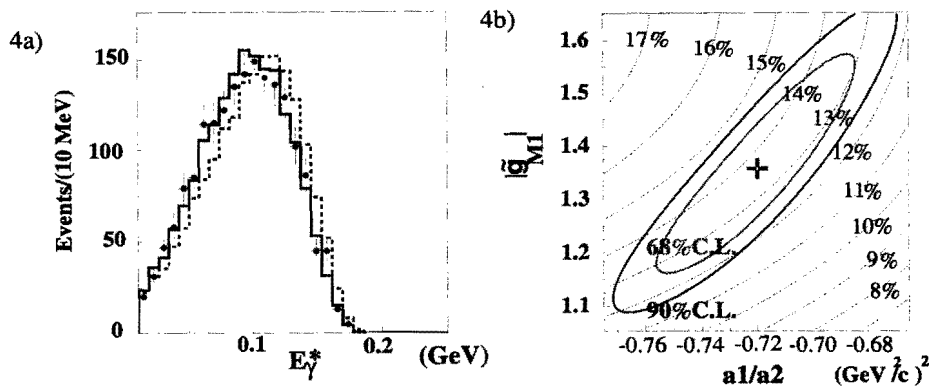

Figure 22: a) E_γ^* spectrum of data (dots), Monte Carlo using a constant $|g_{M1}|$ (dashed histogram), Monte Carlo with E_γ^* dependent form factor (solid histogram); b) Likelihood contours of a_1/a_2 and $|\tilde{g}_{M1}|$; Constant asymmetry contours calculated from the data are superimposed

a model of the neutral kaon due to Giersche and Munz [33] in which the lighter d quark circles the heavier s quark, the difference between the constituent s and d quark masses can be inferred. A first attempt to observe E1 emission (which would be the sixth CP violation effect if observed) by a likelihood fit from the KTeV data has resulted in

$$|g_{E1}| = 0.035 \pm 0.021(stat).$$

This measurement could be vastly improved with KAMI statistics.

A likelihood fit to measure the relative phase of the two terms shown in equation 8 was performed and the result is shown in Fig. 24. One of the maxima is close to 90°. At present, the two σ displacement of the 105° maximum from 90° may be due to lack of precise knowledge of the $\pi\pi$ phase shifts or subtle effects of the other amplitudes. The other maximum at 38° is an artifact of the fitting process.

Finally, and most speculatively, direct CP violation can take place in the $K_L \to \pi^+\pi^-e^+e^-$ decay via the short distance E1 photon emission. The manifestation of direct CP violation would take place as an asymmetry between positive and negative values of the distribution of $K_L \to \pi^+\pi^-e^+e^-$ decays in $sin\theta_{e^+}cos\phi$ where ϕ is the angle between the normals to the e^+e^- and $\pi^+\pi^-$ planes in the K_L CMS as before and θ_{e^+} is the angle of the positron relative to the direction of the $\pi^+\pi^-$ in the e^+e^- CMS. The double differential cross section in these angles is given by

$$\frac{d\Gamma}{dcos\theta_{e^+}d\phi} = K_1 + K_2cos2\theta_{e^+} + K_3sin^2\theta_{e^+}cos2\phi + K_4sin2\theta_{e^+}cos\phi$$
$$+K_7sin\theta_{e^+}sin\phi + K_8sin2\theta_{e^+}sin\phi + K_9sin^2\theta_{e^+}sin2\phi$$

Under time reversal the K_4, K_7 and K_9 terms reverse sign. Asymmetries in these distributions indicate CP violation. Indeed the asymmetry in the K_9 term is just the asymmetry in ϕ that was generated by the interference of M1 and indirect CP violating bremsstrahlung process. Direct CP violation in the K_7 term where is manifested as an asymmetry in the

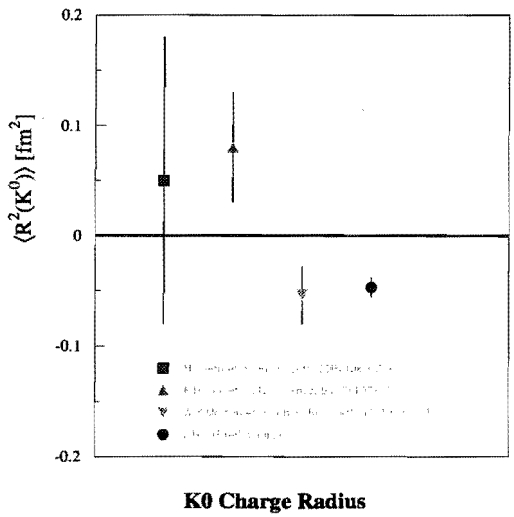

Figure 23: Various measurements of the charge radius of the neutral kaon

$sin\theta_{e^+} sin\phi$ distribution. We show in Fig. 25 the $sin\theta_{e^+} sin\phi$ distribution obtained in a Monte Carlo in which the short distance E1 photon emission has been enhanced by a factor of 100. We show from this same Monte Carlo the asymmetry as a function of a cut against low $M_{e^+e^-}$ masses.

4.3 $K_L \to \pi^0\pi^0 e^+e^-$

Analogous to $K_L \to \pi^+\pi^- e^+e^-$ is the decay $K_L \to \pi^0\pi^0 e^+e^-$. Of course, because the π's are neutral, this mode has no inner bremsstrahlung contribution. Furthermore, gauge invariance and Bose statistics force the $\pi^0\pi^0$ system into an angular momentum $l = 2$ state. As a consequence, the CP conserving charge radius amplitude is the dominant remaining amplitude. In addition, the E2 (CP conserving) and M2 (CP violating) direct photon emission amplitudes can contribute to the decay. Recent theoretical predictions of the branching ratio for $K_L \to \pi^0\pi^0 e^+e^-$ range from 2.3×10^{-11} [76] to 1×10^{-10} [77]. $K_L \to \pi^0\pi^0 e^+e^-$ is of course related to the decay $K_L \to \pi^0\pi^0\gamma$ which is extremely difficult to detect due to backgrounds from $K_L \to \pi^0\pi^0\pi^0$ with one γ undetected.

KTeV has reported preliminary results on the first upper limit for $K_L \to \pi^0\pi^0 e^+e^-$ [78]. From $2.7 \times 10^{11} K_L$ decays a 90% confidence level upper limit of 5.4×10^{-9} was obtained based on the observation of 1 event with an expected background of $0.4^{+0.4}_{-0.3}$ events.

The trigger for $K_L \to \pi^0\pi^0 e^+e^-$ would require 2 tracks and 6 clusters in the CsI calorimeter. The geometric and trigger acceptance is 1.0%. There are many sources of background. In the KTeV analysis the most serious background was from $K_L \to \pi^0\pi^0\pi^0_D$ where π^0_D denotes the Dalitz decay $\pi^0 \to e^+e^-\gamma$. Cuts to suppress the backgrounds in KTeV further reduced the acceptance by an order of magnitude. Including this factor leads to an estimate of 10 events in a year of KAMI running.

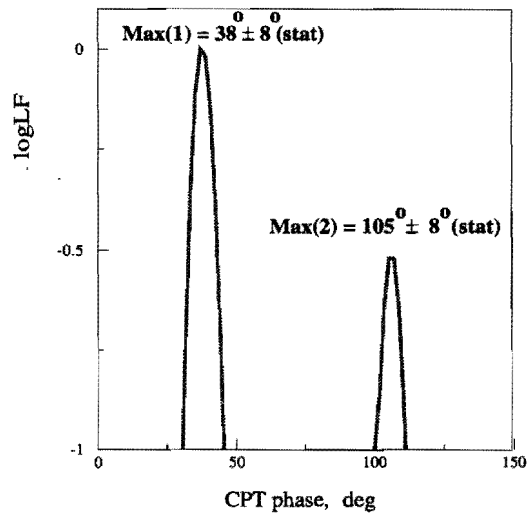

Figure 24: Likelihood fit of the relative phase of the M1 and bremsstrahlung amplitudes using presently available measurements of ϕ_{+-} and δ_0, δ_1

4.4 Decays of the type $K_L \to \gamma^*\gamma$ and $K_L \to \gamma^*\gamma^*$

As described in Section 4.5, the decay $K_L \to \mu^+\mu^-$ is of great importance in studies of the CKM matrix. The short distance part of the amplitude for $K_L \to \mu^+\mu^-$ is directly related to the parameter ρ in the Wolfsenstein parameterization of the CKM matrix [81]. However to extract the short distance behavior the long distance contributions must first be very precisely understood. The contribution from the real photon intermediate state $K_L \to \gamma\gamma \to \mu^+\mu^-$ can be determined from the measured branching fraction of $K_L \to \gamma\gamma$. The contribution from virtual photon intermediate states $\gamma^*\gamma$ and $\gamma^*\gamma^*$ needs to be determined from a detailed study of the form factors of the decays $K_L \to e^+e^-\gamma$, $K_L \to \mu^+\mu^-\gamma$, $K_L \to e^+e^-e^+e^-$ and $K_L \to \mu^+\mu^-e^+e^-$. KAMI will be able to make significant contributions to these studies.

4.4.1 $K_L \to \mu^+\mu^-\gamma$

The interest in $K_L \to \mu^+\mu^-\gamma$ centers on the the $K_L \to \mu^+\mu^-$ decay mode. The $K_L \to \mu^+\mu^-$ rate receives small contributions from short distance processes that are sensitive to the CKM parameter ρ [81–83]. However, the rate is dominated by long distance contributions involving two-photon intermediate states. The total rate can be decomposed according to $B(K_L \to \mu^+\mu^-) = |\mathrm{Re}A|^2 + |\mathrm{Im}A|^2$. The experimental value of the branching ratio $B(K_L \to \mu^+\mu^-) = (7.18 \pm 0.17) \times 10^{-9}$ is almost completely saturated by the absorptive component calculated to be $|\mathrm{Im}A|^2 = (7.07 \pm 0.18) \times 10^{-9}$ [40, 84]. $|\mathrm{Im}A|^2$ is the unitarity bound and corresponds to the case of two real intermediate photons. Short distance and $K_L \to \gamma^*\gamma^*$ contributions make up the dispersive component, $\mathrm{Re}A = \mathrm{Re}A_{SD} + \mathrm{Re}A_{LD}$, which is limited to $|\mathrm{Re}A_{exp}|^2 < 3.7 \times 10^{-10}$ (90% C.L.). $\mathrm{Re}A_{LD}$ can be calculated using the form

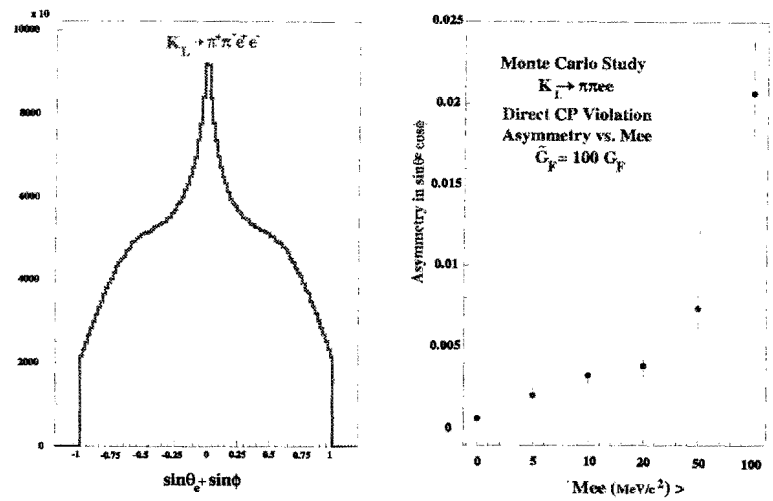

Figure 25: a) The $sin\theta_{e^+}sin\phi$ distribution in which direct CP is supposed to appear as an asymmetry between $sin\theta_{e^+}sin\phi \geq 0.$ and $sin\theta_{e^+}sin\phi \leq 0.$ b) The $sin\theta_{e^+}sin\phi$ asymmetry as a function of M_{ee} mass cut

factor measured from $K_L \to \mu^+\mu^-\gamma$ and ρ is limited with the expression [106]:

$$\rho > 1.2 - \max\left\{ \frac{|\mathrm{Re}A_{exp}| + |\mathrm{Re}A_{LD}|}{3 \times 10^{-5}} \times (\frac{\overline{m}_t(m_t)}{170\mathrm{GeV}})^{-1.55} \times (\frac{|V_{cb}|}{0.040})^{-2} \right\} \tag{24}$$

Also presented are measurements of the form factor according to the models of Bergström, Massó, and Singer (BMS) [45] and of D'Ambrosio, Isidori, and Portolés (DIP) [86]. Each model of the $\gamma^*\gamma$ form factor includes a single free parameter: α_{K^*} for BMS and α for DIP. Both parameters can be determined from the differential and integrated decay rates (i.e. from the dimuon mass distribution and the branching ratio). The final reconstructed $m_{\mu^+\mu^-\gamma}$ distribution is shown in Fig. 26. There are 9327 events in the mass window 490 MeV/c^2 $< m_{\mu^+\mu^-\gamma} <$ 506 MeV/c^2. The normalized Monte Carlo reproduces the mass distribution extremely well over a wide range and predicts 221.9 ± 14.9 background events under the signal mass peak, and above gives $B(K_L \to \mu^+\mu^-\gamma) = (3.66 \pm 0.04_{stat}) \times 10^{-7}$.

In Fig. 27 is shown a model-independent measurement of the form factor as a function of x (bin-by-bin values for $|f(x)|^2$ are given in [105]). The model parameters α_{K^*} and α were measured from the shape of the x distribution by making a log-likelihood comparison with Monte Carlo generated with various parameter values. In this way, the parameters were measured to be ${\alpha_{K^*}}^{Shape} = -0.193^{+0.035}_{-0.049}$ and $\alpha^{Shape} = -1.73^{+0.14}_{-0.18}$, where systematic errors dominated by the placement of the cut on track momentum are included. Integrating

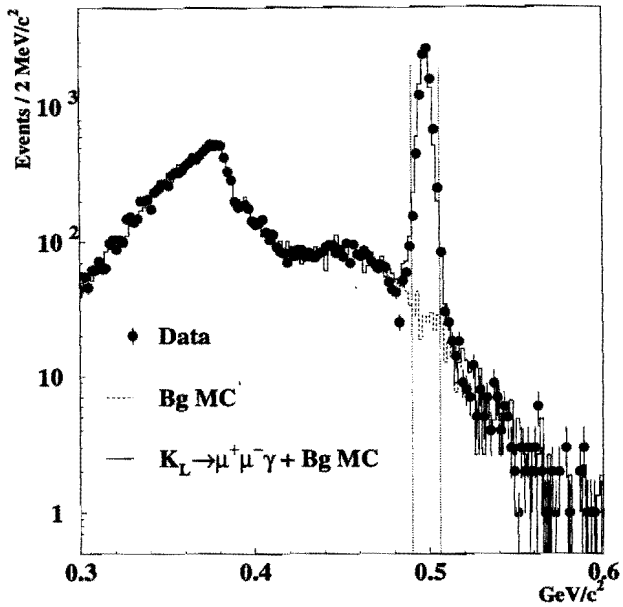

Figure 26: The reconstructed $m_{\mu^+\mu^-\gamma}$ distribution after final cuts. The large peak centered at 380 MeV/c^2 is $K_L \to \pi^+\pi^-\pi^0$. $K_{\mu 3}$ dominates the background from ~400 MeV/c^2 out to 600 MeV/c^2 with a slight enhancement at 450 MeV/c^2 from $K_{\mu 3\gamma}$.

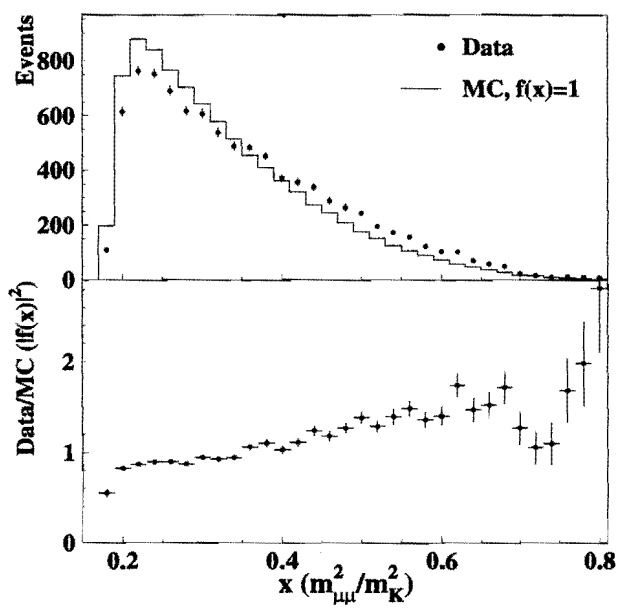

Figure 27: The dimuon mass distributions for data and for Monte Carlo with no form factor (top). The data/Monte Carlo ratio is a direct measurement of the form factor (bottom). The Monte Carlo is normalized to the total number of data events.

the differential decay rate, $B(K_L \to \mu^+\mu^-\gamma)$ was found as a function of α_{K^*} or α, yielding ${\alpha_{K^*}}^{BR} = -0.117^{+0.038}_{-0.037}$ and $\alpha^{BR} = -1.38 \pm 0.12$. The shape and branching ratio measurements were combined to give $\alpha_{K^*} = -0.157^{+0.025}_{-0.027}$ and $\alpha = -1.53 \pm 0.09$.

A limit of $|\mathrm{Re}A_{LD}|_{DIP} < 2.07 \times 10^{-5}$ is obtained using the measured form factor parameters with the DIP model. In forming the $|\mathrm{Re}A_{exp}| + |\mathrm{Re}A_{LD}|_{DIP}$ limit, the measured values of $|\mathrm{Re}A_{exp}|^2$ and $|\mathrm{Re}A_{LD}|_{DIP}$ are converted into Gaussian distributions, the product of which forms a two-dimensional probability distribution. The contour of $|\mathrm{Re}A_{exp}| + |\mathrm{Re}A_{LD}|_{DIP}$ under which 90% of the probability lies in the positive (physical) quadrant is the limit. This procedure yields the result $\rho > -0.2$.

The trigger for $K_L \to \mu^+\mu^-\gamma$ in KAMI will require 2 or more tracks, 2 hits in the muon stack, and at least one electromagnetic cluster in the CsI calorimeter. The acceptance is calculated to be 8.3%. In the KTeV analysis the various cuts and reconstruction efficiencies introduced another acceptance factor of 0.39. Putting these numbers together for a year with $6 \times 10^{13} K_L$ decays KAMI would get a sample of 711,000 events, nearly 100 times the current largest sample from KTeV.

The major background to $K_L \to \mu^+\mu^-\gamma$ arises from $K_L \to \pi^\pm\mu^\mp\nu(K_{\mu 3})$ where the π either decays in flight or punches through the muon shielding, in conjunction with an accidental photon in the CsI calorimeter. Compared to KTeV, KAMI has a shorter decay space between the last tracking plane and the muon shield, and the addition of a tracking plane in the center of the analysis magnet helps to remove "kinks" from decays.

4.4.2 $K_L \to e^+e^-e^+e^-$

The best current result on $K_L \to e^+e^-e^+e^-$ has recently been obtained by KTeV [87]. From a sample of 441 events the branching fraction is measured to be $(3.72 \pm 0.18_{stat} \pm 0.23_{syst}) \times 10^{-8}$. Figure 28 shows the reconstructed invariant mass of the two electron-positron pairs. The QED prediction for this branching fraction [88], neglecting radiative corrections and form factors and using the experimental measurement of the branching fraction of $K_L \to \gamma\gamma$, is $(3.65 \pm 0.09) \times 10^{-8}$. If it is assumed that the form factor factorizes into two terms of the Bergstrom, Masso and Singer type, then a fit yields $\alpha^{eff}_{K^*} = -0.14 \pm 0.16(stat) \pm 0.15(syst)$ where the notation $\alpha^{eff}_{K^*}$ denotes the fact that radiative corrections have not been made. Similarly the D'Ambrosio, Isidori and Portoles form factor is measured as $\alpha^{eff}_{DIP} = -1.1 \pm 0.6(stat)$. One may also look for CP violation in $K_L \to e^+e^-e^+e^-$ in the distribution of the angle ϕ between the planes of the two e^+e^- pairs in the K_L rest frame. The ϕ distribution is proportional to $1 + \beta_{CP}\cos(2\phi) + \gamma_{CP}\sin(2\phi)$ where $\beta_{CP} = \frac{1-|\epsilon r|^2}{1+|\epsilon r|^2}B$, $\gamma_{CP} = \frac{2Re(\epsilon r)}{1+|\epsilon r|^2}C$, where ϵ is the usual CP violation parameter and r is the ratio of the amplitudes of K_1 and K_2 decay to $e^+e^-e^+e^-$ (approximately 1). Ignoring CP violation ($\epsilon = 0$) the formula reduces to the Kroll-Wada formula where the constant B is -(+)0.20 for an odd(even) CP eigenstate. With CP violation, β_{CP} differs from the Kroll-Wada value and γ_{CP} no longer vanishes. There are, however, no predictions for the value of C, and thus γ_{CP}. To improve the resolution in ϕ for the KTeV data only the 264 events with the invariant mass of both e^+e^- pairs greater than 8 MeV/c^2 were used in a fit to the ϕ distribution. One would expect B to be -0.23 accounting for this cut. The fit yields $\beta_{CP} = -0.23 \pm 0.09(stat) \pm 0.02(syst)$, and $\gamma_{CP} = -0.09 \pm 0.09(stat) \pm 0.02(syst)$.

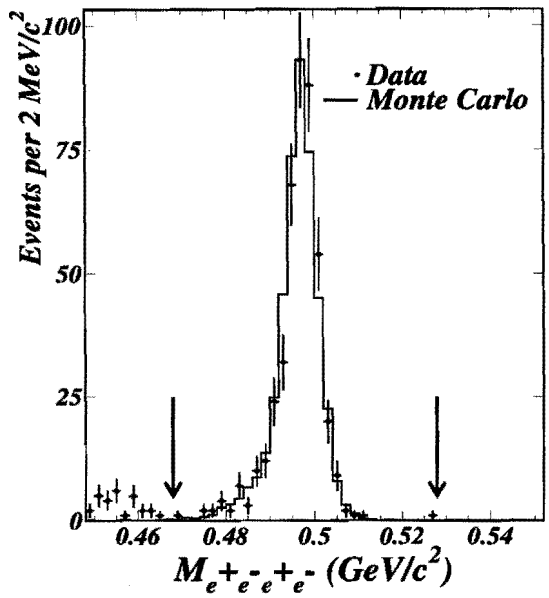

Figure 28: The 4e invariant mass distribution after all cuts except the invariant mass cut. The dots represent the data and the histogram represents the Monte Carlo simulation. There are 436 events in the signal region between the arrows. The decay $K_L \to \pi^{\pm}e^{\pm}\nu e^+e^-$ is seen in the lower mass region.

The trigger in KAMI for $K_L \to e^+e^-e^+e^-$ will require 4 tracks and at least 2 electromagnetic clusters in the CsI. In KTeV, the largest background to this mode was from $K_L \to e^+e^-\gamma$ or $K_L \to \gamma\gamma$ with one or two photon conversions in the apparatus. This background was suppressed by cuts on the minimum track separation of e^+e^- pairs in the first tracking chamber. In KAMI, since there is no material upstream of the first tracking module, this background should be greatly reduced. The calculated acceptance of KAMI for this mode is 3.9%. In KTeV the offline analysis kept 39% of the signal. Thus a KAMI year with $6 \times 10^{13} K_L$ decays would yield a sample of about 34,000 events, 90 times the current sample. This level of statistics will transform the form factor measurement to a highly statistically significant result. Similarly the CP asymmetries will be probed at the 1% level.

4.4.3 $K_L \to \mu^+\mu^-e^+e^-$

The decay $K_L \to \mu^+\mu^-e^+e^-$ is the best mode to determine the form factors of $K_L \to \gamma^*\gamma^*$ since the lepton pairs are definitely defined. KTeV has recently measured [89] the branching fraction of $K_L \to \mu^+\mu^-e^+e^-$ to be $(2.50 \pm 0.41(stat) \pm 0.17(syst)) \times 10^{-9}$, based on the observation of 38 events. Figure 29 shows the fit of the data to the scaled background simulation. We estimate 0.03 background events from $K_L \to \pi^+\pi^-\pi^0_D$ and $K_L \to \pi^+\pi^-e^+e^-$ decays in the signal region. Note that the VMD model of Quigg and Jackson [92], which predicts a branching ratio of 2.37×10^{-9}, is in better agreement with our result than more recent predictions. We have placed an upper limit on the CP violating term of Uy [91],

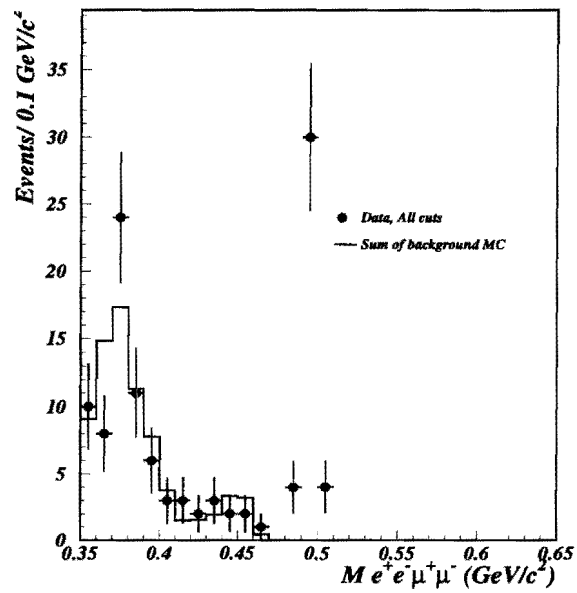

Figure 29: $M_{ee\mu\mu}$ for data (dots) and the scaled sum of $K_L \to \pi^+\pi^-\pi^0_D$ and $K_L \to \pi^+\pi^-e^+e^-$ background simulations (line), with $P_t^2 \leq 250$ (MeV/c)^2.

of $(\frac{g_2}{h_2})^2 \leq 2.77 \times 10^{-4}$ at 90% C.L. using the branching ratio. We have also searched for lepton flavor violation in like-sign lepton decays, and placed a limit $\mathcal{B}(K_L \to e^\pm e^\pm \mu^\mp \mu^\mp) \leq 1.36 \times 10^{-10}$ at the 90% confidence level.

The calculated acceptance of KAMI for $K_L \to \mu^+\mu^-e^+e^-$ is 5.0%. In KTeV, the offline analysis had an efficiency of 22%. So for a KAMI year of 6×10^{13} decays we expect a signal of 1600 events. The main backgrounds are due to two nearly simultaneous decays which is suppressed by cuts on measured vertex quality, and $K_L \to \pi^+\pi^-\pi^0_D$ (π^0_D denotes the Dalitz decay $\pi^0 \to e^+e^-\gamma$) where the $\pi's$ simulate $\mu's$ by punching through the muon absorber. The hermetic photon veto of KAMI will be especially useful in suppressing this background. KTeV also had a physics background due to $K_L \to \mu^+\mu^-\gamma$ decays where the γ converted in the vacuum window. These were removed by cuts on the invariant e^+e^- mass and track separation. These cuts also removed 14% of the signal. KAMI will not have this background because the vacuum window is downstream of the charged particle spectrometer.

4.4.4 $K_L \to e^+e^-\gamma\gamma$ and $K_L \to \mu^+\mu^-\gamma\gamma$

Two decay modes related to $K_L \to \gamma\gamma$, though not especially interesting in themselves, have significant implications for the attempt to observe direct CP violation in $K_L \to \pi^\circ e^+e^-$ and $K_L \to \pi^\circ\mu^+\mu^-$. These are the radiative Dalitz decays $K_L \to e^+e^-\gamma\gamma$ and $K_L \to \mu^+\mu^-\gamma\gamma$. With a typical infrared cutoff of 5 MeV for the photon energies in the kaon center of mass, the electron mode, $K_L \to e^+e^-\gamma\gamma$, has a branching ratio of about 6×10^{-7}, five orders of magnitude higher than the expected rate for $K_L \to \pi^\circ e^+e^-$. Moreover, the peak of the $\gamma\gamma$ invariant mass spectrum in observed events is near the π° mass. With a good calorimeter,

experiments can limit the π° mass range to a few MeV, but the number of $e^+e^-\gamma\gamma$ events in this range still swamps the expected $\pi^\circ e^+e^-$ signal. Further reduction in this background can be achieved by cutting on kinematic variables to remove, for example, events in which the momentum of one of the photons is nearly parallel to that of one of the leptons; this topology is typical of radiative Dalitz decays but uncommon for $\pi^\circ e^+e^-$ events. But even an optimal set of cuts cannot reduce this background to the level of the expected signal, a major impediment to the measurement of $B(K_L \to \pi^\circ e^+e^-)$. KTeV has identified a sample of over 1500 $e^+e^-\gamma\gamma$ events and has verified that their kinematic distributions are generally in agreement with those predicted.

In a similar fashion, $K_L \to \mu^+\mu^-\gamma\gamma$ decays are a serious background to the measurement of $K_L \to \pi^\circ\mu^+\mu^-$. The absolute rate for this decay is much less than the rate for the corresponding electron mode (see Table 2). Unfortunately, the part of the phase space where this decay can be a background to $K_L \to \pi^\circ\mu^+\mu^-$, after the $M_{\gamma\gamma}$ and other kinematic cuts, is not particularly suppressed.

4.5 $K_L \to \mu^+\mu^-$

The decay $K_L \to \mu^+\mu^-$ has a long history of importance in high energy physics. The low rate of this decay was one of the reasons for the proposal of the GIM mechanism which, with the presence of the charm quark, cancels flavor changing neutral currents. The principal contribution to the decay rate is an absorptive process with a two-photon intermediate state. This may be related to the branching fraction for $K_L \to \gamma\gamma$ which yields a lower limit, known as "the unitarity bound" for the $K_L \to \mu^+\mu^-$ branching fraction of $(7.07 \pm 0.18) \times 10^{-9}$. The excess of the decay rate above this value is due to the sum of long-distance electromagnetic contributions and short-distance second-order electroweak diagrams. The latter are dominated by the top quark and are approximately proportional to $|Re(V_{ts}^* V_{td})|^2$ from which ρ in the Wolfenstein parameterization may be derived.

The current experimental knowledge of the branching fraction of $K_L \to \mu^+\mu^-$ is dominated by the result of BNL E-871, [40] who obtain the value $(7.18 \pm 0.17) \times 10^{-9}$, based on a sample of 6200 candidate events with about 1% background. This sample is a factor of 6 more than all other experiments combined.

The trigger in KAMI for $K_L \to \mu^+\mu^-$ would require 2 tracks in the fiber tracker and 2 hits in the muon range stack. The calculated acceptance is 10.5%. This would yield, in one year of running with $6 \times 10^{13} K_L$ decays, a signal of 45,000 events before offline cuts. The principal background is due to $K_L \to \pi^\pm\mu^\mp\nu$ where the π decays or punches through the muon absorber. The endpoint of the $\mu^+\mu^-$ mass distribution is 8 MeV below the K_L mass, requiring good mass resolution to separate these events from the signal. The first level trigger rate for the 2-track 2-muon trigger may be as large as all other charged mode triggers combined, which might, depending on trigger system and DA capacity, require additional trigger requirements with possible loss of acceptance.

4.6 $K_L \to \pi^0\mu^+\mu^-$

Along with the decay $K_L \to \pi^0\nu\overline{\nu}$ that is the principal objective of KAMI, the related decays $K_L \to \pi^0 e^+e^-$ and $K_L \to \pi^0\mu^+\mu^-$ are of considerable interest. Within the standard

model there are three contributions to these modes. [93]. The first is a directly CP violating contribution from electroweak penguin and $W^{\pm}$ box diagrams; only loops with t quarks, which have amplitudes proportional to η in the Wolfenstein parameterization, ultimately contribute. The second contribution is an indirectly CP violating amplitude [94] due to the K_1 component of the K_L. Third, there is a CP conserving component proceeding through $\pi^0\gamma^*\gamma^*$ intermediate states [95], which can be estimated from measurement [96] of the decay $K_L \to \pi^0\gamma\gamma$. The expected branching fraction in the standard model for these decays is in the range $0.3 - 1.0 \times 10^{-11}$. The branching ratio predictions are modified in theories containing particles beyond the standard model that contribute to the penguin and box amplitudes. The minimal supersymmetric standard model mostly predicts reductions in the branching ratios [97], while other supersymmetric models predict enhancements [98].

The best current limits on these modes are from KTeV. Based on the data taken in 1997 for $K_L \to \pi^0 e^+ e^-$ an upper limit at the 90% confidence level of 5.1×10^{-10} was set [99] based on the observation of 2 events with an expected background of 1.06 ± 0.41 events. For $K_L \to \pi^0\mu^+\mu^-$ the 90% confidence level upper limit was [100] 3.8×10^{-10} based on 2 observed events with an expected background of 0.87 ± 0.15 events. Note that these limits are not background free. In particular, there are physics backgrounds due to the decays $K_L \to e^+e^-\gamma\gamma$ and $K_L \to \mu^+\mu^-\gamma\gamma$ where the $\gamma\gamma$ invariant mass coincides with that of the π^0. The branching fractions of these decays have been measured in KTeV [101] [102]. To some extent this background can be suppressed by judicious cuts on the decay kinematics [103].

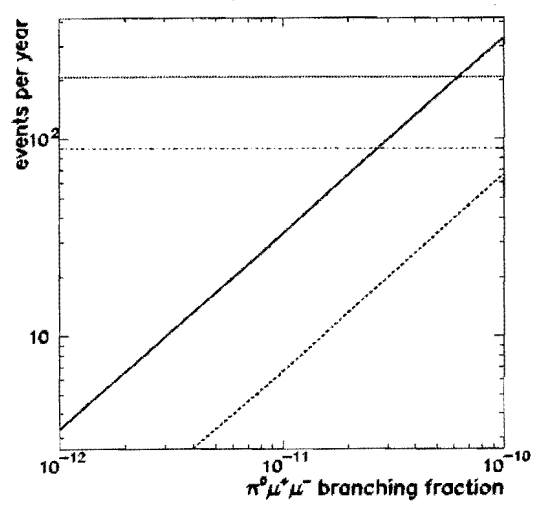

Figure 30: Signal and background rates for $K_L \to \pi^0\mu^+\mu^-$, versus the branching fraction. The diagonal lines show the predicted number of observed signal events in one year for perfect reconstruction efficiency (solid), and 20% reconstruction efficiency (dashed). The horizontal lines show the expected background from $K_L \to \mu^+\mu^-\gamma\gamma$ only (dot-dashed) and also other background sources (dotted).

For the $K_L \to \pi^0 e^+ e^-$ decay in KTeV, rejection of backgrounds from $K_L \to \pi^\pm e^\mp \nu$ decays required additional π/e separation above that of the CsI calorimeter alone. This was achieved by the use of Transition Radiation Detectors. Since we do not at present intend to include TRD's in the KAMI detector we ignore the $\pi^0 e^+ e^-$ mode and concentrate on $\pi^0 \mu^+ \mu^-$.

The trigger for $K_L \to \pi^0 \mu^+ \mu^-$ will have the basic requirements of at least 2 track hits in the last fiber tracker plane, hits in 2 or more tiles at a certain depth of the muon stack, and at least 2 electromagnetic clusters in the CsI calorimeter. We calculate the KAMI acceptance to be 5.5%. If event reconstruction was perfect in one year with $6 \times 10^{13} K_L$ decays the signal event yield versus $\pi^0 \mu^+ \mu^-$ branching fraction is given by the upper diagonal curve in Figure 30. For a branching fraction of 1.0×10^{-11} we expect 33 events. Of course, reconstruction efficiency will not be 100%; in KTeV the reconstruction efficiency after geometric and trigger acceptance was about 20% [104]. If we apply this additional inefficiency we get the lower diagonal curve in Figure 30.

Now we also need to estimate the background, since we know it cannot be entirely eliminated in this analysis. The best estimate we can make now is to extrapolate from the experience of KTeV. Extrapolating from the calculated 0.37 events of the physics background due to $K_L \to \mu^+ \mu^- \gamma\gamma$ yields a prediction of 89.5 events per year. This is shown as the lower horizontal line in Figure 30. If we use the total estimated background in KTeV of 0.87 events the extrapolation yields 209 events per year in KAMI, as shown in the upper horizontal line in Figure 30. These additional backgrounds arise mostly from common K_L decays where pions decay in flight or punch through the muon shielding. KAMI may be better in reducing these backgrounds as it is designed to have less flight path after the last tracking station where decays can take place, and the addition of a tracking plane at the center of the magnet helps to detect "kinks" due to decays within the spectrometer. On the other hand the average momentum of pions is lower, leading to higher decay probabilities.

If we take the signal and background curves of Figure 30 as indications of the range of signal and backgrounds that may be obtained we can calculate the sensitivity of KAMI for $\pi^0 \mu^+ \mu^-$. Figure 31 shows the ratio of the signal divided by the square root of the background for the 4 combinations of signal and background curves in Figure 30. If the signal is in the middle of the range of curves, this corresponds to a 3 σ detection for a branching fraction of about 2×10^{-11}. Once a sample of events is accumulated it may also be possible to extract the numbers of signal and background by likelihood fits to the kinematic distributions of the events, or perhaps by the use of neural network analysis.

One will of course accumulate a sample of $K_L \to \mu^+ \mu^- \gamma\gamma$ during the analysis. The acceptance for this mode is 2.0%, which would yield a sample of 11,000 events in a year compared with the 4 events observed by KTeV.

4.7 Lepton Flavor Violating Modes

The observation of lepton flavor violation (LFV) in neutrino oscillations at SuperK has renewed interest in lepton flavor violation in decay processes. Neutrino oscillation provides a mechanism for lepton flavor violation in a decay process, but predicted rates are far below the sensitivity of any existing or planned experiment. Many extensions of the Standard Model allow or require lepton flavor violating decays at levels far above Standard Model predictions. The neutral Kaon system is an excellent place to search for lepton flavor violating decays

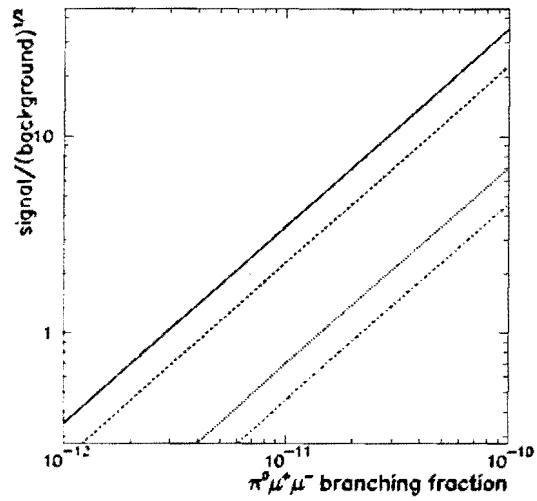

Figure 31: Signal divided by square root of background for $\pi^0\mu^+\mu^-$ in one year of running for the 4 combinations of signal and background shown in Figure 30

which are sensitive to physics beyond the Standard Model. Reference [122] is a survey of LFV kaon decays and the current constraints on supersymmetric parameters imposed by the existing experimental limits.

KTeV has set LFV limits in several decays, and additional limits will be forthcoming. Our experience with KTeV allows us to make reasonable estimates of LFV sensitivities accessible to KAMI.

4.7.1 $K_L \to \pi^0\mu e$

KTeV announced a preliminary limit on this mode at DPF2000 in Columbus [72]. The limit is 4.4×10^{-10} at 90% CL. This limit is a factor of 15 better than the previous limit from E799-I for this mode. The additional data from KTeV99 should reduce this limit by a factor of two. Fig. 32 shows this result included two background events in the signal box from $K_L \to \pi e\nu$ plus accidental photons.

To substantially improve this limit, this source of background must be greatly reduced. However, there is reason to think that this source of background would be substantially reduced in KAMI. One possible source of extra photons is an additional decay which produces a π^0 plus other particles. If the additional particles are not observed, the photons could contribute to the background. KAMI will have superlative vetoes on both charged particles and photons, so backgrounds due to multiple decays should be reduced.

An additional source of accidental photons is π^0 production by neutron interactions in the vacuum window or other material. This source of background will be much reduced in KAMI since the vacuum window will be immediately upstream of the calorimeter. If

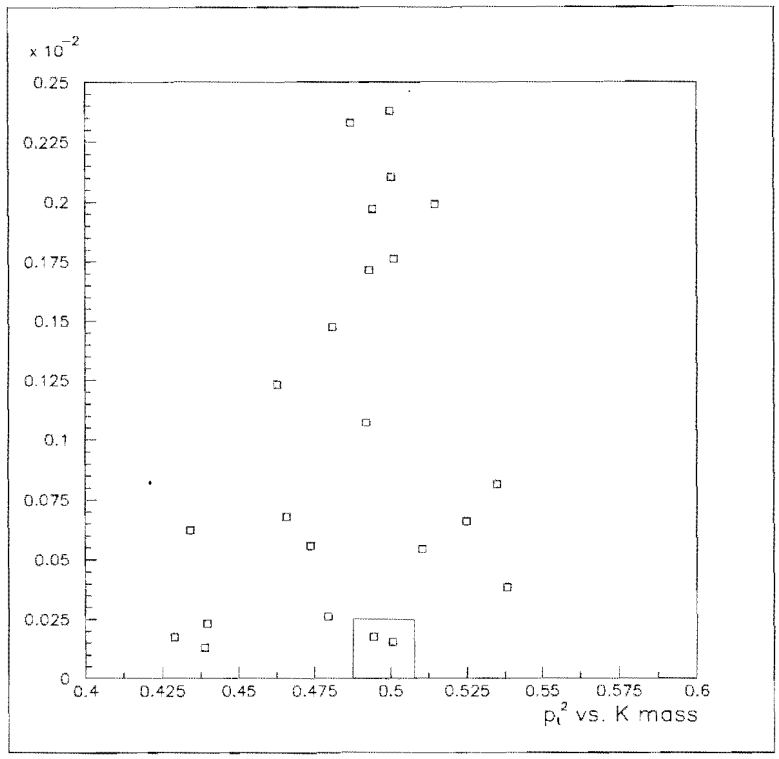

Figure 32: $M_{\pi^0\mu e}$ invariant mass

accidental backgrounds can be controlled, we expect a single event sensitivity (assuming $6 \times 10^{13} K_L$ decays) of about 4×10^{-13}.

In KTeV we used the TRD information to reduce backgrounds from $K_L \to \pi^+\pi^-\pi^0$ with one charged π misidentified as an electron and the other as a muon. We have confirmed with KTeV data that if we remove the cut on TRD information, no additional background enters the signal region. The two-fold particle misidentification causes the $M_{\pi^0\mu e}$ to be reconstructed well below the kaon mass, keeping these events well away from the signal region. We therefore do not expect the lack of TRD information in KAMI to impact the sensitivity in this mode.

4.7.2 $\pi^0 \to \mu^\pm e^\mp$ tagged from $K_L \to \pi^0\pi^0\pi^0$

KTeV announced a preliminary result from this decay at the DPF2000 meeting in August 2000 [72]. The background-free limit was 7.85×10^{-10}, a factor of 22 improvement over the PDG limit. An additional factor of two improvement is expected from the KTeV99 data.

The search requires an electron and a muon with an invariant mass near the π^0 mass, as well as four other photons, consistent with two π^0's, all of which form a kaon mass. These requirements are exceedingly restrictive, leading to a totally background-free limit. We do not yet see any source of backgrounds that might enter at the level of KAMI's flux. Rather, the superior vetoing power of KAMI should only reduce backgrounds further. For a flux of $6 \times 10^{13} K_L$ decays, we expect a single event sensitivity of about 8×10^{-12}.

4.7.3 $K_L \to \mu^\pm\mu^\pm e^\mp e^\mp$

KTeV set a 90% CL limit of 1.36×10^{-10} on this mode, as part of the measurement of the branching ration for $K_L \to \mu^\pm\mu^\mp e^\pm e^\mp$. The background in this mode is expected to come from double decays to semileptonic modes, followed by pion decay to muons. Estimated background in the KTeV data set is 0.02 events from this source, although this background should be reduced with more careful kinematic and tracking cuts. KAMI should achieve a single event sensitivity of 3×10^{-13} in this mode.

4.7.4 Other Lepton Flavor Violating Modes

The current best limit on any kaon decay is BR($K_L \to \mu^\pm e^\mp$)$< 4.7 \times 10^{-12}$ [121]. KTeV did not study this mode, since we could not improve on this limit. However, KAMI should achieve a SES for this mode of $\sim 2 \times 10^{-13}$. Triggering and backgrounds in KAMI for this mode are currently under study. Other LFV modes currently under study in KTeV include $K_L \to \pi^+\pi^-\mu e$ and $K_L \to \pi^0\pi^0\mu e$. In KTeV we expect limits comparable to the limit on $K_L \to \pi^0\mu e$, and would expect comparable improvements in KAMI. Background levels for these decays in KTeV are not yet known but expected to be small.

4.8 Summary

As can be seen from the previous discussion, KAMI offers the opportunity for a rich and diverse physics program in addition to the flagship $K_L \to \pi^0\nu\overline{\nu}$ measurement. The sensitivity reach of KAMI allows for issues of direct CP violation, lepton flavor violation and other new physics phenomena to be probed in important new ways. This has been discussed in detail in Section 1 and in the preceeding sections. Table 14 summarizes KAMI's sensitivity for the various charged modes that have been discussed.

Decay Mode	Branching Fraction (measured or predicted)	Current Best Result (events or 90% C.L.)	Events per Year or Sensitivity for KAMI
$K_L \to \pi^0\mu^+\mu^-$	$0.3 - 1.0 \times 10^{-11}$	$< 3.8 \times 10^{-10}$	$< 2 \times 10^{-11}$
$K_L \to \pi^+\pi^-e^+e^-$	3.2×10^{-7}	6000	678,000
$K_L \to \mu^+\mu^-$	7.2×10^{-9}	6200	45,000
$K_L \to \mu^+\mu^-\gamma\gamma$	9.1×10^{-9}	4	11,000
$K_L \to \mu^+\mu^-\gamma$	3.7×10^{-7}	9327	711,000
$K_L \to e^+e^-e^+e^-$	3.7×10^{-8}	441	34,000
$K_L \to \mu^+\mu^-e^+e^-$	2.5×10^{-9}	38	1600
$K_L \to \pi^0\mu^\pm e^\mp$	-	$< 4.4 \times 10^{-10}$	4×10^{-13} (SES)
$K_L \to \mu^\pm e^\mp$	-	$< 4.7 \times 10^{-12}$	2×10^{-13} (SES)
$\pi^0 \to \mu^\pm e^\mp$	-	$< 7.9 \times 10^{-10}$	8×10^{-12} (SES)
$K_L \to \mu^\pm\mu^\pm e^\mp e^\mp$	-	$< 1.4 \times 10^{-10}$	3×10^{-13} (SES)

Table 14: Summary of the current best results and KAMI sensitivity for various decay modes with charged particles. The KAMI yield or sensitivity assumes one year of running with $6 \times 10^{13} K_L$ decays. SES denotes single event sensitivity.

5 Beams

The KAMI experiment requires a high-intensity primary beam of 3×10^{13} protons per pulse with a flat-top of 1 second and a repetition rate of about 3 seconds. Assuming the Main Injector runs for 2×10^{7} seconds per year, this corresponds to about 2×10^{20} protons per year on the KAMI target. The integrated luminosity for KAMI will be almost 100 times the KTeV luminosity! It is therefore necessary to re-evaluate very carefully all issues having to do with beam loss, maintenance, residual radioactivity and other issues that might be related to this increased luminosity.

KAMI is requesting debunched beam in order to minimize pile-up in the detector. Modest modulation of the beam for ease of monitoring is acceptable.

The overall beam design is along the lines of the "KAMI-far" configuration discussed in the KAMI EOI [108]. The general layout of the primary beam, target, and neutral beam are very similar to the existing KTeV configuration.

The targeting angle will be variable between 10 mr and 20 mr in the vertical plane. Here we assume a 15 mr targeting angle. The full range of targeting angle will not be available without realigning the vertical bend magnets. The design of the target area will be such that this full range of targeting angle can be accommodated.

5.1 Primary Beam

The KAMI primary beam is very similar to the KTeV primary beam. Most of the beam line is in place and tested using 150 GeV primary beam at the end of KTeV running in January 2000. Some issues remain to be dealt with:

- The superconducting bends are to be replaced with conventional magnets. The decision has been made to eliminate superconducting magnets from the external beam lines.
- There was some beam scraping during the test beam run. The apertures are being reevaluated to make sure this will not be a problem in the future.
- The detailed arrangement of the final bend system is yet to be defined. It may be necessary to readjust the positions of the final vertical bends in the primary beam. This is not a large project; the realignment from the KTeV configuration to an appropriate configuration for KAMI running required only a few days.

The beam design has been carried out for 120 GeV beam [109]. A plot of the beam envelope from A0 to the KAMI target is shown in Figure 33.

It is expected that in the near future, Main Injector beam will be delivered to the Meson Area. Then it will be possible to measure the emittance of the Main Injector beam. Given good input data, detailed beam calculations will be redone after which, some additional modifications of the beam design may be necessary. As the beam has already worked at 150 GeV, these additional modifications are expected to be modest.

The intensity of the primary beam in NM1 and upstream of the target should be monitored to assure efficient beam transport. The position of the beam must be monitored and

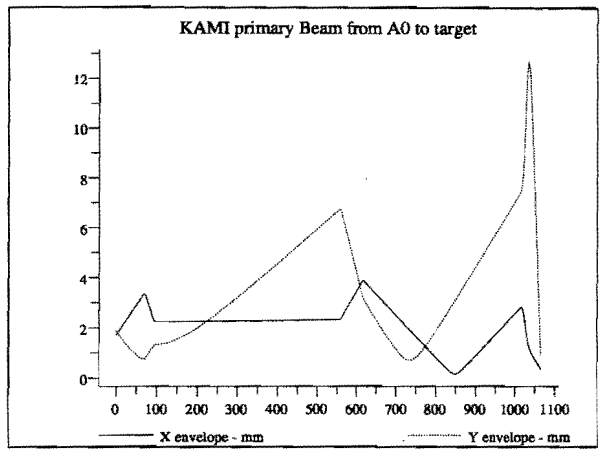

Figure 33: KAMI Primary Beam Envelope

the beam must be kept well positioned on the target. It is assumed that it will again be possible to control the beam using automatic control and compensation software (AUTOTUNE) and that the instrumentation necessary to implement those controls will be in place.

5.2 Target

The target used in the KAMI test run was one interaction length of BeO. The simulations and rate calculations also assume a one interaction length target. A high A material would maximize the kaon flux while minimizing the size of target presented to the collimating system. A short target (the best would be a point) leads to a beam with less halo due to elastic scattering in the collimators. Because the beam halo is recognized as a major source of radiation damage to the CsI calorimeter, and because beam halo is a potential source of background to the measurement of $K_L \rightarrow \pi^0 \nu \overline{\nu}$, the case for a dense, short target is compelling.

One of the concerns associated with using a high-A target is that the ratio of γ/K^0 or of n/K^0 might be compromised. However, GEANT studies of these ratios, shown in Figures 34 and 35, indicate that these ratios are, in fact, not compromised. Note that the number of photons in the neutral beam is reduced to negligible levels by placing a Pb converter in the neutral beam. The attenuation to the kaon beam from a 3 inch lead absorber has been included in the flux estimates presented in Section 2.5. Note that because of the relatively large targeting angles, the kaon flux increases monotonically with increasing target length.

Because of the large amount of energy deposited in the target, it will be necessary to cool the target by flowing He over it. This means that there must be a recirculating system and heat exchanger developed for the target area.

The target must be installed on a removable tray. It will not be possible to have actuators and sensors directly associated with the target. This was attempted in the less intense environment of KTeV, but the devices failed early on in the experiment. Methods for dealing with the very hot target and target environment are yet to be worked out.

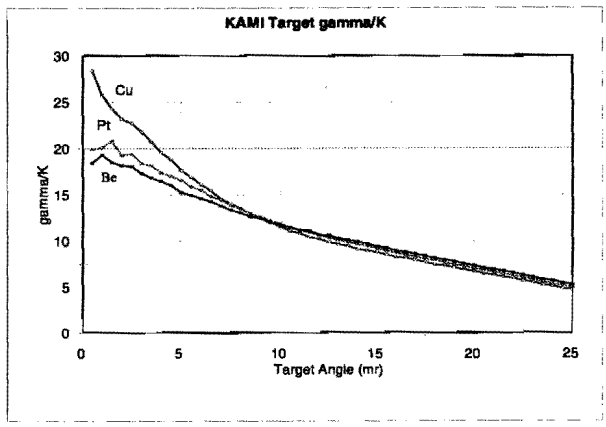

Figure 34: KAMI γ/K^0 production ratios for various targets

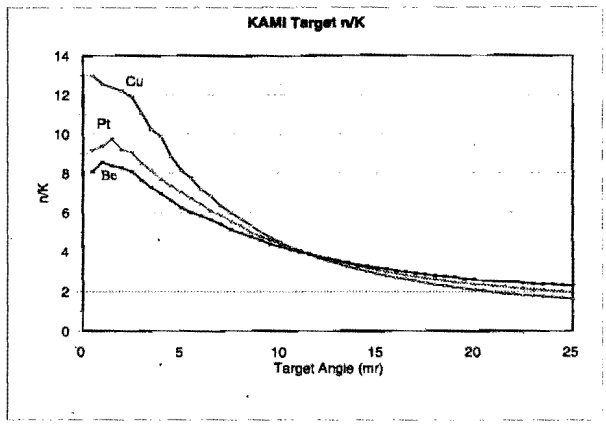

Figure 35: KAMI n/K^0 production ratios for various targets

5.3 Neutral Beam

The neutral beam will be defined by the target and three collimators, all located in NM2. The final collimator will be followed by a sweeping magnet. This final sweeping magnet was determined to be absolutely necessary by tests done during KTeV running. Detailed simulations of the KAMI neutral beam is in progress.

Two of the existing KTeV collimators can be reused. Of course new inserts with a single beam defining hole must be installed. KAMI uses a single neutral beam instead of the two beams used in KTeV. The sweeping system will be similar to that in KTeV. The target will be located in the first sweeping magnet.

As the targeting angle is larger in KAMI than in KTeV, the location of the beam dump will be changed. It will again need to be water cooled using the RAW system currently in place. The dump will start approximately 2.5 meters downstream of the target. The upstream end of the target pile will have to be rebuilt in order to install the new target assembly, initial sweeper and beam dump. The E8 hyperon magnet, which is already in place in the tunnel, will be used as a second sweeper. There will be space for converters and

absorbers, followed by the first of the collimators and NM2S3. The spin rotator magnet is not needed in KAMI (no hyperons make it to the KAMI decay region at these energies), but there is no need to remove it. The slab collimator will be removed. The exact location of the second collimator in NM2 is not yet fixed. It may be necessary to adjust the position of the neutral beam stop and/or the existing jaw collimators to accommodate this new collimator.

The neutral beam will be in vacuum starting shortly downstream of the absorbers as in KTeV. Again, the vacuum will be contiguous to the large window in front of the CsI.

5.4 Alignment

Standard alignment techniques may be used to place the primary beam elements and monitors. The precision of the beam - target alignment is not particularly critical as it was for the ϵ'/ϵ experiment in KTeV.

However, the alignment of the neutral beam defining elements - the target with respect to the three collimators is critical. Studies have shown that the tails on the neutral beam shape are very sensitive to the collimator alignment. Monte-Carlo simulations indicate that the collimator alignment must be better than 200 microns.

In addition, given the intensity of the beam, it will again be critical that the neutral beam pass through the beam hole in the CsI array.

5.5 KAMI Test Run Beam Studies

The 150 GeV beam test run done in January, 2000 revealed a substantial halo closely surrounding the beam. The intensity was seen to be high enough to lead to unacceptable radiation damage to the CsI calorimeter. The angular spread of the halo can also limit the ability to produce a pencil-beam for anticipated special studies.

The test beam conditions have been simulated using a Monte Carlo. This simulation leads to an understanding of the test beam and serves to calibrate the Monte-Carlo. In the process, the physical mechanism(s) contributing to the halo can be understood. The Monte Carlo is then used to understand what changes are required to reduce the halo to acceptable levels, and to determine the tolerances on collimator shapes and placements.

Nuclear coherent elastic scattering is the only mechanism that generates a closely lying halo of the same type of particle as the beam itself. Inelastic processes distribute most of the outgoing energy into pions at relatively large angles compared with the observed halo in the dangerous region of a few milliradians. Occasionally, leading nucleons are produced outside the halo as well as fission products and a swarm of low energy neutrons that continue to interact for microseconds. A GEANT simulation revealed that elastic scattering dominated the beam-halo by several orders of magnitude. Because inelastic processes result in large energy losses, they will be responsible for collimator radioactivity but that is not the issue addressed here.

The known components of the beam are (1) the primary collimator (PC) located 20 meters from the target, (2) the jaws at about 43 meters, and (3) the defining collimator (DC) at about 88 meters. While the apertures of (1) and (3) are not adjustable (except for inserts), the position and orientation are not well known at the sub-millimeter and sub-milliradian levels. As for the 2 jaws (and slab when it is in situ), neither the position nor

orientation is accurately known. The beam is believed to have been clipped by a jaw. Some tuning of the jaw geometry was therefore required to simulate the data. In the simulations, rotations about the z-axis were neglected; perfect angular alignment was assumed between DC and PC. Picture frame collimators were added upstream and downstream of the jaws and upstream of the DC to simulate alignment errors.

The plots to be compared between the data and the simulations are the so-called "ring number" plots. These rings are essentially a measure of the transverse location of decay vertices with respect to the beam axis. In these simulations, a very naive spectrometer was assumed, so the plots are not well simulated at large ring number. For modest ring number the data is well represented by the simulation, as can be seen in Figure 36.

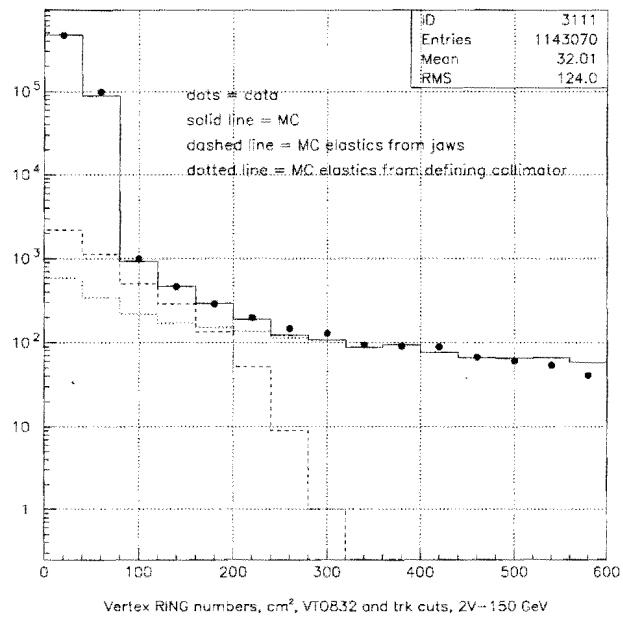

Figure 36: Comparison of "ring number" (essentially a P_t distribution) from the KAMI beam test (dots) and simulation (solid line)

How can halo be reduced for KAMI? One change that suggests itself is to replace the adjustable jaw structure with a precision collimator much like the DC and PC. The configuration used for the KAMI simulation is shown in Figure 37.

Note that this is not exactly the KAMI configuration discussed below. It was felt that the optimization should proceed in small steps to maintain a detailed understanding of the effects of each change from the KTeV/KAMI-Test-Beam calibration configuration. This round of simulations proceeded in three stages. First was to reproduce the KAMI test beam results. Second was to replace the jaws in the neutral beam with a nominal collimator. Finally, an optimized collimator was placed at that location. Results from a simulation of this series of studies is shown in Table 15, and the spectra and illuminations for the final case are shown in Figure 38.

The new collimator is very simple, namely a rectangular solid placed at 43 meters from the target and having an un-tapered square beam hole. Simulations were done with various hole sizes. There is a factor of at least 10 improvement with this precision collimator. Clearly,

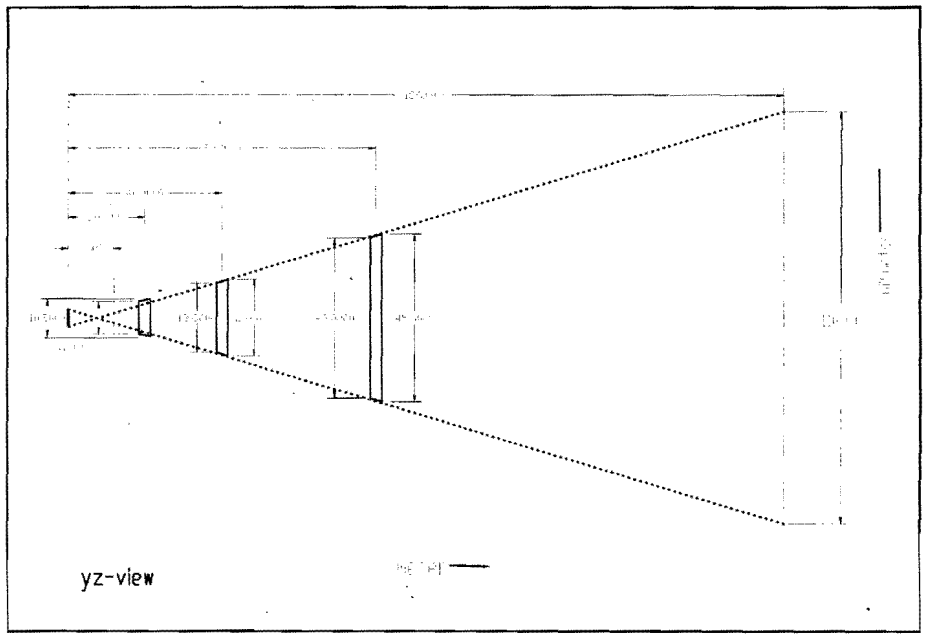

Figure 37: Target and collimator geometry in the vertical plane used to simulate the KAMI beam.

GEANT Simulations - KAMI Tests			
Case	Total Beam Particles	In Beam Hole	Out/In
No. 1	566257	561471	0.85%
No. 2	452629	452202	0.094%
No. 3	395755	395722	0.008%

Table 15: GEANT simulations of 3 center collimator configurations: 1) KAMI Beam test; 2) 2 cm square: 3) optimized for KAMI beam.

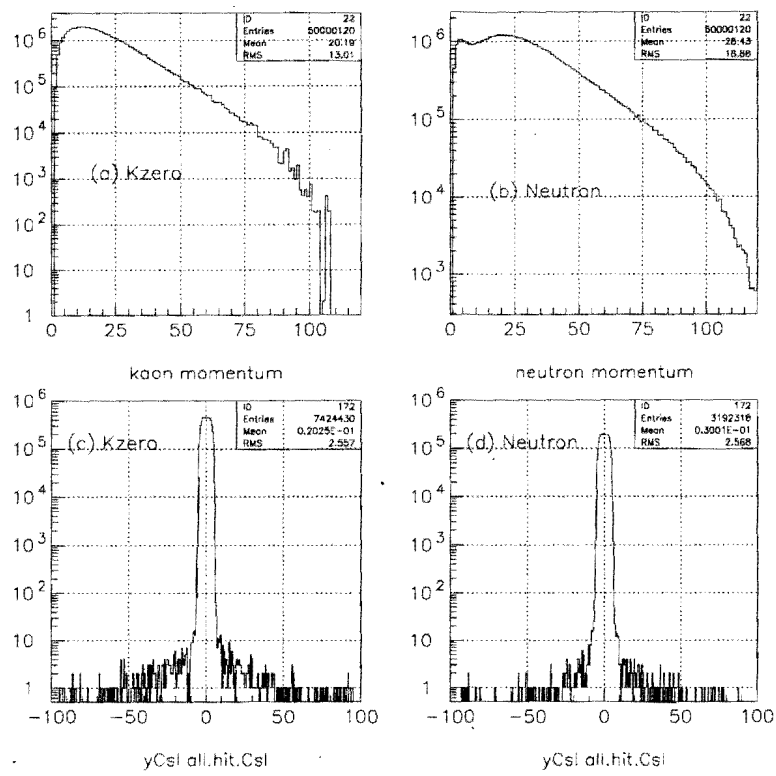

Figure 38: KAMI neutral beam simulation with a precision middle collimator.

a precision collimator between PC and DC is needed, but a more thorough parametric study will very likely reveal better collimator positions along the beam, better aperture shapes, tolerances, and better choices for material which need not be the same for all three collimators.

6 The KAMI Detector

6.1 Overall Geometry

The geometry of the KAMI detector is primarily governed by the stringent requirement of hermetic photon rejection efficiency for the $K_L \to \pi^0 \nu\overline{\nu}$ measurement. The KAMI detector is shown in Figure 8.

The most upstream section of the detector is a 5 m long veto region which is surrounded by the two Mask Anti detectors and vacuum photon veto detectors to reject upstream decays. This section is followed by an 85 m long fiducial region, again completely covered by vacuum photon veto detectors located inside of the vacuum tank.

The detector includes a charged spectrometer, consisting of five fiber tracking modules and a wide-gap analyzing magnet. The fiber tracking modules reside inside the vacuum chamber and integrate with the photon veto system. The vacuum chamber passes through the magnet gap.

The KTeV pure CsI calorimeter will be re-used and will sit just downstream of the vacuum window. The size of the calorimeter will be increased to improve the acceptance for $K_L \to \pi^0 \nu\overline{\nu}$. The gap between the vacuum window and the CsI is filled by two sets of CsI Anti counters to cover any cracks between the vacuum veto system and the CsI. Behind the CsI, the neutral beam is dumped onto a beam-hole calorimeter known as the Beam Anti, designed to veto photons going down the CsI beam hole. Finally, there are multiple layers of iron shielding and muon counters for muon identification. Table 16 shows the locations of all the detector elements.

6.2 Pure CsI Calorimeter

6.2.1 The KTeV Calorimeter

The KTeV CsI calorimeter is the most advanced, high-precision electromagnetic calorimeter currently in use. The calorimeter consists of 3100 pure CsI crystals, 27 radiation lengths long, prepared for optimal resolution and linearity. It is instrumented with low-gain, highly linear photomultiplier tubes (PMTs), each with its own digitizer.

The length of the crystals was chosen to be 27 radiation lengths (50 cm) in order to achieve excellent energy resolution and linearity. There are two sizes of crystals, $2.5 \times 2.5 \times 50.0$ cm^3 crystals in the central region of the calorimeter, and $5.0 \times 5.0 \times 50.0$ cm^3 crystals in the outer region. The two transverse dimensions were chosen to optimize the $K_L \to 2\pi^0$ mass resolution, while minimizing the number of channels. To optimize the resolution and linearity of the calorimeter the Aluminized-Mylar wrapping of each crystal was individually tuned so that the scintillation response along the shower is uniform to the level of 5%. Finally, on average, the actual light yield of the crystals was 20 photo-electrons/MeV, which corresponds to a contribution to the energy resolution of $0.007/\sqrt{\mathrm{E(GeV)}}$.

The signals from the CsI PMTs were digitized at the PMT base in 19 ns time slices, in synch with the RF structure of the KTeV beam. The digitizer is a multi-ranging device with 16 bits of dynamic range in the form of an 8-bit mantissa and a 3-bit exponent. The noise per channel is about 0.8 MeV. The energy resolution of the calorimeter is better than 1% over the energy region of 5 - 100 GeV. The multiple samples allow for additional rejection

	z(up) (m)	z(down) (m)	R(in) (m)	R(out) (m)
Production target	0.00	0.30	-	0.0015
Primary collimator	20.00	22.00	-	0.0029
Defining collimator	60.00	63.00	-	0.0255
Mask Anti 1	95.00	95.70	0.07	0.40
Vacuum Veto 1a	95.70	99.30	0.40	0.90
Mask Anti 2	99.30	100.00	0.07	0.40
Vacuum Veto 1b	100.00	116.00	0.40	0.90
Vacuum Veto 2	116.00	134.00	0.65	1.30
Vacuum Veto 3	134.00	152.00	0.90	1.40
Vacuum Veto 4	152.00	170.00	1.15	1.65
Fiber Tracker 1 (x/y)	170.00	170.05	0.07	1.25
Vacuum Veto 5	170.00	173.00	1.192	1.692
Fiber Tracker 2 (x/y)	173.00	173.05	0.07	1.25
Vacuum Veto 6	173.00	176.00	1.234	1.734
Magnet (gap)	173.00	179.00	1.900	-
Fiber Tracker 3 (x)	176.00	176.05	0.07	1.25
Vacuum Veto 7	176.00	179.00	1.277	1.777
Fiber Tracker 4 (x/y)	179.00	179.05	0.07	1.375
Vacuum Veto 8	179.00	184.00	1.347	1.847
Fiber tracker 5 (x/y)	184.00	184.05	0.07	1.375
Vacuum Veto 9	184.00	186.00	1.375	1.875
Vacuum window	186.00	186.00	-	1.95
CsI Anti 1	186.05	186.30	1.375	1.50
CsI Anti 2	186.30	186.70	1.375	1.50
CsI	186.00	186.50	0.075	1.375
Muon Range Stack	188.00	200.00	0.15	2.00
Beam Anti 1	189.00	190.10	0.075	0.25
Beam Anti 2	195.00	196.10	0.075	0.35
Beam Anti 3	205.00	206.00	-	0.35

Table 16: Locations and inner/outer dimensions of all the KAMI detector elements.

of out-of-time accidental activity. In addition, the time resolution of the system has been found to be 150 psec, using a calibration laser flasher system.

6.2.2 The KAMI Calorimeter

The CsI will be re-stacked for KAMI to form a circular array with a single 15 cm × 15 cm square beam hole. Careful attention will have to be paid to cracks between crystals that can lead to detection inefficiencies. It will be necessary to tilt the array or stack the crystals with a non-projective geometry to prevent cracks from lining up with the trajectory of incident photons. The diameter of the array will be 2.75 m, requiring the addition of 1068 new crystals. The re-stacked calorimeter is shown in Figure 39. The change from a square to a circular array is driven by the desire to minimize the size of the vacuum window which sits immediately upstream of the CsI.

For the KAMI experiment, the important calorimeter considerations include energy resolution, resistance to radiation damage, efficiency to separate nearby photons, and gaps between crystals. Let us discuss these issues in turn.

The energy and position resolution of the calorimeter can be determined from momentum analyzed electrons from $K_L \to \pi^{\pm} e^{\mp} \nu$ decays. The ratio of energy measured in the calorimeter to momentum measured in the spectrometer is shown in Figure 40. For electrons incident over the entire calorimeter, and having momentum from 4-100 GeV, the resolution is $\sigma(E/P) = 0.78\%$. The resolution as a function of momentum, with the estimated contribution from the momentum resolution removed, is shown in Figure 40. The resolution is 1.1% at the KAMI mean photon energy of roughly 6 GeV. Some improvement in the resolution at low energies will be possible, since in KTeV we have masked off typically 50% of the scintillation light to improve the linearity of our PMTs. For KAMI, where sub 1% linearity is not critical, we will remove these masks to increase the scintillation light output and improve the effective noise level.

In one year of running KAMI, we expect that the radiation dose in the center of the calorimeter will be approximately 60 krads. At this dose we expect to see some degradation of the calorimeter's resolution.

The radiation resistance of the CsI crystals has been tested in two ways. First, controlled tests of a small sample of crystals (~17) were performed in which doses of 0.5, 2.5 and 8.0 krads were applied evenly across the length of the crystals. There was considerable recovery from radiation damage after 30 days for doses of 0.5 and 2.5 krads. After 8 krad of exposure the resolution degraded by ~0.2%.

Second, by the end of the 1996-1997 KTeV run, the center of the CsI had been exposed to a dose of ~10 krad. The crystals were exposed to another 10 krad during the 1999 KTeV run. The overall gain in crystals that were exposed to 10 krad was observed to drop by ~25% (the radiation exposure is not uniform over the face of the CsI and is concentrated near the beam holes). The longitudinal response did not change significantly for most channels. Approximately 80 of the 3100 crystals experienced a significant change in longitudinal response. Most of these crystals were from a small number of ingots suggesting a correlation with ingot quality. No significant degradation of the resolution has been observed in these crystals or in the array as a whole.

In the seven years since KTeV purchased its CsI crystals, work has continued on radiation

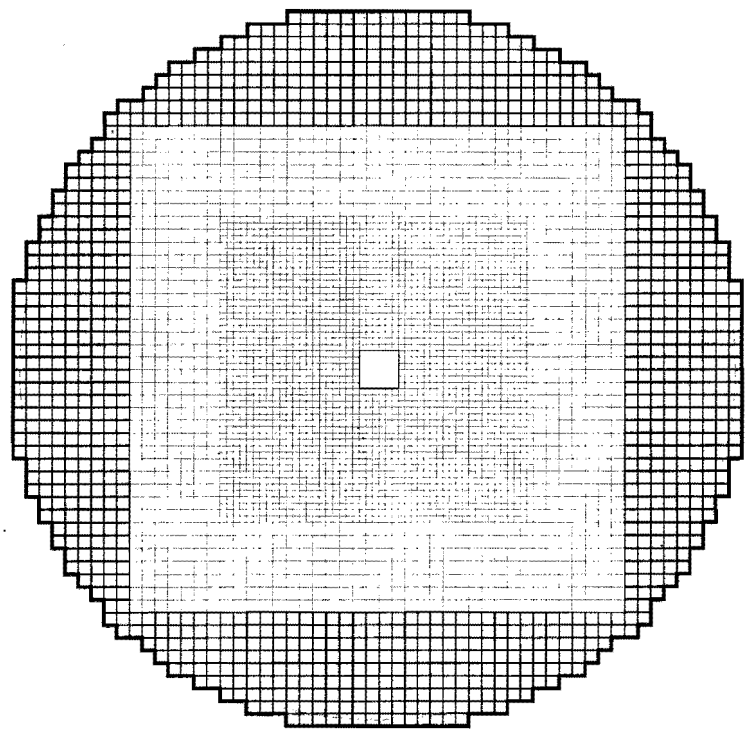

KTeV 1.9mx1.9m SQUARE
BIG=868
SMALL=2232

KAMI Dia=2.75m
BIG OLD =868
BIG EXTRA=1068
BIG TOTAL=1936
SMALL =2232

Figure 39: The KAMI CsI calorimeter.

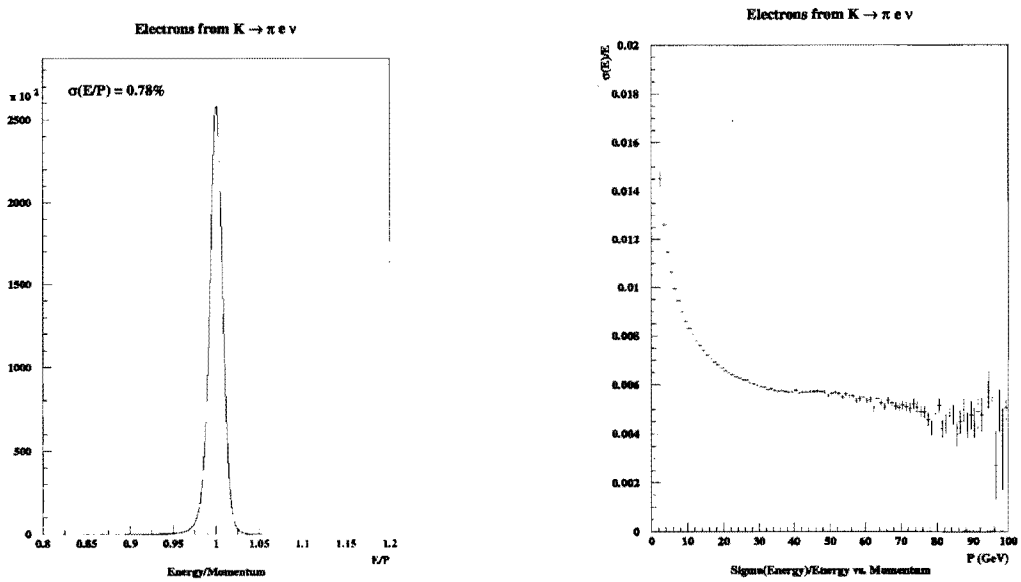

Figure 40: The E/P ratio for electrons from K_{e3} decays in the KTeV CsI calorimeter is shown on the left. The energy resolution vs. momentum for electrons from K_{e3} decays in the KTeV CsI calorimeter is shown on the right. The estimated contribution from the momentum resolution has been removed.

hardness issues. Crystals with improved radiation hardness have been produced at Kharkov in the Ukraine [110]. Radiation hardness of CsI crystals can be improved by including specific impurities in the crystals which compensate for the damage done by absorption of radiation. Sequential doses of 10 krad have been applied over time to crystals produced in this way. After a cumulative dose of 50 krad no color centers are observed and absorption bands are absent. Only a slow increase in the absorption coefficient was observed. These advancements are encouraging. Future KAMI R&D will include radiation studies of these new CsI crystals with the idea of using them around the calorimeter beam hole where the radiation dose is highest.

One of the ways in which $K_L \to 2\pi^0$ events appear as background to $K_L \to \pi^0\nu\overline{\nu}$ is for two of the photons to overlap or fuse in the calorimeter. This background is suppressed by requiring that the photon's transverse distribution of energy in the calorimeter be consistent in shape with typical electro-magnetic clusters. A shape χ^2 is formed using the measured position of the cluster as a lookup for the mean and rms of the energy in each crystal in the cluster. Typically a 7x7 array is used in the 2.5 cm crystals, and a 3x3 array is used in the 5.0 cm crystals. The efficiency of the shape χ^2 requirement from a Monte Carlo simulation of the $K_L \to 2\pi^0$ background is shown in Figure 41 as a function of the distance between photons for the case of photons in the 2.5 cm $\times$ 2.5 cm crystals. Nearby photons can be distinguished 50% of the time when they are separated by roughly the crystal's transverse dimension.

Finally, the CsI calorimeter was constructed to minimize the amount of inactive material between crystals and the size of gaps between crystals. The crystals are wrapped with one layer of 12.5 μm Aluminized-Mylar (and two overlapping layers on one face). In addition, the

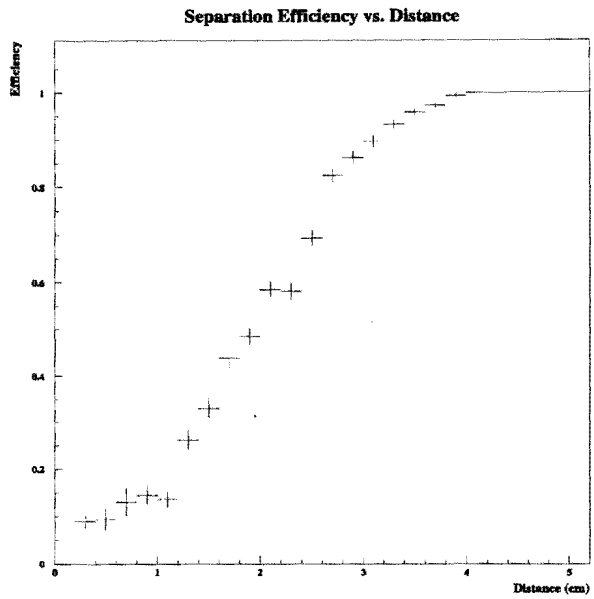

Figure 41: Monte Carlo of the efficiency of separating fused photons vs. the distance between the two photons.

wrapping was secured with a thin layer of backless transfer tape. The inactive material thus comprises only 0.22% of the array in cross-sectional area. Also, gaps between crystals were minimized by pushing horizontally on each individual row of the array. However, on lines extending radially from the beam holes, there are trajectories on which photons will only go through the mylar wrapping. The probability that a photon will lie on such a trajectory is roughly 7×10^{-6}. A more complete simulation is needed to estimate the probability that a photon will convert in the mylar, and lead to a significant energy deposition. In KTeV data itself, the inactive material and gaps between crystals has been seen in an enhancement in the number of events with low electron E/P which occur at the boundaries of crystals. In the 2.5 cm crystals, the E/P ratio is between 0.80 and 0.95 due to crystal boundaries for 9×10^{-5} of all electrons. This will not be adequate for KAMI, but there are several possible solutions which include tilting the array or stacking the crystals with a non-projective geometry. This issue is currently under study.

The front-end electronics used for the KAMI CsI calorimeter will be similar to the electronics used for the calorimeter in KTeV. However, because the KAMI beam will be debunched with no real RF structure, the digitization scheme relative to the phase of the event clock will have to be modified. This will be discussed in Section 6.8.

6.3 Photon Veto detectors

6.3.1 General Design Considerations

One of the most challenging detector issues facing KAMI is the efficient detection of all photons produced by background events along the entire vacuum decay region. Complete

hermeticity and efficient photon detection down to energies as low as a few MeV is required. Achieving the lowest possible detection threshold in the photon veto detectors reduces the background level for $K_L \to \pi^0 \nu\bar{\nu}$ and results in a cleaner measurement. The photon veto systems should also provide reasonably accurate energy and position measurements so that well measured control samples of $K_L \to 2\pi^0$, $K_L \to 3\pi^0$ and $K_L \to \pi^+\pi^-\pi^0$ decays can be used to monitor the global efficiency.

The KAMI photon veto system begins 95 m from the production target and terminates immediately in front of the CsI calorimeter, located 186 m from the target. The photon veto system consists of two Mask Antis at the upstream end of the detector, several sections of barrel vacuum veto detectors, CsI Anti detectors, and a Beam Anti detector. The Beam Anti detector uses a different technology because of its unique requirements and is discussed in Section 6.4. The layout of the photon veto system can be seen in Figure 8 and Table 6.

The distribution of photons from $K_L \to 2\pi^0$ decays that must be efficiently detected by the vacuum veto system are shown in Figure 42. Each entry in the figures corresponds to events with two photons in the CsI calorimeter that pass the nominal event selection cuts described in Section 2.6.2 and two additional photons in the vacuum veto detector. For the two photons in the veto system, the energy spectrum of the one with the higher energy and the spectrum for the lower energy photon are plotted separately. From the energy spectrum of the lower energy photon it is apparent that photons down to very low energies must be vetoed. Fortunately, there is a correlation between the energy of the two photons in the veto system. When one photon has a very low energy the other photon is likely to have a high energy. This is demonstrated in Figure 43. The events in the bottom plot have been weighted by the product of the the energy-dependent inefficiencies of the two photons in the veto system from Table 9.

A fine sampling lead/scintillator calorimeter can satisfy the KAMI background rejection requirements. The photon veto detectors will be constructed of alternating layers of 1 mm thick lead sheets and 5 mm thick scintillator tiles. 1 mm diameter wavelength shifting (WLS) fibers will be inserted into grooves in the the scintillator tiles to efficiently collect photons and transport them to photodetectors mounted outside of the vacuum tank for easy access. The fibers will be spaced at 1 cm intervals and will have a double layer of cladding to minimize losses. The end of the fiber that does not run to the photodetector will be mirrored with an aluminum vacuum evaporation process to increase the light yield. Each piece of scintillator will be wrapped in white Tyvek to maximize light collection and protect the polished surfaces from the lead. The layout of a scintillator tile is shown in Figure 44.

The cost of the photon veto system is of primary concern and a good deal of effort has gone into designing a low-cost, high light-yield device with fast time response. Significant effort has also been devoted to quantifying the photo-electron yield per MIP, the decay time and FWHM of the anode pulse distributions for various combinations of WLS fiber and scintillator. The WLS fibers that have been investigated include Kuraray blue WLS SCSF-B2, Bicron green WLS BCF-92 and Kuraray green WLS Y11. The scintillator samples include Kuraray violet SCSN-88, Bicron BC-404 and BC-400, several IHEP scintillators from extrusion, injection molding and bulk-polymerization techniques as well as injection molded scintillator from a joint Fermilab/NIU collaboration. R&D is still in progress in collaboration with the proposed CKM experiment, the IHEP-Protvino group in Russia as well as Osaka University in Japan. Various photomultiplier tubes have also been evaluated.

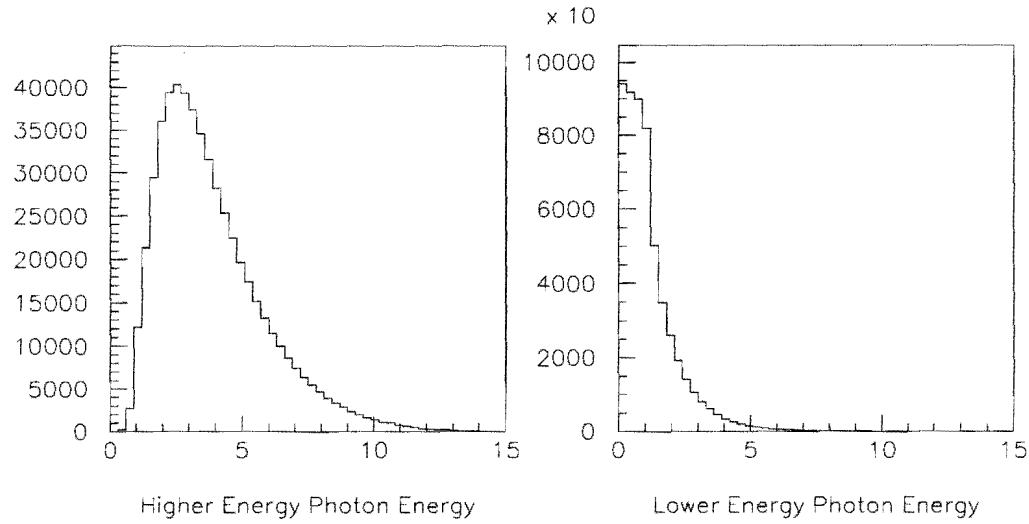

Figure 42: The energy spectra (in GeV) of the two photons in the veto system for $K_L \to 2\pi^0$ decays with two photons in the CsI. The plot on the left is the energy spectrum of the higher energy photon and the plot on the right is the spectrum for the lower energy photon.

So far, we have found several acceptable combinations of fibers and scintillator. The combination of BCF-92 WLS fiber and BC-404 scintillator is a good candidate because of the fast time response and high light yield. BCF-92 fiber combined with IHEP or BC-400 scintillator may also be acceptable. Although the Kuraray Y-11 fiber has a generally greater light yield than BCF-92 fiber, its decay time is a factor of 2 longer. The results of some of these studies are are summarized in Table 17. The scintillator tiles used in these studies were 2 mm thick, compared to the 5 mm thick tiles that have been selected by KAMI. Studies will continue on new IHEP scintillator and new Fermilab/NIU injection molded scintillator sheets.

Other variables that affect the light output include the fiber spacing, the depth of the fiber groove, and the surface finish of the groove. The light output can be boosted further by gluing the fibers into the grooves, though care must be taken to obtain a high quality glue joint. Gluing the fibers complicates the assembly process, so the gain in light yield will have to be weighed against such complications. Scintillator tiles prepared in this way can yield more than 20 photo-electrons/MeV. The choice of photomultiplier tube can also impact the light yield. In particular, green-extended photomultiplier tubes increase the light yield to nearly 30 photo-electrons/MeV. Production procedures must still be developed to obtain results of this quality in large volume.

Lead and scintillator tiles must be assembled into modules that present no cracks or dead areas to incident photons. Alternating scintillator tiles in a module will be clocked at a small angle forming module edges with a saw-tooth pattern. The saw-toothed edges from adjacent modules will interlock with one another, forming a seamless joint without cracks.

The default photodetector is a fast, high-gain photomultiplier tube, though we leave open

WLS Scintillator	Green WLS BCF-92 1 mm	Green WLS Y11(200)M 1 mm	Green WLS Y11(250)M 1 mm	Green WLS Y11(150)M 1.2 mm
IHEP(COMPASS)[a)] τ=2.8 ns	N=6.1	N=10.9	N=8.2	N=10.5
IHEP(exp G2)[a)] τ=2.7 ns	N=6.2 fwhm=8.6 ns τ=5.1 ns	N=11.2 fwhm=15.4 ns τ=11.0 ns	N=8.2	N=12.0
IHEP(CKM)[b)] τ=2.7 ns	N=6.9 fwhm=8.6 ns τ=5.6 ns	N=9.7 fwhm=15.0 ns τ=10.3 ns	N=8.2	N=11.0
IHEP(exp G3)[c)]	N=7.4 fwhm=8.0 ns τ=5.3 ns	N=11.2 fwhm=14.0 ns τ=10.6 ns		
SCSN-88 τ=2.8 ns	N=6.0 fwhm=7.8 ns τ=5.4 ns	N=8.4 fwhm=16.6 ns τ=11.1 ns	N=6.6	N=9.1
BC-400 τ=2.4 ns	N=8.6 fwhm=7.6 ns τ=4.3 ns	N=12.3 fwhm=16.2 ns τ=10.2 ns	N=10.9	N=13.7
BC-404 τ=1.8 ns	N=10.5 fwhm=7.2 ns τ=4.7 ns	N=14.3 fwhm=16.4 ns τ=11.0 ns	N=12.5	N=16.3
BC-404A τ=2.0 ns	N=8.4	N=13.3	N=10.7	N=14.6
BC-408 τ=2.1 ns	N=9.4 fwhm=8.2 ns τ=5.0 ns	N=12.7 fwhm=16.4 ns τ=11.2 ns	N=10.8	N=14.8

Table 17: Preliminary results on the comparison of different scintillating tile/WLS fiber combinations. A THORN EMI 9903KB PMT with a rubidium bialkali photocathode was used. N is the average photo-electron yield per MIP passing through a 2 mm scintillator tile (the KAMI tiles are 5 mm thick); fwhm is the full width half maximum of the output pulse; τ is the decay time constant of the output signal. a) designates injection molded tiles; b) designates tiles fabricated by extrusion; and c) designates tiles manufactured by a bulk-polymerization technique.

the possibility of reading out all of the photon veto detectors with large-area Visible Light Photon Counters (VLPC). Small area VLPCs have been used successfully as photodetectors for scintillating fiber trackers [115, 116] and will be used for the KAMI fiber tracker as well (Section 6.5.1).

The photon veto detectors will utilize the QIE technology first used in KTeV where excellent low-noise performance was achieved without deadtime. QIEs will be used for the front end readout of the photon veto detectors and the CsI calorimeter (see Section 6.8). The anode signals will be digitized at the detector to achieve the lowest possible noise performance. Each channel will also be equipped with a TDC.

6.3.2 Mask Anti detector

The active mask photon detector, called the Mask Anti (MA), is designed to reject upstream $3\pi^0$ and $2\pi^0$ decays to prevent background that can result when their reconstructed decay vertex is shifted into the decay region due to mis-paired photons. A detailed simulation of backgrounds originating from $K_L \to 3\pi^0$ decays indicates the need for two stages of detector, as shown in Figure 8. Each Mask Anti detector is a 27 radiation length deep sampling calorimeter, consisting of alternating layers of 1 mm thick lead sheets and 5 mm thick scintillator sheets. There is a small precision beam hole to allow the neutral kaon beam to enter the long vacuum decay region. The Mask Anti detectors for KAMI will be very similar to the one currently in use by KTeV except for its finer sampling ratio.

6.3.3 Vacuum Veto Detector

The vacuum veto is a fine sampling calorimeter consisting of 1 mm thick lead sheets and 5 mm thick plastic scintillator. The radial dimension of a module will be about 50 cm. The lead and scintillator sheets will be mounted at a 30° angle with respect to the beam axis. The tilted modules improve the detection efficiency for low energy photons by reducing the path length through lead, minimizing sampling losses. This will help in achieving a lower detection threshold which has been shown to reduce background. The vacuum veto modules are located inside the vacuum tank to minimize any dead material traversed by the photons before encountering active detector elements. The first layer of the photon veto modules accessible to incident photons will be scintillator in order to minimize backscattering of low energy photons in the lead.

Two mechanical designs have been considered for the vacuum veto modules. The combination of these two designs provides hermetic coverage and still allows for efficient pumping speed to obtain a good vacuum in the central decay volume. Figure 45 and Figure 46 show the first hermetic barrel design with a 90 layer lead-scintillator sandwich module (about 26.7 X_0). The lead and scintillator sheets are tilted at a 30° angle with respect to the beam direction, as described above. Each vacuum veto section has 12 ϕ sectors and each sector will be divided into 3 readout segments longitudinally (every 30 layers).

The second option consists of trapezoidal lead/scintillator modules with maximum overlap between modules for hermetic coverage, but with sufficient gaps to allow efficient vacuum pumping speed. None of the gaps line up with the trajectory of incident photons. Figure 47 shows the current design for a trapezoidal module. Note that the lead and scintillator sheets

are again mounted at a 30° angle with respect to the beam axis. Figure 48 shows a front view of 8 trapezoidal modules assembled into a vacuum veto section. Figure 49 is a 3-dimensional view of a fully assembled trapezoidal vacuum veto section. The trapezoidal modules can be mounted on guide rails inside the vacuum vessel. This design could be particularly useful in the vicinity of the analysis magnet or between the fiber tracking planes for easy installation and flexibility.

6.3.4 CsI Anti detector

The gap between the vacuum window and the CsI calorimeter must be filled by additional photon veto detectors in order to plug any possible cracks which photons might pass through. These are known as the CsI Anti detectors. There are two stages of CsI Anti; a small detector inside of the blockhouse that houses the CsI, and a large one just upstream of the blockhouse. Due to the limited space available inside of the blockhouse, only a 20 cm ring outside of the CsI can be covered. This is not large enough to detect all of the photons that escape through the end of the vacuum tank. Therefore, another veto detector with a larger outer dimension must be installed between the vacuum window and the blockhouse. The CsI Anti for KAMI is very similar to the one currently in use by KTeV except for its finer sampling ratio and larger volume. The KAMI CsI Anti consists of 1 mm thick lead sheets and 5 mm thick plastic scintillators built into modules that are 25 cm (13 X_0) deep due to the limited available space.

6.3.5 Expected Performance

The inefficiency of a lead/scintillator sampling calorimeter at low energy is limited by sampling effects that occur when a significant fraction of the deposited energy is absorbed in the lead, leaving the observable energy below the detection threshold. Sampling losses can be simulated using standard electromagnetic interaction packages to an accuracy of a few percent. The effect of sampling losses increases for photons with large angles of incidence due to the longer path length through the lead sheets. This effect is mitigated by the 30° angle tilt of the KAMI vacuum veto modules. Simulations of sampling losses in the KAMI photon veto detectors have been performed (see Appendix C) and are reflected in the inefficiencies used to study backgrounds. All of the background studies described in this document are performed with a 10 MeV threshold on the energy of the incident photon, though our studies of sampling losses and scintillator light yield indicate we can likely go lower.

At higher energy, photo-nuclear absorption plays a dominant role. In the latter case, it is possible for a photon to experience a photo-nuclear absorption interaction before it begins to shower. If all of the secondary products in the interaction are neutrons, the interaction may escape detection.

The inefficiency due to the photo-nuclear absorption was first studied in the photon energy region between 185 to 505 MeV at the INS-KEK tagged photon test beam facility with quite encouraging results for CsI crystals and lead/scintillator sampling calorimeters [66]. A collaboration of physicists from KAMI and KEK has performed a more extensive set of inefficiency measurements for various lead/scintillator sampling calorimeters and CsI crystals at the same INS-KEK facility in 1998. Photons in the energy range between 100 to 1000 MeV were studied. Electrons were passed through a ~300 μm thick aluminum foil

emitting radiative photons that illuminate the test device. The momentum of the electron after the photon emission was measured by a spectrometer magnet and an array of scintillation counters. Inherent in this technique is a false-tag probability of ~1% that results from scattering in the foil and multiple bremsstrahlung. The rate of false photon tags required a trigger with coincident activity in the neutron counters that surround the test sample. Thus, the inefficiency measurements from the INS test rely on the assumption that photo-nuclear interactions in the relevant energy range emit a sufficient multiplicity of slow neutrons. This subject has been discussed in great detail in [111]. The number of evaporated neutrons is ~1 or 2 for energies of a few MeV and about 10 for photon energies around 140 MeV. While the detection efficiency for single neutrons in photon veto counters is modest, the detection probability for multiple neutrons is high.

An upper limit can be estimated for the inefficiency which results in the event of single neutron emission from a photo-nuclear interaction from photo-production cross section measurements. The cross section for $\gamma + n \rightarrow 0$ charged particles has been measured to be 11 μb at 7.5 GeV. Scaling to a lead nucleus, including the effects of shadowing which go as $A^{2/3}$, the cross section is ~420 μb. In the worst-case, the 0 charged particle final state is composed of 1 neutron, although most of these final states will consist of many neutral hadrons. The pair production cross section is $\sim$ 50 b, so the relative probability of single neutron emission to pair production is 420 μb/50 b. Hence, a conservative upper limit on the photo-nuclear inefficiency in the event of single neutron emission that is not subsequently detected is 8×10^{-6}. This limit is quite favorable, though it would be useful to have data at lower photon energies.

Figure 50 shows the detection inefficiency due to photo-nuclear interactions as a function of the incident photon energy for lead/scintillator sampling detectors and CsI crystals, respectively, as measured during the INS test. The results clearly demonstrate that inefficiency effects from photo-nuclear interactions are well under control for both CsI and lead/scintillator sampling detectors at medium energies.

The inefficiency for photons above 1 GeV is dominated by photo-nuclear interactions and photo-production of hadrons off nucleons. Based on the INS beam test measurements, the photo-nuclear inefficiency at 1 GeV is 10^{-6} or better. All of the simulations for this proposal use photon inefficiency profiles that plateau at 1.0×10^{-6} for energies >1 GeV.

The CKM collaboration has investigated the photo-production of hadrons off nucleons for energies exceeding 800 MeV. A number of processes have been calculated, including $\gamma + Pb \rightarrow \rho^0 \rightarrow \pi^+\pi^-$, $\gamma + Pb \rightarrow n\pi^+$, $\gamma + Pb \rightarrow \Lambda K^0$, $\gamma + Pb \rightarrow \phi \rightarrow K^+K^-$, and $\gamma + Pb \rightarrow \phi \rightarrow K_L K_S$. The cross sections for these processes range from a few μb to a few mb and correspond to an inefficiency of about 4×10^{-5} if the hadronic final states go undetected [117]. KAMI will have good efficiency for detecting these final states due to the large hadronic cross section of the lead/scintillator detector, high light output and low detection threshold.

While it seems likely that inefficiencies of 10^{-6} can be attained above 1 GeV, this is an area that requires more work. A new beam test is planned to address some of these issues. The photon veto inefficiency for photon energies between 1.5 GeV and 3.5 GeV will be measured for lead/scintillator sampling detectors and CsI crystals. The beam test will take place at the Spring 8 photon factory in Japan beginning in April, 2001.

The effects of operating with a lower detection threshold have been studied for fine

sampling lead/scintillator calorimeters using 1, 5 and 10 MeV thresholds. Figure 51 shows the inefficiency as a function of photon energy for all three thresholds. The inefficiencies are the sum of simulated sampling losses and measured photo-nuclear inefficiencies. The virtues of setting the lowest possible detection threshold are apparent in Figure 52 where the inefficiency curves from Figure 51 have been used to simulate the background level from $K_L \to 2\pi^0$ decays using a simplified detector model [112]. It is clear that a lower detection threshold results in a cleaner measurement, with the background decreasing almost linearly with detection threshold.

Instrumental losses can also contribute to inefficiency, so every effort must be made to design a robust, redundant and well monitored photon veto system. The readout of each veto module will segmented, allowing the fibers from alternating layers of scintillator tiles to be readout by separate photomultiplier tubes. The signal from each tube will be digitized by both a flash ADC (QIE) and a TDC. For large energy deposits the two tubes should register similar readings. This cross-check provides a good indication that the readout chain of the module is healthy. An additional diagnostic will be provided by a laser flasher system similar to the one that was used to monitor the KTeV CsI calorimeter. The laser will operate at approximately 1 Hz and will be used to monitor tube gain and system stability.

Experience in KTeV has shown that high-statistics kinematic distributions for the common kaon decay modes, like K_{e3} and $K_{\pi 3}$, are exquisitely sensitive to a wide variety of physics and detector performance, including the precise locations of detectors and apertures, the exact energy scale of the CsI calorimeter, and details of how processes like bremsstrahlung and multiple scattering are modeled. In the same spirit, we plan to use the copious $K_L \to \pi^0\pi^0\pi^0$ decay mode in KAMI to monitor the photon vetoes and to measure their inefficiency. This will be done by collecting very large samples of both six- and five-cluster all-neutral events. Both of these samples consist almost entirely of $K_L \to \pi^0\pi^0\pi^0$ decays. The five-cluster events we collect will have lost a photon due to intrinsic detector inefficiency, reconstruction inefficiency, or two-cluster fusions. All these phenomena must be measured and monitored in order to determine the $K_L \to \pi^0\pi^0$ background to the $K_L \to \pi^0\nu\bar{\nu}$ signal. We will compare the measured five-photon distributions, normalized to the fully-reconstructed six-photon distributions, in all possible variables, including photon locations, energies, and cluster shapes. Although measurement uncertainties make it impossible to know where the missing photon in a five-cluster event should have been on an event-by-event basis, with a reasonable knowledge of the resolution of the KAMI detectors, we will be able to accurately predict what the five-cluster distributions should look like for a given inefficiency assumption. With high statistics, the distributions will be sensitive to variations in the inefficiency curves for the various detectors, so that we will be able to determine the inefficiency levels by tuning the inefficiency curves in the Monte Carlo simulation until the predicted level and shape of the five-photon distributions matches those seen in the KAMI data.

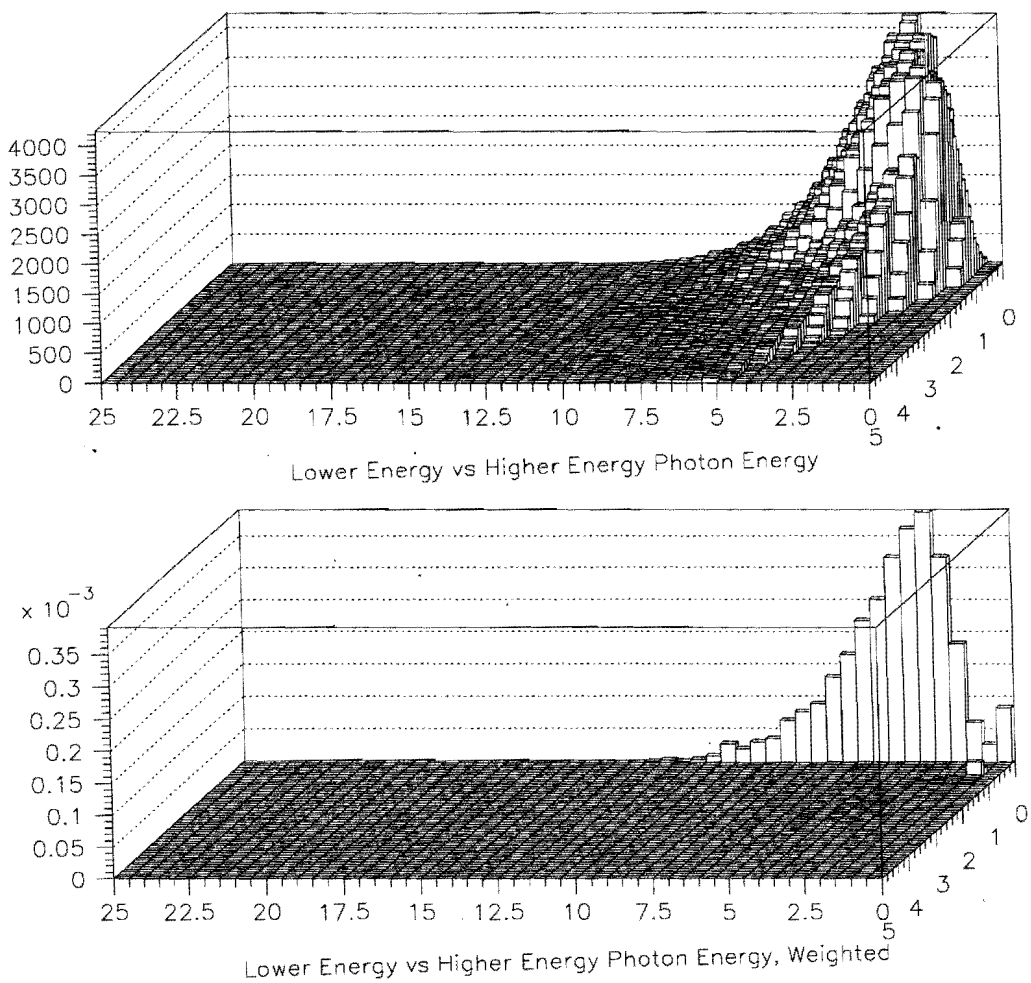

Figure 43: The correlation between the energies (in GeV) of the two photons in the veto system for $K_L \to 2\pi^0$ decays with two photons in the CsI. The events in the bottom plot have been weighted by the product of the inefficiencies of the two photons from Table 9.

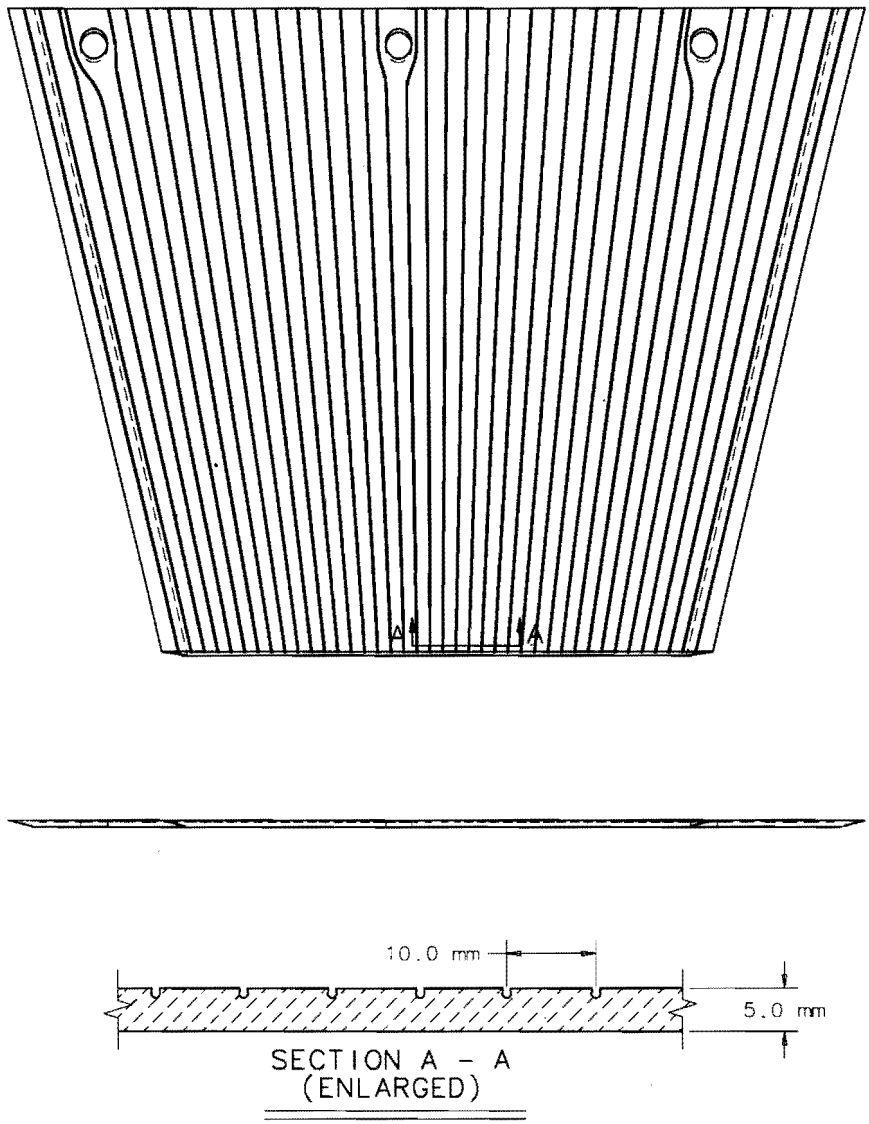

Figure 44: Layout of a scintillator tile with fiber grooves for KAMI.

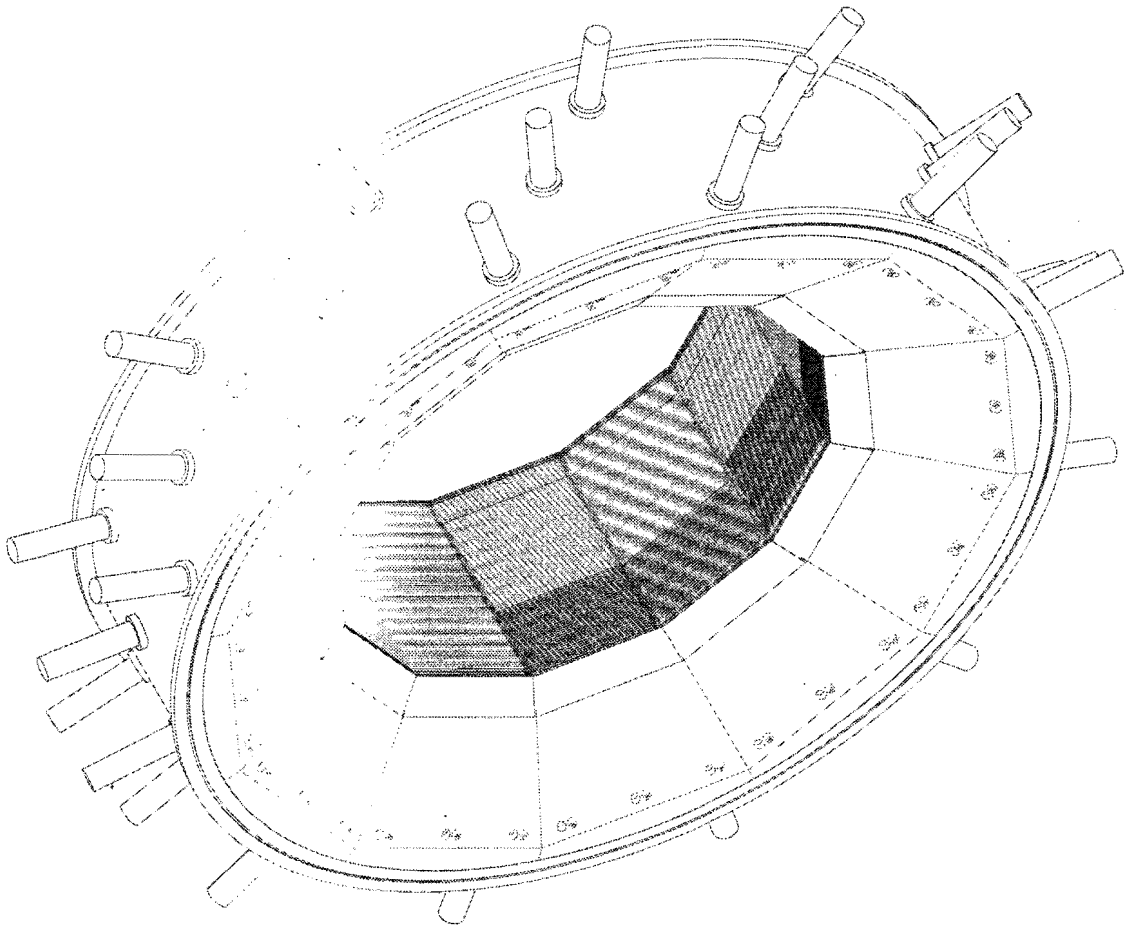

Figure 45: 3D illustration of a 90-layer lead/scintillator hermetic vacuum photon veto barrel section.

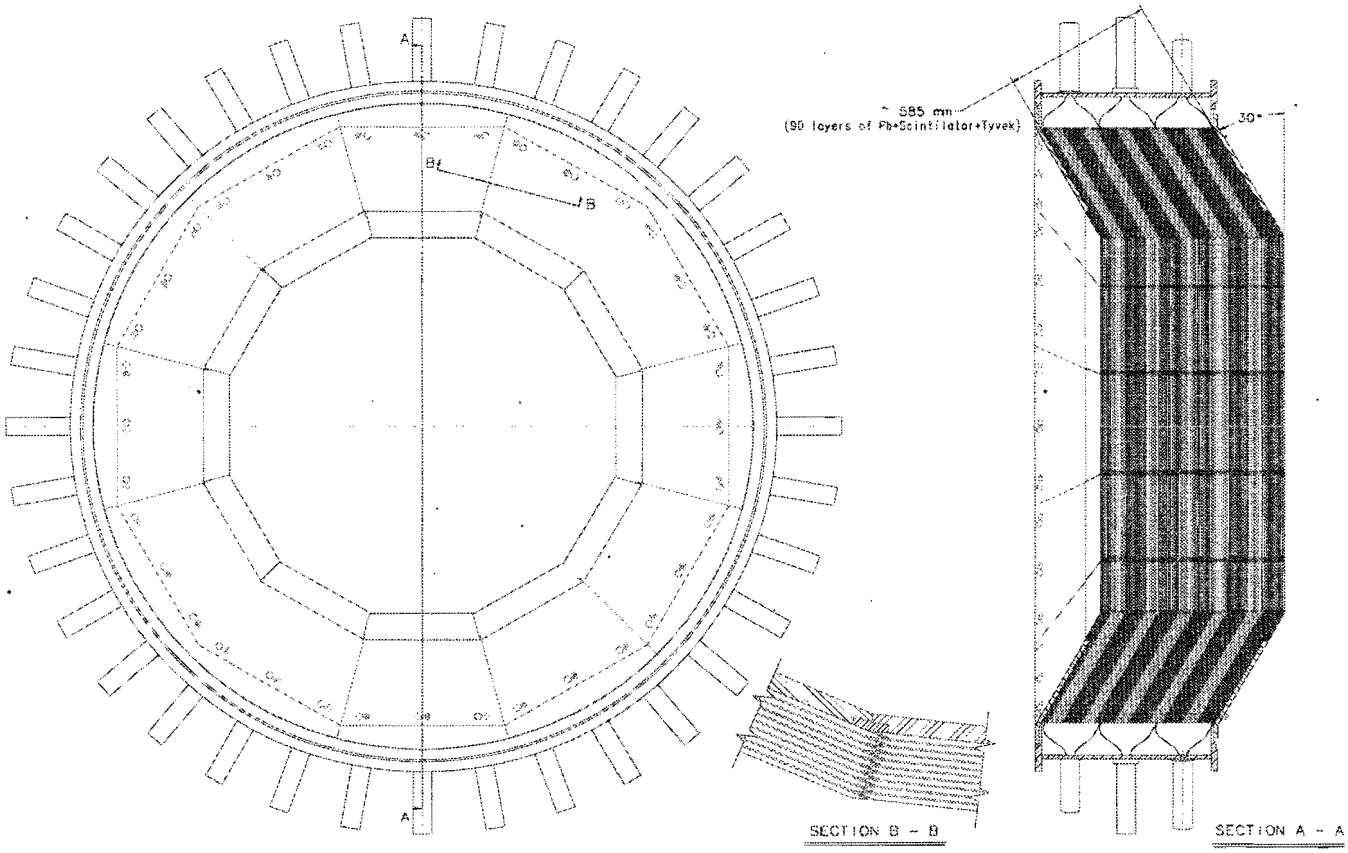

Figure 46: The front view and cross section of a 90-layer lead/scintillator vacuum photon veto design.

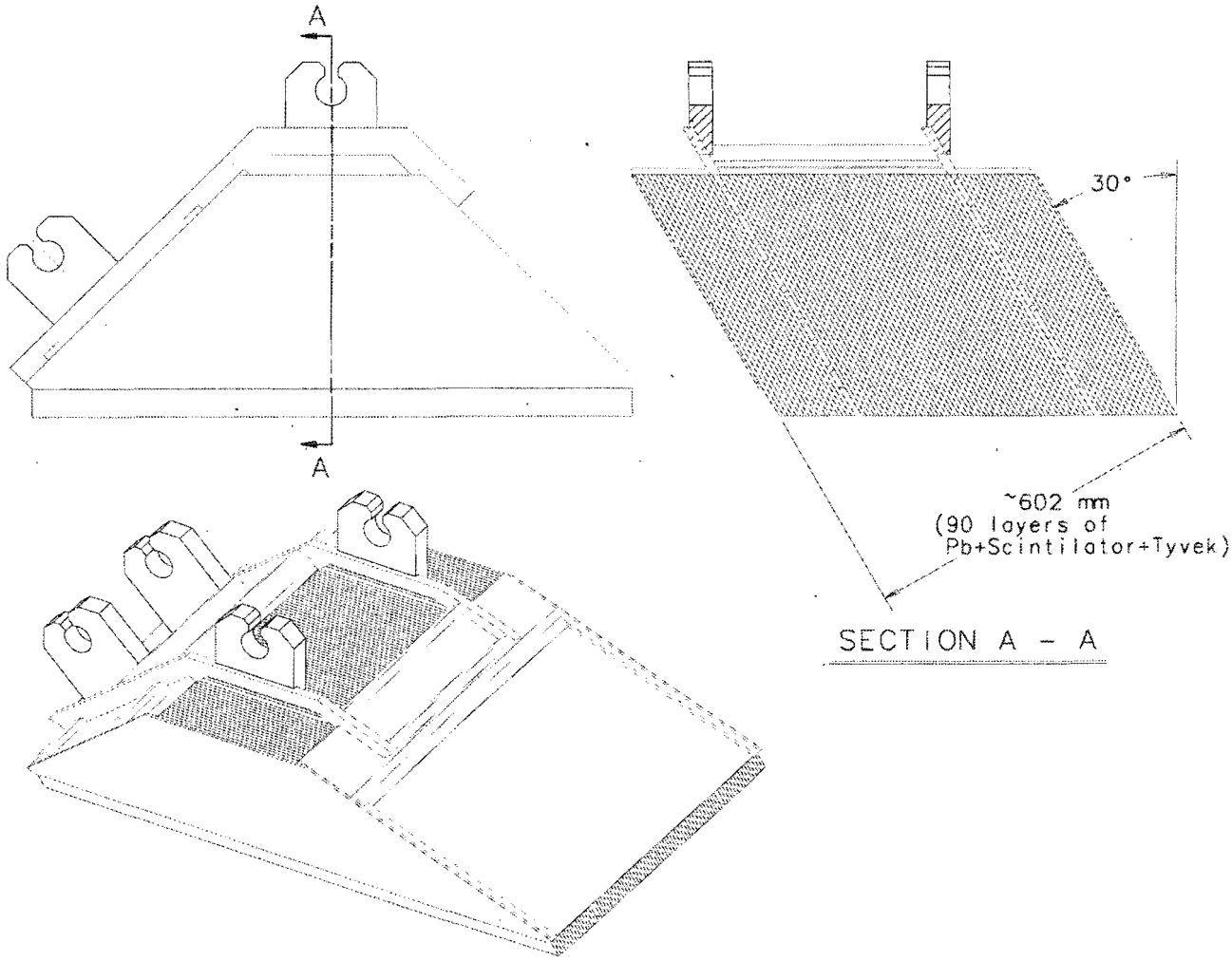

Figure 47: The current design layout of a trapezoidal vacuum veto module.

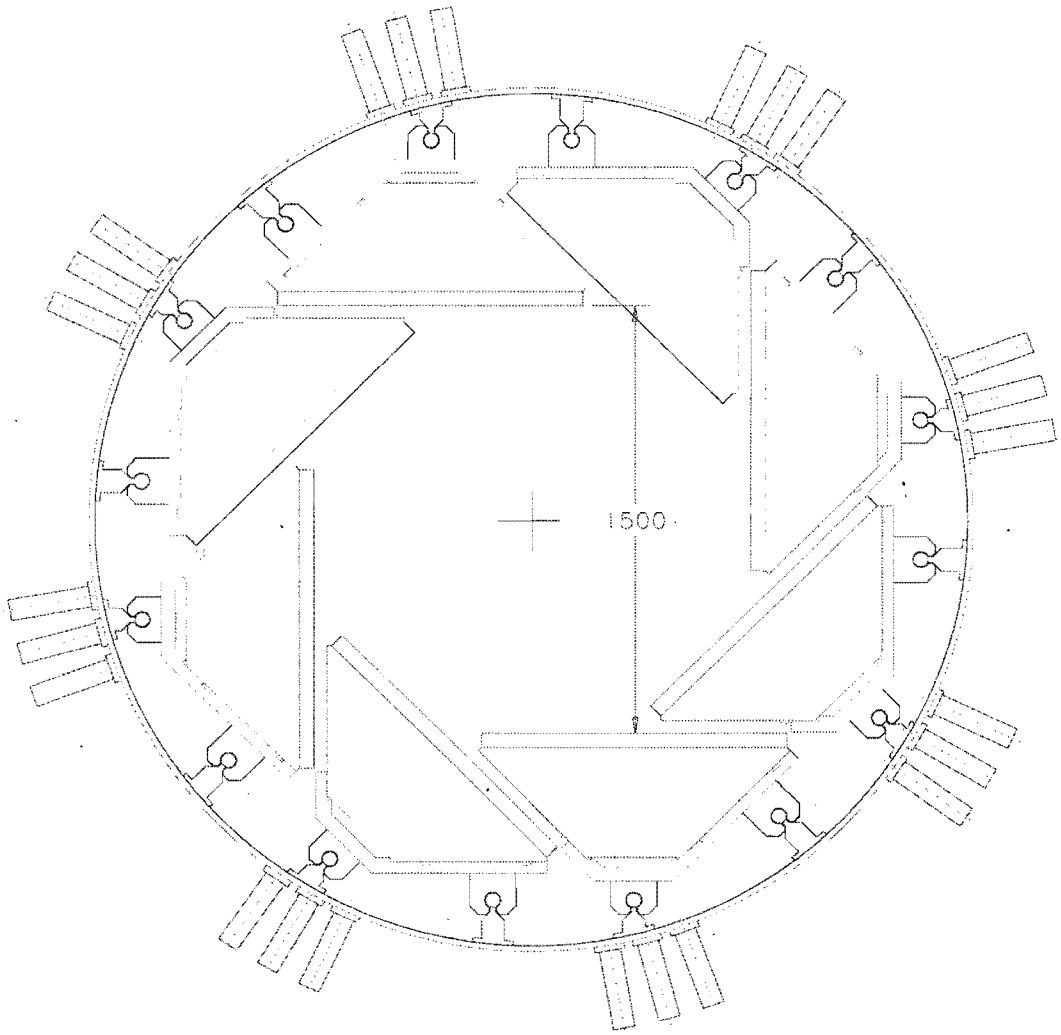

Figure 48: Plan view of 8 trapezoidal modules assembled into a vacuum veto section. The gaps between the modules allow for efficient vacuum pumping, but do not line up with incident photon trajectories.

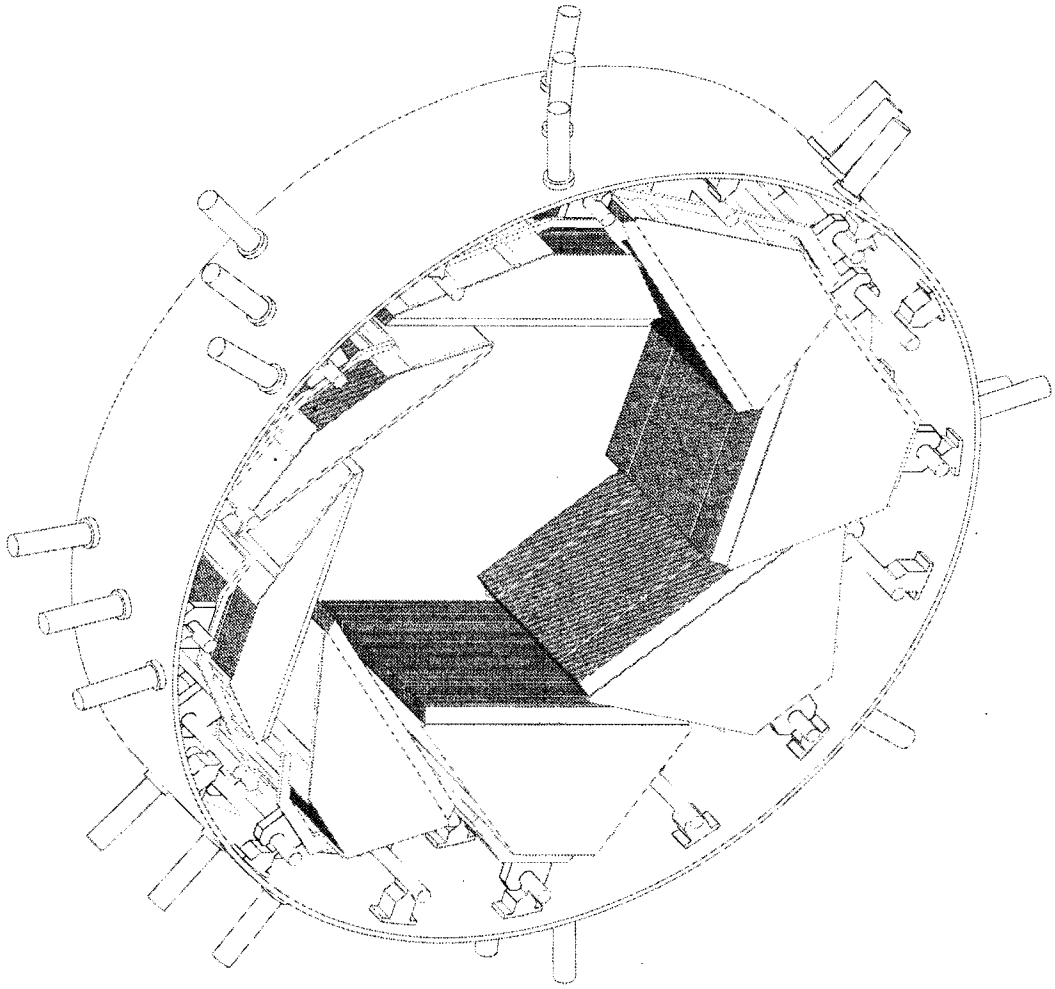

Figure 49: 3D illustration of an fully assembled trapezoidal vacuum veto section.

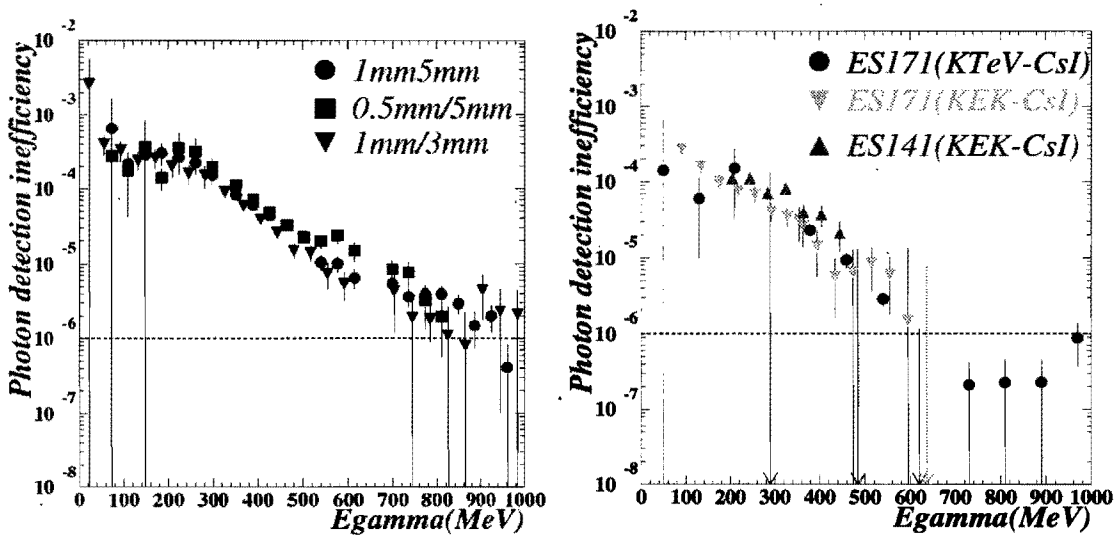

Figure 50: The measured photo-nuclear inefficiencies of several lead/scintillator sampling detectors (left) and pure CsI (right). KAMI will use a lead/scintillator detector with 1 mm thick lead sheets and 5 mm thick scintillator tiles.

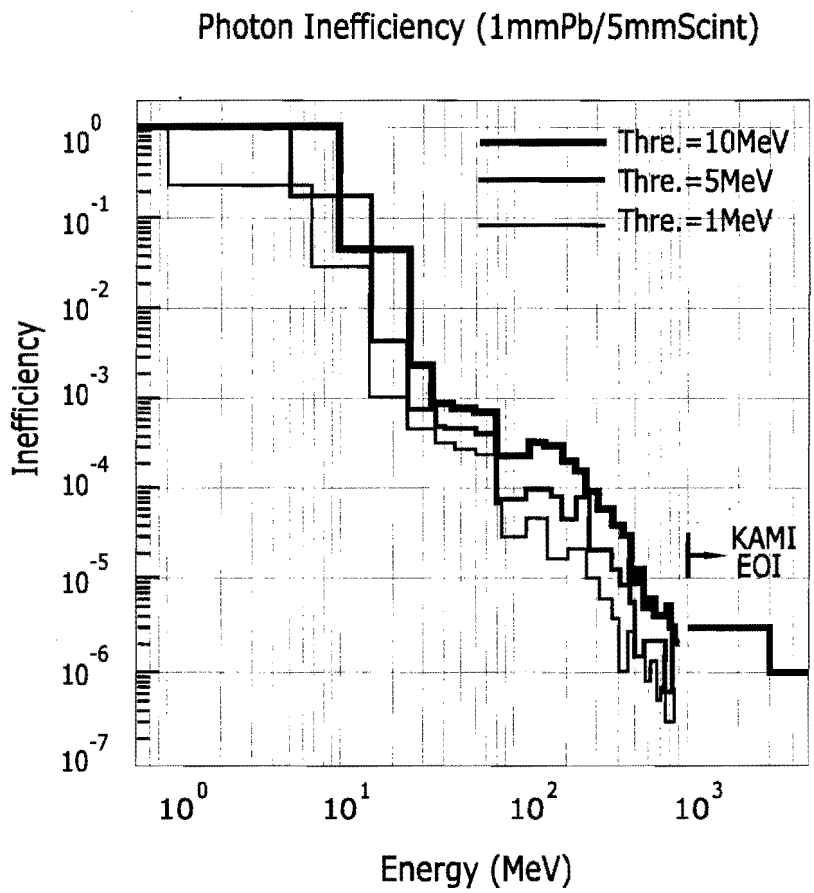

Figure 51: The detection inefficiency due to sampling fluctuations and photo-nuclear interactions as a function of the incident photon energy for fine sampling lead/scintillator calorimeters using detection thresholds of 1, 5 and 10 MeV. The inefficiencies are the sum of simulated sampling losses and measured photo-nuclear inefficiencies.

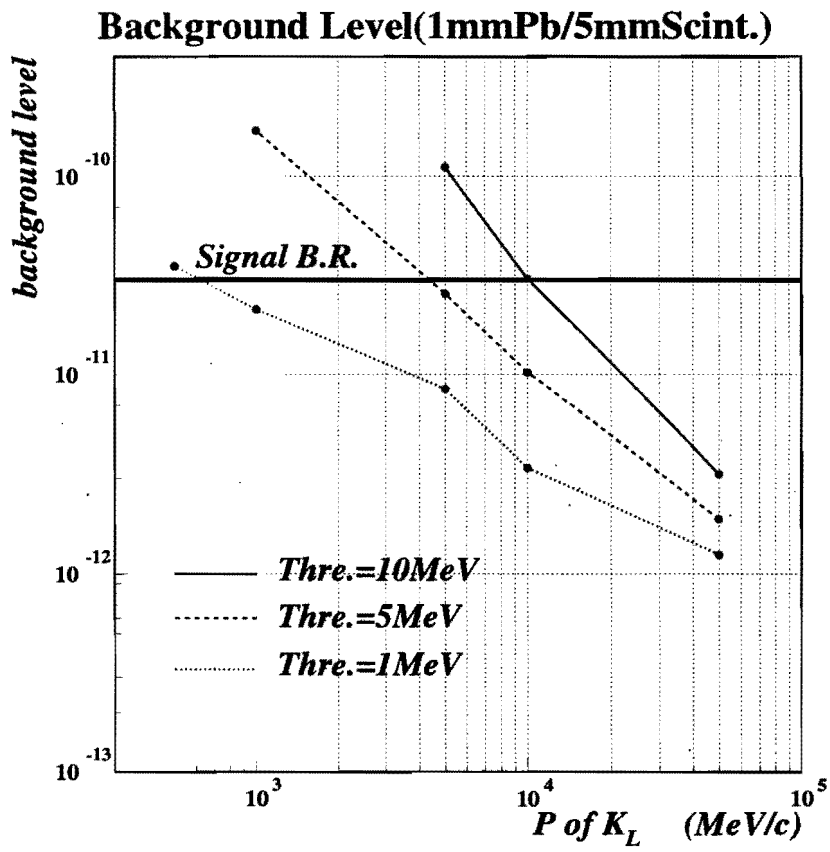

Figure 52: Illustration of the $K_L \to 2\pi^0$ background as a function of the K_L momentum for detection thresholds of 1, 5 and 10 MeV in fine sampling lead/scintillator calorimeters.

6.4 Beam Anti System

One of the critical requirements of the KAMI experiment is to find and veto events which satisfy the $K_L \rightarrow \pi^0\nu\bar{\nu}$ trigger requirements but which have "extra" photons which pass through the 15 cm × 15 cm beam hole in the CsI. Several different neutral kaon modes can generate backgrounds to the $K_L \rightarrow \pi^0\nu\bar{\nu}$ mode if photons from these decays pass through the CsI beam hole and are undetected. The most serious of these is the $K_L \rightarrow \pi^0\pi^0$ mode. A set of three beam anti stations BA1, BA2 and BA3 shown in Fig. 53 have been incorporated into the KAMI spectrometer to deal with these backgrounds.

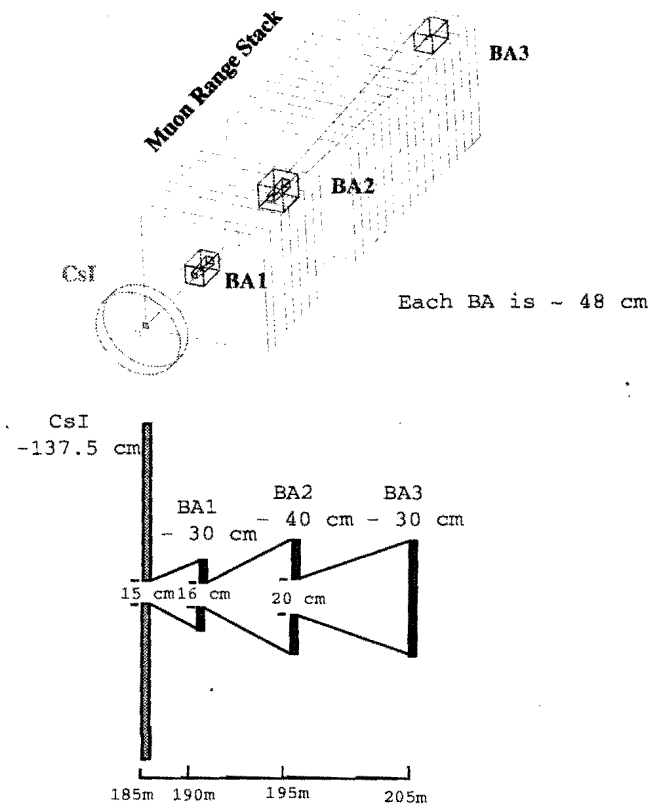

Figure 53: The beam anti configuration

The dimensions and positions of the three BA stations are given in Table 18.

Beam Region Veto	Size	Beam Hole	Position
BA1	$\pm 30cm$	$\pm 8cm$	190 m
BA2	$\pm 40cm$	$\pm 10cm$	195 m
BA3	$\pm 30cm$	-	205 m

Table 18: KAMI Beam Region Veto Configuration

The most difficult operating conditions are experienced in the BA3 counter since this station intercepts the neutral beam. Using data from the 2000 KAMI beam test (see Ap-

pendix I), the neutron flux produced by 3×10^{13} 120 GeV/c protons per spill second with a 15 mrad targeting angle is ~470 MHz. At the nominal neutral beam rate, every photon incident on BA3 will be accompanied by an average of four neutrons, 1.2 of which on average will shower in the 0.9 absorption length BA3 during any 10 ns time window (the design time resolution of BA3). Approximately 1.3% of all $K_L \rightarrow \pi^0\pi^0$ decays between 100 and 185 meters deposit a photon in the neutral beam area of BA3. Overall, we expect that 37% of the K_L decays between z=100m and BA3 will produce a decay product striking at least one of the BA stations.

The z position of BA3 has been chosen to be 205 m downstream of the K_L production target, a compromise between the objective of allowing as many photons as possible from the $K_L \rightarrow \pi^0\pi^0$ decays to separate from the neutral beam, thereby showering in BA3 outside the neutral beam region and limiting the extra K_L decays that take place between the CsI and BA3. Positioned at 205 m, 0.5% of the photons from various background modes that pass through the hole in the CsI are inside the neutral beam region at BA3. An additional 13.4% of K_L decays take place between the CsI and BA3.

At present, the baseline design of the Beam Anti uses $NaBi(W0_4)_2$ crystals [113]. This material has the properties given in Table 19. The material is quite yellow, only reaching 100% transmission at 470 nm but has good radiation damage properties and is a Cerenkov radiator, essential features for operation in the high rate environment of the BA3 neutral beam region.

Property	
Radiation Length	0.98 cm
Moliere Radius	1.77 cm
Absorption Length	22.3 cm
Radiation Hardness	10 Mrad/yr [113]
Density	7.57 gm/cm^3

Table 19: $NaBi(WO_4)_2$ Properties

The ability to distinguish a photon shower in the presence of an average 1.2 neutron showers per event (with energies distributed according to observations of the neutron beam obtained during the KAMI beam test) has been studied with a GEANT simulation of a BA3 detector that has the transverse and longitudinal segmentation ($2\ cm \times 2\ cm \times 2\ cm$ $NaBi(W0_4)_2$ detector elements in ten longitudinal layers) shown in Fig. 54. The fine segmentation is necessary to provide maximum discrimination between a photon shower and coincident neutron showers. It has been kept thin (overall approximately 0.9 absorption lengths) to keep the number of the interacting neutrons to a minimum. The transverse and longitudinal segmentations of BA1 and BA2 are similar. Hodoscopic configurations of $NaBi(W0_4)_2$ are also being considered.

As indicated in Fig. 54, a Hammamatsu R7400U-06 series PMT with a quartz window is the present choice for a photomultiplier for the BA's. This PMT is fast, with the signals comfortably contained within a 5 ns window. In addition, there is little scintillation light from the quartz window. The quartz window is sufficiently radiation resistant with essentially

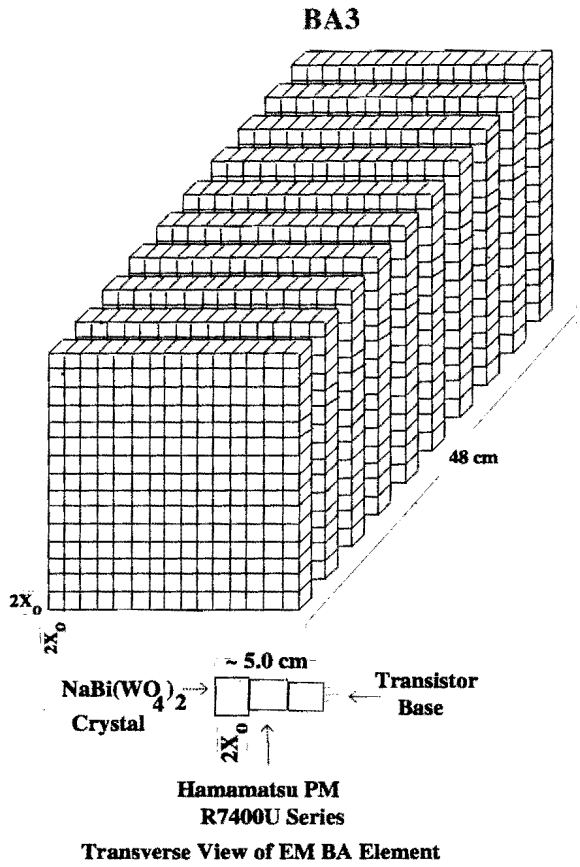

Figure 54: Preliminary configuration of BA3

no loss of transmission in the region of transmission of the $NaBi(W0_4)_2$ ($\geq$ 470nm) up to 44 megaRoentgen exposure to Co^{60} photons [114]. Exposure to 1.4×10^{14} 14 MeV neutrons per photosurface (as compared to the 3.4×10^{13} neutrons with the KAMI neutron beam energy distribution that pass through each photo surface of the BA3 tubes per year in the beam region) produced no discernible loss of transmission.

GEANT calculations indicate that the average number of Cerenkov photons generated by the neutron beam flux is 50/cm^3 in the visible region above 470 nm in a 10 ns time window (arising from the 1.2 neutron showers per 10 ns time interval). Using reasonable assumptions of an efficiency of 10% for transfer of these Cerenkov photons from the 8 cm^3 BA segments to the PMT, a PMT quantum efficiency of 10% and a measured gain of 3×10^5 for the Hammamatsu tube operated at 600 V, this results in an average anode current of approximately 20 μA.

The dynamic range required of the PMT to handle the range of energies of background photons (0.25-50 GeV) expected in the BA in KAMI is approximately 200, within the specifications of the tube. A 0.5 GeV photon will produce on average approximately 5000 Cerenkov photons in any 8 cm^3 segment of the BA (with approximately 500 Cerenkov photons in the satellite segments). With our assumptions of quantum efficiency, capture efficiency of Cerenkov photons, and using the measured gain of the Hammamatsu tube, a signal of approximately 2.5 pC (10 counts in a 0.25pC per count ADC) is produced, with the satellite segments producing 0.5 pC.

Finally, the maximum signals generated by either neutron or photons showers has been investigated to check for possible tube saturation. Using the GEANT calculations, we find that the largest signals are due to photon showers and generate less than 25 pC of charge at our nominal 3×10^5 gain in a 10 ns window. This corresponds to a maximum instantaneous current of 0.4 mA.

We show in Fig. 55 a plot of the photon inefficiency vs. photon energy in the neutral beam region of the proposed BA3 as estimated from GEANT calculations and from data taken during the 2000 KAMI beam tests. The inefficiency in this case is defined as the failure to identify an incident photon in BA3 in the presence of the anticipated flux of interacting neutrons.

The BA3 inefficiency curve for the neutron beam region is generated by a set of cuts designed to identify photons in the presence of a neutron interaction. These cuts are based on the total energy deposited in the BA, the transverse and longitudinal shower shapes and the position of the cluster. An average of 1.2 showering neutrons in a 10 ns time window, distributed according to Poisson statistics is the assumed background from which a photon is to be distinguished. These neutron and photon probabilities are determined from the energy and longitudinal development of the energy deposits in BA3. It is estimated that 80% of the pure neutron events are retained after applying the probability to eliminate photons. The usable $K_L \to \pi^0 \nu\bar{\nu}$ signal events will, of course, be included in the events which have either no activity or only neutron showers in the BA. The results of the BA3 inefficiency studies in the region of the detector shadowed by the neutron beam are shown in Table 20.

Similar inefficiency vs. photon energy cuts are shown in Fig. 55 for the BA regions outside the neutral beam region. In this case, the retention of signal is much greater since there are much lower neutron backgrounds outside the neutral beam region of BA3 and in BA1 and BA2 generally. Inefficiencies similar to those of the CsI are used for the BA outer

Energy Low-High	BA3 Inefficiency
0.000 - 0.100	6.0×10^{-1}
0.100 - 0.500	6.0×10^{-1}
0.500 - 1.000	3.0×10^{-1}
1.000 - 2.000	2.0×10^{-1}
2.000 - 4.000	1.4×10^{-1}
4.000 - 8.000	1.0×10^{-1}
8.000 - 16.000	3.0×10^{-2}
16.000 - 32.000	9.0×10^{-3}
32.000 - 64.000	7.0×10^{-5}
64.000 - infinite	7.0×10^{-5}

Table 20: Photon inefficiencies from a GEANT simulation of the BA3 detector. The inefficiencies are for the portion of the BA3 detector that is shadowed by the neutron beam.

inefficiency curve of Fig. 55.

To indicate the necessary rejection required of BA3, we show in Fig. 56 the photon energy spectrum due to $K_L \to \pi^0\pi^0$ in the inner BA after the two photon CsI trigger and the other veto inefficiencies (photon veto, mask anti, and CsI inner region) have been employed. We find that in a year of operation approximately 37,000 events are still left that would form a background to the experiment if the BA veto was not present. This is to be compared to a total background of approximately 8 events after applying photon veto, mask anti and CsI vetoes to events in which no photon is in the BA region.

The BA events as shown in Fig. 56 are mainly events containing a high energy photon above 20 GeV and a second photon that goes elsewhere in the KAMI detector. In this region of the energy spectrum, the average inefficiency of 10^{-4} required for suppression of background is relatively easy to achieve since a high energy photon shower is quite distinguishable from neutrons with the energy spectrum of the KAMI beam. It is still important to suppress the low energy part of the spectrum where the discrimination between photon and neutrons showers are most difficult. Using the BA inefficiencies obtained from the GEANT study for BA3 and the photon veto inefficiencies obtained from the KEK tests for BA1 and BA2, we obtain the suppression of the BA spectrum shown as the lower curve in Fig. 56. With these inefficiencies, the BA will contribute approximately 13 events (out of 19 total background events) to the background in the $K_L \to \pi^0\nu\bar{\nu}$ signal region.

6.5 Charged Particle Spectrometer

KAMI has proposed a rich and diverse physics program which requires a charged spectrometer for detection of charged mode decays. A charged spectrometer is also required to collect data necessary to monitor the performance of the detector and to accurately calibrate the CsI calorimeter. The KAMI charged particle spectrometer consists of a wide-gap spectrometer magnet and five tracking stations consisting of scintillating fiber planes. The spectrometer is described in detail below.

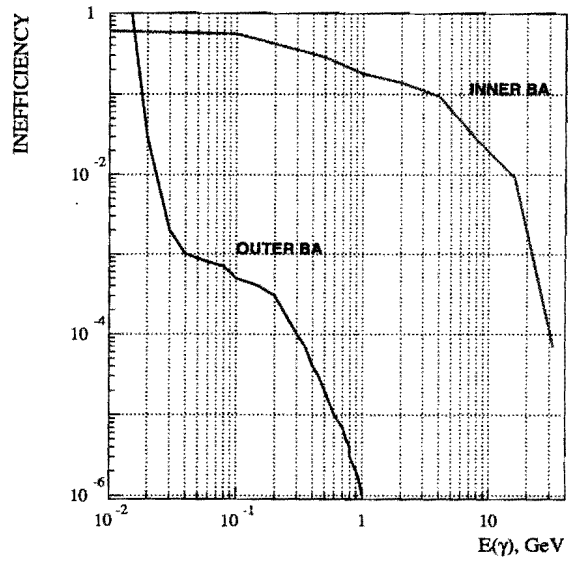

Figure 55: Estimated BA inefficiencies as a function of photon energy outside and inside the neutral beam region for various cuts discussed in the text.

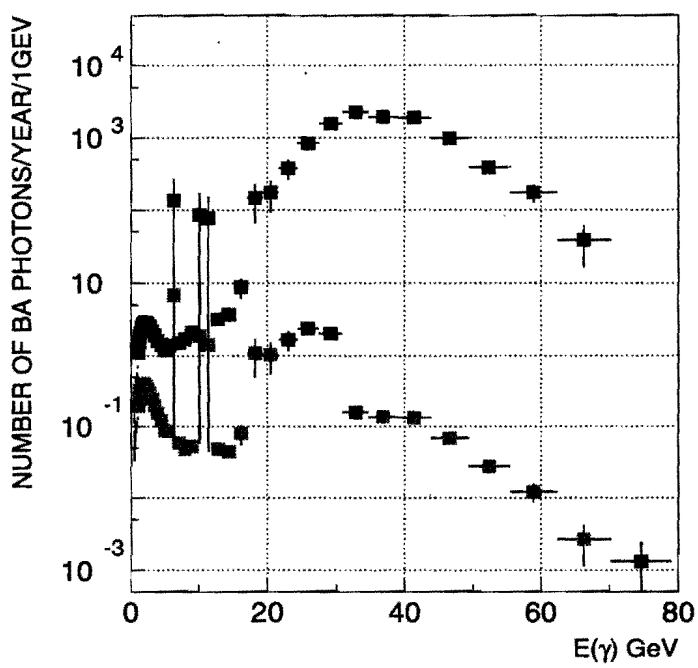

Figure 56: Upper curve: expected photon energy spectrum per year due to $K_L \rightarrow \pi^0\pi^0$ background in the BA system after application of all vetoes *except* the BA itself; lower curve the residual energy spectrum per year that survives the BA veto due to BA inefficiencies.

6.5.1 Scintillating fiber tracker

Great progress has been made by the D0 collaboration at Fermilab in developing scintillating fiber technology with Visible Light Photon Counter (VLPC) readout [115]. A scintillating fiber detector with an early version of the VLPC technology was successfully implemented by the E835 collaboration at Fermilab [116]. KAMI intends to incorporate the techniques and advances of these two groups to build its own scintillating fiber tracker.

The KAMI tracking detectors are made from 500 μm diameter scintillating fibers distributed over 5 tracking stations. Four of the five stations are constructed of four sets of fiber planes in an x/x′ y/y′ configuration. The fifth module is located at the middle of the magnet for redundant measurement of momentum and to reject background events with a kink. This is especially important in rejecting $K_L \to \pi^{\pm}\mu^{\mp}\nu$ backgrounds to $K_L \to \mu^+\mu^-$, for example. This module has only x/x′ planes in order to minimize the thickness of material. The fiber tracking planes will each have a hole in the center for the beam to pass through to avoid backgrounds associated with neutron and kaon interactions. Each of the 5 fiber tracking stations will be supported by a carbon fiber honeycomb structure which will provide more than adequate strength and minimum mass.

The fibers will be read out at both ends allowing for mean-timing of the two signals for use in a charged trigger with a narrow time window. The fibers are also used to veto charged particles which requires fast time response as well.

Visible Light Photon Counters (VLPC) will be used for the fiber readout. The high quantum efficiency of VLPC detectors ($\sim$ 80%) make them particularly attractive, although they must operate at liquid Helium temperature. The basic performance requirements for the VLPC chips are listed in Table 21. These specifications are in line with the VLPC performance obtained by D0 with the exception of the gain variation, which was found to vary considerably with reactor load. The use of a new, more modern reactor facility by the vendor should result in better uniformity. If this does not prove to be the case, the VLPC chips will have to be sorted by gain.

Quantum Efficiency	~80%
Gain	30000 - 40000
Gain Variation	<10%
Linearity	~10%
Dark Count Rate	<10 kHz

Table 21: The Basic performance specifications for the KAMI Visible Light Photon Counter (VLPC) readout for the scintillating fiber tracker detector.

The scintillating fibers will mate with low-attenuation, double-clad clear fiber through a custom optical connector. The clear fiber will have a slightly larger diameter than the scintillating fiber. This step-up in diameter helps to minimize losses at the connector due to small mis-alignments. The optical connectors will bolt into a flange in the vacuum chamber and the clear fiber will connect from the outside. Bundles of clear fiber will be routed to VLPC cassettes in light-tight, flexible, fire-resistant tubing. The VLPC cassettes will be inserted into cryostats located under the vacuum chamber.

D0 obtains a mean yield of ~10 photo-electrons per MIP per fiber with their fiber tracking detector. D0 uses 835 μm diameter scintillating fiber with clear fiber lengths of ~11 m to channel the light to the VLPC cassettes. The attenuation length of the clear fiber is approximately 7 m. KAMI intends to use 500 μm diameter scintillating fiber that will produce less light than the D0 fiber. However, the clear fiber run from the detector to the VLPCs will only be about 4 m for KAMI, resulting in less attenuation that will compensate for the reduced light production. We assume a mean yield of 10 photo-electrons per MIP per fiber for the KAMI tracking system. This is something that will require early verification during R&D for the fiber tracker.

The KAMI fiber tracking system will consist of 74k fibers and twice that many readout channels. A breakdown of the channel count appears in Table 22.

Tracker No.	Plane Type	Size (x/y)	#fibers per Plane	#plane	# Channels
Fiber Tracker 1	xx′yy′	229 x 229 cm	3820	4	15268
Fiber Tracker 2	xx′yy′	238 x 238 cm	3970	4	15868
Fiber Tracker 3	xx′	247 x 247 cm	4115	2	8234
Fiber Tracker 4	xx′yy′	255 x 255 cm	4250	4	17000
Fiber Tracker 5	xx′yy′	269 x 269 cm	4480	4	35864
Total			74,302	18	148,604

Table 22: Breakdown of the number of channels required for the KAMI fiber tracking system.

Because the fiber tracker is located inside the vacuum chamber, it will be necessary to understand the out-gassing characteristics of the fibers. Plans for such studies are currently being developed.

6.5.2 Spectrometer Magnet

The fully hermetic veto system is a critical component of the KAMI spectrometer. In order to maintain hermeticity, it is necessary that the veto system be contiguous through the spectrometer magnet. With the two assumptions:

1. The CsI array is approximately circular with a radius of 2.75 m
2. The radial space required for the veto system is 0.5 m

The magnet aperture must be at least 3.75 meters. A new spectrometer magnet will therefore be required.

We considered using the KTeV spectrometer with a larger gap. But the width of the KTeV magnet coils is just under 2.9 meters. In addition, if the KTeV spectrometer magnet gap is increased (and the beam height is unchanged), a pit must be cut into the floor. A rough estimate prepared by Fermilab FESS is that this would cost about $376k. The full cost of increasing the beam height has not been costed, but just raising the beam pipe through the berm is estimated to cost $226k. This does not include any work that would have to be done in NM2.

The field integral requirements in KAMI are no higher than about 250 MeV/c. This requirement is set by requiring that in searches for two body decays, for example $K_L \to \mu^+\mu^-$ or $K_L \to \mu^\pm e^\mp$, the field integral can be set to the p_t of the decay. Setting the magnet in this way makes it easy to define a restrictive but efficient trigger for the two body modes. Of course, more complex triggers can be developed to limit the trigger rate without placing particular requirements on the field integral.

A new KAMI magnet concept has been developed. The horizontal and vertical apertures are about 3.8 meters. The length of the magnet is 3 meters and the yoke is .45 m thick on the sides and top and bottom. The same conductor that was used for the KTeV spectrometer is used. The number of turns is also the same. The array of conductors in each coil is made taller and narrower (4 turns per layer, 20 layers in each of 4 coils) in order to maintain good field integral uniformity with the much larger gap. A sketch of the magnet is shown in Figure 57. Note that this magnet does not require cutting a hole in the floor, assuming the bottom yoke can be shimmed into place on the floor without any additional structure.

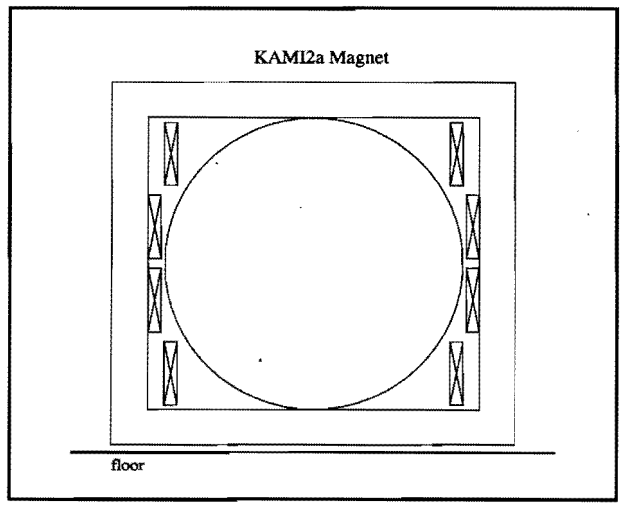

Figure 57: KAMI Spectrometer Magnet. A 3.75 m diameter vacuum vessel is shown inscribed in the magnet aperture. The upper and lower most coils are set in to nest into the inner coils - minimizing the overall length of of the magnet.

This magnet has been modeled using ANSYS. The design concept meets the requirements of the experiment, with the caveat discussed below. The vertical component of the field as a function of distance from the center of the magnet is shown in Figure 58.

One of the problems with a magnet that has an aperture of 3.8 meters is that the fringe fields extend out to very large distances. Though the central field is only a little about 1600 gauss, the field 8 m from the center of the magnet is about 16 gauss on the spectrometer axis! These fields correspond to a field integral of 245 MeV/c. Moving the spectrometer magnet upstream of the CsI far enough so that the fringe field does not compromise the CsI readout reduces the acceptance for many modes unacceptably. Also, with the trackers at reasonable locations with respect to the magnet in terms of acceptance, the tracking would have to be carried out in strong fringe fields.

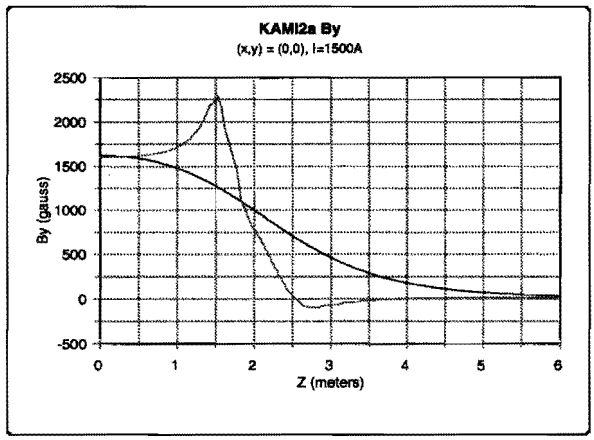

Figure 58: KAMI Spectrometer Magnet - By(gauss) vs Z(meters). The monotonic line is B_y at x=y=0, where the other line is for the field at x=y=1.8m. The field integral at x=y=0 is 245 MeV/c.

We are therefore attempting to design the vacuum system so that the vacuum vessels and flanges provide magnetic shielding in the spectrometer regions upstream of tracker 2 and downstream of tracker 4 - particularly for the CsI. The design of a passive magnetic shielding system is not yet complete. Options such as using multiple flanges and/or additional layers of steel around the vessels, or including active magnetic shielding have not yet been evaluated or ruled out.

6.6 Vacuum System and Vacuum Window

The decay region and spectrometer must be evacuated to at least 10^{-6} torr in order to keep background in $K_L \rightarrow \pi^0 \nu \overline{\nu}$ due to beam interactions in the residual gas to a negligible level. The vacuum region will start in the neutral beam shortly downstream of the absorbers and end at the large vacuum window just upstream of the CsI array. Note that the charged spectrometer is in vacuum. The volume of the KAMI vacuum system is quite large, 450 m^3, about 3x larger than the KTeV vacuum system (not correcting for the volume displaced by the veto counters).

As a point of reference, the KTeV vacuum system had a volume of approximately 150 m^3. The pumping system consisted of two large (50,000 l/sec) oil diffusion pumps backed by Roots blowers and rotary mechanical pumps. The best vacuum obtained in KTeV was below 1.0^{-6} torr, but usual operation was a little over 10^{-6} torr.

In contrast to KTeV, liquid nitrogen baffles will be used between the diffusion pumps and the main vessel. This will minimize the back-streaming of oil from the diffusion pumps and also make it possible to ultimately attain a better vacuum. The addition of liquid nitrogen baffles will reduce the effective pumping speed of the diffusion pumps by roughly a factor of 2. The baffles will probably have to be fabricated to order or in-house. A brief search for baffles for these pumps when we were constructing KTeV indicated that the appropriate baffles were no longer in production. Because of the larger size of the system and because

there will be much more equipment in the vacuum system, additional diffusion pumps will be required.

Given the demanding requirements of the vacuum system, some tests using parts of the existing KTeV vacuum system would be very useful. In particular, adding liquid nitrogen baffles and measuring the change ultimately attainable vacuum would be very useful. These tests would be done with a blanking flange on the vessels (as opposed to the thin window).

The vacuum vessels must contain and support the veto system. Though the detailed design of the vessels await availability of appropriate engineering support, the general concept is understood. The vessels that must support the veto system will be fabricated with internal and external frameworks to support the vetoes. The vessels themselves, other than providing for improved rigidity, will not be primary load carrying devices.

The vacuum pressure must be maintained in spite of the out-gassing load of the scintillator and fibers inside the vacuum chamber. The photon veto system will employ the same "virtual vacuum" technique used for the KTeV ring veto detectors. In this scheme a thin membrane surrounds the scintillator and is pumped separately from the main decay volume.

The vacuum/veto system must pass through the spectrometer magnet. The vacuum vessels and associated mechanical structures must be non-magnetic in that region. In the current design, the sections of the vessel between trackers 2 and 4 will be fabricated of stainless steel. This section will be rigidly attached to the spectrometer magnet. The sections adjacent to the stainless steel section are being designed in such a way as to help provide magnetic shielding for upstream and downstream components - particularly the CsI array. Sections of the vacuum system upstream and downstream of the magnet will be on wheels (again similar to KTeV) to allow for movement due to mechanical and thermal stresses.

The diffusion pumps must be placed in the general area of the decay region. The region near the tracking system, magnet and CsI is too congested to allow for the addition of the large diffusion pumps. In order to maintain pumping speed to the downstream end of the spectrometer, the upstream sections of the vacuum system will be larger than would be necessary to just contain the veto system and associated readout.

One of the major design issues is that of the vacuum window. The KTeV design, kevlar cloth with 0.005" of aluminized mylar clamped between steel flanges, with the required safety factor of 2, worked well. That design was based on detailed modeling and on extensive testing. We will again carry out a program of analysis and testing to design the vacuum window for KAMI. Preliminary calculations, using a safety factor of 2.5 and the same basic design used in KTeV indicate that a window 2.5 times thicker than the KTeV window is appropriate. That window is expected to bow about 7.5". The availability of kevlar of appropriate dimension has not been confirmed. Carbon fiber cloth will also be considered.

The same safety procedures and techniques used in KTeV will be used. That is, it is assumed that when there is a thin window installed and the system is under vacuum, a shield must be in place downstream of the window if personnel are in the experiment hall. This requirement will again be a part of the standard Fermilab interlock system.

6.7 Muon Range Stack

The KAMI muon range stack is designed to trigger on and identify muons from a variety of interesting rare decay modes such as $K_L \to \mu^+\mu^-$, $K_L \to \mu^+\mu^-\gamma$, $K_L \to \mu^+\mu^-\gamma\gamma$,

$K_L \to \mu^+\mu^-e^+e^-$, $K_L \to \pi^0\mu^+\mu^-$, $K_L \to \pi^0\mu^\pm e^\mp$, $K_L \to \mu^\pm e^\mp$ and $\pi^0 \to \mu^\pm e^\mp$. For this purpose we select a range stack of iron absorbers interleaved with scintillator planes. An elevation view of this detector is shown in Figure 59. The transverse dimensions are chosen to be 4 meters square, large enough to completely cover the solid angle subtended by the upstream apparatus but still small enough not to require digging a pit in the existing hall. The total thickness of the iron is 12 m, corresponding to a total muon range of ~12 GeV/c. The stack is divided longitudinally into 27 layers, with thicknesses selected so that each layer corresponds to a 15% increase in momentum. There are 2 gaps in the array to accommodate the first 2 Beam Anti detectors discussed in section 6.4. The muon range stack has a hole to allow the evacuated beam pipe to pass through. The total stack corresponds to about 65 hadronic interaction lengths.

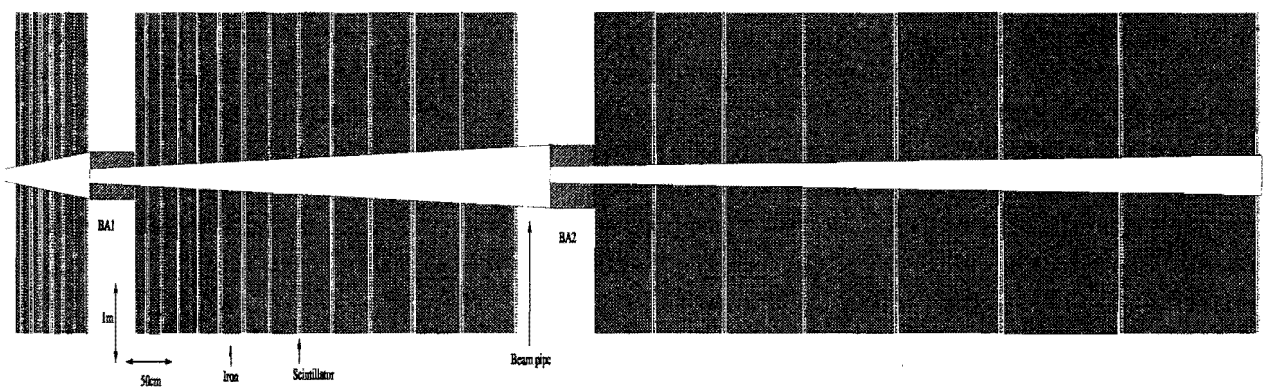

Figure 59: Elevation view of the muon range stack.

Each layer of scintillator is divided into square tiles of 50 cm on a side (with the tiles surrounding the beam pipe cut out as necessary). Thus there are 64 tiles per layer or 1728 in all. This geometry and size is chosen, rather than a hodoscope arrangement, to minimize light propagation paths and thus improve the time resolution of the device. We envision reading out the scintillator with optical fibers to phototubes.

Figure 60 shows the distribution in the transverse dimensions of hits from muons from the decay $K_L \to \mu^+\mu^-$ at a longitudinal position 1m into the stack.

The detector contains about 1300 tons of steel, of which about 400 tons already exists in the KTeV detector but would need fabrication to appropriate sizes. For 2 cm thick scintillators, about 9 tons of scintillator are required. Supposing readout fibers are 5cm apart there is 25m of fiber for each tile, assuming the phototubes are mounted on the outer perimeter of the detector. So 43,200 m of fiber is required. There are 1728 readout channels, each with a phototube plus electronics similar to that used on the photon vetoes.

6.8 Electronics

There are two main requirements of the KAMI electronics. First, it must be dead-timeless in the sense that all hits occurring in a time interval of several hundred ns around the trigger

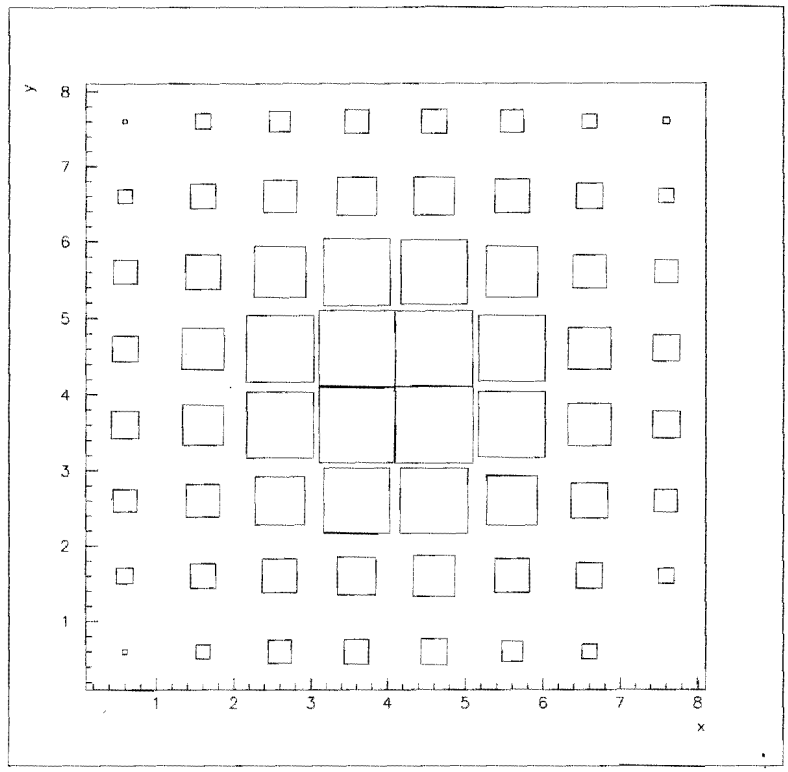

Figure 60: Distribution in the transverse plane of hits from $K_L \to \mu^+\mu^-$ decays at 1m depth in the muon range stack.

must be detected and recorded. [1] Furthermore there must be sufficient buffering to avoid a reduction in the effective live beam flux due to trigger latency and the eventual transfer of data to the DAQ.

All veto and CsI photomultiplier tubes will be read out by a charge integrating encoder (QIE), a technique first used in KTeV [118]. The current version of this chip is being developed for the CMS HCAL project. In addition to a multi-range integrator the chip has an on-board FADC. The dynamic range of the CMS QIE is 13 bits . If a larger range proves necessary for some detectors an attenuated copy of the signal would be sent to a second QIE. A major difference between the CMS and KAMI operating conditions is that in KAMI the signals to be sampled will arrive asynchronous to the clock. Studies on prototype CMS parts have shown integrated charge errors less than 1% in asynchronous conditions. The CMS QIE is specified to run at a clock rate of 40MHz although operation at 50MHz should also be possible. This speed is satisfactory for the CsI and most vetoes. The inner BA, which will be subjected to the full neutral beam, will be instrumented with two QIEs operating on opposite clock phases to yield an effective integration period of 10 ns. An important feature of the QIE is that it is fully pipelined. So, in principle there is no deadtime associated with this type of readout.

The single largest channel-count system is the scintillating fiber tracker. Most fibers will

[1] This information is vital for monitoring veto performance since a hit occurring prior to a trigger event may affect efficiency.

be instrumented at both ends in order to use time-difference and mean-time to facilitate hit matching between the two views of fiber planes and rejection of out-of-time hits. In addition hardware mean-timing may be used in forming charged mode triggers. The fibers will likely also be used as a charged veto.

The typical M.I.P signal (10 p.e.) out of the VLPC is expected to be about 24 fC. However in order to maintain high efficiency for tracks passing near the edge of a fiber we must plan on operating at a threshold of about 2.5 fC, corresponding to 1 p.e.. The VLPC risetime is sufficiently fast to permit timing to a level of ± 1 ns [119]. The output of the VLPC will be conveyed by a short (< 30 cm) flex circuit cable to an amplifier and discriminator mounted on the detector. This function would be conveniently satisfied by the ASDQ, an 8 channel amplifier/shaper/discriminator ASIC developed for the CDF run II central chamber. Although the tail cancelling shaper in this chip will likely suffer some overshoot with the VLPC signal shape this should not be a problem given the relatively low rate per fiber. The ASDQ amplifier and shaper sections are linear up to about 120 fC so overload should not be a problem. A back-up solution would be to build an amplifier/discriminator from commercially available transimpedance amplifiers (*e.g.* LM359, AD8015, SA5212) and comparators (*e.g.* AD96687, SPT9687, MAX9687). The discriminator differential output will be conveyed by a short (< 10 m) cable to a TDC located in racks nearby within the experimental hall.

Currently there are several nearly dead-timeless TDCs that have been developed for existing or planned experiments. All of these are based on custom or semi-custom ASICs which have been optimized for that particular experiment's DAQ architecture and conditions, *e.g.* beam time structure. A crucially important TDC specification for any of the KAMI veto detectors is the minimum double pulse separation (DPS) since an unrecorded pulse would contribute to veto inefficiency. Redundant readout by the QIE should mitigate this effect to some extent. Moreover, recording both edges of the discriminated pulse is desirable to avoid pile-up inefficiency in the discriminator. We list below a number of possible solutions for TDCs with 1 ns resolution or better.

FPGA

Recently, the makers of FPGA chips have added high-speed I/O capabilities to their devices to serve communications applications. Companies such as Altera and Quicklogic have included techniques to allow a "source synchronous" mode in which the multiple data channels are received in a stream and are clocked by a single attending clock. The chips include a phase locked loop to multiply the input frequency by at least eight times. It turns out that these devices can serve to input time-sensitive pulses at a rate of 840 MHz, which corresponds to about 1.25 ns. This is adequate for most TDC applications. We have studied the feasibility of using these chips and believe that a suitable device with up to 128 channels per card can be built, with no dead time. The chip we would consider at this time is of the Altera Mercury family, an EP1M120-5, which has eight high-speed input ports per chip. A card would contain 16 of these chips. One high-speed port would input the common start or stop for the entire card.

JMC96

The JMC96 was developed by the Univ. of Michigan for the CDF tracking TDCs. Of the three chips described here it has the smallest DPS = 10 ns. The data is stored in

a two level pipeline of lengths $5\mu s$ and $2\mu s$. Since the foundry no longer supports the process only the spare chips at Michigan would be available. Only the most critical high rate vetoes should use this chip due to the limited availability.

TMC

The TMC chip is currently being used by the D0 muon system. Since it is produced on a sea-of-gates chip, availability is not a problem. The minimum DPS is equal to the system clock period (25 ns) for leading and trailing edges independently. It handles 4 channels per chip, as compared to the single channel JMC96.

$\mathcal{F}\infty$

The $\mathcal{F}\infty$ also employs sea-of-gates technology and was developed for the COMPASS experiment [120]. It contains eight channels per chip with 25 ns DPS. However, the edges are not processed independently so to record both edges of pulses shorter than 25 ns would requiring dedicating half of the channels to recording the trailing edges. The chip contains extensive logic for matching trigger hits to data. Rather than being pipelined, the hit processing is data driven such that the chip is limited to recording 7 hits per trigger and 16 hits per channel during the time needed to match hits to triggers (≤ 800 ns).

6.9 Trigger and Data Acquisition System

The KAMI experiment will operate in the presence of kaon decay rates of several megahertz. The more common decays include $K \to \pi e \nu$ and $K \to \pi^0\pi^0\pi^0$, both of which will be of key importance for calibrating the KAMI detector. Large samples of these decays will have to be collected in order to monitor the response of the CsI calorimeter and to understand and track the efficiency of the photon veto detectors.

In addition to these high-statistics calibration and monitoring samples, KAMI wants to search for or measure a variety of rare decays, including charged modes such as $K \to e^+e^-e^+e^-$ and $K \to \pi^+\pi^-e^+e^-$, as well as the flagship neutral mode $K_L \to \pi^0\nu\overline{\nu}$. The diversity of the KAMI physics program is a key aspect of this proposal, but the variety of triggers required to meet this objective will place additional demands on the trigger systems.

In general, the KAMI trigger will follow the general framework of the generally successful KTeV trigger, with a few differences. First, all detector systems will have fully digital, multi-level pipelined readout. This will simplify data handling by eliminating the need for long delay cables and signal conditioning. It will essentially eliminate deadtime, since data collected when the trigger logic is busy can be processed once the trigger is done with the earlier event. And it will allow comprehensive testing and debugging to be performed by injecting simulated data into the pipeline at each stage. Second, the KAMI trigger will adopt a more uniform format, using whenever possible VME as a general-purpose interface, rather than the mixture of VME, Fastbus, FERA, and CAMAC that was used by KTeV. This will allow greater standardization of control, monitoring, and readout functions than was possible in KTeV. KAMI will use modern DSP and FPGA-based technologies, rather than 1970's-vintage LeCroy modules, in its trigger logic. KAMI will also make sure that the technologies adapted will work reliably with the planned data rates, and will take advantage whenever possible of commercial networking and switching solutions.

Some additional complications arise in the KAMI trigger because of the unbunched KAMI beam. The pipelined readout will be synchronous, which means that signals may be divided between adjacent buckets. One technique for dealing with this would be to use overlapping buckets, say 20 ns long but collected at 100 MHz. Then an event that lies near the edge of one bucket will lie in the middle of another. Alternatively one could attempt to combine data from two adjacent 10 ns buckets.

6.9.1 L1 Trigger

The first-level trigger for KAMI will run synchronously, at a rate between 50 and 100 MHz. It will correlate signals from several detector systems to look for indications of an interesting decay in a particular time slice. Data from the CsI calorimeter, the fiber tracker systems, the photon vetoes, and the muon range stack will be collected in a first-level readout buffer. Pipelined logic will look for photon veto signals, fiber tracker hits, muon range stack hits, and significant CsI energy deposition, and produce signals describing the activity found, which will be collected and processed synchronously by global first-level trigger logic. If the global logic identifies a combination of signals of interest (which might be, for example, energy over 2 GeV in each quadrant of the CsI, in a time slice with fewer than 2 photon veto signals over threshold), a Level 2 Interrupt will be generated which will be sent back to the first-level pipeline buffers and will initiate the transfer of several time slices of data to a second-level pipeline. The level 1 trigger logic should be designed to keep the rate of Level 2 Interrupts to 600 kHz or less.

We expect that roughly half of the Level 2 Interrupt rate will be due to the neutral decay $K_L \to \pi^0\pi^0\pi^0$. The other half will be due to the various charged decay modes. Among the charged modes, the four-track decays (including $ee\mu\mu$, $eeee$, and $\pi\pi ee$) will contribute relatively little to the rate (unless the rate of noise hits in the fiber trackers is very high), while the rate from dimuon modes should be limited by a two-muon-hit requirement. The most problematic charged mode for the trigger is $K_L \to \mu e$, which is difficult to distinguish from $K_{\mu 3}$ decays without kinematic calculations or additional particle ID information.

6.9.2 L2 Trigger

Data in the Level 2 pipeline buffer will be downloaded to Level 2 trigger processors based on FPGA and DSP technology. These processors will, in the first instance, correlate the data from within each detector system. For example, they will determine the number of distinct energy clusters in the CsI in order to identify six-photon or five-photon candidate-events for calibration and photon veto monitoring, as well as two-photon events that could be $\pi^0\nu\bar{\nu}$ candidates. Level 2 processors will also correlate the hits in the fiber tracker system to look for sets of hits in geometrical roads that could have been left by charged tracks.

A simple Level 2 trigger might stop here, with a determination of cluster and track multiplicity. A simple two-cluster requirement for the $K_L \to \pi^0\nu\bar{\nu}$ mode would result in a Level 3 Interrupt rate on the order of 10 kHz. We expect that the Level 3 Interrupt rate will be dominated by other triggers, including five and six-cluster neutral triggers and the various charged-mode triggers. It is not yet known whether kinematic constraints will be required to keep the total rate of Level 3 Interrupts to the maximum of 100 kHz or so that the Data

Acquisition system will be able to accept. If additional constraints are required, the Level 2 trigger logic could determine quantities such as the total transverse momentum in the CsI, or it could correlate tracker information with CsI information to determine, for example, the number of electrons in an event (tracks pointing to clusters of similar energy), or the number of photons (clusters not pointed to by tracks) But the overall goal of the trigger system will be to make the simplest possible selection criteria consistent with reducing the Interrupt rate to a manageable level.

6.9.3 L3 Trigger and DAQ

When a Level 3 Interrupt is generated, data from the Level 2 pipeline buffers will be transferred to a DAQ pipeline buffer. The DAQ computers will build the event by collecting all the data from the various DAQ pipeline buffers and transferring them to the DAQ computer farm, where more complete event reconstruction and filtering will be performed (the Level 3 Trigger). By using about 200 Level 3 processors in parallel, we can budget roughly 10 ms of processing time per event at Level 3. At Level 3, it should be possible to make kinematic cuts to drastically reduce the $K \to \mu e$ rate, and to select prescaled, clean samples of $\pi^0\pi^0\pi^0$ events for photon veto efficiency studies. Also, complete tracking will be performed which should reduce the four-track event rate to something on the order of the real rate of four-track decays, which is below 1 kHz. We aim for a total Level 3 Trigger rate of not more than 15 kHz. Assuming an average event size of 20 kB, this would result in a formidable data-logging rate of some 300 MB/s, or 3 PB per 10^7 seconds of running. The trigger rates are summarized in Table 23.

KAMI will collaborate with the Fermilab Computing Division and other concurrent experiments to design a data acquisition system with a common architecture. Most of the details remain to be worked out, but a basic overall design is shown in Figure 61.

Event Type	Maximum Rate	Latency
Kaon Decays in KAMI	10 MHz	1μs
Level 2 Interrupts	600 kHz	20μs
Level 3 Interrupts	100 kHz	10 ms
Save to Permanent Medium	15 kHz	—

Table 23: Summary of the trigger rates discussed in the text.

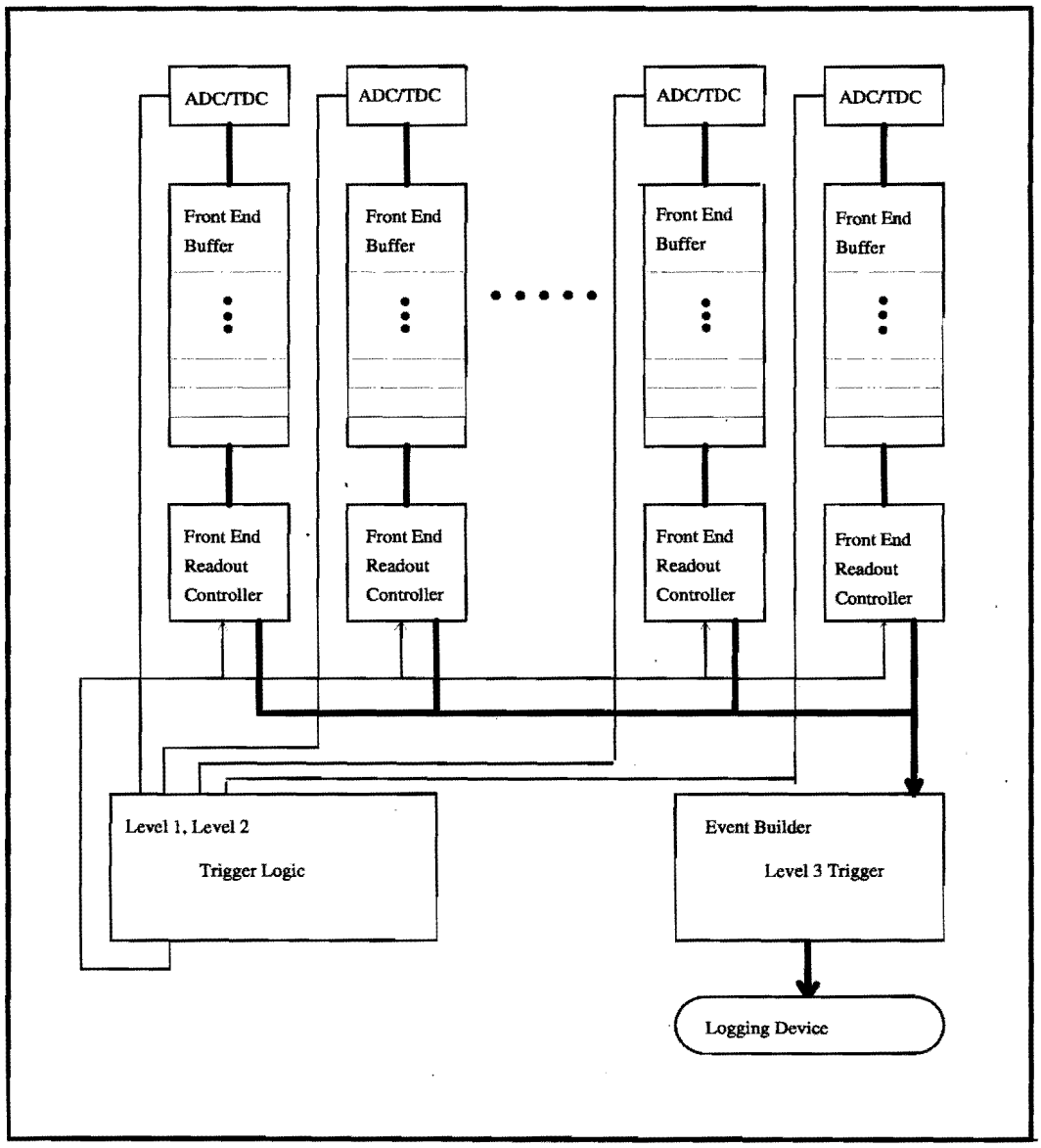

Figure 61: Basic architecture of the KAMI data acquisition system.

7 Alternative Methods for Separating Signal and Background

7.1 Maximum Likelihood Analysis of Background in Beam Anti

While it may appear that the level of background under the signal region can be estimated from the observation of the dominant $2\pi^0$ background below and above the signal region, there are problems with this approach. With the assumed inefficiencies and cuts, as shown in Figure 18 there are effectively are no background events above the signal region. Relaxing cuts will allow us to change the background level to obtain events above the signal region and determine if they follow the pattern that we expect from the baseline inefficiencies. However, changing the cuts will change the complex effect of the vetoes and the background rejection, so that it is not clear that the inefficiencies can be measured in this way. Finally, even if both sidebands were present, there would still be the need to depend on a Monte Carlo to determine the shape of the background under the signal.

However, study of the energy spectra in the veto detectors themselves can give additional independent information about the level of background to supplement the direct observation of background in the low P_t spectrum. For example, if we restrict ourselves to events in the signal region, approximately two thirds of the background under the signal is expected to come from events in which there is a photon in the BA3 detector. A careful likelihood analysis of the shower development in that detector should give us a way of estimating the level of that part of the background due to this class of events.

For example, after all analysis cuts, a sample of events containing an unknown fraction of $K_L \to \pi^0\nu\bar{\nu}$ decays and various backgrounds will be selected. The direct method of estimating backgrounds using Monte Carlos of the the various background modes will not only be sensitive to uncertainty in veto inefficiencies as it was discussed above but also to the mix of modes that contribute to the background. An alternative method is to *measure* both signal and background rates by analysis of the veto shower distributions which are to first order independent of the inefficiency problems and integrate over all background modes. In particular, analysis of the Beam Anti shower distributions can distinguish between signal and background for events in which a background photon is in the Beam Anti.

As it was shown in Section 6.4, the entire background rate (except for approximately 8 events/year) will come from events where at least one photon interacts in the Beam Anti. $K_L \to \pi^0\nu\bar{\nu}$ events will have only neutron interactions in the Beam Anti or no deposited energy at all. The longitudinal position of the most upstream interaction, Z_{int}, can be measured for each event in the present Beam Anti design with longitudinal segmentation. The distribution of Z_{int} is shown in Figure 62 for signal and background events. The number of signal and background events can be measured by maximizing the likelihood

$$L(s,b) = \frac{(s+b)^N \cdot e^{-(s+b)}}{N!} \prod_{i=1}^{N} \frac{s \cdot P_s(z_i) + b \cdot P_b(z_i)}{s+b}$$

where s and b are rates for signal and background, respectively, N is the number of events in the sample, P_s and P_b are distributions of Z_{int} for signal (neutron showers or no deposited energy) and background (photon showers), normalized to one. The Poisson term in front of

the product reflects the probability to get N events in the sample for given s and b rates. By maximizing $L(s,b)$, one can obtain a best estimate for both signal and background rates and their statistical uncertainties after all selection cuts.

The sensitivity of this method has been tested with Monte Carlo simulations. A sample of 100 signal events was generated according to P_s and was mixed with background events generated according to P_b. The number of background events in a sample was varied from 10 to 10000. The maximum likelihood method was applied to a sample and the number of reconstructed signal events (s) were compared to $s_{true} = 100$. The method was found to be unbiased. The statistical uncertainty on s is a function of the number of background events and is summarized in Table 24.

Although we expect a signal-to-background ratio of about 4:1 after all cuts, the method remains very sensitive at much higher background rates. The main advantage of this method is that it is not sensitive to uncertainties in veto inefficiencies because the Z_{int} distribution does not depend on photon energy. Also, both P_s and P_b distributions will be experimentally measured with high precision. For example, P_s can be measured by the response of the Beam Anti for completely reconstructed $K_L \to \pi^+\pi^-\pi^0$ decays (with no missing particles) collected simultaneously with the $K_L \to \pi^0\nu\overline{\nu}$ sample. P_b can be estimated by measuring the Beam Anti response $K_L \to \pi^+\pi^-\pi^0$ decays with one photon pointing into the Beam Anti.

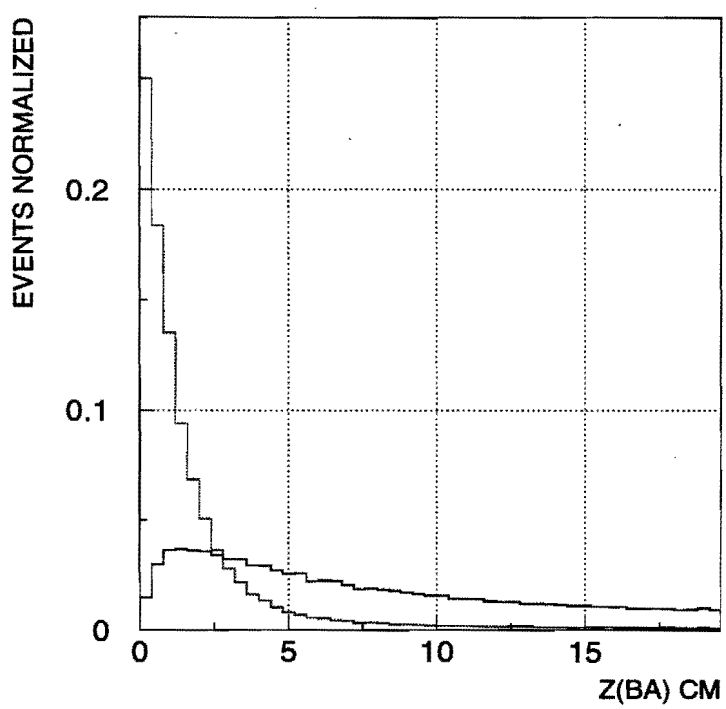

Figure 62: Longitudinal distribution of the most upstream interaction in the Beam Anti for signal and background. The signal distribution (extended z distribution) is due to events with neutron interactions only and background (early showering peak) are events with photon interaction superimposed on neutron interactions.

N signal	N background	S/B	Stat. err. on signal	Increase in stat err. due to background
100	10	10	±11	1.1
100	50	2	±12	1.2
100	100	1	±13	1.3
100	500	0.2	±18	1.8
100	1000	0.1	±22	2.2
100	5000	0.02	±25	2.5
100	10000	0.01	±45	4.5

Table 24: Statistical uncertainty on signal rate measurement as a function of background level. The background level is for a sample of events before the likelihood analysis is applied. The last column is a ratio of the statistical error and $\sqrt{N_{signal}}$.

7.2 Neural Networks and Selection of $K_L \to \pi^0\nu\overline{\nu}$ Decays

7.2.1 Introduction

The Neural Network technique has become increasingly popular over the last couple of years in feature recognition and function mapping problems with a wide spectrum of applications. High energy physics is no exception with its demanding on-line and off-line analysis tasks. To date, neural network algorithms have been applied to $\gamma - \pi^0$ discrimination in calorimeter measurements [124], in hadronic jet reconstruction [125], in the hadronic decays of Z-boson [126], in track finding algorithms [127] [130] and elsewhere. Neural networks could find application in KAMI as an additional tool for understanding the distribution of signal and background events in conjunction with more traditional techniques.

7.2.2 Training of Networks

Two classes of events can be separated by maximally exploiting rather small differences in their distributions many different parameters. The degree of separation increases as the number of parameters is increased. Before applying the neural net to the problem of event class differentiation, it is necessary to train the network. For this exercise the back-propagation algorithm with a three-layer net is applied(see Figure 63), where the first layer is for input values X_k, the second layer is the so called "hidden" layer and the third layer is the output.

7.2.3 The Input Values for Training

For this example, the odd pairing background from $K_L \to 2\pi^0$ events is considered where each π^0 contributes a photon with $E_\gamma > 1$ GeV. The two missing photons both have an energy less than 20 MeV. The P_t of the π^0, the P_t of each individual photon, the reconstructed Z-vertex Z_V and the distance between the two clusters δS in the CsI calorimeter are all calculated for both $K_L \to \pi^0\nu\overline{\nu}$ signal and background events.

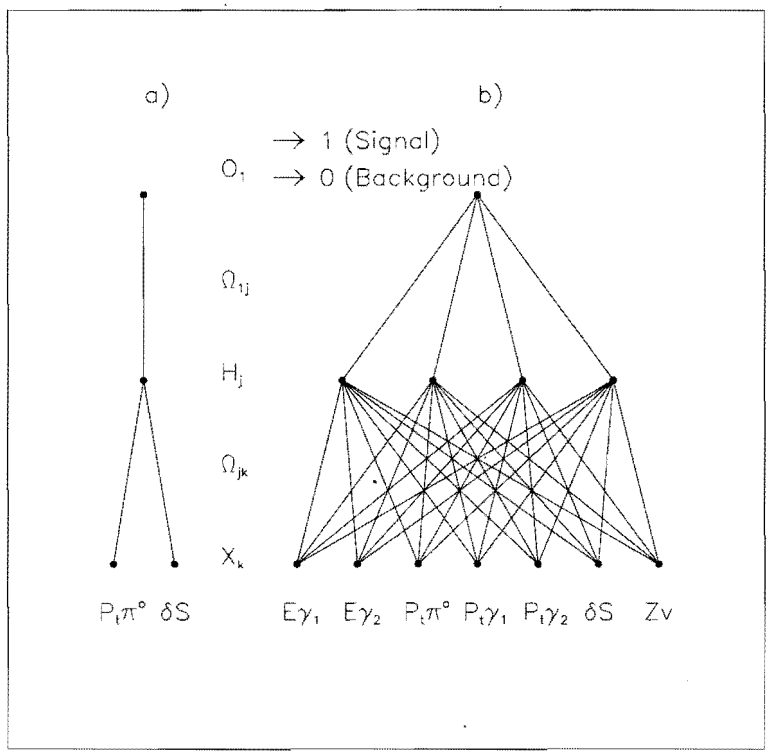

Figure 63: Three-layers neural nets: a) with two input nodes; b) with seven input nodes.

7.2.4 Training and Result

As a first example, a simple neural network is investigated using two input parameters; $X_1 = P_{t\pi^0}$ and $X_2 = \delta S$. The neural network output for a sample of events that were not used for the training procedure after 10 "epochs" and 100 epochs are shown in Figure 64 and Figure 65.

After only ten epochs, the procedure cannot separate the signal from background. However, after one hundred epochs, we can begin to distinguish the signal from background.

If additional parameters are input to the neural network ($E_{\gamma 1}$, $E_{\gamma 2}$, $P_{t\gamma 1}$, $P_{t\gamma 2}$ and Z_V), the differentiation between signal and background becomes more pronounced. The output from the neural network after 10 epochs (see Figure 66) and after one hundred epochs is shown in Figure 66 and Figure 67, respectively. It is clear that additional input parameters sharpen the differentiation between signal and background.

Neural networks are a potentially useful tool for understanding the distribution of signal and background events in KAMI. However, there is a danger of relying too heavily on "black boxes" without understanding the underlying mechanisms. KAMI will continue to develop such tools primarily for the purpose of cross checking the consistency of results obtained by more traditional methods.

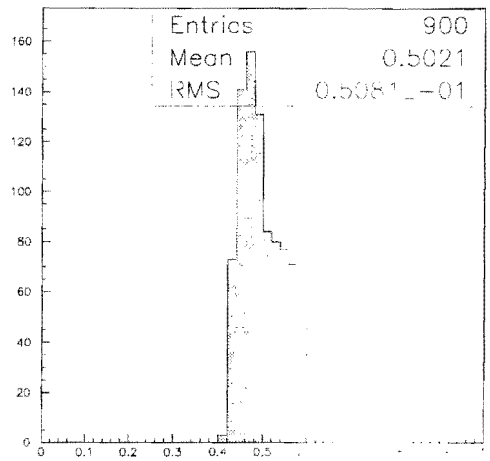

Figure 64: The neural network output distribution for a net with input values $P_{t\pi^0}$ and δS after ten epochs.

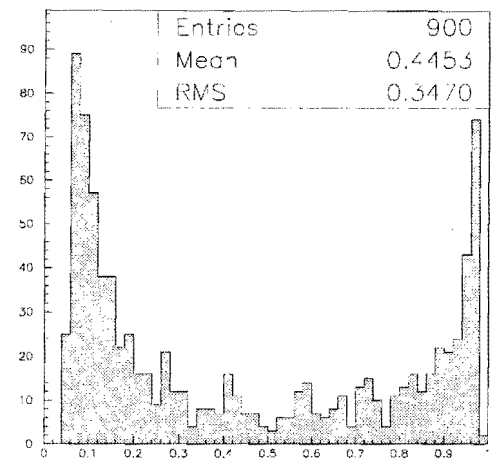

Figure 65: The neural network output distribution for a net with input values $P_{t\pi^0}$ and δS after one hundred epochs.

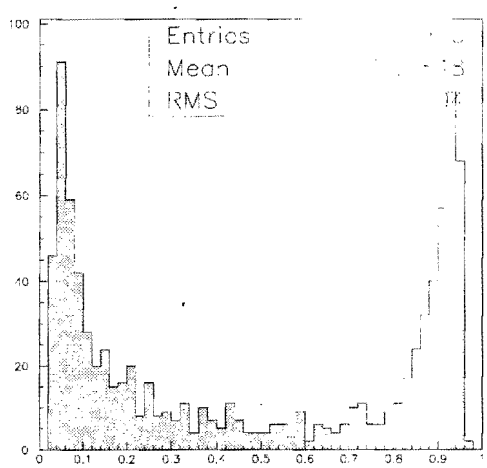

Figure 66: The neural network output distribution for a net with input values $P_{t\pi^0}$ and δS, $E_{\gamma 1,2}$, $P_{t\gamma 1,2}$ and Z_V after ten epochs.

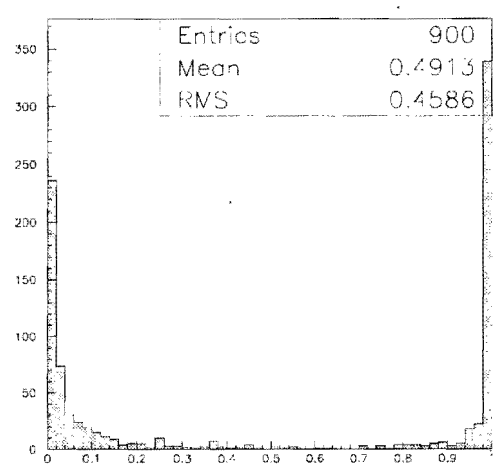

Figure 67: The neural network output distribution for a net with input values $P_{t\pi^0}$ and δS, $E_{\gamma 1,2}$, $P_{t\gamma 1,2}$ and Z_V after one hundred epochs.

References

[1] Brown R, et al. *Nature* 163:82 (1949)

[2] Pais A. *Phys. Rev.* 86:663 (1952); Gell-Mann M. *Phys. Rev.* 92:833 (1953)

[3] Dalitz R. *Phys. Rev.* 94:1046 (1954)

[4] Lee TD, Yang CN. *Phys. Rev.* 104:254 (1956)

[5] Cabibbo N. *Phys. Rev. Lett.* 10:531 (1963)

[6] Kobayashi M, Maskawa T.

[7] Christenson JH, Cronin JW, Fitch VL, Turlay R. *Phys. Rev. Lett.* 13:138 (1964)

[8] Glashow SL, Iliopoulos J, Maiani L. *Phys. Rev. D* 2:1285 (1970)

[9] Gaillard MK, Lee BW. *Phys. Rev. D* 10:897 (1974); Gaillard MK, Lee BW, Shrock RE *Phys. Rev. D* 13:2674 (1976)

[10] A.R. Barker and S.H. Kettell, Annu. Rev. Nucl. Part. Sci.**50**, 249 (2000).

[11] Littenberg L, Valencia G. *Annu. Rev. Nucl. Part. Sci.* 43:729 (1993)

[12] Hagelin J, Littenberg L. *Prog. Part. Nucl. Phys.* 23:1 (1989); Ritchie J, Wojcicki S. *Rev. Mod. Phys.* 65:1149 (1993); Buchholz P, Renk B. *Prog. Part. Nucl. Phys.* 39:253 (1997)

[13] Buchalla G, Buras AJ, Lautenbacher ME. *Rev. Mod. Phys.* 68:1125 (1996)

[14] Buras AJ, Fleischer R. In *Heavy Flavors II,* ed. AJ Buras, M Lindner, pp. 65 Singapore: World Sci. (1997), also hep-ph/9704376

[15] Buras AJ. In *Probing the Standard Model of Particle Interactions,* ed. Gupta R, De Rafael E, David F, Morel A, Vol. I, Ch. 5, New York, Elsevier Sci. (1999), also hep-ph/9806471

[16] D'Ambrosio G, Isidori G. *Int. J. Mod. Phys.* A13:1 (1998)

[17] Winstein B, Wolfenstein L. *Rev. Mod. Phys.* 65:1113 (1993); Bertolini S, Fabbrichesi M, Eeg JO *Rev. Mod. Phys.* 72:65 (2000) *Prog. Theor. Phys.* 46:652 (1973)

[18] Wolfenstein L. *Phys. Rev. Lett.* 51:1945 (1983)

[19] Buras AJ, Lautenbacher ME, Ostermaier G. *Phys. Rev. D* 50:3433 (1994)

[20] Jarlskog C. *Phys. Rev. Lett.* 55:1039 (1985); Jarlskog C. *Z. Phys. C* 29:491 (1985); Jarlskog C and Stora R. *Phys. Lett.* B208:268 (1988)

[21] Leutwyler H, Roos M. *Z. Phys. C* 25:91 (1984)

[22] Caso C, et al. *Euro. Phys. J.* C3:1. http://pdg.lbl.gov (1998)

[23] Marciano WJ. In Ref. [68] (2000)

[24] J.Adams *et al.*, Phys. Rev. Lett. **80**, 4123(1998).

[25] L.M. Sehgal and M. Wanninger, Phys. Rev. **D46**, 1035(1992); *ibid.* **D46**, 5209(E)(1992); P. Heiliger and L.M. Sehgal, Phys. Rev. **D48**, 4146(1993); J.K. Elwood *et al.*, Phys. Rev. **D52**, 5095(1995); J.K. Elwood *et al.*, *ibid.*, **D53**, 2855(E)(1996); J.K. Elwood *et al.*, *ibid.*, **D53**, 4078(1996).

[26] A. Alvati-Harati *et al.*, Phys. Rev. Lett. **84**, 408 (2000).

[27] Wilczek F, Zee A. *Phys. Rev. Lett.* 42:421 (1979); Cahn R, Harari H. *Nucl. Phys.* B176:135 (1980)

[28] Eichten E, Lane K. *Phys. Lett.* B90:125 (1980); Dimopoulous S, Ellis J. *Nucl. Phys.* B182:505 (1981); Shanker O. *Nucl. Phys.* B206:253 (1982); Haber HE, Kane GL. *Phys. Rep.* 117:75 (1985); Bigi II. *Phys. Lett.* B166:238 (1986); Pati J, Stremnitzer H. *Phys. Lett.* B172:441 (1986); Campbell BA, et al. *Int. J. Mod. Phys.* A2:831 (1987); Langacker P, Sankar SU, Schilcher K. *Phys. Rev. D* 38:2841 (1988); Mukhopadhyaya B, Raychaudhuri A. *Phys. Rev. D* 42:3515 (1990); Gagyi-Palffy Z, Pilaftsis A, Schilcher K. *Nucl. Phys.* B513:517 (1998); Lee BW, Shrock RE, *Phys. Rev. D* 16:1444 (1977)

[29] Buchalla G, Buras A. *Nucl. Phys.* B548:309 (1999)

[30] Buchalla G, Buras A. *Phys. Rev. D* 57:216 (1998) and references therein

[31] Buras AJ, et al. *Nucl. Phys.* B566:3 (2000)

[32] Sehgal LM. *Phys. Rev.* 183:1511 (1969)

[33] W.I Giersche and C.R. Munz, Phys. Rev. **C53**, 2549(1996).

[34] D'Ambrosio G, Isidori G, Portolés J. *Phys. Lett.* B423:385 (1998)

[35] Gómez Dumm D, Pich A. *Phys. Rev. Lett.* 80:4633 (1998)

[36] Valencia G. *Nucl. Phys.* B517:339 (1998)

[37] Knecht M, Peris S, Perrottet M, de Rafael E. *Phys. Rev. Lett.* 83:5230 (1999)

[38] Geng CQ, Ng JN. *Phys. Rev. D* 41:2351 (1990)

[39] Inami T, Lim CS. *Prog. Theor. Phys.* 65:297 (1981)

[40] D.Ambrose *et al.*, Phys. Rev. Lett. **84**, 1389 (2000).

[41] Ambrose D, et al. *Phys. Rev. Lett.* 81:4309 (1998)

[42] Kekelidze V, et al. In Ref. [71]

[43] Ecker G, et al. *Phys. Lett.* B189:363 (1987); Cappiello L, D'Ambrosio G. *Nuov. Cim.* 99A:153 (1988)

[44] Numao T. *Mod. Phys. Lett.* A7:3357 (1992)

[45] Bergström L, Massó E, Singer P. *Phys. Lett.* B131:229 (1983)

[46] Fanti V, et al. *Phys. Lett.* B458:553 (1999)

[47] Quinn B. In Ref. [72], Wah, Y. In Ref. [71].

[48] Burkhardt H, et al. *Phys. Lett.* B199:139 (1987)

[49] Gjesdal S, et al. *Phys. Lett.* B44:217 (1973)

[50] Angelopoulos A, et al. *Phys. Lett.* B413:232 (1997)

[51] Alavi-Harati A, et al. *Phys. Rev. D* In press (2000); also hep-ex/0010059 (2000)

[52] Alavi-Harati A, et al. *Phys. Rev. D* 62:112001 (2000)

[53] Heiliger P, et al. *Phys. Rev. D* 47:4920 (1993)

[54] Alavi-Harati A, et al. *Phys. Rev. Lett.* 83:917 (1999)

[55] Taegar S. In Ref. [69] (1999)

[56] Contalbrigo M. In Ref. [70] (2000)

[57] A. Alavi-Harati *et al.*, Phys. Rev. D **61**, 072006 (2000).

[58] M. Weaver *et al.*, Phys. Rev. Lett. **72**, 3758 (1994).

[59] J. Adams *et al.*, Phys. Lett. B **447**, 240 (1999)

[60] A. J. Malensek,"Empirical Formula for Thick Target Particle Production'" Fermilab Report FN-341 (1981).

[61] J. Marriner, Beams Division Report to the Fermilab PAC, June 2000.

[62] N.G. Deshpande and G. Eilam, PRL **53**, 2289 (1984).

[63] M. K. Gaillard and B. W. Lee, PRD **10**, 897 (1967).

[64] J. Ellis, M. K. Gaillard and D. V. Nanopoulos NPB **109**, 213 (1976).

[65] G. Buchalla and A. J. Buras, NPB **548**, 309 (1999).

[66] T. Inagaki *et al. Nucl. Instrum. Methods* A **359**, 478 (1995).

[67] I-H. Chiang *et al.* "K0PI0 - a Search for $K_L \to \pi^0 \nu\overline{\nu}$ ", NSF proposal, November (1999).

[68] Rosner JL and Winstein B, eds. *Kaon Physics,* Proc. Chicago Conf. Kaon Phys., June 1999 Chicago: Univ. Chicago Press (2000)

[69] Arisaka K and Bern Z, eds. *Proc. Meet. DPF, UCLA, Jan. 1999.* http://www.dpf99.library.ucla.edu (1999)

[70] J. Tran Thanh Van, ed. *Proc. XXXV Rencontres de Moriond, Les Arcs, France, March 2000* Paris: Ed. Frontieres (2000)

[71] *Proc. XXX Int. Conf. High Energy Phys., Osaka, Japan, July 2000* Singapore: World Sci. (2001)

[72] *Proc. Meet. DPF, Columbus OH, August 2000* Singapore: World Sci. (2001)

[73] W. D. Apel *et al. Nucl. Phys.* B **154**, 189 (1979).

[74] L. G. Pondrom, *Phys. Rep.* **122**, 57 (1985).

[75] B. Cox, to be published in the proceedings of the Conference on CP Violation Physics, Ferrara, Italy, 2000.

[76] P.Heiliger and L.M.Sehgal, Phys. Lett. B **307**, 182 (1993).

[77] R.Funck and J.Kambor, *Nucl. Phys.* B **396**, 53 (1993).

[78] M.Arenton, to be published in proceedings of BCP4 conference, Ise, Japan, 2001.

[79] V. Flaminio *et al.* "Compilation of Cross-Sections III: p and $\overline{p}$ Induced Reactions," CERN-HERA 84-01 (1984).

[80] M. Cavalli-Sforza *et al. Lettere Al Nuovo Cimento* **18** 174 1977.

[81] G. Belanger and C. Q. Geng, Phys. Rev. D **43**, 140 (1991);

[82] J. L. Ritchie and S. G. Wojcicki, Rev. Mod. Phys. **65**, 1149 (1993).

[83] L. Wolfenstein, Phys. Rev. Lett. **51**, 1945 (1983).

[84] L. M. Sehgal, Phys. Rev. **183**, 1511 (1969).

[85] Whitmore J. *Nucl. Instrum. Methods Phys. Res., Sect. A* 409:687 (1998); Bown C, et al. *Nucl. Instrum. Methods Phys. Res., Sect. A* 369:248 (1996)

[86] G. D'Ambrosio, G. Isidori and J. Portoles, Phys. Lett. B **423**, 385 (1998).

[87] A.Alavi-Harati *et al.*, submitted to PRL, E.Halkiadakis, Ph.D. Dissertation, Rutgers University, 2001.

[88] T.Miyazaki and E.Takasugi, Phys. Rev. D **8**, 2051 (1973).

[89] A.Alavi-Harati *et al.*, submitted to PRL.

[90] L.Zhang and J.L.Goity, Phys. Rev. D **57**, 7031 (1998).

[91] Z.Uy, Phys. Rev. D **43**, 802 (1991).

[92] C.Quigg and J.D.Jackson, LBL preprint UCRL-18487 (1968).

[93] J.F.Donoghue, B.R.Holstein, and G.Valencia, Phys. Rev. D **35**, 2769 (1987); F.J.Gilman and M.B.Wise, Phys. Rev. D **21**, 3150 (1980), and refernces therein.

[94] J.F.Donoghue and F.Gabbiani, Phys. Rev. D **51**, 2187 (1995).

[95] G.D'Ambrosio and J.Portoles, *Nucl. Phys.* B **492**, 417 (1997); G.Ecker, A.Pich, and E.deRaphael, Phys. Lett. B **237**, 481 (1990), P.Heiliger and L.M.Sehgal, Phys. Rev. D **47**, 4920 (1993).

[96] A.Alavi-Harati *et al.*, Phys. Rev. Lett. **83**, 917 (1999).

[97] A.J.Buras, P.Gambino, M.Gorbahn, S.Jager, and L.Silvestrini, *Nucl. Phys.* B **592**, 55 (2000).

[98] A.J.Buras, G.Colangelo, G.Isidori, A.Romanino and L.Silvestrini, *Nucl. Phys.* B **566**, 3 (2000).

[99] A.Alavi-Harati *et al.*, Phys. Rev. Lett. **86**, 397 (2001).

[100] A.Alavi-Harati *et al.*, Phys. Rev. Lett. **84**, 5279 (2000).

[101] A.Alavi-Harati *et al.*, hep-ex/0010059.

[102] A.Alavi-Harati *et al.*, Phys. Rev. D **62**, 112001 (2000).

[103] HB Greenlee, Phys. Rev. D**42**, 3724 (1990).

[104] M.Sadamoto, Ph.D. Dissertation, Osaka University, 1999.

[105] A.Alavi-Harati *et al.*, submitted to PRL, G.B.Quinn, Ph.D. Dissertation, University of Chicago, 2000.

[106] A. J. Buras and R. Fleischer, in *Heavy Flavours II*, edited by A. J. Buras and M. Lindner, (World Scientific, 1997), p. 65.

[107] Donald *et al.*, *Nucl. Phys.* B **61**, 333 (1973)

[108] E. Cheu *et al.*, "An Expression of Interest to Detect and Measure the Direct CP Violating Decay $K_L \to \pi^0 \nu\overline{\nu}$ and Other Rare decays at Fermilab Using the Main Injector" FERMILAB-PUB-97-321-E, Sep 1997.

[109] T. Kobilarcik,"Main Injector Beam to the New Muon and Meson Areas," FERMILAB-TM-2105.

[110] A. M. Kudin, Private Communication.

[111] T. Inagaki *et al.*, "Measurement of the $K_L \to \pi^0 \nu\overline{\nu}$ decay," KEK proposal, (June 1996).

[112] K. Manabe, "Bottom Up Study of $K_L \to \pi^0 \nu\overline{\nu}$ Experiment", Master's Thesis, Osaka University, March, 2000.

[113] G.I. Britvich *et al.* Nucl. Instr. and Meth. **A**231, 64(1992).

[114] M. Kasahara, private communication, Hamamatsu Corporation (Oct., 2000).

[115] B. Baumbaugh *et al.*, IEEE Trans. Nucl. Sci. **43**, 1146 (1996).

[116] M. Ambrogiani *et al.*, Nucl. Phys. Proc. Suppl. **78**, 479 (1999).

[117] J. Frank *et al.*, "A proposal for a precision Measurement of the Decay $K^+ \to \pi^+\nu\overline{\nu}$ and Other Rare K^+ Processes at Fermilab Using the Main Injector", CKM Proposal, (April 2001)

[118] T. Zimmerman and M. Sarraj, IEEE Trans. Nucl. Sci. 43, (1996) 1683.

[119] M Atac et al., Nucl. Instr. Meth. A320 (1992) 155.

[120] See H. Fischer et al., hep-ex-9911009 and also acam-messelectronic gmbh at www.acam.de

[121] D.Ambrose *et al.*, Phys. Rev. Lett. **81**, 5734 (1998).

[122] A. Belyaev *et al.*, "Charged Lepton Flavour Violation in Kaon Decays in Supersymmetric Theories", CERN-TH/2000-213.

[123] Phys. Rev. Lett. **83**, 22 (1999).

[124] W. S. Babbage et al., Nucl. Instr. and Meth. **A330**, 482 (1993).

[125] L. Lönnblad et al., Phys. Lett. **B278**, 181 (1992).

[126] D. Buskulic et al., (ALEPH Collaboration), Phys. Lett. **B313**, 549 (1993).

[127] C. Peterson, Nucl. Instrum. Methods **A279**, 537 (1989).

[128] M. Gyulassy et al., Comput. Phys. Commun. **66**, 31 (1991).

[129] A. Yuille et al.,Proceedings of 1991 IEEE INNS International Joint Conference on Neural Networks, Vol. 1, pp 7-12, Seattle, WA (1991).

[130] M. Ohlsson et al., Comput. Phys. Commun. 71, 77 (1992).

A Comparison with the BNL KOPIO Experiment

The Fermilab Physics Advisory Committee has requested that we provide a comparison of the relative merits of KAMI and the KOPIO experiment at Brookhaven National Laboratory. The primary goal of KOPIO is to obtain ~40 signal events per year with a signal-to-background (S/B) ratio of 2:1 (60 events total). KAMI proposes to obtain ~90 signal events per year with a S/B ratio of 4.6 (110 events total). Both experiments define a "year" of running to be equivalent to 2/3 of a calender year, or approximately 2.0×10^7 seconds. KOPIO expects 6.1×10^6 pulses, each with a 3.6 second cycle time, a 1.6 second flat-top and 1.0×10^{14} protons. For the same running period, KAMI would expect 7.3×10^6 pulses, each with a 3 second cycle time, a 1 second flat-top and 3×10^{13} protons.

There are many ways to compare the relative merits of the two experiments. We will focus here on the basic fundamental requirements necessary to make measurements of this nature:

1. Signal-to-background ratio;
2. The flux of kaons and neutrons;
3. Rate and acceptance.

Our studies indicate that at a very fundamental level, the higher kaon energy available in KAMI (20 GeV compared to 0.75 GeV of KOIPO) gives us an advantage in all three areas. The additional kinematic constraints available to KOPIO are not added merits but absolute necessities in order to execute the experiment at low energy. We seek to determine the break even point in terms of kaon energy, where at low energy one has the advantage of kinematics, while at high energy one has the advantage of better photon vetoing.

A.1 Signal and Background

We have performed a detailed simulation with a realistic detector at five different K_L momenta (500 MeV/c, 1 GeV/c, 5 GeV/c, 10 GeV/c, and 50 GeV/c) to investigate the interplay between kinematical constraints and photon veto inefficiencies [1]. Four different scenarios have been considered. They are:

1. The simple case, where no additional constraints are available and the only applied cut is on the P_t of the π^0;
2. The case where the decay vertex is directly measured;
3. The case where the energy of the kaon is directly measured;
4. The case where both the decay vertex and the kaon energy are measured.

In each case, we optimize the signal-to-background (S/B) by cutting on the relevant kinematic variable to obtain a measurement of η that is accurate to 10%. The simulation assumes a detector with the expected responses for the photon veto detectors and the calorimeter,

micro-bunching, and photon pointing. The photon inefficiencies are those shown in Figure 80. The results of these extensive studies are reported in [1], with the salient features highlighted below.

For the KOPIO apparatus, we assume that the calorimeter has an energy resolution of $3\%/\sqrt{E}$, the photon-pointing preradiator has an angular resolution of 25 mrad and the kaon time-of-flight resolution is 5%. For KAMI, the CsI calorimeter has an energy resolution of $1\%/\sqrt{E}$.

Figure 68 shows the results of the study. We caution that one should not take the absolute level of the S/B too seriously, but the relative merits of the kinematical constraints should serve as a guide to the advantages that high energy kaons provide. Both curves in Figure 68 have a steep slope with respect to kaon energy because of the improved efficiency for vetoing photons at higher energy. At 500 MeV, a 10% measurement of η cannot be attained. It should be noted that at low energy (~1 GeV) full kinematics is absolutely necessary to obtain the S/B necessary to make a viable measurement, and that a deficiency in any of the kinematical handles (poor kaon energy measurement or photon angular resolution) make it impossible to obtain a S/B>1. However, at higher energy (~20 GeV), the S/B begins at about 5. From this we conclude that the measurement of $K_L \to \pi^0 \nu\bar{\nu}$ at higher energies involves less risk than attempts at lower energy.

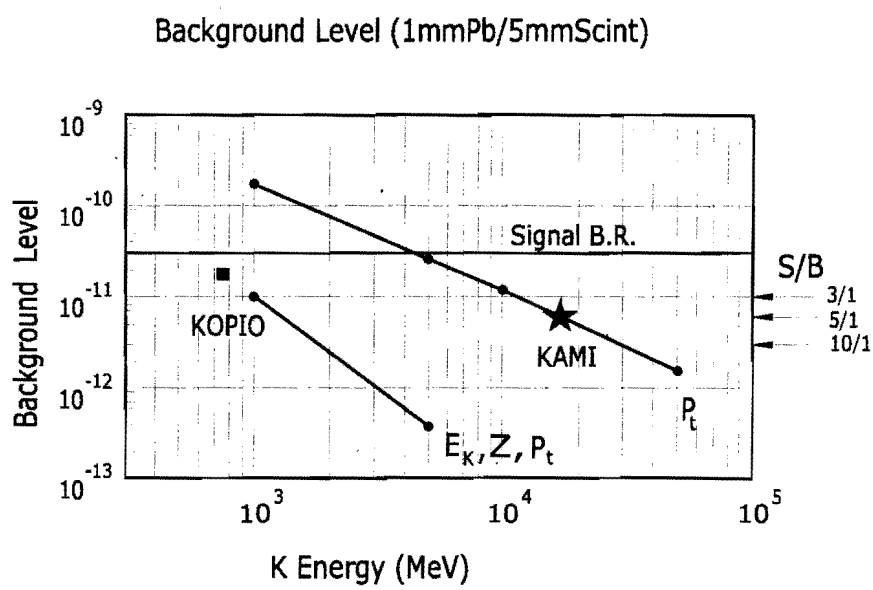

Figure 68: The results of the signal-to-background (S/B) study demonstrating the relative merits of kinematical constraints at low energy and photon vetoing at high energy.

A.2 Particle Production and Beam Characteristics

The advantages of high energy provide KAMI with a relatively large kaon production cross section allowing for a relatively small beam size (0.41 μstr) and a neutron-to-kaon ratio of ~7:1 (~470 MHz of neutrons) with no beryllium absorber. In order to obtain a sufficient number of $K_L \to \pi^0 \nu\overline{\nu}$ decays at low energy, KOPIO is forced to utilize a large "flat ribbon" beam 500 μstr in size with a neutron-to-kaon ratio of ~100:1 (~30 GHz of neutrons). Working in such a low energy, high-rate, very large solid angle beam, something that has not been attempted before, could be problematic. Using a beam with some similar characteristics to that proposed by BNL, a KEK experiment attempting to measure $K^+ \to \pi^+ e^+ e^-$ has observed a sea of low-energy neutrons. From our experience, all important effects from a neutron halo are much reduced at higher energy where beams are naturally of smaller solid angle and the experiment is situated further from the production target.

The KOPIO proponents argue that most of the neutrons are of too low an energy to be of any concern, and that they are much more spread out in time than the expected signals from decay photons. Nevertheless, given that both detectors have a Beam-Anti or beam catcher that must live in such environments, this is a concern.

Anti-neutron production could be another problem at low energy. Anti-neutrons can and do produce π^0's even at rest; and if there is a component of anti-neutrons in the halo, this could be even more serious than neutrons in faking photons in the detector. Of course at higher energies, neutrons and anti-neutrons behave for all intents and purposes identically, so KAMI is immune from this concern.

A.3 Rate and Acceptance

KAMI and KOPIO both operate in an environment with a high rate of of kaon decays. Accidental losses from kaon decays will have a significant impact on the final event yields of both experiments. KAMI will run with a debunched beam in order to spread out the rate of accidental activity in the detector. KOPIO operates with a micro-bunched beam by necessity which can only exacerbate accidental losses. KAMI has taken a very conservative approach to estimating accidental losses, which add up to 45%, by defining a 20 ns veto window in the vacuum veto detector and a 10 ns veto window in the Beam Anti. KOPIO uses a 2 ns veto window and quote a 10% loss from accidentals even though their decay rate and neutron flux is higher than KAMI's. In the absence of accidental losses, KAMI would collect ~160 events per year compared to ~72 events per year for KOPIO. Both experiments will obviously work as hard as possible to minimize the magnitude of accidental losses.

KAMI has an acceptance for $K_L \to \pi^0 \nu\overline{\nu}$ of that is approximately 7 times larger than KOPIO. This factor of 7 results from the combined geometry and performance of the calorimeter and the relative beam sizes. The KAMI CsI calorimeter is a circular array with a diameter of 2.75 m, block sizes of 2.5 cm × 2.5 cm × 27 radiation lengths near the beam hole and 5 cm × 5 cm × 27 radiation lengths elsewhere. The energy resolution of the KAMI CsI calorimeter is ~1%. KOPIO has chosen a 5.2 m ×5.2 m Shashlyk based calorimeter with a resolution response of ~8% and a granularity of 10 cm. Perhaps the most important issue besides the obvious geometric advantage (e.g. cluster separation and fusion cuts), the CsI calorimeter also performs as a superior photon veto for background events with more than

2 photons in the calorimeter.

Because of the rather elaborate photon converter that KOPIO is forced to use in order to reconstruct the π^0 decay photons, besides the loss in acceptance, there is lateral spreading of the resulting electromagnetic showers. In order to obtain the desired resolution, the BNL group must add in calorimeter channels corresponding to a region of diameter of about 120 cm [2]. The corresponding figure for the KAMI calorimeter is just 15 cm.

A final point of comparison is related to the charged particle spectrometer implemented in KAMI but absent in KOPIO. KAMI is not a single decay mode experiment. The spectrometer gives KAMI sensitivity to all K_L and π^0 decay modes. KTeV has demonstrated this principle well. In the most current compilation from the Particle Data Group, there are only two K_L rare decay results that are not from KTeV.

KAMI and the KOPIO experiment at Brookhaven National Laboratory are both designed to detect the very rare decay $K_L \rightarrow \pi^0 \nu \overline{\nu}$. The approaches of the two efforts are complementary. KAMI is a high energy experiment which relies on the many advantages available at high energy. KOPIO is a low energy experiment which relies on a time-structured beam, time-of-flight and reconstruction of photon directions to kinematically reject background. Both experiments rely heavily on the performance of photon veto detectors, though the efficiency for vetoing photons is a more critical parameter for KAMI. Both experiments should go forward. Consistent results from the two measurements, which have very different systematics, would give the community confidence in the implied conclusions. In the event that these results imply a deviation from the Standard Model, confirmation from a second independent group would be an important statement.

References

[1] K. Manabe, "Bottom Up Study of $K_L \to \pi^0 \nu\overline{\nu}$ Experiment", Master's Thesis, Osaka University, March, 2000.

[2] I-H. Chiang *et al.* "K0PI0 - a Search for $K_L \to \pi^0 \nu\overline{\nu}$ ", NSF proposal, November (1999).

B Results From The 2000 KAMI Beam Test

B.1 KAMI Measurements of Neutral Hadron Beam Rates

A beam test for KAMI was performed at the beginning of 2000, immediately following the 1999 KTeV run. Using a 150 GeV proton beam incident on a 30 cm long Beryllium Oxide target, the kaon and neutron rates in a secondary neutral hadron beam were measured and compared with predictions. The measurements were made with beam-detector (targeting) angles of 12, 15 and 20 milli-radians. The experiment took place at the Fermilab Tevatron and used the KTeV beamline and detector.

B.1.1 Overview of the Measurement

The neutral hadron rates were measured using the KTeV detector at Fermilab. This detector was designed to measure $Re(\epsilon'/\epsilon)$ and to search for rare kaon decays using an 800 GeV proton beam that produces kaons in the energy range 20-200 GeV. The test-beam results presented here used a 150 GeV proton beam resulting in kaon energies that are several times smaller than what the KTeV detector was designed for. Our charged spectrometer is only sensitive to kaon energies above 20 GeV; to measure the kaon rate and spectrum down to 6 GeV we used the CsI calorimeter [1] to detect the six photons from $K_L \to 3\pi^0$ decays. Extracting the absolute kaon rate and spectrum requires large corrections due to acceptance (few percent) and decay fraction ($\sim$ 8%). However, a precise Monte Carlo simulation of the KTeV detector has been developed for the $Re(\epsilon'/\epsilon)$ analysis [2] which can be used to determine the acceptance for this measurement to good precision. As a systematic check, $K_L \to \pi^+\pi^-\pi^0$ decays can also be used to verify the kaon rate and energy spectrum for kaon energies above 20 GeV.

The neutral beam rate, consisting of neutrons and kaons that did not decay, was measured using a six-interaction length Uranium Calorimeter (UCAL) placed in the beam. The UCAL had 100% geometric acceptance for beam-particles that did not decay. The neutron rate was determined from the difference in the total UCAL rate and the measured kaon rate from $K_L \to 3\pi^0$ decays.

B.1.2 Definition of Flux

The measured hadron flux ($\mathcal{F}_{HAD}$) is the number of hadrons per unit solid-angle per incident proton on the 30 cm long BeO target. The exact definition is

$$\mathcal{F}_{HAD} = \left(\frac{N_{HAD} \cdot \mathrm{PS}}{\epsilon_{acc} \cdot \mathrm{DK_{cor}}}\right) \times \left(\frac{10^6}{N_p \cdot \epsilon_{live} \cdot \epsilon_{tgt} \cdot d\Omega}\right) \tag{25}$$

$$= (NCOR) \times (N2F) \tag{26}$$

where

- N_{HAD} is the experimentally measured number of hadrons (neutrons and/or kaons) after all off-line analysis cuts.

- PS is the trigger pre-scale.
- ϵ_{acc} is the signal acceptance. For kaon decays this includes both geometric acceptance and analysis cuts. For neutrons (and kaons that do not decay) the geometric [UCAL] acceptance is 100% and the analysis efficiency is taken as the efficiency of the trigger.
- $\mathrm{DK_{cor}}$ is the decay-fraction correction. For neutrons we have $\mathrm{DK_{cor}} = 1$ since the 15 minute life-time is too large to notice. ~8% of the kaons decay before hitting the UCAL, so $\mathrm{DK_{cor}} \sim 0.92$ for kaons that hit the UCAL.
- N_p is the total number of protons delivered to the target.
- ϵ_{live} is the trigger live-time (typically above 95%).
- ϵ_{tgt} corrects for the effective target length seen by the beam.
- $d\Omega$ is the solid angle of the secondary beam which is 0.212 ± 0.004 μstr for this measurement.

The factor 10^6 in the numerator converts the flux units to $\times 10^{-6}$/prot/μstr. Note that Eq. 25 is separated into two parts, $NCOR$ and $N2F$ as shown in Eq. 26. The quantity $NCOR$ depends explicitly on which hadron (k or n) is under study. The quantities that contribute to $N2F$ (N to $\mathcal{F}$ conversion) depend only on the run conditions.

B.1.3 KTeV Beamline and Detector

The Main Injector was used to inject protons into the Tevatron, which were then delivered to the KTeV target. Since the KTeV beamline was designed to transport 800 GeV beam, significant modifications were made to accommodate the 150 GeV beam.

The beam intensity during the test was $\sim 5 \times 10^{11}$ protons per pulse, where each pulse is 40 seconds in duration and repeats every 80 seconds. This intensity is about ten times *less* than the nominal KTeV intensity, resulting in nearly 100% trigger live time. Although KTeV was designed with two nearly parallel kaon beams, one of the beam holes was plugged for this measurement so that only one beam entered the KTeV decay volume.

The vacuum decay region is 90-159 meters from the target. This is followed by a magnetic spectrometer with four drift chambers, a Cesium Iodide (CsI) electromagnetic calorimeter, photon vetoes and a Uranium hadron calorimeter (UCAL) located behind one of the CsI beam holes. Helium bags filled most of the air gaps in the spectrometer in order to reduce the amount of material in which particles can scatter.

The CsI calorimeter consists of 3100 individual crystals [1] and with its multi-range DPMT readout [3] energies from a few MeV up to 100 GeV were accurately recorded. The calorimeter has two 15×15 cm^2 beam holes to allow two neutral beams to pass through without interaction; the UCAL (see below) was placed behind one of these beam holes. The CsI performance is shown in Figure 69 which shows the ratio of CsI cluster energy to track-momentum (E/p) for $K_L \to \pi^{\pm} e^{\mp} \nu$ decays. The peak at 1.0 is due to electrons and positrons; the distribution below 1.0 is due to the charged pions. Figure 69 is from data at the end of the week-long beam test, after which the CsI calorimeter had not been calibrated

for three weeks; the mean E/p had drifted by almost 2% and the resolution had degraded to 2% (from 1%). Although this is not optimal for the $Re(\epsilon'/\epsilon)$ analysis, it is still an excellent calorimeter for measuring the kaon rates with $K_L \to 3\pi^0$ decays.

The UCAL consists of 15 layers of Uranium and Kuraray SCSN-88 scintillator. Each U-slab has dimension $46 \times 46 \times 4.3$ cm^3, corresponding to 0.41 nuclear interaction lengths, or 13.4 radiation lengths. The Uranium is contained in a 0.7 mm steel casing, which adds 1.4 mm Fe per layer, or 21 mm total. The total mass is about 2,800 kg (about 1/3 of the CsI mass). Each scintillator channel has dimension $43.2 \times 43.2 \times 1.0$ cm^3; the scintillation light was brought to a PMT via Kuraray SCSF-B21 wavelength shifting fibers. The PMT gains were a $few \times 10^5$ and one MIP contributes roughly 15 photo-electrons per channel. Each PMT signal was digitized *twice* using 11-bit FERA ADC modules. The first set of ADCs had unity gain and served to measure the energy spectrum of the beam. A second set of ADCs followed a $\times 10$ amplifier in order to allow muon calibration using the same PMT high voltage.

After calibrating the UCAL channels relative to one another with muons, the final overall calibration from MIPs to "hadron GeV" was done using $\Lambda \to p\pi^-$ decays. The KTeV-E832 regenerator [2], which is a 1.7 meter long stack of scintillator plates, was placed in the neutral beam at 122 meters from the primary target. This secondary target was used to generate Λ's via the reaction $K^0 + n, p \to \Lambda + X$. The $\Lambda \to p\pi^-$ decay products were momentum analyzed in the magnetic spectrometer. There are more than 13 thousand momentum-tagged protons which hit the UCAL, and the background-to-signal ratio is 1.4%. The $\Lambda \to p\pi^-$ calibration resulted in 2.7 "hadron" GeV/MIP compared to 2.6 GeV/MIP from a GEANT simulation. The ratio of energy measured in the UCAL to the track momentum of the tagged proton is shown in Figure 70. The peak is centered at 1.00 (by definition) and the width is 18.5%. The E/p response of the UCAL to protons varies by less than 3% with respect to the momentum of the protons and the width of the E/p peak changes from 25% at 20 GeV to 15% at 120 GeV. The same study was performed with a GEANT-based simulation. GEANT predicts an 8% E/p variation with proton momenta and slightly worse resolution.

The trigger for $K_L \to 3\pi^0$ decays required at least 2 GeV of energy deposited in the CsI crystals near the beam hole. The on-line Level 3 filter software then selected events with six clusters of energy in the CsI array. A UCAL self-trigger selected events in which the 15-channel analog sum exceeded 0.8 MIPs, or about 2 "hadron" GeV. No software filter was applied to the UCAL triggers.

B.1.4 Kaon Rates

The number of kaons in the beam was determined by counting the number of fully reconstructed $K_L \to 3\pi^0$ decays, and then correcting for the acceptance. The kaon energy spectrum and flux, at $Z = 90$ meters from the target, was determined by correcting for the acceptance and decay fraction in each kaon energy bin. The corrected kaon energy spectrum is shown in Figure 71 along with a Malensek-based prediction [4]. At all three beam-detector angles the kaon energy peak in the data is a few GeV higher than the prediction. As a systematic check, the kaon energy spectra above 20 GeV are compared between $K_L \to 3\pi^0$ and $K_L \to \pi^+\pi^-\pi^0$ decays. These two independent analyses show excellent agreement in both the spectral shape and absolute flux.

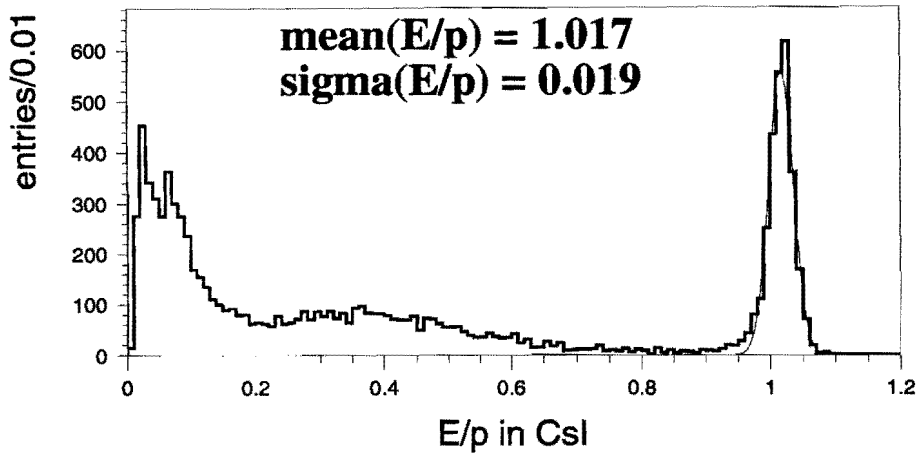

Figure 69: E/p measured in the CsI calorimeter at the end of the beam test with 150 GeV protons on target. The mean and sigma are from a Gaussian fit in the region $0.90 < E/p < 1.10$.

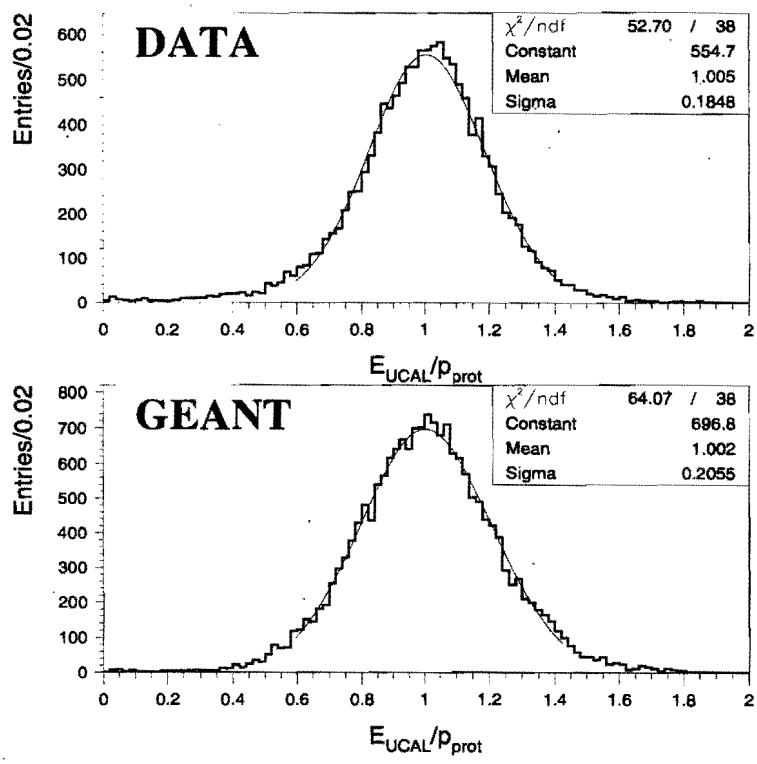

Figure 70: Ratio of UCAL energy to track momentum for protons tagged via $\Lambda \to p\pi^-$ decays. The top plot is for data; the bottom plot is from a GEANT-based simulation.

The absolute kaon flux defined by Eq. 25 is shown in Figure 72 as a function of the beam-detector angle. The statistical errors are all less then 3% and hence the total errors are dominated by the following systematic errors: 20% from effective target length correction, 5% from proton beam loss corrections, 5% from MC acceptance and 2% from the solid angle. Note that most of these systematic uncertainties are *correlated* among the different beam-detector angles. The relative systematic uncertainty between different beam-detector angles comes from an effective target length correction which is about 0.65.

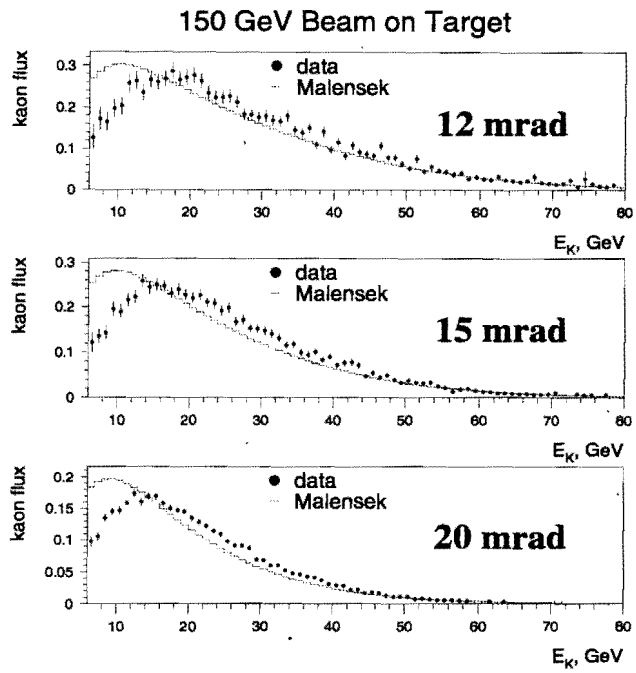

Figure 71: The corrected kaon energy spectrum based on $K_L \to 3\pi^0$ decays, at 12, 15 and 20 milliradians. The data are shown with solid dots and the Malensek-based prediction is shown by the histogram. The flux units (vertical axis) are $\times 10^{-6}/\text{prot}/\mu\text{str}/GeV$.

B.1.5 Neutron Rates

The analysis of the UCAL consists of summing the energies in the 15 active layers and applying tight veto cuts to reject charged particles passing through the beam hole and hitting the UCAL. Veto cuts were applied to the CsI calorimeter, drift chambers, and the muon and photon veto systems. Events with early activity in the UCAL are also rejected. The analysis efficiencies are 0.77, 0.91 and 0.96 at 12, 15 and 20 mrad beam-detector angles, respectively. The total flux of neutrons and kaons in the UCAL $\mathcal{F}_{(n+k)}$, is defined by Eq. 25. The neutron flux is obtained by subtracting the kaon flux,

$$\mathcal{F}_n = \mathcal{F}_{(n+k)} - \mathcal{F}'_k \times (1 - \text{DK}'_{\text{cor}}) \tag{27}$$

where $\text{DK}'_{\text{cor}} \simeq 0.1$ is the estimated fraction of kaons which decay before hitting the UCAL, and whose hadronic decay products do not hit the UCAL. The neutron energy spectrum at

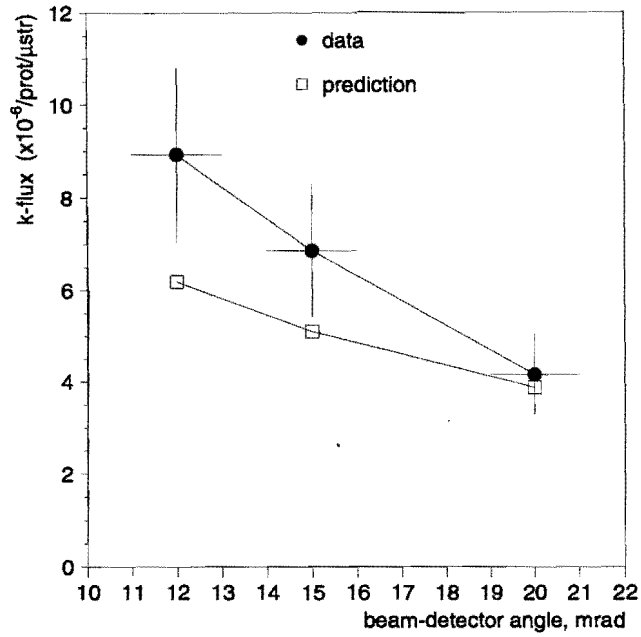

Figure 72: The kaon flux for energies above 6 GeV vs. beam-detector angle. Both data from this experiment (dots) and the predictions (open squares) are shown.

20 milli-radians is shown in Figure 73, along with a GEANT-based prediction. The absolute flux vs. beam-detector angle is shown in Figure 74, along with predictions [5].

The ratio of neutrons to kaons is shown in Figure 75. This ratio is very insensitive to the target length correction so the uncertainty is largely free of systematics. The data show that the n/k ratio is almost TWO TIMES smaller than predictions.

B.1.6 Flux and Absorber Studies

The measured kaon flux is compared with the Malensek prediction in Table B.1.6. Note that for both the data and Malensek predictions the kaon flux is for $E_K > 6$ GeV at $Z_K = 90$ m. The errors on the data are dominated by the 20% uncertainty in the effective target-length correction. The errors on the predictions are based on the ± 1 mrad uncertainty in the beam-target angle. The data are consistent with the predictions at the 2-σ level.

The data prediction with 150 GeV beam seems to under-estimate the kaon energy peak by several GeV. The measured average kaon energy (above 6 GeV) is 2 GeV higher than Malensek-based predictions.

The measured neutron fluxes are almost a factor of 2 *lower* than predictions. To get the neutron flux, the kaon flux must be subtracted,

$$\mathcal{F}_n = \mathcal{F}_{(n+k)} - \mathcal{F}_k \times (1 - \mathrm{DK}'_{\mathrm{cor}}) \tag{28}$$

where $\mathrm{DK}'_{\mathrm{cor}}$ is the fraction of kaons which decay before hitting the UCAL, and whose hadronic decay products do not hit the UCAL. The absolute neutron flux is shown below in

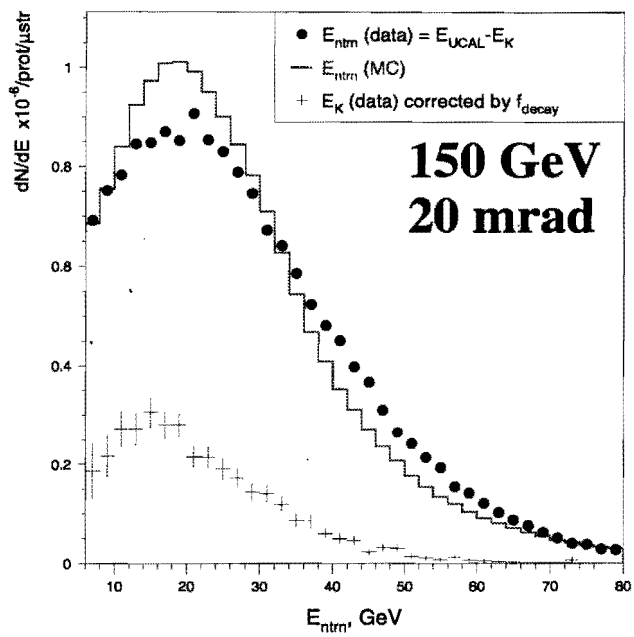

Figure 73: Neutron energy spectrum with 150 GeV beam at 20 mrad. The data are shown in **dots** after subtracting the kaon energy spectrum (crosses) at the UCAL Z-location. The thick line histogram is a GEANT-based prediction after re-scaling to have the same area as the data.

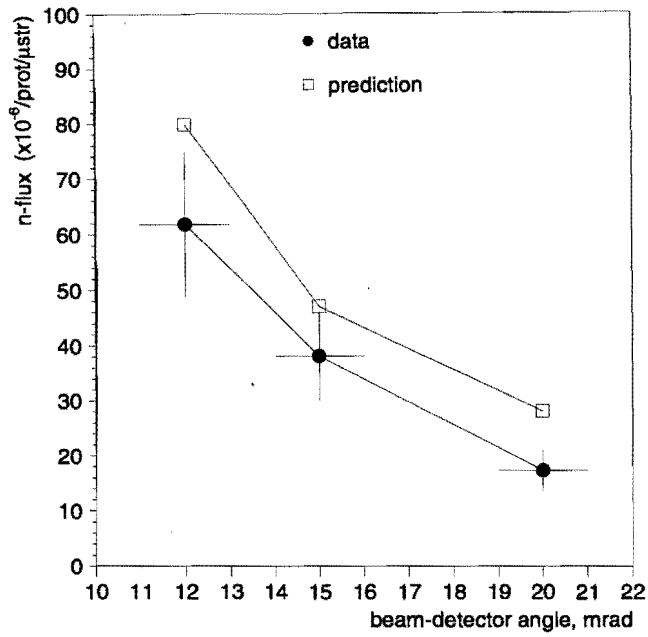

Figure 74: The neutron flux ($\mathcal{F}_n$) for energies above 2 GeV vs. beam-detector angle. Both data from this experiment (dots) and the predictions (open squares) are shown.

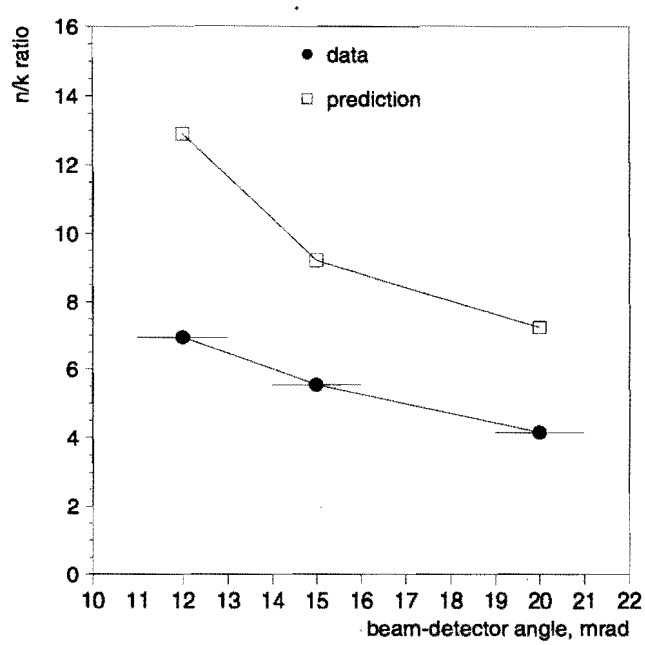

Figure 75: The neutron/kaon ratio vs. beam-detector angle.

Table B.1.6. The 150 GeV beam predictions for $\mathcal{F}_n$ were obtained by scaling the 120 GeV predictions by 150/120.

Figure 76 shows the n/k ratio vs. Be absorber thickness for all four beam energy/target angles. Also shown is the relative n/k ratio relative to the n/k ratio with no Be absorber. This shows that the n/k ratio dependence on Be is very nearly constant regardless of the production spectrum; 10" Be reduces n/k by 30%, 20" Be reduces n/k by about a factor of two and 38" Be reduces n/k by about a factor of three. We also found that the kaon energy spectrum is *not* distorted by the 20"Be.

B.1.7 Summary

This report describes the neutral hadron flux analysis using data from the 2000 KAMI beam test. The proton beam energies were 800 and 150 GeV, the latter intended to be near the nominal KAMI beam energy of 120 GeV. At 150 GeV the neutron and kaon flux was measured at three beam-target angles: 12, 15 and 20 mrad. The K_L flux was measured using $K_L \to 3\pi^0$ decays, and was successfully checked with $K_L \to \pi^+\pi^-\pi^0$ decays for $E_K > 20$ GeV. The neutron flux was measured using a six-interaction length Uranium Calorimeter behind one of the CsI beam holes; it was calibrated with muons and with tagged protons from $\Lambda \to p\pi^-$ from the regenerator. The measured fluxes were compared with predictions, and in general the agreement was good to well within a factor of two. Some of the main results and conclusions from this analysis are:

- the absolute neutron flux is $30 \pm 10\%$ lower than predictions (Fig. 74) at all targeting angles;.
- the absolute kaon flux is 30% higher (at 12 and 15 mrad) and comparable (at 20 mrad) with the Malensek-based predictions (Fig. 72);
- the measured n/k ratios are a factor of 2 lower than the predictions (Fig. 75);
- With 150 GeV beam the kaon energy spectrum is a few GeV "stiffer" than Malensek-based predictions;

target angle (mrad)	$\mathcal{F}_k$ (data)	$\mathcal{F}_k$ (predict)	data/predict ratio	$< E_K >$ (data)	$< E_K >$ (predict)
12 ± 1	8.92 ± 1.87	6.18 ± 0.25	1.44 ± 0.28	27.72	25.47
15 ± 1	6.86 ± 1.44	5.10 ± 0.18	1.34 ± 0.26	25.16	22.95
20 ± 1	4.16 ± 0.87	3.87 ± 0.20	1.07 ± 0.20	21.51	19.66

Table 25: Kaon flux ($\mathcal{F}_k$) vs. target angle compared with Malensek predictions; $E_K > 6$ GeV and $Z_K = 90$ m. The incident proton beam energy is 150 GeV with no Be absorber in the neutral beam. The flux units are $\times 10^{-6}$/prot/μstr and the errors are systematic only. $< E_K >$ refers to the average kaon energy in GeV.

target angle (mrad)	$\mathcal{F}_{(n+k)}$ (data)	$\mathcal{F}_k$ (data)	$1 - \mathrm{DK}'_{\mathrm{cor}}$	$\mathcal{F}_n$ (data)	$\mathcal{F}_n$ (predict)	data/predict ratio
12	69.8	8.9	0.90	61.8	79.8	0.77
15	44.2	6.9	0.90	38.0	47.0	0.81
20	21.0	4.2	0.90	17.3	28.0	0.62

Table 26: Summary of absolute neutron flux with $E_n > 2$ GeV, and comparison with predictions. The incident beam energy is 150 GeV with 0" Be absorber in the neutral beam. All flux ($\mathcal{F}$) units are $\times 10^{-6}$/prot/μstr.

- At both 150 and 800 GeV beam, the neutron energy spectrum peak is consistent with GEANT-based predictions. However, the data distributions are broader than the simulations
- Adding Beryllium absorber does *not* change the kaon energy spectrum, but it changes the neutron energy spectrum by preferentially absorbing higher energy neutrons;

B.2 Beam Test Results for a Prototype Beam Anti

In January and February of 2000, at the end of the Fermilab fixed target run, the KTeV experiment devoted several days to various studies pertinent to the KAMI experiment. Among the studies performed was that of the operation of a calorimeter prototype (BAG) based on quartz detectors. The BAG calorimeter consisted of 20 layers of quartz where each layer was $0.059X_0$ thick. The quartz layers were interspersed with $0.44X_0$ thick lead sheets. The overall thickness was about 10.5 radiation lengths. The Cerenkov light was detected by 35 PMTs positioned on both sides of the detector, 4 rows on one side and 3 rows on the other side, 5 PMTs in each row.

The KTeV detector configuration was modified by moving the KTeV transition radiation detector system transverse to the beam so that they covered the beam regions. In addition one of the two beams was blocked so that one of the two beam holes in the CsI detector could permit access to the BAG test calorimeter which was stationed directly behind the CsI. In this configuration, decay products from the neutral K decays could be used to study the response of the BAG to electrons. In addition, we were able to collect data on the response of the BAG to muons.

A clean electron sample in the BAG was obtained by selecting K_{e3} decays by kinematic cuts and determining the pion and electron nature of the two charged tracks using the eight station TRD system. Additional verification of the pion identity of one of the tracks was obtained by requiring that the track identified as a pion by the TRD go into the CsI so that an E/p cut could be made.

With these criteria, a very clean sample of electrons passing though the hole in the CsI and striking the BAG could be obtained. The energy spectrum for these events is shown in Fig. 77 in units of minimum ionizing pulse heights (MIPs) where a MIP is the most probable response to a minimum ionizing track. The x axis in this plot is $\ln(E/E_\mu)+1$. The feature

in this plot at zero MIPs is the pedestal obtained by recording events in which both charged particles went into the CsI and no track intersected the BAG.
A 34k sample of almost pure electrons were obtained in this way. These are the events that comprise the large group at centered at 4. No track failed to give a signal in the detector and only a very few events (approximately 8) were significantly below the the large electron signal. The nature of these few events was determined by varying the TRD cuts on tracks allowing particles other than electrons into the BAG. The variation of the peak at 1 MIP obtained by the varied TRD cuts cuts suggests that these few events were muons, most likely due to a $K_{\mu 3}$ background. The total BAG inefficiency for electrons estimated from the study of this spectrum, which was limited by K_{e3} statistics, is $\leq 3 \times 10^{-5}$ or less. This is to be compared to the inefficiency goal of 0.1% for photons with energy greater than 10 GeV.

The response of the BAG to muons is shown in Fig. 78 A clean sample of 19.7k muons was obtained by closing collimators in the KTeV neutral beam and making a muon run.
The lower edge of the muon spectrum obtained in this way is shown on a greatly expanded scale in Fig. 78, A very clean separation of the 1 MIP peak from threshold (determined to be at zero) is seen. There are four events below the lower edge of the Landau distribution due to the muons. From this we infer that the inefficiency for seeing muons is at most 2×10^{-4}.

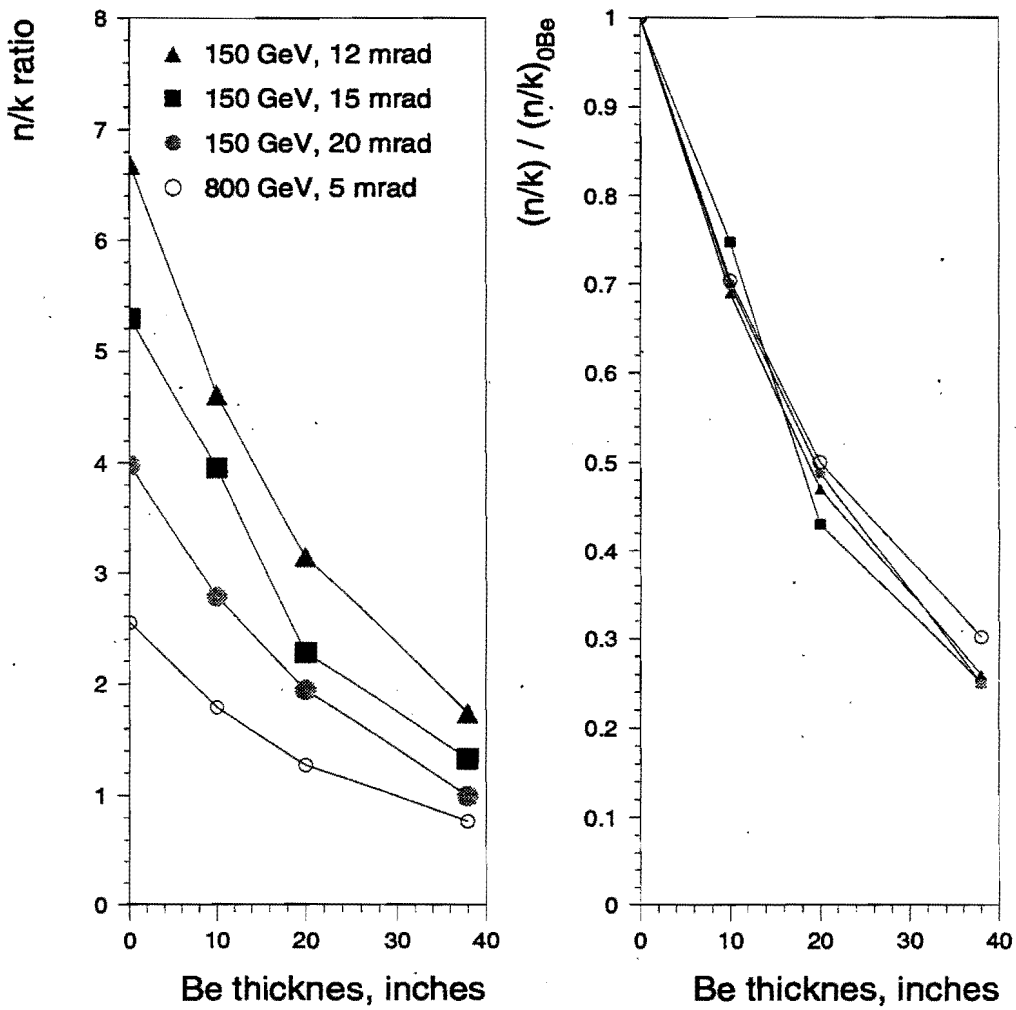

Figure 76: The neutron to kaon ratio (n/k) is shown as a function of Be absorber thickness (left). The right plot shows the n/k ratio *relative* to the n/k ratio with no Be absorber.

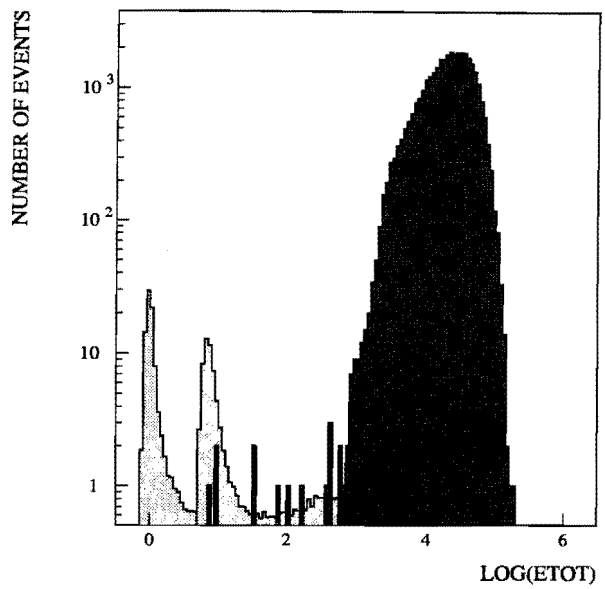

Figure 77: Electron energy spectrum in the BAG obtained in the KAMI beam test from K_{e3} decays in units of MIPs; the x axis is $\ln(E/E_\mu)+1$; the peak at zero is the pedestal, the intermediate peak at 1 MIP is the peak due to charged particles mainly muons and the large peak centered at 4 is the electron peak

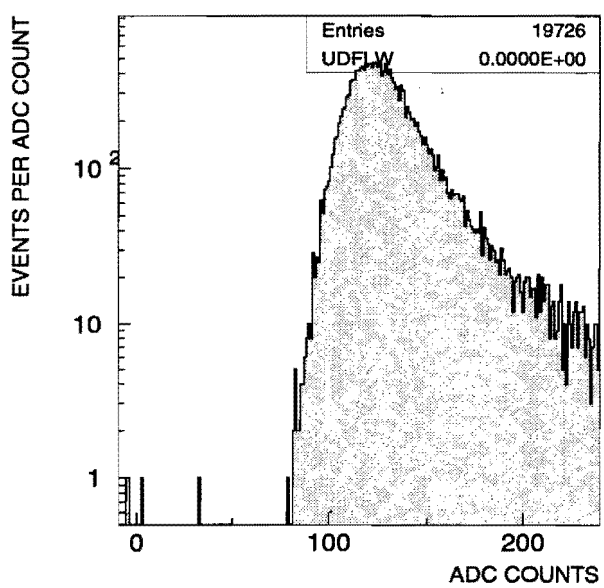

Figure 78: Muon energy spectrum in the BAG obtained in the KAMI beam test

References

[1] A.J. Roodman, "The KTeV Pure CsI Calorimeter," Proceedings of the VII International Conference on Calorimetry (World Scientific, 1998)

[2] Phys. Rev. Lett. **83**, 22 (1999).

[3] J. Whitmore, Nuclear Instruments and Methods in Physics Research A 409 (1998) 687-690.

[4] A. J. Malensek,"Empirical Formula for Thick Target Particle Production"' Fermilab Report FN-341 (1981).

[5] E.Edwards *et. al.*,, Phys. Rev **D18**, 76 (1978),
J.Engler *et. al.*,, Nucl. Phys. **B84**, 70 (1975).

C Photon Veto Inefficiency

Since the major background for the $K_L \to \pi^0\nu\overline{\nu}$ signal results from the decay $K_L \to \pi^0\pi^0$ with two missing photons, understanding the sources of detection inefficiency for the photons is important.

There are three mechanisms by which photons can escape detection:

- Punch through where the photon travels through the detector without an interaction. This effect can be calculated easily from the photon cross section;
- Sampling effect in lead-scintillator sandwich detector, where most of energy is absorbed in the lead and the amount of energy deposited in the scintillator is below the detection threshold. This effect can be studied using EGS or GEANT simulations.
- Photo-nuclear interaction where a photon excites heavy nuclei producing multi-neutron final states. This is more difficult to simulate than the sampling effect.

C.1 Inefficiency Due to Photo-Nuclear Interactions

In order to understand the detection inefficiency due to the photo-nuclear interactions, a collaboration of physicists from the three future $K_L \to \pi^0\nu\overline{\nu}$ experiments initiated experiment ES171 at KEK Tanashi in Japan. Figure 79 shows the plan view of the experiment. Electrons from the synchrotron passed through a ~300 μm thick aluminum foil and emitted radiative photons. Three different incident electron energies, 430, 750, and 1100 MeV, were used. The momentum of the electron after the photon emission was measured by a spectrometer magnet and 32 scintillators placed at the focal plane of the spectrometer. Each scintillator covered a 10 MeV/c momentum bin. The difference between the incident electron energy and the energy of the electron after the radiation gave the energy of the radiated photon. The radiated photon went through active collimators and hit the detector under study, located downstream. The detector was surrounded by 12 liquid scintillator (NE213) counters to detect neutrons emitted from a photo-nuclear interaction.

In the analysis, the neutrons in the neutron counters were distinguished from photons based on the TOF and the pulse shape from the liquid scintillator. More than one neutron was required to tag a photo-nuclear interaction. The efficiency for tagging the interaction was estimated by fitting the multiplicity of neutrons with a Poisson distribution.

The number of incident photons was estimated by using a pre-scaled sample of photons which deposited an amount of energy consistent with the energy loss of the electron measured in the spectrometer.

The detection inefficiency was measured for the following three detectors.

- An alternating stack of 1 mm thick lead sheets and 5 mm thick scintillator plates, totaling 18 radiation lengths;
- An alternating stack of 0.5 mm thick lead sheets and 5 mm thick scintillator plates;
- A 3x3 array of pure CsI crystals. Each crystal was 5 cm x 5 cm x 50 cm (27 X_0).

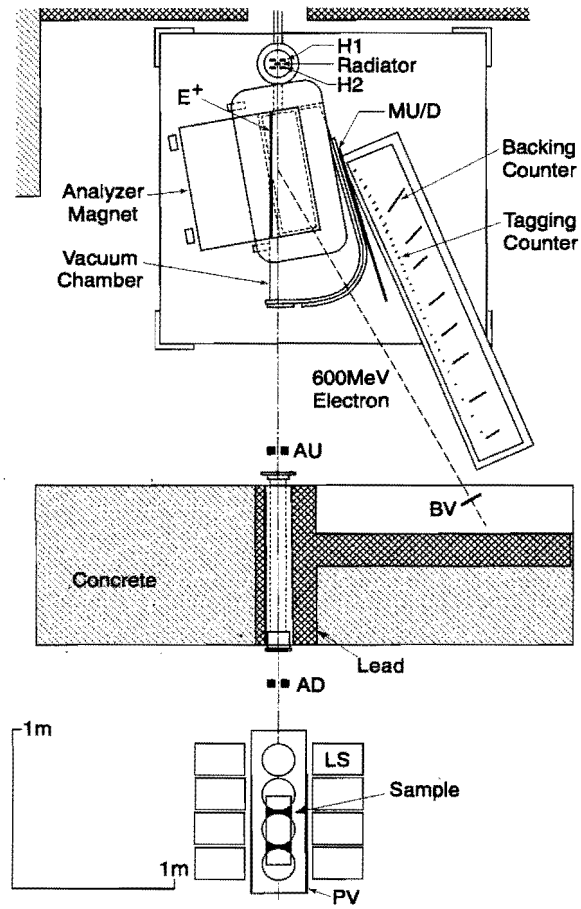

Figure 79: Plan view of the ES171 experiment.

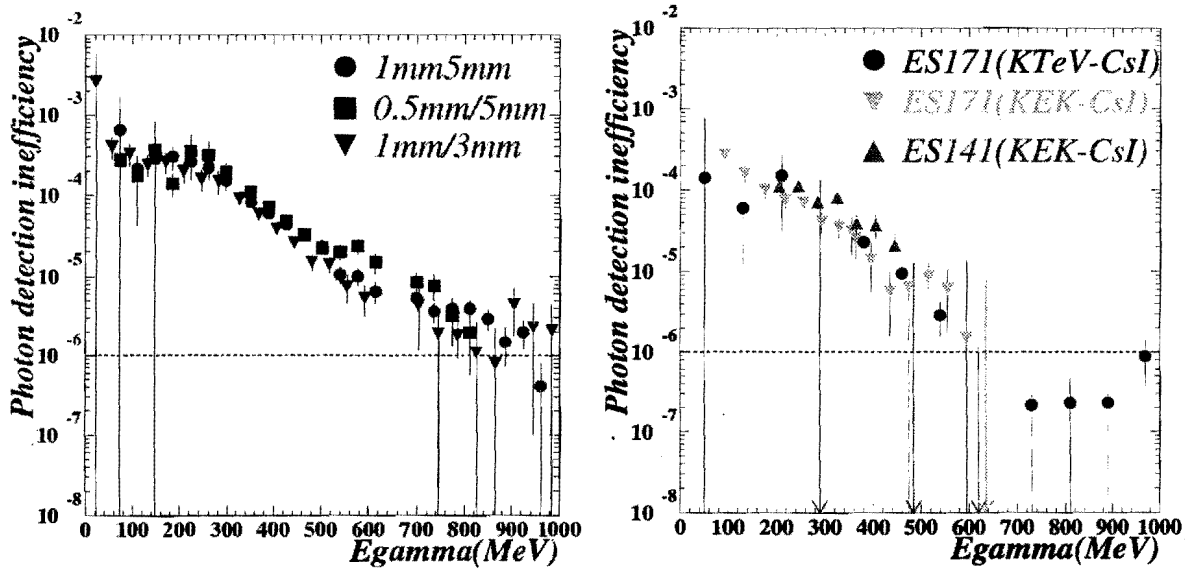

Figure 80: The plot on the left shows the inefficiency of lead/scintillator sampling detectors due to photo-nuclear interactions for 3 different sampling ratios. The default design for KAMI consists of 1 mm thick lead sheets and 5 mm thick scintillator tiles. The plot on the right shows the inefficiency of a pure CsI detector due to photo-nuclear interactions. The data in both plots was taken with a 10 MeV detection threshold.

Figure 80 shows the detection inefficiency due to photo-nuclear interactions as a function of the incident photon energy for the lead/scintillator sandwich detector and the CsI, respectively,. The threshold is set is to the equivalent of 10 MeV incident photons. The inefficiency is a strong function of the photon energy, and it drops from 3×10^{-4} at 100 MeV to 1×10^{-6} at 1000 MeV.

C.2 Total Inefficiency Including Sampling Effects

The detection inefficiency due to electromagnetic interactions was estimated using the EGS simulation code. Figure 81 shows the combined photon detection inefficiency due to sampling effects and photo-nuclear interactions. The threshold was set to the equivalent of a 10 MeV incident photon. For photon energies below 30 MeV, the effect due to sampling effects dominates while the effect due to photo-nuclear interaction is dominant above 30 MeV.

In Figure 81 the inefficiency above 1 GeV is corresponds to the requirement given in the KAMI EOI [1], which conservatively assumes that the inefficiency is flat for higher energies. A new beam test is planned to measure the photon veto inefficiency between 1.5 GeV and 3.5 GeV in April 2001 at the Spring 8 photon factory in Japan.

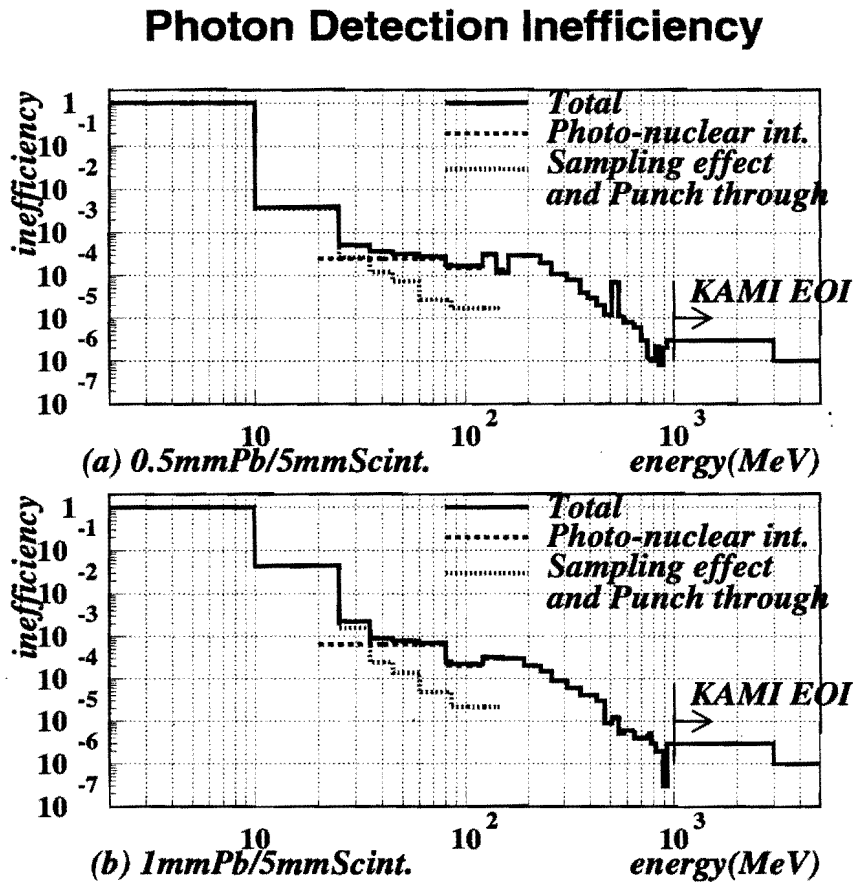

Figure 81: Total detection inefficiency as a function of the incident photon energy for (a) 0.5 mm Pb/5 mm scintillator and (b) 1 mm Pb / 5 mm scintillator sampling ratios. The detection threshold is 10 MeV.

References

[1] E. Cheu *et al.*, "An Expression of Interest to Detect and Measure the Direct CP Violating Decay $K_L \to \pi^0 \nu \overline{\nu}$ and Other Rare decays at Fermilab Using the Main Injector" FERMILAB-PUB-97-321-E, Sep 1997.

D Overview of FCNC Processes

D.1 General Considerations

The processes induced by Flavour Changing Neutral Currents (FCNC) play an important role in the study of weak decays and in verifying the Standard Model (SM) predictions for the mechanism of CP violation. Due to the unitarity of the CKM quark mixing matrix V_{CKM}, these processes cannot take place at tree level since the matrix elements of the corresponding non-diagonal currents vanish.

However, FCNC processes can take place via loop diagrams containing internal quarks and intermediate bosons, although with very low probability. The contributions from the various diagrams with different quark loops are unequal, as they usually depend on the quark mass. We shall consider the FCNC decays $K^+ \to \pi^+\nu\bar{\nu}$ and $K_L^0 \to \pi^0\nu\bar{\nu}$ (see the diagrams in Figure 82). These decays are of particular interest and are called "gold-plated decays" since they can be predicted in the SM framework with very high theoretical accuracy.

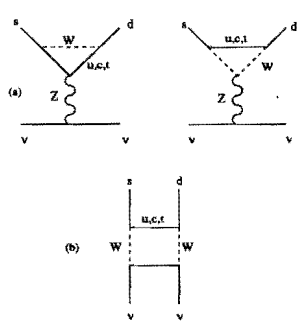

Figure 82: Diagrams for FCNC $s \to d\nu\bar{\nu}$ decays ($K \to \pi\nu\bar{\nu}$ decays): a) penguin diagrams, b) box diagram.

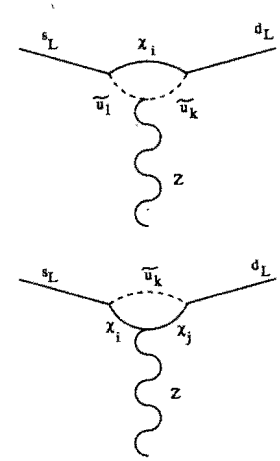

Figure 83: Diagrams containing SUSY contributions to the $Zd\bar{s}$ vertex.

The $K \to \pi\nu\bar{\nu}$ decays in the SM framework are treated in detail in a number of papers, reviews and monographs [1-25]. We enumerate here the interesting aspects of these decays.

a) The main contribution to the FCNC processes is made by the region of very small distances $r \sim 1/m_t$, $1/m_Z$. Therefore in this case, a very accurate description for strong interactions is possible in the framework of perturbative QCD in the leading logarithmic order (LLO) with corrections in the next to leading order (NLO) approximation.

b) The calculation for the matrix element $\langle\pi|H_w|K\rangle_{\pi\nu\bar{\nu}}$ requires one to relate the quark-level processes to hadronic ones. This is difficult, as it involves long-distance physics. However, this can be avoided by using a novel renormalizing procedure developed by Inami and Lim [5]. Through isotopic-spin symmetry, the matrix element $\langle\pi|H_w|K\rangle_{\pi\nu\bar{\nu}}$ can be related to $\langle\pi|H_w|K\rangle_{\pi e\nu}$, the matrix element of the well-known decay mode $K^+ \to \pi^0 e^+\nu_e$.

The difficulties with long-distance physics is therefore minimized in the ratio $BR(K^+(K^0) \to \pi^+(\pi^0)\nu\bar{\nu})/BR(K^+ \to \pi^0 e^+ \nu)$.

c) Since the effective vertex $Zd\bar{s}$ in the diagrams of Figure 82 is determined by the region of small distances $R \sim 1/m_t$, $1/m_Z$, these processes are also sensitive to the contributions from new heavy objects (e.g., supersymmetric particles — see Figure 83). Consequently, the comparison of the experimental results with reliable theoretical estimates in the SM framework allows us to search for new physics in these rare decays.

D.2 Physics of $K \to \pi\nu\bar{\nu}$ decays in the Standard Model

As was shown in [22,23,1 and 4] the decay $K_L^0 \to \pi^0\nu\bar{\nu}$ is governed by direct CP-violation mechanism or more precisely by interference between direct CP-violation amplitude $s \to d\nu\bar{\nu}$ and amplitude for $K^0 \rightleftarrows \bar{K}^0$ mixing.

Define the decay amplitudes

$$a = A(K^0 \to \pi^0\nu\bar{\nu}) \quad ; \quad \bar{a} = A(\bar{K}^0 \to \pi^0\nu\bar{\nu}) \tag{29}$$

and related value $\lambda_{\pi\nu\bar{\nu}}$ for the decays $|K_{L;S}^0\rangle = p|K^0\rangle \mp q|\bar{K}^0\rangle$

$$\lambda_{\pi\nu\bar{\nu}} = \left(\frac{q}{p}\right) \cdot \frac{\bar{a}}{a} \tag{30}$$

Thus $A(K_{L;S}^0 \to \pi^0\nu\bar{\nu}) = pa \mp q\bar{a} = pa\left[1 \mp \left(\frac{q}{p}\right) \cdot \frac{\bar{a}}{a}\right] = pa\left[1 \mp \lambda_{\pi\nu\bar{\nu}}\right]$
and the ratio between the corresponding decay rates is

$$\frac{\Gamma(K_L^0 \to \pi^0\nu\bar{\nu})}{\Gamma(K_S^0 \to \pi^0\nu\bar{\nu})} = \left|\frac{pa - q\bar{a}}{pa + q\bar{a}}\right|^2 = \left|\frac{1 - \lambda_{\pi\nu\bar{\nu}}}{1 + \lambda_{\pi\nu\bar{\nu}}}\right|^2 = \frac{1 - 2Re\lambda_{\pi\nu\bar{\nu}} + |\lambda_{\pi\nu\bar{\nu}}|^2}{1 + 2Re\lambda_{\pi\nu\bar{\nu}} + |\lambda_{\pi\nu\bar{\nu}}|^2} \tag{31}$$

As is well known $\left|\frac{q}{p}\right| = \left|\frac{1-\varepsilon}{1+\varepsilon}\right| \simeq 1 - 2Re\varepsilon = 1 + O(10^{-3})$; $\left|\frac{\bar{a}}{a}\right| = 1$ with very good precision because there are no different amplitudes with different scattering phases in the final state. Thus $|\lambda_{\pi\nu\bar{\nu}}| = 1 + O(10^{-3})$ and

$$\lambda_{\pi\nu\bar{\nu}} \simeq e^{2i\vartheta} \tag{32}$$

From (31) and (32) the ratio of the decay rates is

$$\frac{\Gamma(K_L^0 \to \pi^0\nu\bar{\nu})}{\Gamma(K_S^0 \to \pi^0\nu\bar{\nu})} = \frac{1 - cos2\vartheta}{1 + cos2\vartheta} = tg^2\vartheta \tag{33}$$

In the CP conserving limit $a = \bar{a}$ and $\lambda_{\pi\nu\bar{\nu}} = 1$ ($\vartheta = 0$). Thus the decay $K_L^0 \to \pi^0\nu\bar{\nu}$ is forbidden in this limit and would go only through CP violation mechanism as an interference

between amplitudes of $K^0 \rightleftarrows \bar{K}^0$ mixing and direct FCNC $s \to d\nu\bar{\nu}$ decay (ϑ in (32) and (33) is a phase between these two amplitudes).

Let us also obtain the model independent relation between the decay widths $\Gamma(K_L^0 \to \pi^0\nu\bar{\nu})$ and $\Gamma(K^+ \to \pi^+\nu\bar{\nu})$ [23]. From isotopic symmetry the ratio of the amplitudes $A(K^+ \to \pi^+\nu\bar{\nu})/A(K^0 \to \pi^0\nu\bar{\nu}) = \sqrt{2r_s}$ ($r_s = 0.954$ is correction factor for isotopic symmetry breaking and phase space differences).

From this amplitude ratio

$$\frac{\Gamma(K_L^0 \to \pi^0\nu\bar{\nu})}{\Gamma(K^+ \to \pi^+\nu\bar{\nu})} = \left| \frac{pA(K^0 \to \pi^0\nu\bar{\nu})\left[1 - \left(\frac{q}{p}\right) \cdot \frac{\bar{a}}{a}\right]}{\sqrt{2r_s}A(K^0 \to \pi^0\nu\bar{\nu})} \right|^2 \simeq \frac{|1 - \lambda_{\pi\nu\bar{\nu}}|^2}{4r_s} =$$

$$= \frac{|1 - exp(2i\vartheta)|^2}{4r_s} = \frac{1 - cos2\vartheta}{2r_s} = \frac{1}{r_s} sin^2\vartheta.$$

Thus $\Gamma(K_L^0 \to \pi^0\nu\bar{\nu}) < \frac{1}{r_s}\Gamma(K^+ \to \pi^+\nu\bar{\nu})$, or

$$BR(K_L^0 \to \pi^0\nu\bar{\nu}) < \frac{\tau(K_L^0)}{\tau(K^+)} \cdot \frac{1}{r_s} BR(K^+ \to \pi^+\nu\bar{\nu}) = 4.37 \cdot BR(K^+ \to \pi^+\nu\bar{\nu}) \tag{34}$$

It is possible also to explain directly the CP violation in the decay $K_L^0 \to \pi^0\nu\bar{\nu}$. The CP-parity of $\pi^0\nu\bar{\nu}$ system in this decay is $CP|\pi^0\nu\bar{\nu}\rangle = CP|\pi^0\rangle \cdot CP|\nu\bar{\nu}\rangle \cdot (-1)^L$, where L is relative angular momentum between $|\pi^0\rangle$ and $|\nu\bar{\nu}\rangle$. For spinless K^0 and π^0 mesons $L = J$, where J is angular momentum of $|\nu\bar{\nu}\rangle$. In the rest frame for this system lefthanded neutrino and righthanded antineutrino have the summed angular momentum $J = 1$. Thus $CP|\pi^0\nu\bar{\nu}\rangle = CP|\pi^0\rangle \cdot (-1)^J \cdot CP|\nu\bar{\nu}\rangle = (-1)(-1) \cdot CP|\nu\bar{\nu}\rangle = CP|\nu\bar{\nu}\rangle$. In the lepton flavory conserving approximation (e.g. for $K_L^0 \to \pi^0\nu\bar{\nu}$ decay with production neutrino and antineutrino of the same generation - $\nu_e\bar{\nu}_e$,$\nu_\mu\bar{\nu}_\mu$, $\nu_\tau\bar{\nu}_\tau$) $|\nu\bar{\nu}\rangle$ system must have quantum numbers $J^{PC} = 1^{++}$ or 1^{--} [4]. But $K_L^0 = \frac{1}{\sqrt{1+|\varepsilon|^2}}\left[|K_2^0\rangle + \varepsilon|K_1^0\rangle\right]$ has the main component $|K_2^0\rangle$ with $CP = -1$ and the decay $K_L^0 \to \pi^0\nu\bar{\nu}$ is going with CP violation. It must be emphasized that the same analysis holds also for $K_L^0 \to \pi^0 l^+ l^-$ decays if the production of l^+l^- pair is governed by the FCNC box or electroweak penguin diagrams (with Z^0 or one photon exchange). In this case $CP|l^+l^-\rangle = +1$ and CP-parity of $|\pi^0 l^+ l^-\rangle$ system is also positive ($CP|\pi^0 l^+ l^-\rangle = CP|l^+l^-\rangle = +1$; $K_L^0 \to \pi^0 l^+ l^-$ decay is going with CP violation).

In the SM the amplitudes of $K \to \pi\nu\bar{\nu}$ decays are governed by the FCNC loop diagrams of Fig. 82 at short distances (SD). After the "renormalization" of hadronic structure effects by normalizing on $K^+ \to \pi^0 e^+ \nu_e$ decay rate the long distant (LD) contributions to $K \to \pi\nu\bar{\nu}$ are negligible [9,11,12]. From the loop diagrams of Fig. 82 it is possible to calculate amplitudes of $K \to \pi\nu\bar{\nu}$ processes and to obtain the SM predictions for these decays for any single type of neutrino flavory (see [1-3,8,13-18]):

$$A(K^+ \to \pi^+\nu\bar{\nu}) = \frac{G_F}{\sqrt{2}} \cdot \langle\pi^+\nu\bar{\nu}|H_w|K^+\rangle \cdot \left(\frac{\alpha}{2\pi \sin^2\vartheta_w}\right) \cdot [\lambda_c F(x_c) + \lambda_t F(x_t)] \tag{35}$$

$$A(K^0 \to \pi^0 \nu\bar{\nu}) = \frac{G_F}{\sqrt{2}} \cdot \langle \pi^0 \nu\bar{\nu} | H_w | K^0 \rangle \cdot \left(\frac{\alpha}{2\pi \sin^2 \vartheta_w} \right) \cdot [\lambda_c F(x_c) + \lambda_t F(x_t)] \tag{36}$$

$$A(\bar{K}^0 \to \pi^0 \nu\bar{\nu}) = \frac{G_F}{\sqrt{2}} \cdot \langle \pi^0 \nu\bar{\nu} | H_w | \bar{K}^0 \rangle \cdot \left(\frac{\alpha}{2\pi \sin^2 \vartheta_w} \right) \cdot [\lambda_c^* F(x_c) + \lambda_t^* F(x_t)] \tag{37}$$

$$A(K_L^0 \to \pi^0 \nu\bar{\nu}) \simeq A(K_2^0 \to \pi^0 \nu\bar{\nu}) = \frac{1}{\sqrt{2}} [A(K^0 \to \pi^0 \nu\bar{\nu}) - A(\bar{K}^0 \to \pi^0 \nu\bar{\nu})] =$$
$$= \frac{G_F}{\sqrt{2}} \cdot \langle \pi^0 \nu\bar{\nu} | H_w | K^0 \rangle \cdot \left(\frac{\alpha}{\sqrt{2} \cdot 2\pi \sin^2 \vartheta_w} \right) \cdot 2[Im\lambda_c \cdot F(x_c) + Im\lambda_t \cdot F(x_t)] \tag{38}$$

$F(x_c)$, $F(x_t)$ in (35)-(38) are the known functions of the variables $x_c = (m_c^2/m_W^2)$ for c-quarks and $x_t = (m_t^2/m_W^2)$ for t-quarks for the loop diagrams in Fig. 82 (the Inami-Lim functions [5]). After taking into account the QCD corrections in the LLO and NLO approximations we get $F(x_c) = (9.5 \pm 1.4) \cdot 10^{-4}$ and $F(x_t) = 1.53 \pm 0.05$ [1,17,18,25] (the accuracy of QCD calculations improves with the growth of quark mass).

The values λ and $\lambda_i = V_{id} V_{is}^* (i = c; t)$ in (35)-(38) are determined by the elements of the CKM matrix V_{CKM} [26,27]:

$$\begin{pmatrix} d' \\ s' \\ b' \end{pmatrix} = \begin{pmatrix} V_{ud} & V_{us} & V_{ub} \\ V_{cd} & V_{cs} & V_{cb} \\ V_{td} & V_{ts} & V_{tb} \end{pmatrix} \begin{pmatrix} d \\ s \\ b \end{pmatrix} = V_{CKM} \begin{pmatrix} d \\ s \\ b \end{pmatrix} \tag{39}$$

The matrix V_{CKM} in the Wolfenstein parametrisation [28] is presented as an expansion over the small parameter $\lambda = V_{us} = 0.2196 \pm 0.0023$. Including terms up to order λ^4, the V_{CKM} matrix has the form

$$V_{CKM} = \begin{pmatrix} 1 - \frac{\lambda^2}{2} & \lambda & A\lambda^3(\varrho - i\eta) \\ -\lambda & 1 - \frac{\lambda^2}{2} & A\lambda^2 \\ A\lambda^3(1 - \varrho - i\eta) & -A\lambda^2 & 1 \end{pmatrix} + O(\lambda^4). \tag{40}$$

In this representation the V_{CKM} matrix is defined by four parameters λ ; $A = \frac{V_{cb}}{\lambda^2}$; ρ ; $i\eta$, i.e. by three real values and one phase, which is responsible for the description of CP violation in the SM weak interactions. The modified parameters

$$\bar{\rho} = \rho \left(1 - \frac{\lambda^2}{2} \right) \ ; \ \bar{\eta} = \eta \left(1 - \frac{\lambda^2}{2} \right), \tag{41}$$

are introduced to improve the accuracy of the V_{CKM} decomposition to an accuracy not worse than $O(\lambda^6)$. The complex quantities in expressions (35)-(38)

$$\lambda_i = V_{id} \cdot V_{is}^* \qquad (i = c; t), \tag{42}$$

have the following forms:

$$\left.\begin{array}{rcl} Re\,\lambda_c & \simeq & -\lambda\left(1-\frac{\lambda^2}{2}\right)+O(\lambda^5) \\ Im\,\lambda_c & \simeq & -\eta A^2\lambda^5+O(\lambda^7) \\ Re\,\lambda_t & = & -A^2\lambda^5\left(1-\frac{\lambda^2}{2}\right)(1-\bar{\rho})+O(\lambda^7) \\ Im\,\lambda_t & = & \eta A^2\lambda^5+O(\lambda^9) \end{array}\right\} \tag{43}$$

Since $F(x_c)/F(x_t) \sim 10^{-3}$, the contribution of the c-quark induced terms is only significant for real parts of matrix elements in (35)-(38) due to enchancement by factor $Re\lambda_c$ ($Re\lambda_c \sim \lambda$ is much larger than $Re\lambda_t, Im\lambda_c, Im\lambda_t < \lambda^5$). Therefore

$$\begin{array}{rcl} |[\lambda_c F(x_c)+\lambda_t F(x_t)]-[\lambda_c^* F(x_c)+\lambda_t^* F(x_t)]|^2 & = & 4|Im\lambda_c\cdot F(x_c)+Im\lambda_t\cdot F(x_t)|^2 \simeq \\ & \simeq & 4(Im\lambda_t)^2\cdot F(x_t)^2 = \\ & = & 4\eta^2\lambda^{10}\cdot A^4\cdot F(x_t)^2 = \\ & = & 4\eta^2|V_{cb}|^4\lambda^2 = 4\bar{\eta}^2\sigma|V_{cb}|^4\lambda^2 \end{array} \tag{44}$$

and

$$\begin{array}{rcl} |\lambda_c F(x_c)+\lambda_t F(x_t)|^2 & = & [Re\lambda_c\cdot F(x_c)+Re\lambda_t\cdot F(x_t)]^2+[Im\lambda_c\cdot F(x_c)+ \\ & + & Im\lambda_t\cdot F(x_t)]^2 \simeq \\ & \simeq & [Re\lambda_c\cdot F(x_c)+Re\lambda_t\cdot F(x_t)]^2+[Im\lambda_t\cdot F(x_t)]^2 = \\ & = & \left[-\lambda^5\left(1-\dfrac{\lambda^2}{2}\right)A^2F(x_t)(\rho_0-\bar{\rho})\right]^2+ \\ & + & \left[\lambda^5\left(1-\dfrac{\lambda^2}{2}\right)A^2F(x_t)\sigma\eta\right]^2 = \\ & = & \lambda^{10}\cdot A^4\cdot F(x_t)^2\cdot\dfrac{1}{\sigma}\left[(\rho_0-\bar{\rho})^2+(\sigma\bar{\eta})^2\right] = \\ & = & \lambda^2\cdot|V_{cb}|^4\cdot F(x_t)^2\cdot\dfrac{1}{\sigma}\left[(\rho_0-\bar{\rho})^2+(\sigma\bar{\eta})^2\right] \end{array} \tag{45}$$

Here the following notations have been introduced

$$\left.\begin{array}{rcl} \rho_0 & = & 1+\dfrac{F(x_c)}{A^2\lambda^4F(x_t)}1+\dfrac{P_0}{A^2F(x_t)} \\ & = & 1+\triangle = 1.42\pm 0.06; \\ \sigma & = & \dfrac{1}{(1-\frac{\lambda^2}{2})^2} = 1.050; \\ A & = & \dfrac{|V_{cb}|}{\lambda^2}. \end{array}\right\} \tag{46}$$

The quantity $\triangle = P_0/A^2F(x_t) = F(x_c)/A^2\lambda^4F(x_t) = 0.42\pm 0.06$ is connected with c-quark contribution.

To avoid problems with the hadronic matrix element $\langle \pi\nu\nu|H_w|K\rangle$ the well-known $K^+ \to \pi^0 e^+ \nu_e$ decay amplitude can be used:

$$A(K^+ \to \pi^0 e^+ \nu_e) = \frac{G_F}{\sqrt{2}} \cdot \langle \pi^0 e^+ \nu_e | H_w | K^+ \rangle \lambda. \tag{47}$$

Because of isotopic symmetry it is possible to find the ratios

$$\left| \frac{\langle \pi^+ \nu\bar{\nu} | H_w | K^+ \rangle}{\langle \pi^0 e^+ \nu_e | H_w | K^+ \rangle} \right|^2 = 2r_+ \tag{48}$$

and

$$\left| \frac{\langle \pi^0 \nu\bar{\nu} | H_w | K^0 \rangle}{\langle \pi^0 e^+ \nu_e | H_w | K^+ \rangle} \right|^2 = r_0 \tag{49}$$

where $r_+ = 0.901$ and $r_0 = 0.944$ are correction factors that arise to account for the isotopic symmetry breaking and the phase space differences for $K^+ \to \pi^0 e^+ \nu_e$, $K^+ \to \pi^+ \nu\bar{\nu}$ and $K^0 \to \pi^0 \nu\bar{\nu}$ decays.

From (33)-(47) one can obtain the SM predictions for the branching ratios of the $K^0 \to \pi^0 \nu\bar{\nu}$ and $K^+ \to \pi^+ \nu\bar{\nu}$ decays [17]:

$$\begin{aligned}
BR(K_L^0 \to \pi^0 \nu\bar{\nu})\,|_{SM} &= \left[BR(K^+ \to \pi^0 e^+ \nu_e) \cdot \frac{\tau(K_L^0)}{\tau(K^+)} \cdot \frac{3\alpha^2}{2\pi^2 \sin^4 \vartheta_w} \cdot r_0 \right] \cdot \\
\cdot R_0 \frac{1}{\lambda^2} \cdot |Im\lambda_t \cdot F(x_t)|^2 &= R_0 \cdot \lambda^8 A^4 F(x_t)^2 \cdot \sigma |\bar{\eta}|^2 = \\
&= R_0 \cdot |V_{cb}|^4 \cdot F(x_t)^2 \cdot \sigma |\bar{\eta}|^2 = \\
&= 3.28 \cdot 10^{-5} \cdot |V_{cb}|^4 \cdot F(x_t)^2 \cdot \sigma |\bar{\eta}|^2 = \\
&= (3.1 \pm 1.3) \cdot 10^{-11}
\end{aligned} \tag{50}$$

$$\begin{aligned}
BR(K^+ \to \pi^+ \nu\bar{\nu})\,|_{SM} &= R_+ \cdot \frac{1}{\lambda^2} \cdot |\lambda_c F(x_c) + \lambda_t F(x_t)|^2 = \\
&= R_+ \cdot \lambda^8 A^4 F(x_t)^2 \cdot \frac{1}{\sigma} [(\rho_0 - \bar{\rho})^2 + (\sigma\bar{\eta})^2] = \\
&= R_+ \cdot |V_{cb}|^4 \cdot F(x_t)^2 \cdot \frac{1}{\sigma} [(\rho_0 - \bar{\rho})^2 + (\sigma\bar{\eta})^2] = \\
&= 7.50 \cdot 10^{-6} |V_{cb}|^4 \cdot F(x_t)^2 \cdot \frac{1}{\sigma} [(\rho_0 - \bar{\rho})^2 + (\sigma\bar{\eta})^2] = \\
&= (8.2 \pm 3.2) \cdot 10^{-11}
\end{aligned} \tag{51}$$

Here $\alpha = 1/129$, $\sin^2 \vartheta_w = 0.23$, $BR(K^+ \to \pi^0 e^+ \nu_e) = 4.82 \cdot 10^{-2}$;
$R_+ = \left[BR(K^+ \to \pi^0 e^+ \nu_e) \cdot \frac{3\alpha^2}{2\pi^2 \sin^4 \vartheta_w} \cdot r_+ \right] = 7.50 \cdot 10^{-6}$; $\tau(K_L^0)/\tau(K^+) = 4.17$;
$R_0 = \left[BR(K^+ \to \pi^0 e^+ \nu_e) \cdot \frac{3\alpha^2}{2\pi^2 \sin^4 \vartheta_w} \cdot r_0 \cdot \frac{\tau(K_L^0)}{\tau(K^+)} \right] = R_+ \cdot \frac{\tau(K_L^0)}{\tau(K^+)} \cdot r_0/r_+ = 3.28 \cdot 10^{-5}$.

From (50), (51) one can obtaine

$$\frac{BR(K_L^0 \to \pi^0\nu\bar{\nu})|_{SM}}{BR(K^+ \to \pi^+\nu\bar{\nu})|_{SM}} = \frac{\tau(K_L^0)}{\tau(K^+)} \cdot \frac{r_0}{r_+} \cdot \frac{(\sigma\bar{\eta})^2}{(\rho_0 - \bar{\rho})^2 + (\sigma\bar{\eta})^2} < \frac{\tau(K_L^0)}{\tau(K^+)} \cdot \frac{r_0}{r_+} \cdot = 4.35, \qquad (52)$$

which can be compared with the model independent limit from (34).

One of the most important points to be made here is that the theoretical predictions for the rate of $K \to \pi\nu\bar{\nu}$ decay are very precise; $\sim 1-2\%$ for $BR(K_L^0 \to \pi^0\nu\bar{\nu})$ and $\simeq 5\%$ for $BR(K^+ \to \pi^+\nu\bar{\nu})$. In the latter case the uncertainty is dominated by the virtual c-quark contribution. However the numerical estimations of the $BR(K_L^0 \to \pi^0\nu\bar{\nu})$ and $BR(K^+ \to \pi^+\nu\bar{\nu})$ given in (50) and (51) are characterized by uncertainties which are much larger than the theoretical uncertainties above. This is due to the uncertainty of the CKM parameters which are input to the calculations.

The values for the CKM matrix elements V_{td}, V_{ts} and V_{tb} are not obtained directly from top decays but indirectly from other data and from the unitarity requirements on V_{CKM}. One of these unitarity constraints has the form

$$V_{ud} \cdot V_{ub}^* + V_{td} \cdot V_{tb}^* = -V_{cd} \cdot V_{cb}^* \qquad (53)$$

or for vectors on complex plain $(\bar{\rho}, i\bar{\eta})$

$$A\lambda^3(\bar{\rho} + i\bar{\eta}) + A\lambda^3[1 - (\bar{\rho} + i\bar{\eta})] = A\lambda^3$$

After normalizing by $A\lambda^3$ the unitarity condition can be graphically represented as a triangle in the complex $(\bar{\rho}, i\bar{\eta})$ plane as shown in Figure 84.

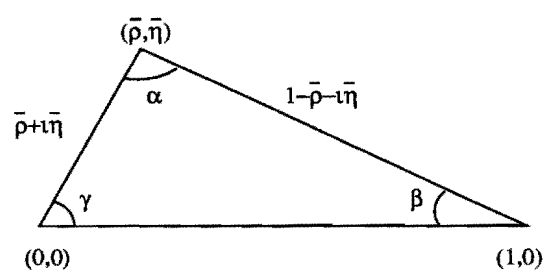

Figure 84: Graphical representation in the $\bar{\rho}$, $i\bar{\eta}$ plane of the unitarity condition $V_{ud}V_{ub}^* + V_{td}V_{tb}^* = -V_{cd}V_{cb}^*$.

Figure 85 is an idealized diagram showing the connection between the position of the apex of the triangle $(\bar{\rho}, \bar{\eta})$ and various physical processes. In reality, the current theoretical and experimental uncertainties constrain $\bar{\rho}$ and $\bar{\eta}$ to lie in the region shown in Figure 86. Detailed analyses of the V_{CKM} matrix are given in refs. [29]- [33]. Table 27 presents the new values of the relevant SM parameters which can be used for numerical estimates of of various decay rates. For example, from the values of the Table 27 the decay rates in (50) and (51) are $BR(K_L^0 \to \pi^0\nu\bar{\nu})\,|_{SM} = (2.6 \pm 0.9) \cdot 10^{-11}$ and $BR(K^+ \to \pi^+\nu\bar{\nu})\,|_{SM} = (7.4 \pm 1.7) \cdot 10^{-11}$.

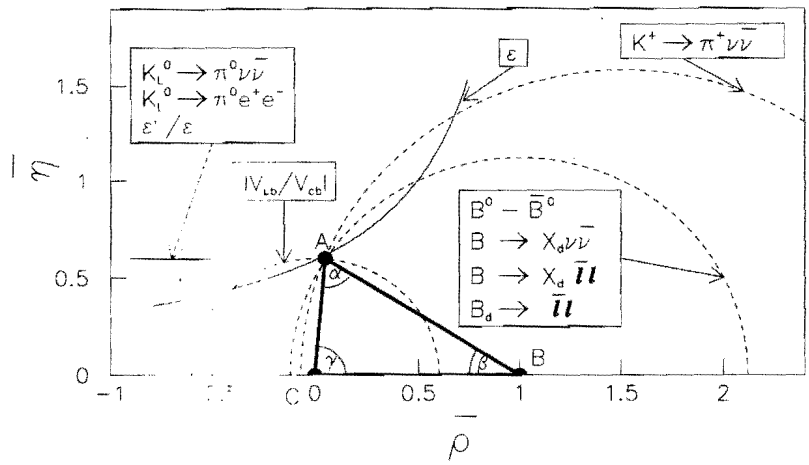

Figure 85: The ideal unitary triangle. For illustration, the value of $\bar{\eta}$ has been chosen to be higher than the fitted central value (reproduced from [14, 15]).

D.3 Other rare kaon decays arise by FCNC processes

There are a number of other rare kaon decay processes that arise from short distance (SD) effects that are also sensitive to direct CP violation and to searches for New Physics. Among these decays are $K_L^0 \to \pi^0 l^+ l^-$ and $K_L^0 \to \mu^+\mu^-$. Separation of direct CP violation from other processes is more complicated for these decays because of the significant influence of long distance (LD) effects connected with one photon and two photon exchange diagrams.

D.3.1 $K_L^0 \to \pi^0 l^+ l^-$ decays

Let us consider $K_L^0 \to \pi^0 f\bar{f}$ decays with $f = \nu; l^-$. $A(K_2^0 \to \pi^0 f\bar{f})$ is the CP violating amplitude (direct CP violation) and $A(K_1^0 \to \pi^0 f\bar{f})$ is the CP conserving amplitude. Thus (see Figure 87)

$$A(K_L^0 \to \pi^0 f\bar{f}) = [A(K_2^0 \to \pi^0 f\bar{f})]_{CP-direct} + [\varepsilon \cdot A(K_1^0 \to \pi^0 f\bar{f})]_{CP-indirect}. \tag{54}$$

For short distance $K_L^0 \to \pi^0 \nu\bar{\nu})$ decays, the amplitudes $A(K_2^0 \to \pi^0 \nu\bar{\nu})$ and $A(K_1^0 \to \pi^0 \nu\bar{\nu})$ are comparable (see (3)) and because of the small of mixing parameter $\varepsilon \simeq 2.3 \cdot 10^{-3}$ the indirect CP violation effect in $K_L^0 \to \pi^0 \nu\bar{\nu}$ is negligibly small [35]. But for $K_L^0 \to \pi^0 l^+ l^-$ decays the situation is changed dramatically by the influence of LD effects in photon exchange diagrams.

It was shown in [4] that in LD region the one-loop diagram with a virtual Z^* is heavily suppressed (as $(m_K/m_Z)^2$) with respect to the corresponding diagram with a virtual γ^*:

$$\frac{BR(K_1^0 \to \pi^0 \nu\bar{\nu})_{LD}}{BR(K_1^0 \to \pi^0 l^+ l^-)_{LD}} \simeq \frac{BR(K_S^0 \to \pi^0 \nu\bar{\nu})_{LDz}}{BR(K_S^0 \to \pi^0 l^+ l^-)_{LD\gamma}} < \frac{m_K^2}{m_Z^2} \cdot \frac{\alpha_{em}}{\alpha_w} < 10^{-7}. \tag{55}$$

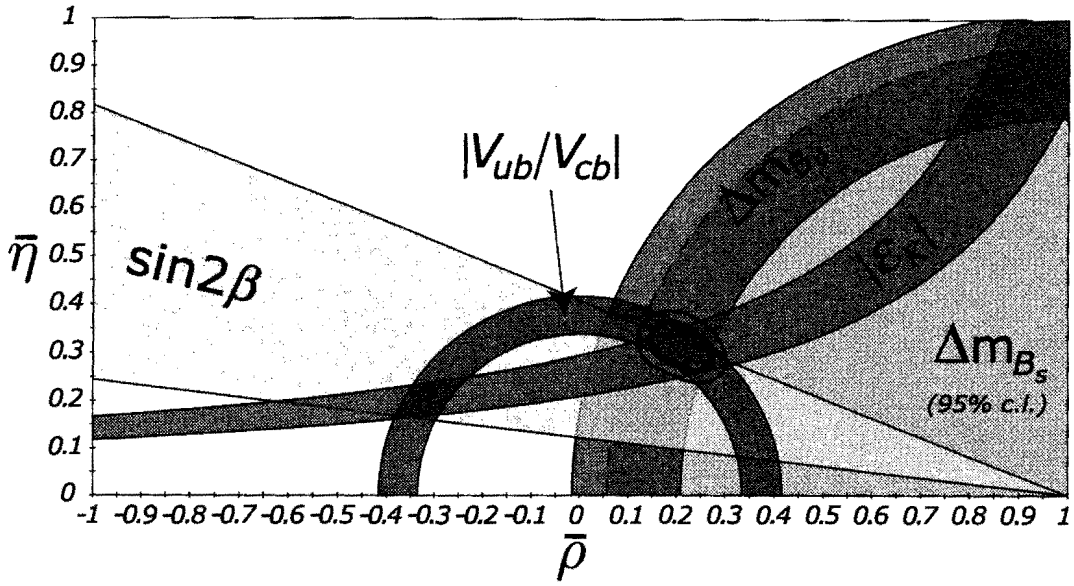

Figure 86: The limitations for parameters of the unitary triangle from existing data for ε, Δm_{B_d}, Δm_{B_s}, $|V_{ub}/V_{cb}|$, $\sin 2\beta$ (from $B^0(\bar{B}^0) \to J/\psi\, K_S^0$) — see [30].

Thus, $A(K_1^0 \to \pi^0 l^+ l^-)_{LD} \gg A(K_2^0 \to \pi^0 l^+ l^-)$ and the indirect CP violation effects in $K_L^0 \to \pi^0 l^+ l^-$ can be significant and comparable with the direct CP violation component. The SM diagrams for $K_L^0 \to \pi^0 l^+ l^-$ decay are shown in Figure 88a,b.

It is clear from Figure 88 and from the previous discussion that there are three contributions for these modes. The first is a direct CP violation contribution from the short distance electroweak penguin and $W^\pm$ box diagram. The second contribution is the indirect CP violation amplitude due to the K_1^0 component of K_L^0. The third contribution is connected with the two photon diagram (Figure 88c). This component is CP conserving. The $K_L^0 \to \pi^0 l^+ l^-$ decay is discussed in the framework of SM in [3], [4], [14]- [16], [20], [25], [36], [37].

We will consider all three contributions to this decay using $K_L^0 \to \pi^0 e^+ e^-$ as an example. After this, the decay $K_L^0 \to \pi^0 \mu^+ \mu^-$ will be discussed as it is potentially interesting for study in KAMI.

$$|K_L^0\rangle \;\propto\; \underset{\llcorner \to \pi^0 l^+ l^-}{|K_2^0\rangle} \;+\; \varepsilon \cdot \underset{\llcorner \to \pi^0 l^+ l^-}{|K_1^0\rangle}$$

Direct	Indirect
CP violation	CP violation
in the decay	due to $|K_1^0\rangle \rightleftarrows |K_2^0\rangle$
amplitude	mixing

Figure 87: Direct and indirect CP violation in the decay $K^0 \to \pi^0 l^+ l^-$

D.3.2 $K_L^0 \to \pi^0 e^+ e^-$ decay with direct CP violation.

The decay $K_L^0 \to \pi^0 e^+ e^-$ is governed by the SD FCNC electroweak penguin and box diagrams in Figure 88, with the main contribution from the operators

$$Q_{7V} = (\bar{s}d)_{V-A} \cdot (\bar{e}e)_V; \quad Q_{7A} = (\bar{s}d)_{V-A} \cdot (\bar{e}e)_A. \tag{56}$$

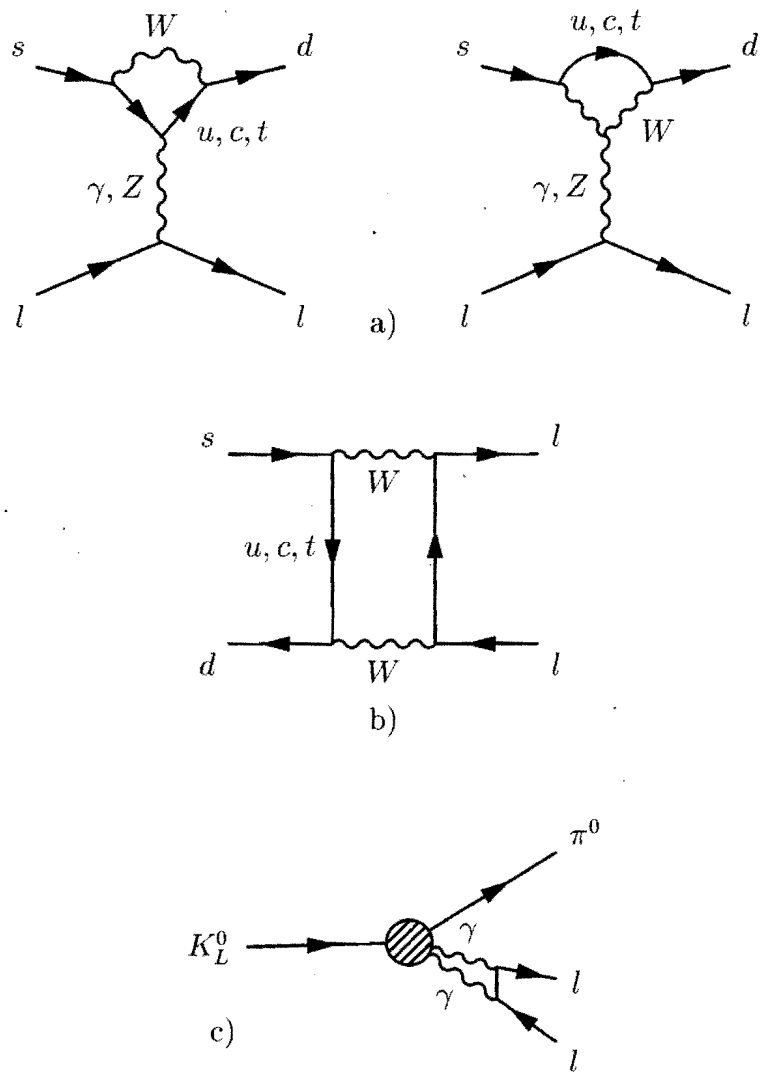

Figure 88: Diagrams for $K_L^0 \to \pi^0 l^+ l^-$ decays a) Electroweak penguine diagrams
b) box diagram
c) two-photon exchange diagram ($K_L^0 \to \pi^0 \gamma^* \gamma^* \to \pi^0 l^+ l^-$)

The branching ratio for the direct CP violating amplitude is

$$\begin{aligned} BR(K_L^0 \to \pi^0 e^+ e^-)_{CP-dir} &= \left[\frac{1}{V_{us}^2} \cdot \frac{\tau(K_L^0)}{\tau(K^+)} \cdot \left(\frac{\alpha}{2\pi}\right)^2 \cdot BR(K^+ \to \pi^0 e^+ \nu_e)\right] \cdot \\ &\cdot \left[\tilde{Y}_{7A}^2 + \tilde{Y}_{7V}^2\right] \cdot (Im\lambda_t)^2 = K_e \left[\tilde{Y}_{7A}^2 + \tilde{Y}_{7V}^2\right] \cdot (Im\lambda_t)^2 \end{aligned} \tag{57}$$

Here $K_e = \frac{1}{V_{us}^2} \cdot \frac{\tau(K_L^0)}{\tau(K^+)} \cdot (\frac{\alpha}{2\pi})^2 \cdot BR(K^+ \to \pi^0 e^+ \nu_e) = 6.3 \times 10^{-6}$ and the amplitudes $\tilde{Y}_{7A}$ and $\tilde{Y}_{7V}$ are determined by Inami-Lim functions for loop diagrams with the variable $x_t = m_t^2/m_W^2$:

$$\left.\begin{aligned} \tilde{Y}_{7A} &= -\frac{1}{\sin^2\vartheta_w} \cdot Y_0(x_t) \\ \tilde{Y}_{7V} &\simeq B_0 + \frac{1}{\sin^2\vartheta_w} \cdot Y_0(x_t) - 4Z_0(x_t) \end{aligned}\right\} \tag{58}$$

The effective mass of the t-quark is $m_t = 167 \pm 5$ GeV [31][2], and the loop diagram functions are

$$\left.\begin{aligned} Y_0(x_t) &= 0.96 \left(\frac{m_t}{165GeV}\right)^{1.55} = 0.98 \pm 0.06 \\ Z_0(x_t) &= 0.66 \left(\frac{m_t}{165GeV}\right)^{1.90} = 0.68 \pm 0.04 \\ B_0 &\simeq 3.0 \end{aligned}\right\} \tag{59}$$

where $B_0 \simeq 3$ from QCD in the NLO approximation. From (58), (59) one obtains

$$\tilde{Y}_{7A}^2 + \tilde{Y}_{7V}^2 = 38.8 \pm 2.9 \tag{60}$$

and [17], [18]

$$\begin{aligned} BR(K_L^0 \to \pi^0 e^+ e^-)_{CP-dir} &= K_e \left[\tilde{Y}_{7A}^2 + \tilde{Y}_{7V}^2\right] \cdot (Im\lambda_t)^2 \\ &= 2.45 \cdot 10^{-4} \cdot (Im\lambda_t)^2 \\ &= 2.45 \cdot 10^{-4} \cdot \sigma|\bar{\eta}|^2 \cdot A^4\lambda^{10} \\ &= 2.45 \cdot 10^{-4} \cdot \sigma|\bar{\eta}|^2 \cdot |V_{cb}|^4 \cdot \lambda^2 \\ &= (4.6 \pm 1.8) \cdot 10^{-12} \end{aligned} \tag{61}$$

or from the values of parameters in Table 27

$$BR(K_L^0 \to \pi^0 e^+ e^-)_{CP-dir} = (4.1 \pm 1.3) \cdot 10^{-12}. \tag{62}$$

D.3.3 $K_L^0 \to \pi^0 e^+ e^-$ decay with indirect CP violation.

Indirect CP violation in $K_L^0 \to \pi^0 e^+ e^-$ decays is due to $K^0 \leftrightarrow \bar{K}^0$ mixing and can be estimated as

$$\begin{aligned} BR(K_L^0 \to \pi^0 e^+ e^-)_{CP-indir} &= BR(K_S^0 \to \pi^0 e^+ e^-) \cdot \frac{\tau(K_L^0)}{\tau(K_S^0)} \cdot |\varepsilon|^2 \\ &= 3.0 \cdot 10^{-3} \cdot BR(K_S^0 \to \pi^0 e^+ e^-). \end{aligned} \tag{63}$$

[2]Here m_t is effective mass of the t-quark. This effective mass is connected with the pole mass in D0 and CDF measurements ($m_t^{pol} = 174.3 \pm 5.1$ GeV [34]) by the relation $m_t = m_t^{pol}\left[1 - \frac{4}{3} \cdot \frac{\alpha_s(m_t)}{\pi}\right]$ [15], [16].

The $K_S^0 \to \pi^0 e^+ e^-$ branching ratio has yet to be measured but an upper limit of $BR(K_S^0 \to \pi^0 e^+ e^-)_{exp} < 1.5 \cdot 10^{-7}$ exists [40]. The expected value of $BR(K_S^0 \to \pi^0 e^+ e^-)$ is $\sim 10^{-9} \div 10^{-10}$.

From CHPT it is possible to use the data from $K^+ \to \pi^+ e^+ e^-$ to obtain the limit

$$\frac{\Gamma(K_S^0 \to \pi^0 e^+ e^-)}{\Gamma(K^+ \to \pi^+ e^+ e^-)} = \frac{BR(K_S^0 \to \pi^0 e^+ e^-)}{BR(K^+ \to \pi^+ e^+ e^-)} \cdot \frac{\tau(K^+)}{\tau(K_S^0)} = |r|^2 \leq 0.25 \tag{64}$$

which leads to

$$\begin{aligned} BR(K_S^0 \to \pi^0 e^+ e^-) &\leq BR(K^+ \to \pi^+ e^+ e^-) \cdot \frac{0.25 \cdot \tau(K_S^0)}{\tau(K^+)} = \\ &= (2.94 \pm 0.14) \cdot 10^{-7} \cdot 1.80 \cdot 10^{-3} = 5.3 \cdot 10^{-10} \end{aligned} \tag{65}$$

and

$$BR(K_L^0 \to \pi^0 e^+ e^-)_{CP-indir.} \leq 3.0 \cdot 10^{-3} \cdot 5.3 \cdot 10^{-10} = 1.6 \cdot 10^{-12}. \tag{66}$$

It is possible that $BR(K_S^0 \to \pi^0 e^+ e^-)_{exp}$ will be measured in future by KLOE [41] and $NA48$ [42], leading to a more definite value for $BR(K_L^0 \to \pi^0 e^+ e^-)_{CP-indir}$.

There is an additional complication associated with the interference between the vector part of $A(K_L^0 \to \pi^0 e^+ e^-)_{CP-dir}$ and $A(K_L^0 \to \pi^0 e^+ e^-)_{CP-indir}$ which must be considered for any future measurement of direct CP violation in $K_L^0 \to \pi^0 e^+ e^-$.

D.3.4 $K_L^0 \to \pi^0 e^+ e^-$ without CP violation.

The CP conserving amplitude of the $K_L^0 \to \pi^0 e^+ e^-$ decay is governed by the two photon exchange mechanism with an intermediate $\pi^0 \gamma^* \gamma^*$ state (see diagram in Figure 88). To estimate the absorptive amplitude for the decay $K_L^0 \to \pi^0 \gamma^* \gamma^* \to \pi^0 e^+ e^-$, data from KTeV for $K_L^0 \to \pi^0 \gamma\gamma$ can be used [43]. KTeV obtained the first evidence for a low-mass $\gamma\gamma$ signal as predicted by $O(p^6)$ chiral perturbation theory calculations which include vector meson exchange contributions [37], [44]. From KTeV data the value for the effective vector coupling $a_V = -0.72 \pm 0.05 \pm 0.06$ was measured. This value of a_V suggests that the CP conserving contribution for $K_L^0 \to \pi^0 e^+ e^-$ can be estimated as

$$BR(K_L^0 \to \pi^0 e^+ e^-)_{CP-conserv.} \simeq (1 \div 2) \cdot 10^{-12}. \tag{67}$$

This contribution is $2 - 3$ orders of magnitude larger than predictions based upon $O(p^4)$ CHPT calculations which are helicity suppressed. At the same time, vector exchange terms from $O(p^6)$ calculations are not helicity suppressed (they correspond to the D-wave exchange of two photons). The CP conserving amplitude does not interfering with the CP non-conserving amplitude.

In the future, the value of $BR(K_L^0 \to \pi^0 e^+ e^-)_{CP-conserv.}$ can be more precisely evaluated from further studies of the low $m(\gamma\gamma)$ part of $K_L^0 \to \pi^0 \gamma\gamma$ decays and with a form

factor analysis of $K_L^0 \to \pi^0\gamma e^+e^-$ and $\pi^0 e^+e^-e^+e^-$, which is important for estimation of the dispersive amplitude in $K_L^0 \to \pi^0\gamma^*\gamma^* \to \pi^0 e^+e^-$. The relative weight of the CP conserving contribution can be constrained by appropriate kinematical cuts (due to the different Dalitz-plot distributions of the CP conserving and CP violating components).

D.3.5 $K_L^0 \to \pi^0\mu^+\mu^-$ decay.

The decay rate of $K_L^0 \to \pi^0\mu^+\mu^-$ is approximately a factor of 5 smaller than $K_L^0 \to \pi^0 e^+e^-$ due to reduced phase space. In addition, the helisity suppressed CP-conserving contribution $K_L^0 \to \pi^0(\gamma^*\gamma^*)_{SD} \to \pi^0\mu^+\mu^-$ seems to be significantly greater than $K_L^0 \to \pi^0(\gamma^*\gamma^*)_{SD} \to \pi^0 e^+e^-$ because of the mass of m_μ. But as was shown in 1.2.4, the main role plays the helisity nonsuppressed component $K_L^0 \to \pi^0(\gamma^*\gamma^*)_{LD} \to \pi^0 e^+e^-$. Thus the total relative weights of CP-conserving contributions to $K_L^0 \to \pi^0 e^+e^-$ and $K_L^0 \to \pi^0\mu^+\mu^-$ may be are not so different. The difference in the background for $K_L^0 \to \pi^0 e^+e^-$ and $K_L^0 \to \pi^0\mu^+\mu^-$, on the other hand, can be substantial and favors the muon mode (see for example [45]).

D.3.6 Experimental situation for $K_L^0 \to \pi^0 l^+l^-$

The best upper limits for the decays $K_L^0 \to \pi^0 e^+e^-$ and $K_L^0 \to \pi^0\mu^+\mu^-$ have been obtained by KTeV [46], [47]

$$BR(K_L^0 \to \pi^0 e^+e^-) \;<\; 5.1 \cdot 10^{-10} \tag{68}$$

$$BR(K_L^0 \to \pi^0\mu^+\mu^-) \;<\; 3.4 \cdot 10^{-10}. \tag{69}$$

These limits are still two orders of magnitude above their expected rates in the SM.

The main experimental difficulty in the search for $K_L^0 \to \pi^0 e^+e^-$ is the "Greenlee background" from the radiative decay $K_L^0 \to e^+e^-\gamma\gamma$ with a rather large branching ratio of $\sim 6 \cdot 10^{-7}$ [48]. The two photon invariant mass has a spectrum which includes the mass of the π^0, so that a component of this decay is indistinguishable from the $\pi^0 e^+e^-$ mode. To deal with this background a high-precision photon calorimeter must be used to minimize the background from $m(\gamma\gamma)$ near the π^0. Additional kinematical cuts are also needed to reduce the radiative background. The similar background from $K_L^0 \to \mu^+\mu^-\gamma\gamma$ is reduced due to the mass of muons.

To further increase of sensitivity of $K_L^0 \to \pi^0 l^+l^-$, future searches will have to rely on subtraction of the radiative background on a statistical basis by measuring the background with to very high precision and by subtracting the $m(\gamma\gamma)$ sidebands.

D.3.7 $K_L^0 \to \mu^+\mu^-$ decay

The branching ratio of $K_L^0 \to \mu^+\mu^-$ can be presented in a form

$$BR(K_L^0 \to \pi^0\mu^+\mu^-) = (ReA_{\mu\mu})^2 + (ImA_{\mu\mu})^2_{LD}. \tag{70}$$

The absorptive LD amplitude $(ImA_{\mu\mu})_{LD}$ in (70) is dominated by the process $K_L^0 \to \gamma\gamma$ with two real photons (on mass shell) converting $\mu^+\mu^-$ pair. The square of this amplitude can be precisely calculated in QED as

$$\begin{aligned}(ImA_{\mu\mu})^2_{LD} &= \left(\frac{\alpha^2 m_\mu^2}{2m_K^2\beta_\mu}\cdot\left[ln\frac{1-\beta_\mu}{1+\beta_\mu}\right]^2\right)\cdot BR(K_L^0\to\gamma\gamma)\\ &= 1.20\cdot 10^{-5}\cdot(5.92\pm 0.15)\cdot 10^{-4} = (7.09\pm 0.18)\cdot 10^{-9}, \end{aligned} \tag{71}$$

with $\beta_\mu = \sqrt{1-\frac{4m_\mu^2}{m_K^2}} = 0.905$ (unitary lower limit of $BR(K_L^0\to\mu^+\mu^-)$ [49]).
The dispersive amplitude $ReA_{\mu\mu}$ contains two components

$$ReA_{\mu\mu} = (ReA_{\mu\mu})_{SD} + (ReA_{\mu\mu})_{LD} \tag{72}$$

The long distance amplitude $(ReA_{\mu\mu})_{LD}$ is determined by an intermediate state with two virtual off-shell photons (see diagram in Fig. 89a).

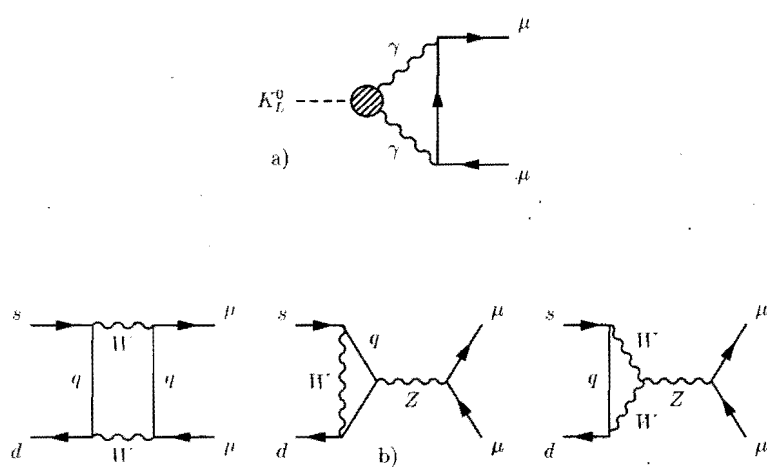

Figure 89: Diagrams for $K_L^0 \to \mu^+\mu^-$ decay:
a) two-photon exchange diagram ($K_L^0 \to \gamma^*\gamma^* \to \mu^+\mu^-$)
b) FCNC SD electroweak penguine and box diagrams

Most interesting is the short distance part of the dispersive amplitude which depends upon the FCNC loop diagrams in Figure 89b and can be presented as

$$\begin{aligned}(ReA_{\mu\mu})^2_{SD} &= \left[\frac{\alpha^2\cdot BR(K^+\to\mu^+\nu_\mu)}{\pi^2\sin^4\vartheta_W}\cdot\frac{\tau(K_L^0)}{\tau(K^+)}\lambda^8\right]\\ &\cdot\left[\frac{Re\lambda_c}{\lambda}P_0(Y)+\frac{Re\lambda_t}{\lambda^5}Y(x_t)\right]^2\\ &= K_\mu\left[\frac{Re\lambda_c}{\lambda}P_0(Y)+\frac{Re\lambda_t}{\lambda^5}Y(x_t)\right]^2\end{aligned}$$

$$
\begin{aligned}
&= 1.68 \cdot 10^{-9} A^4 Y(x_t)^2 \cdot \frac{1}{\sigma}(\rho_0' - \bar{\rho})^2 \\
&= (1.53 \pm 0.15) \cdot 10^{-9} A^4 (\rho_0' - \bar{\rho})^2 \\
&= (6.9 \pm 1.5) \cdot 10^{-10} (\rho_0' - \bar{\rho})^2 \\
&= (8.7 \pm 3.6) \cdot 10^{-10}
\end{aligned} \tag{73}
$$

(see [3], [17], [18]). Here: $K_\mu = \left[\frac{\alpha^2 \cdot BR(K^+ \to \mu^+ \nu_\mu)}{\pi^2 \sin^4 \vartheta_W} \cdot \frac{\tau(K_L^0)}{\tau(K^+)} \lambda^8\right] = 1.68 \cdot 10^{-9}$; $\rho_0' = 1 + \frac{P_0(Y)}{A^2 Y^2} = 1.23 \pm 0.03$, determined by virtual c-quark loops in Figure 89b and includes QCD corrections in the NLO approximation; the QCD corrected (η) function $Y(x_t) = \eta Y_0(x_t) = 1.026 \pm 0.06$ and $Y_0(x_t) = 0.98 \pm 0.05$ is determined in (59). The experimental value $BR(K_L^0 \to \mu^+\mu^-) = (7.15 \pm 0.16) \cdot 10^{-9}$ [50], [34] nearly saturates the unitarity bound from $(ImA_{\mu\mu})^2_{LD}$ (71):

$$
\begin{aligned}
(ReA_{\mu\mu})^2_{exp} &= BR(K_L^0 \to \mu^+\mu^-) - (ImA_{\mu\mu})^2_{LD} = \\
&= (7.15 \pm 0.16) \cdot 10^{-9} - (7.09 \pm 0.18) \cdot 10^{-9} = \\
&= (0.06 \pm 0.24) \cdot 10^{-9} < 3.7 \cdot 10^{-10} (90\% C.L.)
\end{aligned} \tag{74}
$$

This can be used to obtain the an upper limit for the short distance term

$$
|ReA_{\mu\mu}|_{SDmax} < |ReA_{\mu\mu}|_{exp} + |ReA_{\mu\mu}|_{LD}. \tag{75}
$$

In the framework of the SM this can be used to determine a limit on the CKM matrix parameter $\bar{\rho}$

$$
|\bar{\rho} - \rho_0'| = \frac{|ReA_{\mu\mu}|_{SD}}{(2.6 \pm 0.3) \cdot 10^{-5}} \tag{76}
$$

and

$$
\begin{aligned}
\bar{\rho} &> \rho_0' - \frac{|ReA_{\mu\mu}|_{SDmax}}{(2.6 \pm 0.3) \cdot 10^{-5}} = \\
&= (1.23 \pm 0.03) - \frac{|ReA_{\mu\mu}|_{SDmax}}{(2.6 \pm 0.3) \cdot 10^{-5}} > \\
&> (1.23 \pm 0.03) - \frac{|ReA_{\mu\mu}|_{exp} + |ReA_{\mu\mu}|_{LD}}{(2.6 \pm 0.3) \cdot 10^{-5}}.
\end{aligned} \tag{77}
$$

To evaluate $\bar{\rho}$ one needs to find the long distance component of the dispersive amplitude $|ReA_{\mu\mu}|_{LD}$. For this analysis [51], [52] the experimental data for the form factor of the $K_L^0 \gamma^* \gamma^*$ vertex is used.
As was shown in [51]

$$
(ReA_{\mu\mu})^2_{LD} = \frac{2\alpha^2 m_\mu^2 \beta_\mu}{\pi^2 m_K^2} \cdot BR(K_L^0 \to \gamma\gamma) \cdot |ReR(m_K^2)|^2, \tag{78}
$$

with

$$R(q^2) = \frac{2i}{\pi^2 q^2}\int d^4k \frac{[q^2k^2-(q\cdot k)^2]}{k^2(q-k)^2\cdot[(p-k)^2-m_\mu^2]}.f[k^2;(p-k)^2]. \tag{79}$$

Here $p^2 = m_\mu^2$; $f[q_1^2;q_2^2] = f[k^2;(p-k)^2]$ is the transition form factor for $K_L^0 \to \gamma^*\gamma^*$; $k^2 = q_1^2$ and $(p-k)^2 = q_2^2$ where q_i are the momentum transfers for γ_i in $f(q_1^2;q_2^2)$.

To determine $(ReA_{\mu\mu})_{LD}$, one needs information about the form factor $f(q_1^2;q_2^2)$ which can be obtained by KAMI in a model independent way by analysis of $K_L^0 \to \mu^+\mu^-e^+e^-$ decays.

Currently, the only available information is for the form factor $f(q^2;0)$ in the decays $K_L^0 \to \mu^+\mu^-\gamma$ and $K_L^0 \to e^+e^-\gamma$ (KTeV, [52]). To extrapolate from $f(q^2;0)$ to $f(q_1^2;q_2^2)$ the vector dominance model of [51] was used and the upper limit of $(ReA_{\mu\mu})_{LD}$ was estimated:

$$\begin{aligned}(ReA_{\mu\mu})_{LD} &= \left[\frac{2\alpha^2 m_\mu^2\beta_\mu\cdot BR(K_L^0\to\gamma\gamma)}{\pi^2 m_K^2}\right]^{\frac{1}{2}}|5.25+3.47\alpha+3(1+2\alpha+\beta)ln\frac{\Lambda}{m_\beta}| \\ &= 1.61\cdot 10^{-5}|5.25+3.47\alpha+3(1+2\alpha+\beta)ln\frac{\Lambda}{m_\beta}|. \end{aligned} \tag{80}$$

Here $\alpha = -1.53\pm0.09$ [52] and β are parameters of the form factor $f(q_1^2;0)$; $ln\frac{\Lambda}{m_\beta}$ is a cut-off parameter; $(1+2\alpha+\beta)ln\frac{\Lambda}{m_\beta} = (0\pm0.69)$ from perturbative QCD. Thus

$$(ReA_{\mu\mu})_{LD} = 1.61\cdot 10^{-5}[0.06\pm0.31\pm0.69] = (0.10\pm1.21)\cdot 10^{-5} \tag{81}$$

or

$$(ReA_{\mu\mu})_{LD} < 1.7\cdot 10^{-5}(90\%C.L.). \tag{82}$$

From this value and from (74), (75) and (77)

$$\left.\begin{aligned}(ReA_{\mu\mu})^2_{SD} &< 1.3\cdot 10^{-9}(90\%C.L.) \\ (ReA_{\mu\mu})_{SD} &< 3.6\cdot 10^{-5}(90\%C.L.)\end{aligned}\right\} \tag{83}$$

$$\bar{\rho} > -0.3(90\%C.L.) \tag{84}$$

(see [50,52]). The upper limit for $(ReA_{\mu\mu})^2_{SD}$ plays a very important role in the search for New Physics in rare kaon decays.

D.3.8 $K_L^0 \to e^+e^-$ decay

In the SM this decay is strongly suppressed for V-A interactions by helicity conservation. For this decay

$$
\begin{aligned}
(ImA_{ee})^2 &= \frac{\alpha^2 m_e^2}{2m_K^2\beta_e} \cdot \left(ln\frac{1-\beta_e}{1+\beta_e}\right)^2 \cdot \Gamma(K_L^0 \to \gamma\gamma) \\
&= \frac{\alpha^2}{2}\left(\frac{m_e}{m_K}\right)^2 \cdot \left(2ln\frac{m_e}{m_K}\right)^2 \cdot BR(K_L^0 \to \gamma\gamma) = 2.70 \cdot 10^{-12} \qquad (85)
\end{aligned}
$$

$(\beta_e = \sqrt{1-\frac{4m_e^2}{m_K^2}} \simeq 1 - \frac{2m_e^2}{m_K^2};\ \frac{1-\beta_e}{1+\beta_e} \simeq \frac{m_e^2}{m_K^2})$.

In the framework of CHPT it is possible to estimate $(ReA_{ee})^2_{LD}$ and to obtain [53], [54]

$$
BR(K_L^0 \to e^+e^-)|_{SM} = (9.0 \pm 0.5) \cdot 10^{-12} \qquad (86)
$$

in good accordance with the experimental value [55]

$$
BR(K_L^0 \to e^+e^-)|_{exp} = (8.7^{+5.7}_{-4.1}) \cdot 10^{-12}. \qquad (87)
$$

For this decay the helicity suppression of $(ReA_{ee})_{SD}$ is negligibly small:

$$
(ReA_{ee})^2_{SD} \simeq (ReA_{\mu\mu})^2_{SD} \cdot \frac{BR(K^+ \to e^+\nu_e)}{BR(K^+ \to \mu^+\nu_\mu)} \simeq 2 \cdot 10^{-14}. \qquad (88)
$$

Due to strong suppression of this decay in the SM its careful study can be used to search for New Physics effects.

D.4 B-meson experiments and unitarity triangle

In the B-meson system the story is much longer and more complicated. Many of the same authors have studied the theoretical limitations of the B sector measurements [1-3,13-18]. A summary of their conclusions is as follows:

1. The present uncertainty on $|V_{td}|$ measured with the B_d mixing parameter $x_d = \Delta m_{Bd}/Gamma_{Bd}$ is already dominated by the uncertainties in the lattice calculations of f_{B_d} and B_{B_d}. This is a theoretical limitation common to most of the hadronic B decays.

2. The x_s/x_d ratio of these observables is significantly less sensitive to lattice calculation uncertainties. Currently, the B_s mixing parameter x_s has not yet been firmly established. This would be measured in future hadronic B production experiments, where particle identification is crucial for distinguishing B_s from B_d events.

3. Among the conventional measurements of the unitarity triangle angles α, β and γ expected from the B factories, only β from the measurement of $B^0 \to \psi K_S(K_L)$ is free from significant theoretical uncertainties.

4. α measured with $B^0 \to \pi^+\pi^-$ suffers from significant "penguin pollution" which must be overcome before this measurement can be useful for CKM parameter determinations. The isospin analysis required to control this problem requires measurements of modes which are probably too low in branching ratio to be well measured with the available luminosity.

5. The B sector analogies of the ultra-rare kaon decays; $B^0 \to X_d\nu\bar{\nu}$, $B^0 \to X_s\nu\bar{\nu}$, $B_d^0 \to \mu^+\mu^-$ and $B_s^0 \to \mu^+\mu^-$ are likewise theoretically clean. The Standard Model branching ratios for these modes are believed to be beyond the sensitivity of all proposed experiments.

The B sector experiments have more than ample experimental insurance. Eight experiments are in process of working or under construction: Babar, Belle, CDF, CLEO-III, Dzero, HERA-B, BTeV and LHCB.

The most theoretically unambiguous constraint on V_{CKM} can be obtained in 2 types of measurements.

a) The intensity of $B_d^0 \rightleftarrows \bar{B}_d^0$ and $B_s^0 \rightleftarrows \bar{B}_s^0$ mixing depends on Δm_{B_d} and Δm_{B_s}, the mass differences between the "heavy" and "light" eigenstates of B^0 mesons.

$$\left.\begin{aligned} \Delta m_{B_d} &\simeq \frac{G_F^2}{6\pi^2} m_W^2 m_{B_d} f_{B_d}^2 B_{B_d} \eta_B S(x_t) |V_{td}V_{tb}^*|^2 \\ \Delta m_{B_s} &\simeq \frac{G_F^2}{6\pi^2} m_W^2 m_{B_s} f_{B_s}^2 B_{B_s} \eta_B S(x_t) |V_{ts}V_{tb}^*|^2 \end{aligned}\right\}.$$

Here $S(x_t)$ is the corresponding Inami-Lim function for the box diagrams responsible for $B^0 \rightleftarrows \bar{B}^0$ mixing; $\eta_B = 0.55 \pm 0.01$ is QCD correction factor; $f_{B_d}^2$, B_{B_d}, $f_{B_s}^2$, B_{B_s} are coupling constants and decay parameters for B_d^0 and B_s^0 mesons and m_{B_d}, m_{B_s} are their masses. The values of the coupling constants and decay parameters are obtained from lattice QCD calculations and have large systematic uncertainties. Thus, it is much more convenient to use the ratio:

$$R_{\Delta m_B} = \frac{\Delta m_{B_d}}{\Delta m_{B_s}} = \frac{m_{B_d}}{m_{B_s}} \cdot \frac{f_{B_d}^2}{f_{B_s}^2} \cdot \frac{B_{B_d}}{B_{B_s}} \cdot \frac{|V_{td}|^2}{|V_{ts}|^2} = \frac{m_{B_d}}{m_{B_s}} \cdot \frac{1}{\xi^2} \left|\frac{V_{td}}{V_{ts}}\right|^2. \tag{89}$$

Here

$$\xi = f_{B_s} \cdot \sqrt{B_s} / f_{B_d} \cdot \sqrt{B_d} = 1.14 \pm 0.06$$
$$\Delta m_{B_d} = (0.473 \pm 0.016) ps^{-1}$$
$$\Delta m_{B_s} > 15.0\, ps^{-1} (95\%\ C.L.)$$

Thus

$$R_{\Delta m_B} < 3.0 \cdot 10^{-2} \text{ and } \left|\frac{V_{ts}}{V_{td}}\right| > 5.0\ (95\%\ C.L.). \tag{90}$$

b) Another important measurement is the search for a CP asymmetry in the decays $B_d(\bar{B}_d^0) \to J/\psi K_S(K_L)$. For $B_d(\bar{B}_d^0) \to J/\psi K_S$:

$$\begin{aligned} A_{CP} &= \frac{[B(t)^0 \to J/\psi K_S^0] - [\bar{B}(t)^0 \to J/\psi K_S^0]}{[B(t)^0 \to J/\psi K_S^0] + [\bar{B}(t)^0 \to J/\psi K_S^0]} \\ &= -a_{\psi K_S^0} \cdot \sin \triangle M_{B_d} t = -\sin 2\beta \cdot \sin \triangle M_{B_d} t \end{aligned} \tag{91}$$

The first results of measurements from CDF, electron B factories BaBar (SLAC), Belle (KEK) and LEP data yield an average value of [33]:

$$\langle a_{\psi K^0} \rangle = \langle \sin 2\beta \rangle = 0.48 \pm 0.16 \tag{92}$$

The SM prediction is $\sin 2\beta \mid_{SM} = 0.70 \pm 0.07$. It is expected that the precision for these very important asymmetry measurements will increase significantly in the next several years.

D.5 Over-constraining the Unitary Condition and Detecting Effects Beyond the SM

In this section we discuss over-constraining the unitary triangle, with due emphasis on the measurements of $K \to \pi\nu\nu$ as they provide theoretically clean constraints. This makes it possible to see effects beyond the SM, and we enumerate some of the possibilities here. This subject has been widely discussed in the recent literature, and we summarize the key ideas.

The apex of the unitary triangle can be reconstructed from measurements of $BR(K^+ \to \pi^+\nu\bar{\nu})$ and $BR(K_L^0 \to \pi^0\nu\bar{\nu})$ as the crossing of an ellipse and a horizontal line as shown in Figure 90. In addition, the combined $K \to \pi\nu\nu$ measurements can determine $\sin(2\beta)$ without being affected by the uncertainty on $|V_{cb}|$. This is enumerated in table 28 and denoted as $\sin(2\beta)|_K$. The expected measurement accuracy is $\sigma(\sin 2\beta) \mid_K = 0.07$ [17,18]. This is comparable to the expected precision on $\sin(2\beta)$ derived from the CP asymmetry in $B_d^0, \bar{B}_d^0 \to J/\psi\, K_S^0$, which is $0.06 - 0.08$. This value is denoted as $\sin(2\beta)|_B$. A possible outcome of the future K-meson and B-meson experiments is shown in Figure 90.

As a result, one will be able to independently obtain information on direct CP-violating processes from K and B experiments. Obviously, if the SM is correct then $\sin 2\beta \mid_B \;=\; \sin 2\beta \mid_K$, as all CP-violating phenomena in the SM are described by a single phase.

It is worth noting that $K \to \pi\nu\nu$ and $B_d^0(\bar{B}_d^0) \to J/\psi K_S$ are distinctly different processes, so that new physics might differentiate between the two. The FCNC decays $K \to \pi\nu\bar{\nu}$ are loop processes and therefore the $Zd\bar{s}$ vertex in these decays is especially sensitive to the contributions from new interactions. On the other hand, the decays $B_d^0(\bar{B}_d^0) \to J/\psi\, K_S$ can proceed at tree level via $b \to c\bar{c}s$ and $\bar{b} \to \bar{c}c\bar{s}$.

Regarding CP violation, the CP asymmetry $a_{\psi K_S}$ is caused by the relative phase between the $B_d^0 \rightleftarrows \bar{B}_d^0$ mixing amplitude and that of the tree-level $b \to c\bar{c}s$ decay [57]. On the other hand, CP violation in the $K_L \to \pi^0\nu\bar{\nu}$ decay is due to the relative phase between the $K^0 \rightleftarrows \bar{K}^0$ mixing amplitude and the FCNC amplitudes of $s \to d\nu\bar{\nu}$ shown in Figure 82.

New physics such as supersymmetry, where there are additional Higgs doublets and other mechanisms of CP violation, may differentiate between K and B measurements [57]. In the

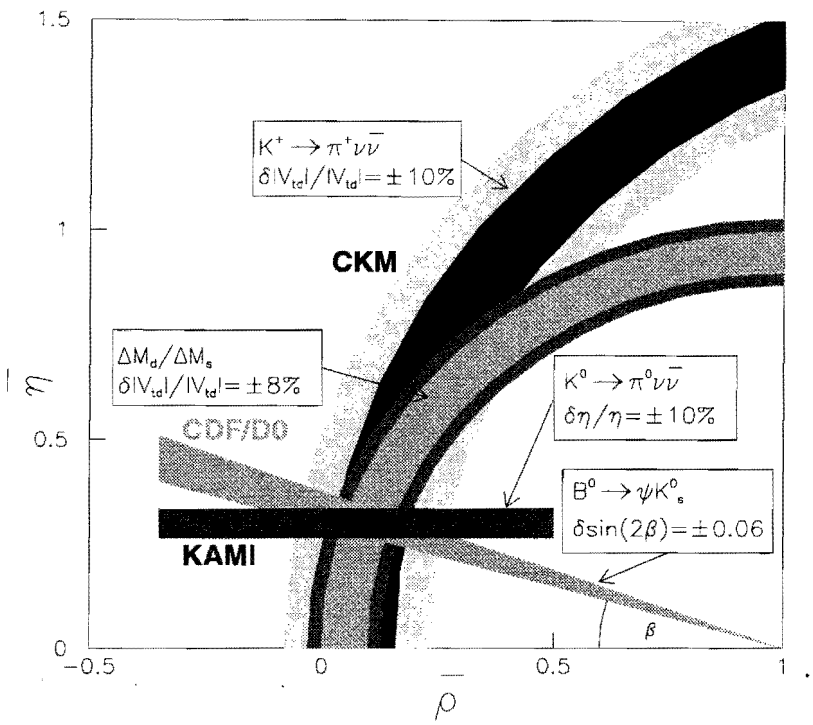

Figure 90: A possible outcome for $\overline{\eta}$, $\overline{\rho}$, and β obtained from future K-meson and B-meson experiments. The light region includes possible theoretical uncertainties in BR($K^+ \to \pi^0 \nu\overline{\nu}$ connected with the influence of c-quarks [58].

$B_d^0(\bar{B}_d^0) \to J/\psi\, K_S$ decays these mechanisms are very likely to manifest themselves in the $B_d^0 \rightleftarrows \bar{B}_d^0$ mixing amplitudes, which are loop diagrams at small distances and sensitive to the contribution from new heavy particles. The first order process $b \to c\bar{c}s$ would remain in this case essential unchanged. The $a_{\psi K_S^0}$ asymmetry in the B-decays would now be determined not only by the CKM phase (which leads to the β angle) but also by a new additional phase β_d. Consequently, the $\alpha_{\psi K_S}$ asymmetry will change and will have the form $a_{\psi K_S} = \sin(\beta + \beta_d)$.

As previously mentioned, new mechanisms for the $K \to \pi\nu\bar{\nu}$ decays may influence considerably the FCNC loop processes which are sensitive to effects at small distances. In this case, the ratio of BR($K^+ \to \pi^+\nu\bar{\nu}$) to BR($K_L^0 \to \pi^0\nu\bar{\nu}$) is very likely to change, also changing the value for $\sin 2\beta|_K$. Hence if new mechanisms for CP violation exist, the values for $\sin 2\beta|_B$ and $\sin 2\beta|_K$ may become significantly different, and the proposed future K experiments may be able to detect this.

The experimental limits for FCNC processes, presented in table 29, still leave a large region to search for new physics in $K \to \pi\nu\bar{\nu}$ decays. Such effects were dealt with in a number of papers [18,20,35,57,59-75].

The new physics considered encompasses new heavy particles, new interactions at small

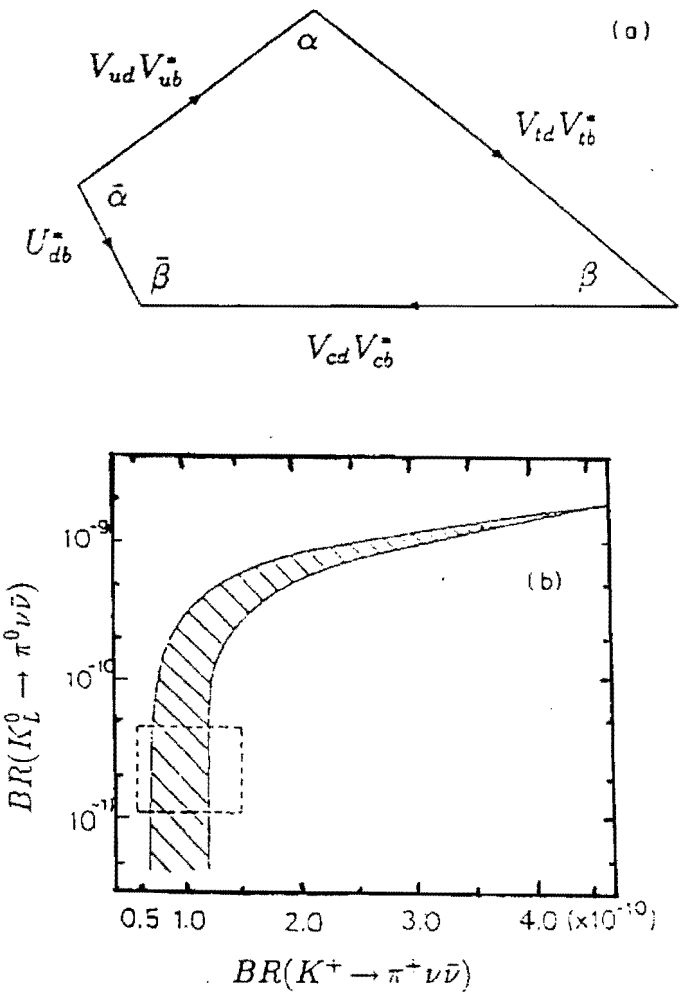

Figure 91: A model with four generations of fundamental fermions with quark doublets [38]. a) Unitary quadrangle for this model. b) The correlation between $BR(K^+ \to \pi^+\nu\bar{\nu})$ and $BR(K_L^0 \to \pi^0\nu\bar{\nu})$ in this model; the dotted line rectangle corresponds to the SM predictions.

distances, and new mechanisms of CP violation, which are characterized by additional complex parameters (new phases). As shown in table 29, numerous predictions have been made as to the possible modification to the FCNC processes, in particular, for rare K-meson decays.

As shown in [60], in nearly all models with new physics but with only left-handed neutrinos, the effective Hamiltonian describing $K \to \pi\nu\bar{\nu}$ decays has the form:

$$H_{eff} = \frac{2G_F}{\sqrt{2}} \cdot \frac{\alpha}{\pi \sin^2 \vartheta_w} \lambda_t \cdot \bar{s}\gamma^\mu (X_L P_L + X_R P_R) d \cdot \bar{\nu}_l \gamma_\mu P_L \nu_e + (\text{herm.conjug.}). \tag{93}$$

Here $P_L = (1 - \gamma_5)$ and $P_R = (1 + \gamma_5)$, which correspond to left and right handed currents (with X_L and X_R). Hamiltonian (93) leads to the following branching ratios for $K \to \pi\nu\bar{\nu}$ decays:

$$BR(K^+ \to \pi^+\nu\bar{\nu}) = 7.50 \cdot 10^{-6} \left| \frac{\lambda_t (X_L + X_R)}{\lambda} \right|^2 \tag{94}$$

$$BR(K_L^0 \to \pi^0\nu\bar{\nu}) = 3.28 \cdot 10^{-5} \left| Im \left[\frac{\lambda_t (X_L + X_R)}{\lambda} \right] \right|^2. \tag{95}$$

In the limit of the SM, as one can see from the comparison of (94) and (95) with (50) and (51), X_R and X_L reduces to $X_R = 0$ and $X_L = F(x_t) + \lambda^4 \lambda_c P_0 / \lambda_t$. In different models with new physics, the expressions for X_L and (or) X_R are modified, as it will be shown in what follows by several examples.

In models with an additional generation of fundamental fermions, the unitarity conditions for the V_{CKM} matrix no longer hold. For example, instead of the unitarity relation $V_{ud} \cdot V_{ub}^* + V_{cd} \cdot V_{cb}^* + V_{td} \cdot V_{tb}^* = 0$, the valid relation would be $V_{ud} \cdot V_{ub}^* + V_{cd} \cdot V_{cb}^* + V_{td} \cdot V_{tb}^* = -V_{t'd} V_{t'b}^*$ which is represented by a quadrangle (see Figure 91). In these models, the amplitude X_L acquires an additional term: $X_L = (X_L)_{SM} + \frac{\lambda_{t'}}{\lambda_t} F(x_{t'})$.

Depending on the mass $m_{t'}$ the quantity $F(x_{t'})$ lies within the limits $1.5 \leq F(x_{t'}) \leq 5$. At sufficiently large values of $\frac{\lambda_{t'}}{\lambda_t}$ the contribution from the fourth generation of quarks to the probabilities (94) and (95) may be quite significant and result in considerable deviations from the SM predication in estimating the branching ratio for $K \to \pi\nu\nu$ decays. For instance, ref. [62] gives the following limitations for the branching ratios of FCNC decays of K-mesons in the model with 4 generations of fundamental fermions (having accounted for constraints arising from Δm_K, Δm_{B_d}, Δm_{B_s}, Δm_D): $BR(K^+ \to \pi^+\nu\bar{\nu}) \simeq (0.7 - 4.4)10^{-10}$, $BR(K_L^0 \to \pi^0\nu\bar{\nu}) \simeq (0.05 - 10)10^{-10}$ (see also Figure 91).

The estimates of the branching ratios for $K \to \pi\nu\bar{\nu}$ and $K_L^0 \to \pi^0 l^+ l^-$ decays in different variants of supersymmetric models (SUSY) are of particular interest [63-69].

We now consider a more general variant of the SUSY model, where new mechanisms of CP violation and changes of quark flavors may take place. The contribution from supersymmetric particles may quite noticeably change the $Zd\bar{s}$ vertex, which will have a very significant impact on the branching ratios of kaon FCNC decays. In the general case, such processes are described by 4 quark operators of the form $\frac{1}{M^2}(\bar{f}f)(\bar{f}f)$ where M is some mass scale. Another SUSY contribution is related with the so-called chromomagnetic operators of the type $\frac{1}{M}\bar{q}\sigma^{\mu\nu} f_{\mu\nu} q$ which influences the photon or gluon radiation ($f_{\mu\nu}$ field). These operators manifest themselves in $BR(K_L^0 \to \pi^0 l^+ l^-)|_{CP-dir}$ and in ε'/ε [65, 66, 68, 69].

Supersymmetric models lead to the following modification of the X_L amplitude in (94), (95)

$$X_L = (X_L)_{SM} + \frac{\tilde{\lambda}_t}{\lambda_t} H(x_s) = X. \tag{96}$$

Here $\tilde{\lambda}_t$ and $H(x_s)$ are defined by the masses and mixing of supersymmetric particles which make an additional contributions to the amplitudes of FCNC processes. The contributions depend on three effective constants: Λ_t (accounts for the $Zd\bar{s}$ vertex modification) and $\Lambda_g^{\pm}$ (accounts for the contribution from chromomagetic operators). Here $\Lambda_t = \tilde{\lambda}_t H(x_s)$ and similar expressions are for $\Lambda_g^{\pm}$ with loop functions which describe chromomagnetic penguin diagrams.

In other words the supersymmetric contribution leads to the following modification of the expressions for probabilities of the FCNC processes:

$$\lambda_t \cdot O(x_t) \to \lambda_t O(x_t) + \Lambda_t(\Lambda_g^{\pm}) \tag{97}$$

Here λ_t is related to the CKM matrix, Λ_t describes the contribution from new processes in the $Zd\bar{s}$ vertex, and $\Lambda_g^{\pm}$ are chromomagnetic operators. Some upper estimates have been obtained for these quantities:

$$|\Lambda_t| \lesssim 3 \cdot 10^{-3} \left(\frac{500\text{GeV}}{m_{\tilde{q}}}\right) \text{ and } |\Lambda_g^{\pm}| < 10^{-4} \left(\frac{500\text{GeV}}{m_{\tilde{q}}}\right). \tag{98}$$

The supersymmetric contribution to the X_L amplitude has a rather complicated character and depends on the various supersymmetric models being considered, which are characterized by different masses and mixing mechanisms of new particles as well as by some other peculiarities. Various scenarios which lead to essentially different results, have been considered. Additional constraints on the model parameters, brought forward by the experimental data on ε'/ε and $BR(K_L^0 \to \mu^+\mu^-)_{SD}$, have been taken into account.

Different supersymmetric contributions influence, each in its own way, the decay probabilities $BR(K^+ \to \pi^+\nu\bar{\nu})$, $BR(K_L^0 \to \pi^0\nu\bar{\nu})$ and $BR(K_L^0 \to \pi^0 l^+ l^-)_{CP-dir}$. For instance, chromomagnetic penguin operators make a contribution only to $K_L^0 \to \pi^0 l^+ l^-$ and do not change predictions for the other $K \to \pi\nu\bar{\nu}$ decays. On the other hand, the $K_L^0 \to \pi^0\nu\bar{\nu}$ decay is insensitive to certain supersymmetric models where direct CP violation is no longer defined by the V_{CKM} phase (which is quite small in such models), but by new mechanisms. This is the reason why it is so important to carry out experimental studies of all the three rare K-meson processes and to compare the data to theoretical predictions in different variants of supersymmetric models.

We present here the results of the most consistent and conservative analysis from [65,66]. Various phenomenological scenarios of CP violation are treated in the analysis, where: a) $Im\Lambda_t = 0$ and $Im\Lambda_g^{\pm} \neq 0$, b) $Im\Lambda_t \neq 0$ and $Im\Lambda_g^{\pm} = 0$, c) $Im\Lambda_t \neq 0$ and $Im\Lambda_g^{\pm} \neq 0$. At the same time various assumptions on λ_t are made, which now can differ from the preferred SM values, but satisfy the unitarity condition of CKM matrix (e.g., the case has been considered where $Im\lambda_t = 0$ described above). To characterize qualitatively the influence of the parameters λ_t and Λ_t on the probability of rare FCNC kaon decays we present the relevant estimates in Table D.5 [66].

Different scenarios of the model [65,66] give the following limits for the decay probabilities:

$$\left.\begin{array}{ll} BR(K^+ \to \pi^+\nu\bar{\nu}) & < 2.7\cdot 10^{-10}\ (< 1.7\cdot 10^{-10}) \\ BR(K_L^0 \to \pi^0\nu\bar{\nu}) & < 4\cdot 10^{-10}\ (< 1.2\cdot 10^{-10}) \\ BR(K_L^0 \to \pi^0 e^+e^-)_{CP-dir} & < 6\cdot 10^{-11}\ (< 2\cdot 10^{-11}). \end{array}\right\} \tag{99}$$

Here in the brackets are the most probable limitations, which do not demand extreme assumptions. It should be noted that in this model, for the variant with $Im\lambda_t = 0$, $BR(K_L^0 \to \pi^0\nu\bar{\nu})$ has a very small value ($< 10^{-14}$ [35]).

Less stringent limitations quoted in [63,64] seem to be artificial and hardly probable, though they cannot be completely neglected because of possible compensations between different supersymmetric contributions.

Other variants of supersymmetric extensions of the Standard Model were also considered. For instance, papers in [67] analyze rare K and B-meson data and CP violation in the framework of 'least expansion' to the SM in which new processes with flavor and CP violation are absent (the so-called MSSM model with MFV (Minimal Flavor Violation) requirement). In this version, one complex phase in the CKM matrix remains as the sole source of CP violation. Quark flavor mixing is also defined by this matrix. The contributions from supersymmetric particles and new Higgs doublets manifest themselves through the corrections to the loop diagrams describing the processes of $K^0 \rightleftarrows \bar{K}^0$ and $B^0 \rightleftarrows \bar{B}^0$ mixing, FCNC decays, etc. The main contributions to these corrections are made by the charged Higgs bosons $H^\pm$ and supersymmetric charginos χ_j^+ $(j = 1,2)$, which interact with bottom d-, s-, b-quarks and top superquarks $\tilde{u}, \tilde{c}, \tilde{t}$. The contribution from supersymmetric particles in this case tends to reduce the $K \to \pi\nu\nu$ and $K_L^0 \to \pi^0 l^+ l^-$ branching ratios [67]:

$$\left.\begin{array}{l} 0.65 \le \dfrac{BR(K^+ \to \pi^+\nu\bar{\nu})_{MSSM}}{BR(K^+ \to \pi^+\nu\bar{\nu})_{SM}} \le 1.03 \\ 0.41 \le \dfrac{BR(K_L^0 \to \pi^0\nu\bar{\nu})_{MSSM}}{BR(K_L^0 \to \pi^0\nu\bar{\nu})_{SM}} \le 1.03 \\ 0.48 < \dfrac{BR(K_L^0 \to \pi^0 e^+e^-)_{CP-dir.\,MSSM}}{BR(K_L^0 \to \pi^0 e^+e^-)_{CP-dir.\,SM}} < 1.1 \end{array}\right\} \tag{100}$$

If the probabilities for these decays significantly exceed the SM predictions, it will imply, that more complicated mechanisms of CP violation, which are not described by one CKM phase, take place in nature.

In the supersymmetric model of [70] all CP violation in K decays are due to a FCNC sd-transition with gluino exchange, and the CKM matrix does not contain complex elements. This mechanism makes no contribution to the CP violating $s \to d\nu\bar{\nu}$ decay. Therefore in the model under consideration the $K_L^0 \to \pi^0\nu\bar{\nu}$ branching ratio will be very small. At the same time, the branching ratio for $K^+ \to \pi^+\nu\bar{\nu}$, which has CP-conserving as well as CP violating amplitudes, will be comparable with the SM predictions.

In models with technicolor, the probabilities for the $K \to \pi\nu\bar{\nu}$ decays may be one or two orders of magnitude larger than the SM predictions, which is due to the influence of new interactions on the $Zd\bar{s}$ vertex [71]. In fact, the existing data for the $K^+ \to \pi^+\nu\bar{\nu}$ and $K_L^0 \to \mu^+\mu^-$ decays is used to constrain the technicolor model parameters. The resulting limits on the technicolor parameters still allows for a possible increase of 1-10 times the SM prediction of the $K^+ \to \pi^+\nu\bar{\nu}$ and $K_L^0 \to \pi^0\nu\bar{\nu}$ branching ratio.

The branching ratios for $K \to \pi\nu\bar{\nu}$ decays can also change by considerable amounts in several exotic theories including supersymmetric models with R parity violation, models with leptoquarks as well as in some other models with significant modification of the structure of the FCNC [60, 61].

In conclusion, table 29 presents the data and the possible manifestations of new physics in rare $K^+ \to \pi^+\nu\bar{\nu}, K_L^0 \to \pi^0\nu\bar{\nu}$ and $K_L^0 \to \pi^0 e^+ e^-$ decays, which were discussed in [60-75]. It shows that future experiments on the studies of rare kaon decays provide a unique opportunity to perform high precision tests of CP violation and flavor mixing within and beyond the SM. It was also stated, that in the kaon system large SUSY effects are naturally expected in any model with non-universal soft-breaking terms. The proposed $K \to \pi\nu\bar{\nu}$ experiments have a real possibility of obtaining one of the first evidence for new physics including supersymmetry extensions of the Standard Model [13, 18, 20, 68, 76].

D.6 Lepton flavor violating processes in kaon decays

The main decay processes with lepton flavor violation (LFV) are summarized in Table 31. For completeness, LFV results from K^+ decays are also included.

From purely statistical considerations, there is a clear opportunity for KAMI to perform (in parallel with the main $K_L \to \pi^0\nu\bar{\nu}$ measurement) considerably more sensitive searches for many of these modes to the level $\sim 10^{-13}$. Careful investigation of possible background limitations for these searches must be done, and some are already under way.

Even sensitivities of 10^{-13} for kaon LFV processes appear modest compared with sophisticated new proposals to search for $\mu \to e\gamma$ [84] and $\mu^- + A \to e^- + A$ [85] LFV processes to the level $< 10^{-14} \div 10^{-16}$. But it is very important to stress that the searches for LFV in kaon decays are complimentary to the $\mu \to e\gamma$ searches. Kaon decays are the only processes that are sensitive to $s \to d\mu\bar{e}$ interactions. Such decays could exhibit very exceptional properties and open a unique possibility to study lepton flavor violation with more favorable conditions for certain hypothetical selection rules connected with fundamental generation number conservation. In other words, for these decays a change of generation in the leptonic sector can be compensated by a corresponding change of generation in the quark sector ([86], see also [45, 87, 88]). Let us introduce the generation number $G_1 = 1$ for the first fundamental fermion generation and $G_2 = 2$ for the second one (for antifermions $G_1 = -1$; $G_2 = -2$). As is seen from diagrams in Figure 92, it is possible to classify different processes according to changing ΔG, as follows from Table 32.

The strength of hypothetical ΔG selection rule is unclear now. A new perspective in the search for LFV effects in kaon decays to compare with muon processes will open only if this strength is meaningful and every next order in ΔG will lead to significant suppression of corresponding decay rates to compare with lower order processes.

In the diagrams in Figure 92, the decay processes are governed by the exchange of a "horizontal" intermediate boson H^0. But it is also possible to consider kaon decay LFV processes $s \to d\mu\bar{e}$ which are governed by the exchange of leptoquarks Y^*. Amplitudes for $s \to d\mu\bar{e}$ processes of the pseudoscalar and axial-vector type (for $K_L^0 \to \mu\bar{e}$ decay) or vector, scalar and tensor structure (for $K \to \pi\mu\bar{e}$ decay) with the "horizontal" H^0 boson exchange

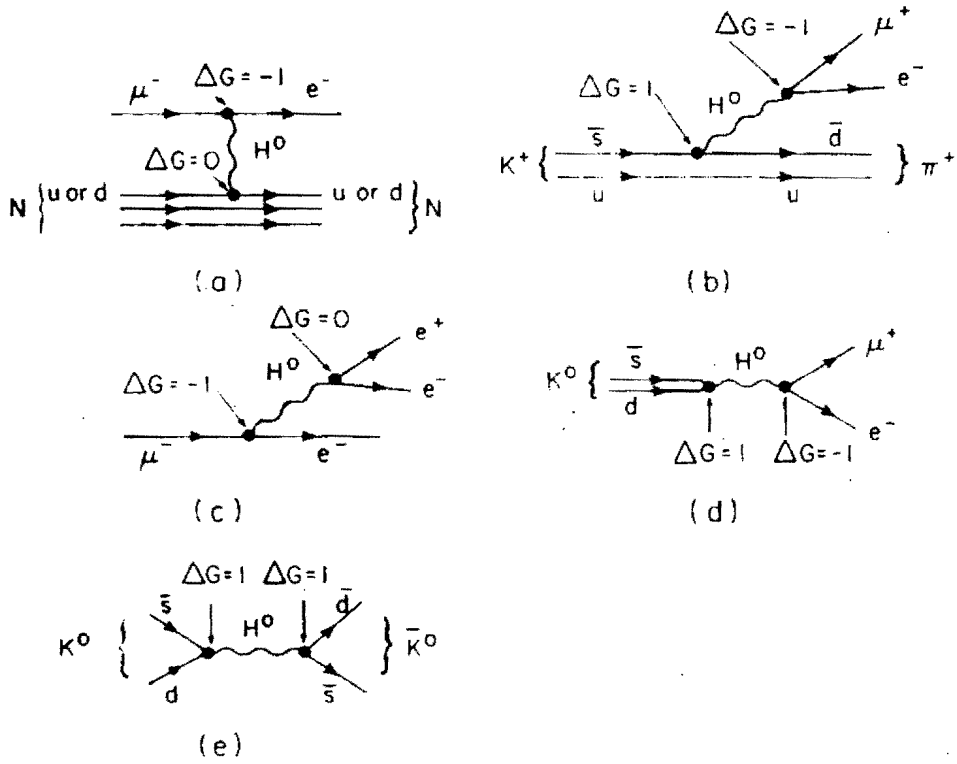

Figure 92: Diagrams for LFV processes and $K^0 \rightleftarrows \bar{K}^0$ mixing in horizontal boson exchange model with ΔG selection rule.

can be presented with the help of general generation number conserving operators [60]:

$$\left.\begin{array}{l} Q_{V,A} = \frac{g_H^2}{2M_H^2}\bar{d}\gamma_\mu[C_{Lq}P_L + C_{Rq}P_R]s \quad \cdot \quad \bar{\mu}\gamma^\mu[C_{Ll}P_L + C_{Rl}P_R]e + \text{h.c.} \\ Q_{S,P} = \frac{g_H^2}{2M_H^2}\bar{d}[C'_{Lq}P_L + C'_{Rq}P_R]s \quad \cdot \quad \bar{\mu}[C'_{Ll}P_L + C'_{Rl}P_R]e + \text{h.c.} \end{array}\right\} \tag{101}$$

Where $P_L = (1-\gamma_5)$; $P_R = (1+\gamma_5)$; C, C' are constants.

Calculation of the branching ratios for $K \to \mu e$ and $K \to \pi\mu e$ decays for the interactions in (101) are presented for illustration in Figure 93 as a function of the scale parameter M_H (for $g_H = g$ – a weak constant; $C, C' = 1$).

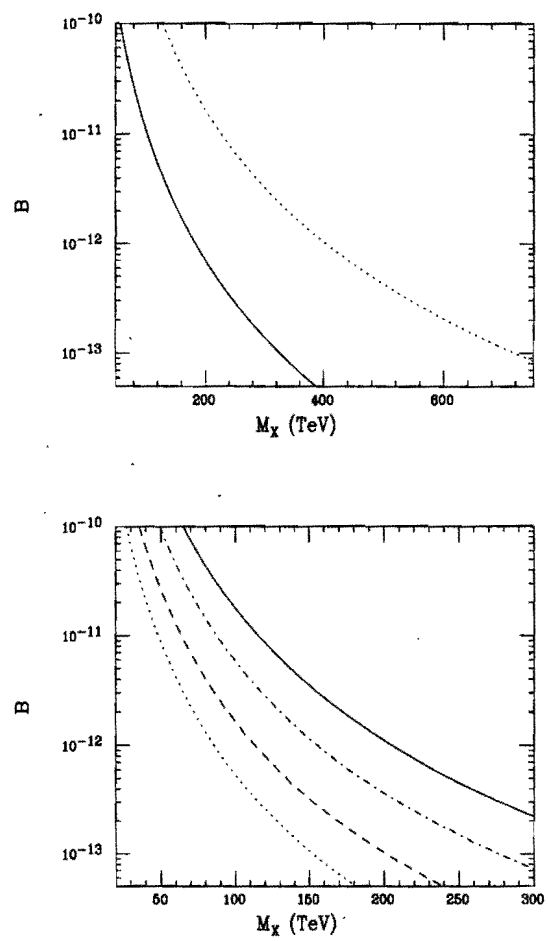

Figure 93: Branching fractions for $K_L \to e\mu$ (a) and $K \to \pi e\mu$ (b) as function of the scale parameter $M_X = M_H$ in (101) (assuming $g_X = g$ – weak constant). In (a) the solid (dotted) curves correspond to A(P) exchange. In (b) the K_L^0 mode is represented by the solid (S) and dashed (V) curves while the K^+ mode is represented by the dash-dotted (S) and dotted (V) curves (see [60]). Here V, A, S, P correspond to vector, axial-vector,scalar and pseudoscalar interactions, respectively.

There are other interesting models for $s \to d\mu e$ processes in supersymmetrc theories with

R-parity non-conservation [89, 90], in left-right models with heavy Majorana neutrinos [91] and in leptoquark exchange models [92].

LFV processes are known to take place in both the minimal supersymmetric models (MSSM) and in its modifications which include violation of R-parity. In the context of the MSSM, rare kaon decays allow one to correlate (s)quark and (s)lepton mixing, while in R-violating supersymmetry one can probe non-trivial products of Yukawa couplings.

Within framework of the MSSM the magnitudes of the predicted rates depend on the details of the masses and mixings of sparticles including the sneutrinos. Maximal contributions for $K_L^0 \to \mu^\pm e^\mp$ decays are expected from the box diagrams involving chargino and neutralino exchange. However, the universal GUT-scale parameters for sfermions and gauginos, when limited from the similar pure lepton decays $\mu \to e\gamma$ and $\mu \to e^+e^+e^-$, lead to hopelessly low branching ratios of order $10^{-16} \div 10^{-18}$. Only a fine tuning of GUT parameters can make such searches more interesting within this framework.

The situation can be very different in R-parity violating supersymmetric models, as pointed out in [89,90]. In this case, the gauge symmetry of the SUSY model allows additional Yukawa coupling terms in the superpotential of the form $\lambda L_i L_j \bar{E}_k$, $\lambda' L_i Q_j \bar{D}_k$, $\lambda'' \bar{U}_i \bar{D}_j \bar{D}_k$. Here the $L(Q)$ are the left-handed lepton (quark) superfields and the $\bar{E}$ ($\bar{D}$, $\bar{U}$) are corresponding right-handed fields. Each of these terms has three Yukawa couplings. For example the first term is

$$\lambda_i jk(L_i L_j \tilde{\bar{E}}_k + L_i \tilde{L}_j \bar{E}_k + \tilde{L}_i L_j \bar{E}_k)$$

. This term involves a single SUSY state and violates the R-parity of MSSM. For electroweak SU(2) and color SU(3) symmetry it was shown that there are 45 R-violating couplings. Certainly, there are many experimental constrains on this set of constants (non-observation of proton decay and some exotic processes, lepton universality, non-observation of possible modification of different SM processes). In spite of these limitations it was stated in [89] that it is still possible that several R-violating operators may be large and useful limitations for some of them can be obtained from existing upper limits for LFV kaon decays and from their future searches. In this class of models, $\mu \to e\gamma$ occurs at the one loop level, $\mu \to 3e$, $\mu \to e$ conversion, $K_L^0 \to \mu^\pm e^\mp$ and $K \to \pi\mu^\pm e^\mp$ decays may occur at tree level via different combinations of couplings. Thus, LFV kaon decays have the possibility to provide important complimentary information for R-parity violating processes.

For illustration, it is possible to consider the $d\bar{s} \to l_j^- l_k^+$ interaction with an effective Lagrangian written in terms of quark and lepton fields

$$\begin{aligned}\mathcal{L}_{d\bar{s}\to l_j^- l_k^+} &= \frac{1}{m^2_{\tilde{\nu}_i}}\left[\lambda^*_{ijk}\lambda'_{i12}(\bar{s}_R d_L(\bar{l}_{jL} l_{kR}) + \lambda_{ikj}\lambda'^*_{i12}(\bar{s}_L d_R)(\bar{l}_{jR} l_{kR})\right] - \\ &\quad - \frac{\lambda'^*_{ji1}\lambda'_{ki2}}{2m^2_{\tilde{u}_i}}(\bar{s}_R\gamma_\mu d_R)(\bar{l}_{jL} l_{kL}). \end{aligned} \tag{102}$$

The tree diagrams for $K^0 \to l_j^- l_k^+$ and $K \to \pi l_j^- l_k^+$ decays are presented in Figure 94.
The calculations from (102) and upper limits for $K_L^0 \to \mu^\pm e^\mp$ decays (Table 31) give limitations for the values of $\lambda\lambda'/m_{\tilde{\nu}}$ and $\lambda\lambda'/m_{\tilde{u}}$ with sneutrino ($\tilde{\nu}$) and up squark ($\tilde{u}$) contributions

$$\left.\begin{aligned}\lambda_{i21}\lambda'_{i12}\left(\tfrac{100\,\mathrm{GeV}}{m_{\tilde{\nu}}}\right) &\le 6.2\cdot 10^{-9} \\ \lambda_{i21}\lambda'_{i12}\left(\tfrac{100\,\mathrm{GeV}}{m_{\tilde{u}}}\right) &\le 1.9\cdot 10^{-7}\end{aligned}\right\} \tag{103}$$

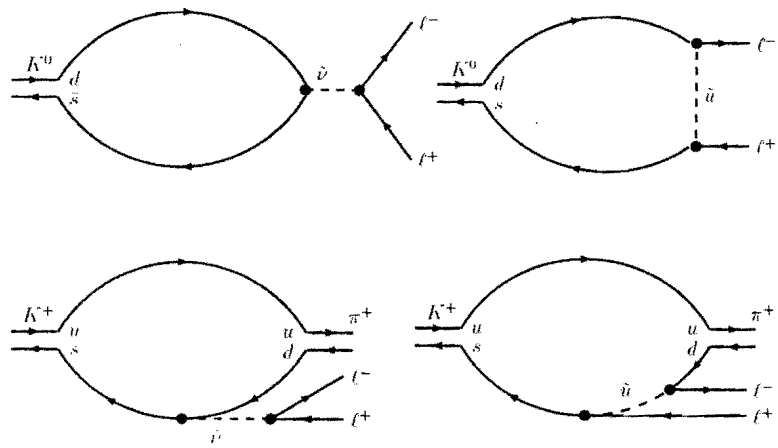

Figure 94: Diagrams for $K \to \mu e$ and $K \to \pi\mu e$ in SUSY model with R-parity non-conservation [89]

From $K \to \pi l_j^- l_k^+$ decays the upper limits for $\lambda\lambda'/m_{\tilde{\nu}}$ and $\lambda\lambda'/m_{\tilde{u}}$ are 1-2 orders of magnitude larger than in (103).

The decay $K_L^0 \to \mu^\pm e^\mp$ was considered also in the left-right $SU(2)_R \circledast SU(2)_L \circledast U(1)_{B-L}$ gauge model which includes new W_R intermediate bosons and heavy Majorano neutrino [91]. It was shown that $BR(K_L^0 \to \mu^\pm e^\mp)$ can be considerably enhanced due to the presence of left- and right-handed currents in the loop diagrams for this decay. Even the existing upper limit for $BR(K_L^0 \to \mu^\pm e^\mp)$ gives important constraints for the parameters of the $L \circledast R$ models. Thus, new more sensitive searches for this decay are quite desirable. It was stated in [91] that $K_L^0 \to \mu^\pm e^\mp$ could be sensitive to LFV mechanisms that do not manifest themselves in muons decays and $\mu \to e$ conversion.

Further searches for LFV kaon decays are very important since they offer complementary information on possible theories of lepton flavor non-conservation. In some instances the information available from kaon decays is unique and not accessible in muon processes.

$\lambda = \lvert V_{us}\rvert = 0.2196 \pm 0.0023$
$\bar{\rho} = 0.223 \pm 0.038$
$\bar{\eta} = 0.316 \pm 0.039$
$\lvert V_{cb}\rvert = (41.0 \pm 1.6) \cdot 10^{-3}$
$\lvert V_{ub}\rvert = (35.5 \pm 3.6) \cdot 10^{-4}$
$A = V_{cb}/\lambda^2 = 0.819 \pm 0.049$
$\sin 2\beta = 0.70 \pm 0.07$
$m_t = \bar{m}_t = 167 \pm 5$ GeV
$F(x_t) = 1.53 \pm 0.05$
$\rho_0 = 1 + \dfrac{P_0}{A^2 \cdot F(x_t)} = 1 + F(x_c)/A^2\lambda^4 F(x_t) = 1.42 \pm 0.06$
$\xi = f_{B_s}\sqrt{B_s}/f_{B_d}\sqrt{B_d} = 1.14 \pm 0.06$
$m_{B_d^0} = 5.2792$ GeV
$m_{B_s^0} = 5.3693$ GeV
$m_w = 80.41$ GeV

Table 27: Main parameters of CKM matrix and Standard Model which are important for evaluation of $K \to \pi\nu\nu$ branching ratios and other values [32, 34] – see also [29-31],[33].

Branching ratios of $K \to \pi\nu\bar{\nu}$ decays in the SM (see (50) and (51))

$$BR(K^+ \to \pi^+\nu\bar{\nu}) = 4.06 \cdot 10^{-11} A^4 F(x_t)^2 \cdot \frac{1}{\sigma}[(\rho_0 - \bar{\rho})^2 + (\sigma\bar{\eta})^2] =$$

$$= 4.06 \cdot 10^{-11} \left[\left(\frac{Im\lambda_t}{\lambda^5} F(x_t) \right)^2 + \left(\frac{Re\lambda_c}{\lambda} P_0 + \frac{Re\lambda_t}{\lambda^5} F(x_t) \right)^2 \right]$$

$$BR(K_L^0 \to \pi^0\nu\bar{\nu}) = 1.78 \cdot 10^{-10} A^4 F(x_t)^2 \sigma(\bar{\eta})^2 = 1.78 \cdot 10^{-10} \left(\frac{Im\lambda_t}{\lambda^5} F(x_t) \right)^2$$

Reduced branching ratios:

$$B_1 = \frac{BR(K^+ \to \pi^+\nu\bar{\nu})}{4.06 \cdot 10^{-11}} \; ; \; B_2 = \frac{BR(K_L^0 \to \pi^0\nu\bar{\nu})}{1.78 \cdot 10^{-10}}$$

From (50) and (51):

$$Im\lambda_t = \lambda^5 \frac{\sqrt{B_2}}{F(x_t)}$$

$$Re\lambda_t = -\lambda^5 \left[\frac{\frac{Re\lambda_c}{\lambda} P_0 + \sqrt{B_1 - B_2}}{F(x_t)} \right]$$

From (8) :

$$Re\lambda_t = -A^2\lambda^5(1-\bar{\rho})\frac{1}{\sqrt{\sigma}}$$

$$Re\lambda_c = -\frac{\lambda}{\sqrt{\sigma}}$$

$$\bar{\rho} = 1 + \frac{P_0 - \sqrt{\sigma(B_1 - B_2)}}{A^2 F(x_t)}$$

$$\bar{\eta} = \frac{\sqrt{B_2}}{\sqrt{\sigma} A^2 F(x_t)}$$

$$V_{td} = A\lambda^3(1 - \bar{\rho} - i\bar{\eta})$$

$$|V_{td}| = A\lambda^3 \cdot \sqrt{(1-\bar{\rho})^2 + \bar{\eta}^2}$$

These values can be determined from measurements of branching ratios for $K \to \pi\nu\bar{\nu}$ decays i.e. B_1 and B_2

We introduce

$$\frac{1-\bar{\rho}}{\bar{\eta}} = \sqrt{\sigma} \frac{[\sqrt{\sigma(B_1 - B_2)} - P_0]}{\sqrt{B_2}}$$

Then

$$\sin 2\beta = \frac{2\bar{\eta}(1-\bar{\rho})}{(1-\bar{\rho})^2 + \bar{\eta}^2} = \frac{2r_s}{1 + r_s^2}$$

The precision ofon $\sin 2\beta$ does not depend on uncertainties on $F(x_t)$ or on the precision of m_t and $|V_{cb}|$.Thus the result for $\sin 2\beta$ from $K \to \pi\nu\bar{\nu}$ decays is dependent only on the precision of measurements of B_1 and B_2 and from calculation of $P_0 = F(x_c)/\lambda^4$

$$\text{For SM } \sin 2\beta \mid_K = \frac{2r_s}{1 + r_s^2} = a_{\psi K_S^0} = \sin 2\beta \mid_B$$

Table 28: Determination of $\sin 2\beta$ and $|V_{td}|$ from branching ratios $BR(K^+ \to \pi^+\nu\bar{\nu})$ and $BR(K_L^0 \to \pi^0\nu\bar{\nu})$ (see [15-18]).

	$BR(K^+ \to \pi^+ \nu\bar{\nu})$	$BR(K_L^0 \to \pi^0 \nu\bar{\nu})$	$BR(K_L^0 \to \pi^0 e^+ e^-)_{CP-dir}$	Note
Standard Model prediction	$(7.4 \pm 1.7) \cdot 10^{-11}$	$(2.6 \pm 0.9) \cdot 10^{-11}$	$(4.1 \pm 1.3) \cdot 10^{-12}$	with values of SM parameters from Table 27.
Experimental data	$(15^{+34}_{-12}) \cdot 10^{-11}$ [77]	$< 5.9 \cdot 10^{-7}$ [78] (90% C.L.)	$< 5.1 \cdot 10^{-10}$ [47] (90% C.L.)	From isospin symmetry there is a model independent limit: $BR(K_L^0 \to \pi^0 \nu\bar{\nu}) < 4.4 BR(K^+ \to \pi^+ \nu\bar{\nu}) \leq 2.9 \cdot 10^{-9}$ (90% C.L.)

Models with new physics	$R_{(1)} = \mathrm{BR}(\pi^+ \nu\bar{\nu}) / \mathrm{BR}(\pi^+ \nu\bar{\nu})_{SM}$	$R_{(2)} = \mathrm{BR}(\pi^0 \nu\bar{\nu}) / \mathrm{BR}(\pi^0 \nu\bar{\nu})_{SM}$	$R_{(3)} = \mathrm{BR}(\pi^0 e^+ e^-)_{CP-dir} / \mathrm{BR}(\pi^0 e^+ e^-)_{CP-dirSM}$	
Super symmetry models with general flavour and CP violation and with modification of $Zd\bar{s}$ structure [65, 66, 68]	< 4	$< 14 - 18$	$< 22 - 29$	The most probable limitations are: $R_{(1)} < 2.2$ $R_{(2)} < 4.3$ $R_{(3)} < 10$
[64] (with some additional mechanisms)	≤ 3 ($\leq 6,5$)	≤ 8 (< 45)	≤ 7 (< 45)	Values of $R_{(3)} \gtrsim 10$ can be due to influence of chromomagnetic operators. Very large values of $R_{(1)}, R_{(2)}$ and $R_{(3)}$ as a rule have been obtained without taking into account all experimental limitations ([63]), or by fine tuning of some model parameters and are not very probable.
[63]	< 12	< 130	≤ 120	

Table 29: Branching ratios $BR(\pi^+ \nu\bar{\nu})$, $BR(\pi^0 \nu\bar{\nu})$ and $BR(\pi^0 e^+ e^-)_{CP-dir}$ for various new physics scenarios.

	$R_{(1)}$	$R_{(2)}$	$R_{(3)}$	
Minimal SUSY with Minimal Flavor Violation (MFV). No new mechanisms of CP violation [67,68]	0.65 – 1.03	0.41 – 1.03	0.48 – 1.1	The decay probabilities are modified due to the supersymmetry corrections in the loop diagrams. In this model the decay probabilities as a rule are reduced in comparison with SM predictions.
SUSY with real CKM matrix and new mechanisms of CP violation (sd transition with gluino exchange) [70].	0.2 – 2	$\ll 1$		$R_{(2)}$ is very small since the CKM phase is $\simeq 0$ and the gluino exchange mechanism makes very small contributions to $K_L^0 \to \pi^0 \nu\bar{\nu}$.
Model with 4 fundamental generations of quarks and leptons [62]	0.9 – 6	0.2 – 36		Instead of a unitary triangle, there is instead a unitary quadrangle
Technicolor [71]	$< 1 - 10$	$< 1 - 10$		$K^+ \to \pi^+ \nu\bar{\nu}$ and $K_L^0 \to \mu^+\mu^-$ data can be used to obtain the limits for the parameters of technicolor models.
Model with lepton flavor violation for the decay $K_L^0 \to \pi^0 \nu_i \bar{\nu}_j$ [23]		CP conserving process can be dominant for this decay		For SM CP conserving decay $K_L^0 \to \pi^0 \nu\bar{\nu}$ is very small ($\sim 10^{-14}$) [35].
L-R model with W_L and W_R and X_L and X_R amplitudes. In this model there is an additional scalar interaction which gives a CP conserving input to $K \to \pi\nu\bar{\nu}$ [72]	1	1.3		In this model the scalar operator gives additional CP conserving input even to $K_L^0 \to \pi^0 \nu\bar{\nu}$ (in distinction from V-A interaction of SM). Additional interaction modifies the soft part of π^0 momentum spectrum in $K_L^0 \to \pi^0 \nu\bar{\nu}$ and increases $R_{(2)}$ by $\sim 30\%$.
Anomalous interactions in the triple boson WWZ vertex [73]	0.1 – 2.8			It was shown that if the anomalous coupling constant of WWZ interaction Δg_1^z varies from -0.2 to +0.2, the ratio $R_{(1)}$ can vary from 0.1 up to 2.8. This ratio is not sensitive to Δg_5^z.
Several variants of MSSM, two doublet Higgs models, several other theories [20,60,61,74,75]	1	1		If quark mixing and CP violation is governed by the properties of CKM matrix (in the same way as in the SM) the branching ratios of $K \to \pi\nu\bar{\nu}$ decays would be the same as in the SM.

Table 29: (continuation)

Λ_t	BR	λ_t from SM	λ_t is not from SM, but satisfies the unitarity requirements of the quark mixing matrix
$\Lambda_t > 0$	$BR(K_L^0 \to \pi^0 \nu\bar{\nu})$	$0.7 \cdot 10^{-10}$	$0.9 \cdot 10^{-10}$
	$BR(K_L^0 \to \pi^0 e^+ e^-)_{CP-dir}$	$1.1 \cdot 10^{-11}$	$1.3 \cdot 10^{-11}$
	$BR(K^+ \to \pi^+ \nu\bar{\nu})$	$1.7 \cdot 10^{-10}$	$2.0 \cdot 10^{-10}$
$\Lambda_t < 0$	$BR(K_L^0 \to \pi^0 \nu\bar{\nu})$	$0.8 \cdot 10^{-10}$	$4.0 \cdot 10^{-10}$
	$BR(K_L^0 \to \pi^0 e^+ e^-)_{CP-dir}$	$2.0 \cdot 10^{-11}$	$5.9 \cdot 10^{-11}$
	$BR(K^+ \to \pi^+ \nu\bar{\nu})$	$1.7 \cdot 10^{-10}$	$2.7 \cdot 10^{-10}$

Table 30: The dependence of branching ratios for decays $K \to \pi\nu\bar{\nu}$ and $K_L^0 \to \pi^0 e^+ e^- \mid_{CP-dir}$ in the SUSY model [66] on the parameters λ_t and Λ_t.

	Upper limit (90% C.L.)	Expected Statistical sensitivity in KAMI experiment
$BR(K_L^0 \to \pi^0 \mu e)$	$4.4 \cdot 10^{-10}$ [80]	4×10^{-13}
$BR(K_L^0 \to \pi^+ \pi^- \mu e)$	-	$\sim 10^{-13}$
$BR(K_L^0 \to \pi^0 \pi^0 \mu e)$	-	$\sim 10^{-13}$
$BR(K_L^0 \to \mu^\pm \mu^\pm e^\mp e^\mp)$	1.36×10^{-10} [52]	3×10^{-13}
$BR(K_L^0 \to \mu e)$	$4.7 \cdot 10^{-12}$ [79]	-
$BR(K^+ \to \pi^+ \mu^+ e^-)$	$2.8 \cdot 10^{-11}$ [82]	-
$BR(K^+ \to \pi^+ \mu^- e^+)$	$5.2 \cdot 10^{-10}$ [83]	-
$BR(K^+ \to \pi^- \mu^+ e^+)$	$5.0 \cdot 10^{-10}$ [83]	-
$BR(K^+ \to \pi^- \mu^+ \mu^+)$	$3.0 \cdot 10^{-9}$ [83]	-
$BR(K^+ \to \pi^- e^+ e^+)$	$6.4 \cdot 10^{-10}$ [83]	-

Table 31: Lepton flavor violation in kaon decays

First order	$\Delta G = 0$	$K^+ \to \pi^+ \mu^+ e^-$; $K_L^0 \to \mu^\mp e^\pm$;$K_L^0 \to \pi^0 \mu^\mp e^\pm$
Second order	$\lvert\Delta G\rvert = 1$	$\mu \to 3e$; $\mu \to e\gamma$; $\mu^- N \to e^- N$;
Third order	$\lvert\Delta G\rvert = 2$	$K^0 \rightleftarrows \bar{K}^0 (\Delta m(K_1^0 - K_2^0))$; $\mu^- e^+ \to \mu^+ e^-$; $K^+ \to \pi^+ \mu^- e^+$

Table 32: Classification of some rare generation changing processes.

References

[1] G. C. Branco et al., CP violation, Clarendon Press, Oxford, 1999

[2] I.I. Bigi, A.I. Sanda, CP violation, Cambridge University Press, 2000

[3] G. Buchalla et al., Rev. Mod. Phys. **68**, 1125 (1996).

[4] G. D'Ambrosio, G. Isidori, Int. Journ. of Mod. Phys. **A13**, 1 (1998).

[5] T. Inami and C. S. Lim, Prog. Theor. Phys. **65**, 297 (1981).

[6] J. Ellis, J. S. Hagelin, Phys. Lett. **B192**, 201 (1983);
Nucl. Phys. **B217**, 189 (1983).

[7] C. O. Dib et al., Mod. Phys. Lett. **A6**, 3573 (1991).

[8] G. Buchalla, A. J. Buras, Nucl. Phys. **B412**, 106 (1994);
Phys. Rev. **D54**, 6782 (1996).

[9] D. Rein, L. S. Sehgal, Phys. Rev. **D39**, 3325 (1989).

[10] W. Marciano, Z. Parsa, Phys. Rev. **D53**, R1 (1996).

[11] M. Lu, M. Wise, Phys. Lett. **B324**, 461 (1994).

[12] S. Faifer, Nuov. Cim, **110A**, 397 (1997).

[13] A. J. Buras hep-ph/0101336

[14] A. J. Buras hep-ph/9711217, TUM-HEP-299/97.

[15] A. J. Buras, R. Fleischer, hep-ph/9704376, TUM-HEP-275/97, TTP 97-15.

[16] A. J. Buras, hep-ph/9806471, TUM-HEP-316/98.

[17] G. Buchalla, A. J. Buras, hep-ph/9901288, Nucl. Phys. **B548**, 39 (1999).

[18] A. J. Buras, hep-ph/9905437. Lectures at 14 Lare Louise Winter Institute, February 1999.

[19] G. Buchalla, hep-ph/9912369, CERN-TH/99-325;
G. Buchalla, hep-ph/0002207, CERN-TH/2000-057.

[20] G. Isidori, hep-ph/9902235;
G. Isidori, hep-ph/9908399.

[21] A. R. Barker, S. H. Kettell, hep-ph/0009024

[22] L. Littenbery, Phys. Rev. **D39**, 3322 (1989).

[23] Y. Grossman, Y. Nir, Phys. Lett. **398**, 163 (1997);

[24] L.G. Landsberg, Preprint IHEP 2000-27, Protvino,2000; Yad.Fiz. (in press) 2001.

[25] S. Bosch et al., Nucl. Phys., **B565**, 3 (2000).

[26] N. Cabibbo, Phys. Rev. Lett. **53**, 531 (1963).

[27] M. Kobayashi, and T. Maskava, Prog. Theor. Phys. **49**, 652 (1973).

[28] L. Wolfenstein, Phys. Rev. Lett. **51**, 1945 (1983).

[29] M. Bargiotti et al., Riv. Nuov. Cim. **23**, 1 (2000), hep-ph/0001293.

[30] P. Faccioli, hep-ph/0011269.

[31] A. Stocchi, hep-ph/0012215.

[32] M. Ciuchini et al. hep-ph/0012308, LAL 0077.

[33] S. Mele, hep-ph/0103040.

[34] D. E. Groom et al.(PDG), Europ. Phys. Journ. **C15**, 1 (2000).

[35] G. Buchalla, G. Isidori, hep-ph/9806051, Phys. Lett. **B440**, 170 (1998),

[36] A. J. Buras et al., Nucl. Phys. **B423**, 349 (1994).

[37] J. F. Donoghue, F. Gubbiani, Phys. Rev. **D51**, 2187 (1995).

[38] C. O. Dib et al., Phys. Lett. **B218**, 487 (1989), Phys. Rev. **D39**, 2639 (1989).

[39] G. D.'Ambrosio et al., hep-ph/9808289,

[40] V. Kekelidse (Collab. NA48), Talk at ICHEP 2000, Osaka, July 2000.

[41] J. Lee-Franzini, The second DAΦNE Phys. Handbook (ed. L.Maiani et al.), LNF, Frascati, 1995, p.761.

[42] R. Bartley et al., Proposal P253/CERN(SPSC), CERN/SPSC 2000-003,

[43] A. Alavi-Harati et al. Phys.Rev.Lett **83**, 917 (1999).

[44] G. D'Ambrosio, J. Portoles, Nucl. Phys. **B497**, 417(1997).

[45] J. Ritche, S. Wojcicki. Rev. Mod. Phys. **65**, 1149 (1992).

[46] A. Alavi-Harati et al. Phys.Rev.Lett **86**, 397 (2001).

[47] A. Alavi-Harati et al. Phys.Rev.Lett **84**, 1389 (2000).

[48] H.B. Greenlee, Phys. Rev. **D42**, 3724 (1990).

[49] L.M. Sehgal, Phys. Rev. **D183**, 1511 (1969).

[50] D. Ambrose et al., Phys. Rev. Lett. **84**, 1389 (2000).

[51] D. Ambrose et al., Phys. Lett. **423**, 385 (1998).

[52] Y.W.Wah (KTeV), Talk at ICHEP 2000, Osaka, July 2000,
B.Quinn (KTeV Collab.). Talk at Fermilab Seminar, 18 of August 2000.

[53] D.G. Dumn, A. Pich, Phys. Rev. Lett. **80**, 4633 (1998).

[54] G. Valenca, Nucl. Phys. **B517**, 339 (1998).

[55] D. Ambrose et al., Phys. Rev. Lett. **81**, 4309 (1998).

[56] T. Alfolder et al. (CDF collab.) hep-ex/9909003; Phys. Rev. **D61**, 072005 (2000); B. Aubert et al. (BABAR collab.) hep-ex/0102030; A. Abashian et al. (BELLE collab.) hep-ex/0102018;

[57] Y. Nir, hep-ph/9911321, Lectures at the XXVII SLAC Summer School Institute on Particle Physics, 1999;
Y. Nir, hep-ph/9810520, Lectures at the 1998 Europ. School of High Energy Phys., Univ. of St. Andrews, Scotland, Y. Grossman et al., hep-ph/9701231.

[58] P.Cooper, Talk on Run II B Physics Workshop, Fermilab, February 24, 2000.

[59] S. Bergman, G. Perez, hep-ph/0007170.

[60] T. G. Rizzo, hep-ph/9809526.

[61] J. L. Hewet et al., hep-ph/9603391, SLAC-PUB-7088, (1996).

[62] T. Hattori et al., hep-ph/9804412.

[63] G. Collangelo, G. Isidori, JHEP, 09, 009 (1998).

[64] A. J. Buras, L. Silvestrini, Nucl. Phys. **B546**, 299 (1999).

[65] A. J. Buras et al., **B566**, 3 (2000), hep-ph/9908371.

[66] L. Silvestrini, hep-ph/0009284.

[67] A. J. Buras et al., hep-ph/0007085;
A. J. Buras et al., hep-ph/0007313.

[68] G. Isidori, hep-ph/0101121.

[69] J. Ellis, hep-ph/0011396.

[70] S. Back et al., hep-ph/9907572;
hep-ph/0009105.

[71] Z. Xiao et al., hep-ph/9903347; hep-ph/9903348.

[72] Y. Kiyoto, T. Morozumi, hep-ph/9811457.

[73] G. Burdman, hep-ph/9806360;
hep-ph/9811457.

[74] G. Perez, hep-ph/0001037.

[75] G.-Ch. Cho, Eur. Phys. J. **C5**, 525 (1998).

[76] A. Masiero, O. Vives, hep-ph/0007320.

[77] S. Adler et al., Phys. Rev. Lett. **79**, 2204 (1997); Phys. Rev. Lett. **84**, 3768 (2000); hep-ph/0002015.

[78] J. Adams, et al., Phys. Lett. **B447**, 240 (1999), A. Alavi-Harati et al. Phys. Rev. **D61**, 072006 (2000).

[79] D. Ambrose et al., Phys. Rev. Lett. **81**, 5734 (1998).

[80] KTeV preliminary result, Conference of the APS Division of Part. and Fields, Columbus Ohio, Aug. 9-12, 2000

[81] Y.W.Wah (KTeV), Talk at ICHEP 2000, Osaka, July 2000.

[82] R. Appel et al., Phys. Rev. Lett. **85**, 2450 (2000).

[83] R. Appel et al., Phys. Rev. Lett. **85**, 2877 (2000).

[84] L. M. Barkov et al., Research Proposal to PSI, 1999; http://www.icepp.s.u-tokyo.ac.jp/meg.

[85] M. Bachman et al., MECO Proposal to BNL, 1997; http://meco.ps.uci.edu.

[86] R. N. Cahn, H. Harari, Nucl. Phys. **B176**, 135 (1980).

[87] T.S. Kosmas et al., Preprint Univ. of Ioannina IOA: 300/93, Ioannina 1993

[88] J. Bordes et al., Phys. Rev. **D60**, 013005 (1999).

[89] A. Belyaev et al., hep-ph/0008276.

[90] L. Littenberg, R. Shrok, Phys. Rev. Lett. **68**, 443 (1992); hep-ph/0010048.

[91] Z. Gagyi-Palffy et al., Nucl. Phys. **B513**, 517 (1998); Preprint RAL-090, Chilton, 1994.

[92] S. Davidson et al., Z.Phys. **C61**, 613 (1994).